AF den Brok

GEOLOGICA ULTRAIECTINA

Mededelingen van de
Fakulteit Aardwetenschappen der
Rijksuniversiteit te Utrecht

No. 95

An experimental investigation into the effect of water on the flow of quartzite

BAS DEN BROK

Uitgever/distributeur:
Fakulteit Aardwetenschappen
Budapestlaan 4
3584 CD Utrecht
Nederland

CIP-GEGEVENS KONINKLIJKE BIBLIOTHEEK, DEN HAAG

Brok, Sebastianus Willem Josef den

An experimental investigation into the effect of water on the flow of quartzite / Sebastianus Willem Josef den Brok. - Utrecht : Fakulteit Aardwetenschappen der Rijksuniversiteit Utrecht. - (Geologica Ultraiectina, ISSN 0072-1026 ; no. 95)
Proefschrift Rijksuniversiteit Utrecht. - Met samenvatting in het Nederlands.
ISBN 90-71577-49-X
Trefw.: kwarts / gesteente deformatie / drukoplossing.

An experimental investigation into the effect of water on the flow of quartzite

Experimenteel onderzoek naar het effekt van water op het vloeigedrag van kwartsiet

(met een samenvatting in het Nederlands)

PROEFSCHRIFT

TER VERKRIJGING VAN DE GRAAD VAN DOCTOR AAN DE RIJKSUNIVERSITEIT TE UTRECHT, OP GEZAG VAN DE RECTOR MAGNIFICUS, PROF. DR. J.A. VAN GINKEL, INGEVOLGE HET BESLUIT VAN HET COLLEGE VAN DEKANEN IN HET OPENBAAR TE VERDEDIGEN OP VRIJDAG 13 NOVEMBER 1992 DES NAMIDDAGS TE 16.15 UUR

DOOR

SEBASTIANUS WILLEM JOSEF DEN BROK

GEBOREN OP 16 SEPTEMBER 1961 TE VENRAY

PROMOTOR: PROF. DR. H.J. ZWART
CO-PROMOTOR: DR. C.J. SPIERS

Dit proefschrift werd mogelijk gemaakt met financiële steun van de stichting Aardwetenschappelijk Onderzoek Nederland (AWON) van de Nederlandse Organisatie voor Wetenschappelijk Onderzoek (NWO) (projektnr. 751.353.017)

"Wat de mens vóór het begin van de puberteit aan inzicht en kennis verwerft, is meer dan alles wat hij daarna leert."

Schopenauer

Aan mijn ouders

CONTENTS

ABSTRACT/SUMMARY

While it is well known from experimental work that small amounts of water (typically ≤1 vol%) greatly enhance the ductility of quartz rocks and cause a major mechanical weakening effect, the mechanism by which this occurs is poorly understood and the associated rheological behaviour is poorly constrained. This presents a serious problem with regard to understanding and modelling the mechanical behaviour of the quartz-rich continental crust, e.g., motion along major faults and shear zones.

It is widely believed that the 'water-weakening' effect seen in experiments on quartz is caused by the promotion of crystal-plastic deformation processes, and is an intracrystalline effect. Water-related point defects in the quartz crystal lattice are assumed to promote dislocation multiplication and/or mobility, but the question of *how* this actually happens has remained unanswered for almost 30 years. That the weakening mechanism is an intracrystalline process influencing crystal-plasticity is based on the observation of crystal-plastic type microstructures seen in experiments on 'wet' quartz but not on 'dry'. The effect is considered important for natural deformation since quartz tectonites show similar microstructures. In this thesis evidence is presented that solution-precipitation creep (SPC) and water-assisted micro-cracking rather than intracrystalline dislocation-plastic processes are responsible for the water-weakening effects seen in experiments on natural quartzite. The experimentally produced optical deformation microstructures also resemble those observed in many natural quartz tectonites, and it seems likely that the same mechanisms (SPC plus micro-cracking) may be important in nature.

In **chapter 1** the problems and the aims of the present study are defined. In the first part of **chapter 2** the evidence for crystal-plasticity in both naturally and experimentally deformed quartz rocks is critically reviewed. It appears, that this evidence is based mainly on optical and TEM deformation microstructures (undulatory extinction, subgrains, recrystallized grains, core-and-mantle structures, deformation lamellae, high dislocation densities, dislocation walls) and on crystallographic preferred orientations (CPO's). However, though *consistent* with crystal-plastic deformation, it is argued that these features cannot be used as conclusive evidence for plasticity. In most cases, other processes may also be responsible for their origin. In view of this, the experimental literature on the water-weakening effect in quartz rocks is also critically reviewed (the second part of chapter 2). It appears that many experimental results are inconsistent with an intracrystalline water-weakening effect and can be explained by other processes. Thus, it is inferred in chapter 2, that the origin of the water-weakening effect is open to discussion and requires careful attention.

Chapter 3 reports the results of deformation experiments carried out on a natural quartzite (Dongelberg quartzite, Belgium; grain size 150-250 μm) in a Griggs solid-medium deformation apparatus at a temperature of 800°C, a confining pres-

sure of ~1200 MPa, and constant strain rates ($\dot{\varepsilon}$) of 10^{-5}, 10^{-6}, and 10^{-7} s^{-1}. Samples were deformed 'dry' (≤200 ppm H/Si), 'as-received' (~30000 ppm H/Si), and 'wet' (~70000 ppm H/Si, i.e., with ~0.4 wt% added water) to strains up to 46%. The experiments essentially repeat previous experiments by Jaoul et al. (1984) who obtained apparently inconsistent results. These authors reported optical deformation microstructures (undulatory extinction, subgrains, recrystallized grains, deformation lamellae) and CPO's interpreted to indicate dislocation-plastic deformation, whereas the mechanical data were indicative of diffusional creep. The present mechanical data are in broad agreement with those of Jaoul and co-workers: at $\dot{\varepsilon} \leq 10^{-6}$ s^{-1} the 'wet' material showed behaviour consistent with a stress exponent for power law creep of $n \leq 1.3$, suggesting diffusional creep. However, though superficially similar to previous findings, detailed examination showed that the corresponding optical microstructure was characterized by axially oriented intra- and intergranular micro-cracks, plus similar arrays of small, new, sub-euhedral quartz grains. These arrays incorporated abundant micro-scale voids and channel structures, and were inferred to be axially oriented micro-cracks filled with small new grains grown out of solution. Grain boundaries parallel to the shortening direction (Z) often showed sub-euhedral overgrowth features, conspicuously absent on grain boundaries perpendicular to Z. The surface of a single crystal spacer added in line with the quartzite sample in one experiment showed numerous grain-scale indentation pits, indicative of pressure solution. From the mechanical data and microstructures it was concluded that SPC plus micro-cracking were responsible for most of the deformation of the 'wet' deformed material at $\dot{\varepsilon} \leq 10^{-6}$ s^{-1}. It appeared that the apparently 'crystal-plastic' deformation microstructures, including undulatory extinction, subgrains, and 'recrystallized' grains, can also be produced by coupled SPC plus micro-cracking.

In **chapter 4** optical measurements are presented of the c-axes of the old grains in samples deformed 'wet', at $\dot{\varepsilon} \leq 10^{-6}$ s^{-1}, to 40 and 46%strain. *No* significant old-grain CPO was found, supporting the conclusion of chapter 3 that most of the deformation occurred by SPC and micro-cracking. The results differ from the previous work of Den Brok & Spiers (1991), who reported moderately strong CPO's in such samples, because special precautions were taken in the present study, to avoid artificial biasing of the data (i.e., unintentional selective sampling of grains with highest birefringence). The optically measured old-grain CPO's reported in the experimental literature on quartz (Tullis et al. 1973, Jaoul et al. 1984, Dell'Angelo & Tullis 1986) are probably also affected by artificial bias, and may be as weak as those measured in the present study.

Chapter 5 reports a Fourier transform Infra-red (FTIR) spectroscopy study of samples deformed 'as-received' and 'wet' at $\dot{\varepsilon} \approx 10^{-7}$ s^{-1}. The aim was to determine whether or not the water-weakening effects reported in chapter 3 were associated with any changes in intragranular water content, and hence to test further the hypothesis of SPC versus intracrystalline water-weakening. Though the 'wet' samples were maintained for 14-22 days under high P-T conditions and were ≥9 times

weaker than samples deformed 'as-received', on average, added water did not diffuse into the quartz grains within measurement resolution (100-500 ppm H/Si). Similarly, no evidence was found for any diffusion of water out of the grains in samples deformed 'as-received' during experiments of 6-22 days. Since water concentrations of 100-500 ppm H/Si are not sufficient to cause a significant weakening effect in single crystals, it was concluded that intragranular water played no significant role in the observed water-weakening effect. This supports the conclusion that water-weakening seen in experiments on quartzite is caused predominantly by SPC and micro-cracking.

In **chapter 6** the experimental results obtained for 'wet' samples are compared with microphysical models for SPC. The micro- plus grain boundary structure seen in the 'wet' deformed quartzites appear to be most consistent with an SPC-model which assumes a boundary consisting of μm-scale islands bounded by intragranular micro-cracks. Good agreement between the mechanical data and this SPC-model is obtained when the rate of deformation is assumed to be controlled by diffusion within the island-island contacts. These may either (i) have a fine-scale, dynamically stable, internal channel structure with channels of ≤1-25 nm diameter, *or* (ii) the crack-bound island-island contacts may be solid, with mass transfer occurring by water-defect assisted solid-state grain boundary diffusion.

In conclusion (**chapter 7**) the present work has shown that the water-weakening effects seen in experiments on natural quartzite are almost certainly caused by SPC and micro-cracking. It also appears that SPC plus micro-cracking are capable of producing optical microstructures commonly regarded indicative of dislocation-plastic deformation (undulatory extinction, subgrains, 'recrystallized' grains). These microstructures should therefore not be viewed as exclusively diagnostic of dislocation-plastic mechanisms. The implications of the results for the crustal strength profile are also briefly discussed. It appears that SPC is possible in the continental crust under realistic conditions, and that a brittle-ductile transition between 5-25 km is predicted. However, reliable strength profiles appear to be location specific and cannot yet be ideally constructed, since SPC-models predict that the strength is highly grain size and grain boundary structure dependent. The thesis is closed with some suggestions for further research.

Chapter 1

INTRODUCTION: DEFINITION OF PROBLEMS AND AIMS

1.1 GENERAL BACKGROUND

Quartz is a major constituent of the upper and middle crust and so can be expected to play a major role in controlling crustal mechanics and deformation processes. Deformed quartz rocks are common in major fault zones and orogenic belts and show a remarkably wide variety of deformation microstructures and crystallographic preferred orientation (CPO) patterns. Quartz tectonites therefore have a high potential for storing information about deformation history. So, to understand crustal mechanics, for example the mechanics of motion on major crustal shear zones, and to interpret the microstructures observed in deformed quartz rocks, an understanding of the deformation mechanisms and associated rheological properties of quartz rocks is needed (e.g., Kirby 1985, Knipe 1990, Hacker et al. 1990). Much work has been done towards this end, but many problems remain controversial and unresolved (e.g. Paterson 1989, Koch et al. 1989, Kronenberg et al. 1990, Tullis 1990, Evans & Dresen 1991).

Two types of (ductile) deformation mechanisms are commonly believed to be important in quartz rocks in the continental crust namely, crystal-plastic deformation (glide and/or climb of dislocations) and solution transfer (pressure solution) (e.g., Hobbs et al. 1976, Nicolas 1984, Knipe 1989). The former is generally regarded to be far more important than the latter under almost all metamorphic conditions and especially in shear zones (see Hobbs et al. 1976, Wenk & Christie 1991, Schmid & Handy 1991). This view is based mainly on two arguments. Firstly, optical and transmission electron microscopy (TEM) microstructures (such as undulatory extinction, subgrains, recrystallized grains, deformation lamellae, high dislocation densities, dislocation walls, helical dislocations, etc.) regarded as indicative of crystal-plastic deformation are very common in deformed quartz rocks in the continental crust. Secondly, intensely deformed quartz rocks (e.g. mylonites) commonly show strong CPO's, which are also believed to be indicative of crystal-plastic deformation (e.g., Wenk 1985, Law 1990). Accordingly, since quartz is so abundant in the middle and upper continental crust, the mechanical behaviour of that part of the crust is widely assumed to be controlled by *crystal-plastic* deformation (of quartz) (e.g., Kirby 1985, Carter & Tsenn 1987, Ord & Hobbs 1989).

It is widely agreed from deformation experiments on quartz that the presence of water is essential to make quartz flow under the conditions prevailing in the continental crust (e.g., Jaoul et al. 1984, Mainprice & Paterson 1984). This 'water-weakening effect' is widely assumed to be intracrystalline in origin. Water-related point defects in the quartz lattice are assumed to promote the dislocation mobility, and hence make ductile flow of the continental crust possible via crystal-plasticity.

However, the exact mechanism responsible for the water-weakening effect, remains poorly understood to date, and has been source of controversy for almost 30 years (see, e.g., reviews by Blacic & Christie 1984, Koch et al. 1989, Paterson 1989, Tullis 1990).

1.2 DEFINITION OF PROBLEM TO BE ADDRESSED

The main problem concerning the water-weakening effect in quartz is the question of *how* water promotes the dislocation-plastic deformation processes assumed to occur in nature and experiment. When Griggs & Blacic (1964, 1965) first discovered the weakening effect of water, they postulated that water had diffused into the crystal lattice and had facilitated the glide of dislocations. Later, however, McLaren & Retchford (1969) argued that water facilitated dislocation *climb* rather than dislocation glide. Later still, Baëta & Ashbee (1970) argued that water essentially facilitated the *nucleation* of dislocations, and that glide and climb would be as difficult as in 'dry' material. It is still not clear today whether water can facilitate glide, or climb, or the nucleation of dislocations (see comments by Paterson 1989, Tullis 1990, Fitz Gerald et al. 1991).

Aside from the above, other processes may also be responsible for the water-weakening effects seen in quartz, at least in experiments. For example, Kirby & Kronenberg (1984) and Kronenberg et al. (1986) found out that, in experiments on natural single crystals, added water promoted stable micro-cracking rather than crystal-plastic processes. The strains that could be attributed unequivocally to crystal-plastic processes in these samples were only very small (e.g., $\leq$0.5% strain in experiments described by Fitz Gerald et al. 1991). Furthermore, the water-weakening effect seen in 'wet' synthetic single crystals (containing grown-in water) was recently shown to be related to the very specific way in which the water was grown into the crystal lattice (McLaren et al. 1989), and is not expected to be of great importance to processes occurring in the continental crust.

In this thesis, attention is focussed on the water-weakening effects seen in experiments on natural polycrystalline quartz rocks. When deformed, these polycrystals commonly show optical deformation microstructures and old-grain CPO's, believed to be indicative of crystal-plastic deformation (Tullis et al. 1973, Jaoul et al. 1984, Dell'Angelo & Tullis 1986). These experiments are important since they provide perhaps the strongest experimental support for crystal-plastic deformation as the dominant mechanism of crustal deformation. Yet, some of these experiments have also yielded results that seem to be inconsistent with predominance of crystal-plastic mechanisms, the two principal consistencies of which are summarized below:

(i) Kronenberg et al. (1986; but also Rovetta et al. 1986, and Gerretsen et al. 1989) have demonstrated that water cannot diffuse fast enough into quartz to explain the rapid water-weakening effect seen in experiments such as those of Tullis et al. (1973) in terms of an intracrystalline effect. Kronenberg et al. (1986) measured diffusive penetration velocities of less than 1 to 10 μm per day. Yet, quartzites with grain sizes as large as 100 to 200 μm became water-weakened in less than 2 hours in the experiments of Tullis & Yund (1985). Tullis & Yund (1985) suggested that micro-cracks could have been responsible for the relatively rapid uptake of the water, but these never have been observed. This raises the question of how is quartzite made ductile and easily deformable in the presence of added water, but without conventional diffusion of the added water into the grains?

(ii) Jaoul et al. (1981, 1984) determined the flow behaviour of natural quartzites deformed with added water. The quartzites showed a very low stress exponent for power law creep (n=1.2-1.4). This is indicative for a diffusional deformation mechanism, and cannot be explained by dislocation glide and climb, i.e., by crystal-plastic deformation. But the optical and TEM deformation microstructures were reported to be indicative of dislocation creep. How can we explain this?

It is the aim of this thesis to investigate this enigmatic behaviour, in order to find out *how water weakens quartzite.*

1.3 AIMS

In order to answer the above questions, I have repeated certain critical experiments of Jaoul et al. (1984) on natural quartzite (with added water) to obtain renewed microstructural plus mechanical evidence for the predominant deformation mechanisms (e.g., fluid-assisted diffusional creep versus dislocation creep to explain the very low stress exponent reported by Jaoul et al. 1981, 1984), and to look for evidence for micro-cracking (to potentially explain the inferred relatively rapid uptake of water by the grains). The results are presented in chapter 3. In addition, optical CPO studies were carried out to assess the role of crystal-plastic mechanisms versus diffusional mechanisms (chapter 4). Also, Fourier-transform infrared (FTIR) spectroscopy was carried out to measure the intergranular water contents of the deformed, water-weakened samples and to make comparisons with the starting material. This was intended to reveal whether or not water penetrated the quartz grains during the experiments (chapter 5). Lastly, the mechanical data were compared with models for solution precipitation creep (SPC), to assess whether the data are consistent with the models, and thus to gain insight into the operative microphysical processes (see chapter 6). However, in the next chapter, existing evidence for crystal-plastic deformation will first be critically reviewed.

Chapter 2

CRYSTAL-PLASTICITY IN QUARTZ: THE EVIDENCE REVIEWED

In the previous chapter, it was pointed out that the mechanism by which water promotes crystal-plastic processes in quartz is still poorly understood. This clearly needs to be resolved, since water-enhanced crystal-plasticity is believed to be the dominant deformation mechanism in most quartz rocks in the continental crust. In this chapter, existing microstructural and textural evidence for crystal-plastic deformation plus water-weakening in quartz rocks will be critically reviewed, both for naturally and experimentally deformed rocks. It will be shown that whereas the traditional evidence for crystal-plasticity is compelling, other interpretations are also possible, at least in some cases. In view of this, the experimental literature on quartz will also be reviewed, and it will be shown that existing (experimental) evidence for crystal-plasticity and water-weakening is also open to various interpretations. In addition, the review provides important background for the remainder of the thesis.

2.1 'CRYSTAL-PLASTIC' DEFORMATION MICROSTRUCTURES

The deformation microstructures seen in both naturally and experimentally deformed quartz rocks and regarded as indicative of crystal-plastic deformation include undulatory extinction, subgrains, recrystallized grains, core & mantle structures, and deformation lamellae (e.g., Schmid & Handy 1991). These microstructures will be described and discussed below.

2.1.1 Undulatory extinction and subgrains

Undulatory (or undulose) extinction is caused by slight differences in orientation of the crystal lattice within single grains. It is very common, both in naturally as well as experimentally deformed quartz rocks. In most cases the extinction changes in a *dis*continuous way, rather than continuously, so that the old deformed grain is subdivided into a variable number of subgrains. Across the subgrain boundaries, the crystal lattice is commonly rotated by 0.5 to 5°. Transmission electron microscopy (TEM) studies on naturally deformed quartz rocks (White 1971, 1973a, McLaren & Hobbs 1972) have shown that subgrain boundaries consist of cellular dislocation networks, and that subgrains themselves have a low to moderate dislocation density (these dislocations give no rise to undulatory extinction). *Continuous* undulatory extinction is rare in nature. Even when the extinction appears to be *optically*

continuous, TEM-work on naturally deformed quartzites (White 1973a) showed that at least in some cases it was caused by arrays of very narrow subgrains.

Subgrains may be elongated (Fig. 2.1a) or equidimensional (Fig. 2.1b). In nature, elongated subgrains are, almost without exception, oriented sub-parallel to <c>, and the sides are parallel to prismatic planes (e.g., Sander 1911). Equidimensional subgrains have boundaries that are mostly oriented sub-parallel to rhombic, prismatic, and/or basal planes (White 1975). Subgrain boundaries are commonly decorated with fluid inclusions.

Before the nineteen sixties, subgrains and undulatory extinction were believed to be the result of cataclasis (also referred to as *crushed quartz*, or, in the German literature of the time: *Kataklastische Zerquetschung*, *Innere Zertrümmerung*, or *Kataklasstruktur;* e.g. Böhm 1882, Becke 1893, Sederholm 1895, Weinschenk 1902, Sander 1911, Griggs & Bell 1938, Hietanen 1938, Fellows 1943, Riley 1947). But as soon as structural geologists discovered that quite similar microstructures could be developed in deformed metals, and that metallurgists explained these microstructures in terms of dislocation processes, the cataclasic theory of undulatory extinction plus

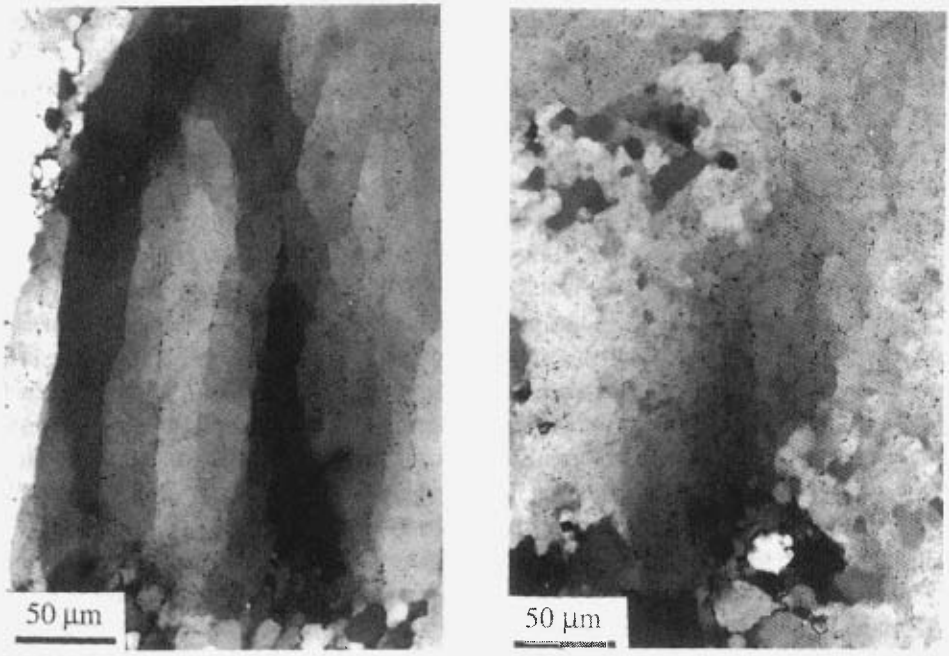

Fig. 2.1 *Optical micrographs (crossed polars) of naturally deformed quartz rocks showing (a) subgrains, elongated parallel to <c>, and (b) equidimensional subgrains. Note the presence of fluid inclusions on the subgrain boundaries.*

subgrain development was abandoned (e.g. Balk 1952, Bailey et al. 1958, Voll 1960, White 1971, 1973a, Bell & Etheridge 1973, and Wilson 1973). In addition, White (1971, 1973a, 1975) and McLaren & Hobbs (1972) demonstrated using TEM the presence of dislocations and dislocation networks in naturally deformed quartz, that looked quite similar to those encountered in crystal-plastically deformed metals. By analogy to theories developed by metallurgists to explain crystal-plastic deformation of metals, undulatory extinction and subgrains in quartz thus became accepted as developed by climb of dislocations into (low energy) dislocation walls, or networks.

In addition to the above, it should be noted that not all the undulatory extinction and subgrains encountered in quartz are necessarily the result of deformation. Crystal growth processes may also produce them. Subgrains parallel to <c> are, for example, developed in spherulitic quartz, and in some types of growth fibres. Note that dislocation networks may also develop by growth processes (e.g. McLaren & Phakey 1965) and by crack healing (e.g. Carstens 1969, Bakker 1992).

2.1.2 Dynamic recrystallization microstructures

Dynamic recrystallization is a process which accompanies crystal-plastic deformation of quartz rocks under appropriate conditions, both in nature and experiment. It is commonly believed to occur by (i) the progressive misorientation of subgrains to form new grains, and/or (ii) the migration of high angle grain boundaries (e.g. Urai et al. 1986). The first process is usually referred to as *rotation recrystallization* (e.g. White 1975, 1976). During this process, subgrains are believed to progressively mis-orientate due to the addition of new dislocations (generated by crystal-plastic deformation) into the dislocation walls (the subgrain boundaries). By definition, subgrains become recrystallized grains when the misfit across the subgrain boundary is more than several degrees.

The second process (grain boundary migration) may be driven by internal strain energy (dislocations, point defects, fluid inclusions), *or* by the grain boundary surface energy. In the latter case (also referred to as *normal grain growth*) the surface energy is decreased by straightening out of irregular grain boundaries and/or by grain growth.

Whereas in metals, transfer of material across grain boundaries mostly occurs in the solid-state, the (sub)grain boundaries in recrystallized quartz rocks commonly contain significant numbers of fluid inclusions (e.g. White & White 1981), so that mass transfer across the grain boundaries may have occurred by solution-precipitation processes as observed in various salt rocks (Urai 1983, Spiers et al. 1986).

Dynamic recrystallization often results in so-called *core-and-mantle structures (e.g. White 1976).* Deformed quartz grains with a core-and-mantle structure have a relatively undeformed core, showing undulatory extinction and subgrains, and have a mantle consisting of recrystallized grains. The transition from the subgrains (in the core) to the recrystallized grains (in the mantle) may be gradual, or may be abrupt.

When the transition is gradual, and when the size and the shape of the subgrains is similar to that of the new recrystallized grains, then this structure is commonly thought of as having been originated by rotation recrystallization (this may have been the case, for example, in Fig. 2.2a & b). More often, however, the subgrains in the center of the old grains are relatively large and elongated compared to the recrystallized grains at the rim of the old grain, and the transition between the subgrains and the new grains is abrupt. In this case, strain-induced grain boundary migration recrystallization is commonly believed to be responsible for the core and mantle structure (this may, for example, be the case in Fig. 2.2c). In both cases, deformation is thought to have been concentrated at the grain boundaries.

Dynamic recrystallization is used as an argument for crystal-plastic deformation (e.g., Schmid & Handy 1991) when it is thought to be driven by internal (crystal-plastic) strain energy.

In nature, new recrystallized quartz grains very commonly occur in planar arrays, which are often oriented parallel to the shortening direction (Z) (e.g., Fig. 2.3). These arrays are sometimes interpreted to be the result of precipitation of new grains in extensional fractures (e.g. Wickham 1972).

2.1.3 Deformation lamellae

Deformation lamellae are found in naturally (Fig. 2.4) and experimentally deformed rocks. They are approximately planar features, commonly 0.5 to 5 μm wide and with a slightly different refractive index, and occur in densely spaced arrays at 30 to 60° to Z. They are mostly sub-basal (the poles to the lamellae make an angle of 10 to 30° to <c>), and they are commonly bended slightly, which gives rise to extinction bands oriented perpendicular to the lamellae (the bending axis is commonly parallel to an <a> axis; e.g. Bailey et al. 1958). In naturally deformed quartz rocks, in many cases, deformation lamellae contain abundant, very fine and densely spaced fluid inclusions, giving the lamellae a brownish colour. The lamellae are then referred to as *Böhm lamellae* (Fig. 2.4b). Deformation lamellae are commonly believed to represent late stage deformation structures, responsible for only very small amounts of strain (e.g. Sander 1911, Riley 1947, Turner 1948, Naha 1958, Christie & Raleigh 1959, Turner & Weiss 1963).

Böhm (1882) and Becke (1893) were among the first who reported the presence of deformation lamellae in naturally deformed quartz rocks. Because of the abundance of very fine inclusions, Becke (1893) concluded that the lamellae were partially healed extensional shear fractures. Others (e.g. Mügge 1898, Sander 1911, Fairbairn 1941, Turner 1948) believed that the lamellae were the result of *translation gliding*, the mechanism of which remained questionable. White (1971, 1973b) has shown that natural deformation lamellae mostly consist of narrow subgrains (with subgrain walls consisting of dislocation networks), and according to him they are essentially recovery

structures in most cases. In some cases, however, deformation lamellae appeared to consist of individual subgrain walls, deformation twins, fractures, or dislocation debris in slip bands.

From experimental work, Christie et al. (1964a) argued that the lamellae consisted of planar arrays of edge dislocations and thus indicative of dislocation glide, but this appeared to be incorrect. These experimental lamellae appeared to be either Brazil twins (McLaren et al. 1967), or consisted of glass (Christie & Ardell 1974), the latter of which suggests that they originated by defectless yielding.

2.1.4 Discussion

The optical deformation microstructures described above are widely regarded as indicative of crystal-plastic deformation. In summary, this is based mainly on the following: (i) the optical deformation microstructures look like those observed in crystal-plastically deformed plus recrystallized metals, and (ii) dislocations, and dislocation networks are produced during deformation that look like those observed in crystal-plastically deformed metals. It will be argued below, however, that while these microstructures are *consistent* with crystal-plastic deformation, they cannot necessarily be used as unambiguous evidence for crystal-plastic deformation.

Firstly, it is clear that the first argument (that optical deformation and recrystallization microstructures *look* like those encountered in plastically deformed metals) cannot be used as an immutable argument that crystal-plastic deformation was dominant, or occurred at all. The resemblance means that these microstructures are consistent with crystal-plastic deformation, but they are also consistent with microstructures expected for cataclasis plus solution transfer. Indeed geologists

Fig. 2.2 *Optical micrographs (crossed polars) of naturally deformed quartz rocks showing (a) recrystallization concentrated along grain boundaries of internally deformed grains. Locally, the transition from the core of the larger grains to the recrystallized mantle is gradual, and the subgrains (in the core) are of similar size as the new grains (in the mantle). In this case, rotation recrystallization may have caused the core and mantle structure. (b) Another example where, locally, the transition from the subgrains in the core grade smoothly into the recrystallized grains of the mantle, indicative of rotation recrystallization. (c) Core and mantle structure where the transition from the larger, elongated subgrains in the core, to the smaller equidimensional recrystallized grains in the mantle, is abrupt. This is indicative for grain boundary migration recrystallization. (d) Another example of abrupt transition from larger elongated subgrains to smaller equidimensional recrystallized grains indicative of grain boundary migration recrystallization.*

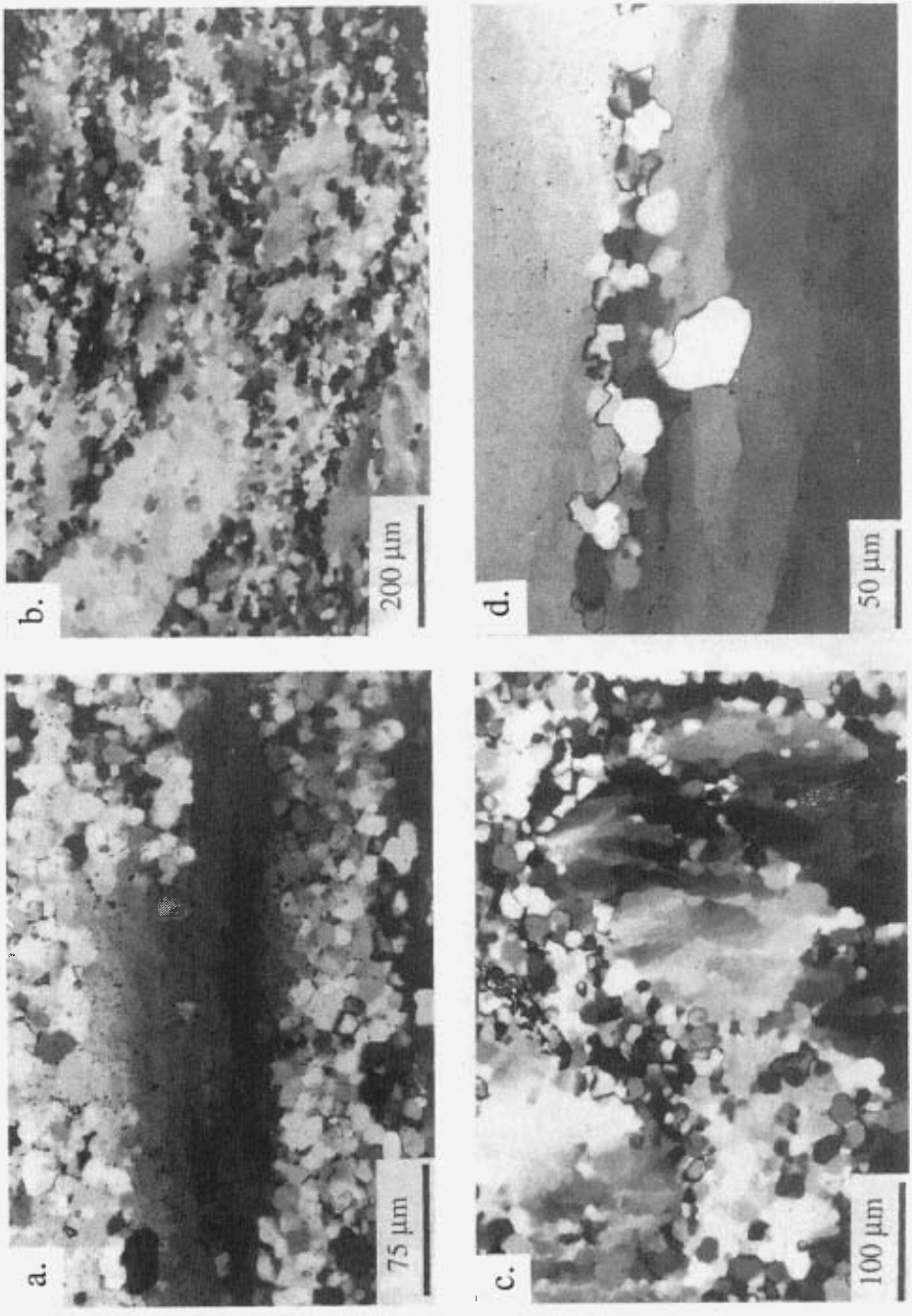

Fig. 2.2 *(Explanation see previous page)*

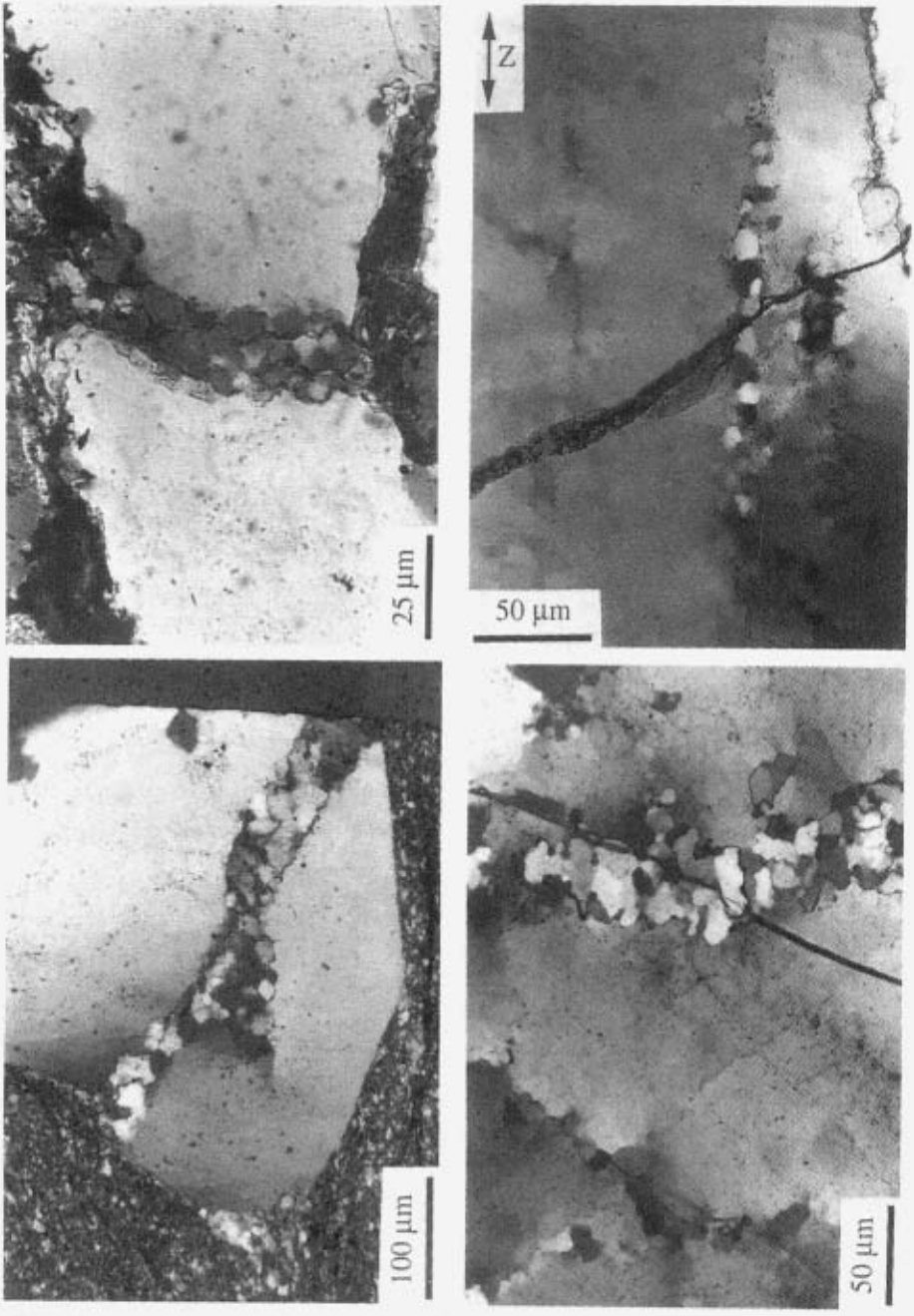

Fig. 2.3 *Optical micrographs (crossed polars) showing arrays of recrystallized grains which are sometimes interpreted as indicative for localized crystal-plastic deformation and subsequent recrystallization (e.g. Tullis et al. 1973 or Bowler 1989), or as extensional cracks, filled in by newly precipitated grains (e.g., Wickham 1972).*

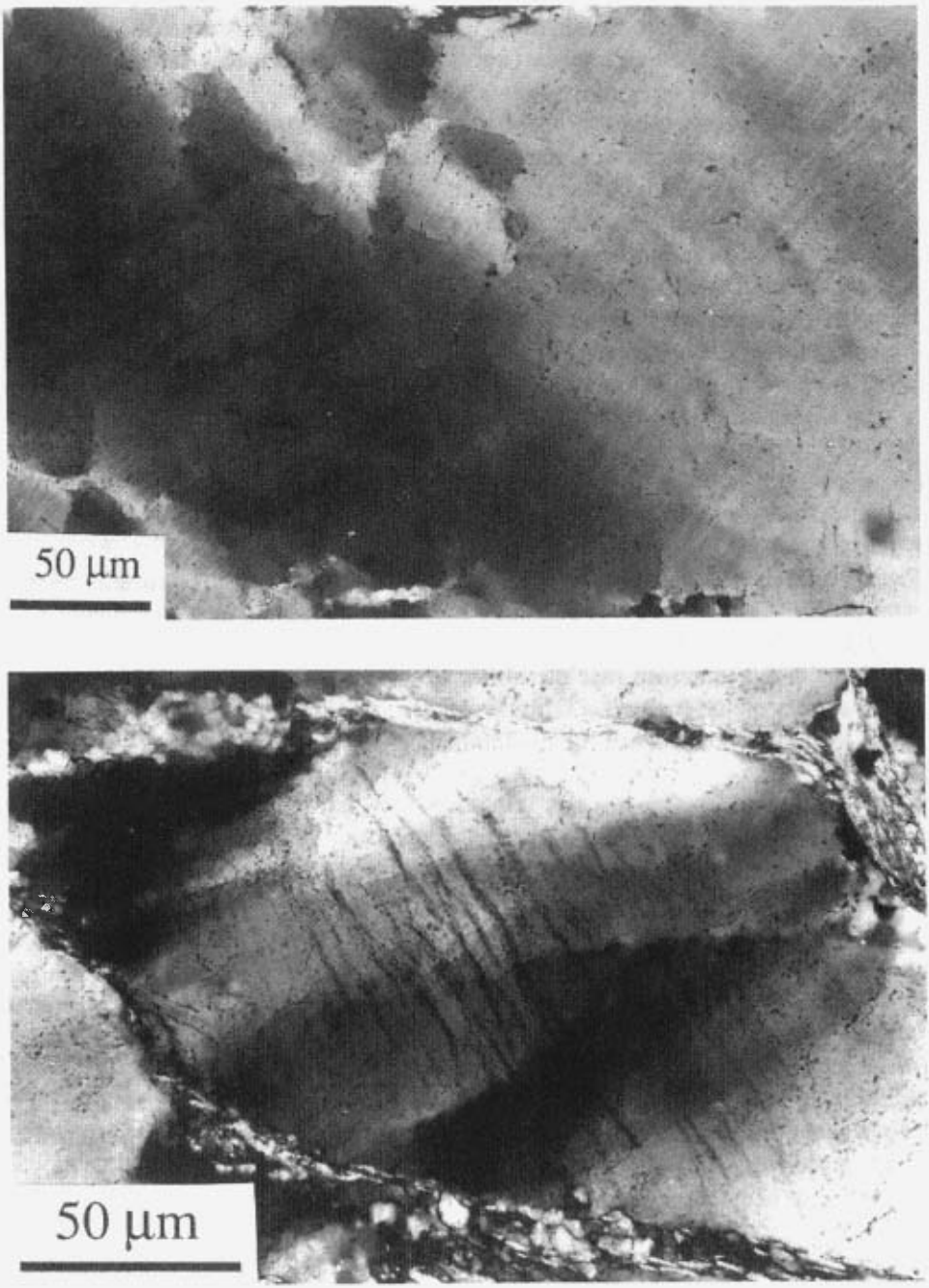

Fig. 2.4 *Optical micrographs (crossed polars) of naturally deformed quartz rocks showing (a) subbasal deformation lamellae, and (b) subbasal Böhm-lamellae, containing large amounts of tiny fluid inclusions.*

previously explained similar microstructures by cataclasis plus crack healing and/or sealing processes by solution transfer (e.g. Becke 1893, Sederholm 1895, Sander 1911, Griggs & Bell 1938).

The same is true for the argument that dislocation structures seen in deformed quartz look like those encountered in crystal-plastically deformed metals. In this case, dislocations may also form by various other deformation processes, such as fracturing and crystal growth (e.g. Carstens 1969, Fitz Gerald et al. 1991, Bakker 1992). Unfortunately, insufficient is presently known about these dislocation-generating processes to be able to say exactly which dislocation structures *can* and *cannot* be developed by, e.g., crystal-plastic deformation versus fracturing and/or crystal growth. Some information may be inferred from crystal growth experiments at hydrostatic and relatively low P-T conditions (e.g., Grant & White 1978), but the morphology of dislocation structures produced, for example, in overgrowths on inhomogeneously stressed polycrystalline natural material at high P-T conditions, remains essentially unclear. Appropriate experiments are lacking. Note further that the presence of dislocations may indicate that *some* crystal-plastic deformation occurred, but the contribution of this to the bulk strain cannot necessarily be deduced.

Finally, the presence of deformation lamellae should not be used as argument for crystal-plastic deformation either, without first finding out how exactly lamellae form, a point previously made by White (1973b).

It is concluded therefore that the above described optical and TEM deformation microstructures are all *consistent* with crystal-plastic deformation, but that they cannot be used as *definitive* evidence for its dominance or even occurrence.

2.2 C-AXES PREFERRED ORIENTATIONS (CPO's)

In naturally deformed quartz rocks (mylonites) CPO's are very common. At present, these CPO's are generally regarded as evidence for crystal-plastic deformation (e.g. Wenk 1985), which is based predominantly on comparison with metals and on computer simulations of CPO development in quartzite by dislocation glide (e.g. Etchecopar 1977, Lister et al. 1978, Jessel & Lister 1990, Wenk et al. 1989). Quite natural looking CPO's have been produced by this method. In materials science, CPO's are widely viewed as evidence for crystal-plastic deformation, and they are assumed not to develop during diffusional creep because of grain boundary sliding.

However, other processes may also be responsible for CPO's. First of all, glide along deformation lamellae (irrespective of the mechanism) is expected to produce CPO's, since lamellae are crystallographically controlled. They are mostly subbasal, so c-axes maxima near Z are expected. Note that Sander (1911) proposed that CPO's in quartz could have originated by slip along regularly spaced crystallographically controlled (shear) fractures. These fractures would later heal by solution-precipitation processes. Secondly, Kamb (1959; see also Green et al. 1970) proposed that CPO's

would develop by stress-controlled selective grain-growth (i.e., by recystallization). The growth of certain grains would be preferred over the growth of others depending on the orientation of the grain's c-axis with respect to the principal stress directions. The driving energy for grain growth may be provided by internal strain (dislocations), elastic distortion (stress), or surface energy (grain boundaries). There is both experimental (e.g. Hobbs 1968) and natural evidence (e.g. Shelley 1989) for the development of CPO's by selective grain growth. Also, in fibrous quartz veins CPO's are developed by selective growth (Cox & Etheridge 1983).

The fact that other mechanisms may be responsible for CPO's in quartz rocks means that one should be cautious using the presence of CPO's in deformed quartz rocks as evidence for crystal-plastic deformation. Only when c-axes are measured in deformed, non-recrystallized grains that lack intragranular fractures and deformation lamellae, can CPO's be considered strong evidence for crystal-plastic deformation. This is, however, mostly not the case. CPO's in natural rocks occur predominantly in recrystallized rocks (Green et al. 1970).

It is concluded therefore that whereas CPO's can be explained by and are consistent with crystal-plastic deformation, they should not be used as definitive, unambiguous evidence for it.

2.3 EXPERIMENTAL EVIDENCE FOR CRYSTAL-PLASTIC DEFORMATION OF QUARTZ

Having reviewed and assessed the microstructural and textural evidence for crystal-plastic mechanisms in naturally and experimentally deformed quartz rocks, we now proceed to review critically the *experimental* work on quartz and remaining (experimental) evidence for crystal-plasticity.

2.3.1 Experiments on 'dry' quartz single crystals

At room temperature and atmospheric pressure, 'dry' quartz (<100 ppm H/Si) fails by rupture along 'faults' in planes of high shear stress (Christie et al. 1964b). These 'faults' are crystallographically controlled. Differential stresses at failure approach the theoretical strength of quartz (~2400 MPa). At confining pressures up to ~2700 Mpa, samples are also brittle, still failing by rupture along crystallographically controlled planes of high shear stress (Christie et al. 1964b). The 'fault' planes are commonly parallel to the basal plane c(1000), to the unit rhombohedra r{10$\underline{1}$1} and z{01$\underline{1}$1}, and rarely to the prisms m{10$\underline{1}$0} and a{1$\underline{2}$10}. At 1300°C, 300 Mpa, and a constant strain rate of ~$10^{-5}s^{-1}$, 'dry' quartz single crystals are still brittle but now very small amounts of dislocations occur near crack tips at the sample ends (Doukhan & Trépied

1985). These dislocations have moved by glide over very small distances (~10 μm).

Very limited amounts of crystal-plastic strain can also be brought about by room temperature *indentation* tests. TEM-work revealed abundant micro-cracks, planar defects (Dauphiné twins) and locally very high densities of tangled dislocations near the cracks (Trépied & Doukhan 1982). Again, the dislocations have moved by glide over very small distances only.

At confining pressures of 1500 to 3000 Mpa, temperatures of 300° to ~700°C, and strain rates of $\sim 10^{-5} s^{-1}$, single crystals may be permanently deformed to very low finite strains. After deformation, the samples (oriented in the O^+ direction, i.e., at 45° to <c> and <a>) show *basal* deformation lamellae (Carter et al. 1961, 1964) over which the crystal has slipped in the crystallographic a<11$\underline{2}$0> direction (Christie et al. 1964a). At higher temperatures and lower strain rates, the deformation lamellae are predominantly oriented parallel to the prism m{10$\underline{1}$0} planes and slip along them occurred parallel to c[0001] (Griggs 1974, Blacic 1975). Heard & Carter (1968) observed that instead of *basal* lamellae, *sub*-basal lamellae were formed at lower strain rates, higher temperatures and lower confining pressure. Sub-basal lamellae are inclined 10° to 20° to the basal plane of quartz, at ~30° to the Z.

The origin of the above-mentioned deformation lamellae is not very clear. Christie et al. (1964a) and Carter et al. (1964) argued that the lamellae would have originated by dislocation glide, the lamellae consisting themselves of parallel arrays of edge dislocations. But McLaren et al. (1967) showed that at least some of the lamellae were actually Brazil twins in samples deformed at 500°C and ~1500 Mpa, and no dislocations were found. In addition to Brazil twins, samples deformed at 700°C showed some isolated, straight screw dislocations parallel to a<11$\underline{2}$0>. In the same samples, Christie et al. (1973) and Christie & Ardell (1974) found instead, that the lamellae were thin, ~50 nm wide zones of glass. Locally, the lamellae were associated with festoons of dislocations that were usually parallel to low-index crystallographic directions, notably <c>, <a> and <c±a>, but most of the quartz between adjacent lamellae was dislocation free. The lamellae therefore most likely originated by defectless, crystallographically controlled yielding and shear, resulting in melting (much like the deformation lamellae encountered in shocked quartz; e.g. Goltrant et al. 1991), with the nucleation of the dislocations being a side effect (see also Blacic & Christie 1984).

Summarizing, experiments have shown that at laboratory strain rates, 'dry' quartz single crystals can only be deformed ductilely at very high pressures, temperatures, and differential stresses. Deformation lamellae developed in these 'dry' samples are probably crystallographically controlled shear fractures rather than a crystal-plastic feature.

2.3.2 The classical hydrolytic weakening experiments and early models

Griggs & Blacic (1964) discovered that small amounts of water would dramatically reduce the strength of quartz and make quartz ductile. They deformed natural single crystals of quartz at a confining pressure of ~1500 Mpa and a temperature of 400 to 1000°C in a Griggs deformation apparatus (Griggs 1967, and see Appendix A) with talc as the confining medium in direct contact with the quartz. When the temperature was high enough to decompose the talc (≥600°C), the strength of the quartz dropped to zero within the sensitivity of their measurements. At a confining pressure of ~1500 Mpa, a temperature of 950°C, and a strain rate of $0.8 \cdot 10^{-5}$ s^{-1}, 'dry' single crystals yielded at a differential stress of ~1900 Mpa, whereas in contact with dehydrating talc they yielded at only ~200 Mpa (Griggs 1967). Griggs & Blacic (1964) reported that the deformed samples showed numerous deformation lamellae from which they inferred that the samples had deformed by glide of dislocations. Griggs & Blacic (1965) suggested that water, given off by the decomposition of the talc, had diffused into the quartz crystal lattice as interstitial point defects, i.e., $(H_2O)_i$, and had hydrolysed silicon-oxygen bonds, according to the chemical reaction:

$$\text{Si-O-Si} + H_2O = \text{Si-OH:HO-Si}$$

Griggs & Blacic proposed that this hydrolysis would reduce the Peierls stress for glide considerably (whence the term *'hydrolytic'* weakening), because the H:H bonds would be much weaker than the Si-O bonds.

It was soon realized by Griggs (1967), however, that only ~1 ppm H/Si would be needed to saturate the dislocations and cause the weakening effect, whereas the strength was reported to smoothly vary with much larger water contents. It was concluded therefore that water believed to be present in the bulk lattice, had to play a key-role in the weakening process too. It was then suggested by F.C. Frank (see Griggs 1967) that dislocations would propagate by dislocation kink migration, and that kinks would develop and move under low stress only when adjacent Si-O-Si bridges would be hydrolysed. Hydrolysis of neighbouring bridges at the kinks was proposed to occur by diffusion of water *through* the lattice. The more water dissolved in the lattice, the easier the dislocations kinks were predicted to propagate. The rate of deformation was thus believed to be governed by the diffusion of the water towards (and together with) the dislocations.

2.3.3 Experiments on 'wet' synthetic quartz

From 1965 onwards, experimental work on the water weakening effect was carried out almost exclusively using 'wet' synthetic single crystals. This material is optically clear and has a varying water content (from ~100 to~5000 ppm H/Si). The crystals have

been grown in NaOH or $Na(CO_3)_2$ solutions at moderate temperatures (300° to 400°C) and pressures (100 to 200 Mpa). Experiments on 'wet' synthetic single crystals were preferred over those on ' dry' natural single crystals with added water (as done by Griggs & Blacic 1964), because (i) the water was already present in the crystal lattice, (ii) samples with different water contents were readily available, and (iii) experiments could be carried out at atmospheric pressure, so that differential stresses could be measured more accurately.

Previously, the water in these 'wet' synthetic single crystals had been believed to be present in the quartz lattice in the form of $(H_2O)_i$ interstitial point defects (e.g. Griggs & Blacic 1965), and weakening was believed to be caused by promotion of the dislocation mobility by the water-related point defect structures. As mentioned above, Griggs (1967) proposed that water facilitated dislocation glide, but according to McLaren & Retchford (1969) water facilitated dislocation *climb* rather than glide, and according to Baëta & Ashbee (1970) the water in these single crystals would facilitate the *nucleation* of dislocations at the water-related interstitial point defects. But Aines et al. (1984) and Gerretsen et al. (1989) have later shown that the water in the 'wet' synthetic material is mainly present in molecular aggregates or clusters rather than point defects. These clusters, with a radius of typically 12 to 80 nm and containing ~200 molecules, were trapped during rapid growth of the quartz. In TEM they show up as planar or lens-shaped strain contrast features, aligned parallel to the prism m{$\underline{1}$100} planes. The water in these clusters has an abnormally high pressure (400 ± 150 Mpa). Furthermore, McLaren et al. (1989) demonstrated that if 'wet' synthetic quartz is heated to more than ~600°C for more than several hours, that rhombic micro-cracks and prismatic dislocation loops are nucleated at the high pressure clusters. With continued heating, the prismatic dislocations grow by climb, and dislocations in the rhomb plane originate by sealing of the rhombic micro-cracks (i.e. by deposition of quartz in the open fractures). Thus, a dislocation density of $\sim 5 \cdot 10^{12}$ m^{-2} is obtained, only by heating of the samples, without deformation. McLaren et al. (1989) suggested that the water-weakening effect was caused essentially by the nucleation of the dislocations and the micro-cracks at the high pressure clusters, and that the *glide* of dislocations in 'wet' synthetic quartz may be as difficult as in 'dry' quartz. The latter was supported by the fact that only very low finite strains could be obtained in 'wet' synthetic quartz before the samples fractured or recrystallized. At atmospheric pressure, strains of only a few percent (typically <5%; e.g. Linker et al. 1984) could be obtained before fracturing occurred; at higher pressures ($P_c \geq 300$ Mpa), and temperatures well above 650°C, plastic strains up to 15% could be obtained (to judge from stress-strain curves; e.g. Morrison-Smith et al. 1976), but detailed accounts of microstructural development at these higher strains are lacking in the literature.

2.3.4 Experiments on 'dry' natural single crystals with added water

Several studies have appeared on the water-weakening effects seen in experiments on natural single crystals deformed with added water (Blacic 1975, Kirby & Kronenberg 1984, Kronenberg et al. 1986, Ord & Hobbs 1986, Fitz Gerald et al. 1991). Whereas Griggs & Blacic (1964) suggested that water had diffused into the quartz as water-related point defects and had caused hydrolytic weakening, Kirby & Kronenberg (1984) and Kronenberg et al. (1986) showed that the weakness of crystals with added water was essentially caused by stable micro-cracking. Only minor crystal-plastic deformation had occurred according to these authors, as was indicated by the local occurrence of deformation lamellae.

Further, Kronenberg et al. (1986), Rovetta et al. (1986) and Gerretsen et al. (1989) demonstrated that no measurable amount of water could be diffused into the quartz at the P-T conditions at which the samples were deformed (T=800°C and P_c=1500 Mpa). According to them, the penetration rate of water into the quartz must have been less than 1 to 10 μm per day at these conditions, whereas samples of ~6 mm diameter could be deformed in several hours. Thus, it was inferred that micro-cracking had played a dominant role in both the deformation, as well as in allowing the water to penetrate the quartz sufficiently fast to cause the local plastic deformation.

Fitz Gerald et al. (1991) performed a detailed microstructural study of such experimentally deformed water-added crystals. It appeared, that even during the initial loading stage, samples had fractured axially on the sample scale. These fractures were healed, and moderate dislocation densities appeared to be developed in the vicinity of the fractures, either by the fracturing process, or by the healing (i.e. crystal growth) processes. The *deformed* samples showed similar microstructures, but greater numbers of fractures, higher dislocation densities, and now complete recrystallization had occurred, predominantly at one end of the samples. Deformation was restricted to the vicinity of the axial fractures (though only ≤0.5% strain) and to the recrystallized end of the sample (see Fig. 2.5). The dislocation microstructures around the healed fractures in the deformed samples showed local transitions from regions with dislocation structures consistent with easy glide and recovery (near the center of the cracks) into regions where dislocation structures indicated that glide and climb had been limited (further away from the center of the cracks). Regions more than 50 to 100 μm away from the crack center showed no dislocations and no permanent deformation. Fitz Gerald et al. (1991) assumed that the reason that the dislocations, which were originated by the fracturing and fracture healing processes, did not move far from the fracture into the undeformed material, was that diffusion of water through the lattice, or through the dislocations, was very slow. Almost all of the deformation was localized in the recrystallized, fine-grained polycrystalline aggregate at the sample ends, and this was postulated to have occurred by crystal-plastic deformation.

2.3.5 Experiments on fine-grained natural polycrystals (flints/novaculites)

Fine-grained quartz polycrystals (commonly novaculite or flint with a grain size of <5 μm) also show water-weakening. Vacuum heated novaculites (containing <100 ppm H/Si) deformed at a temperature of 1019°C, a confining pressure of 950 Mpa, and a strain rate of $1.7 \cdot 10^{-6}$ s^{-1}, yield at a differential stress of ~1740 Mpa, whereas the same material deformed with ~0.4 wt% added water at a temperature of 800°C, a confining pressure of 1590 Mpa, and a strain rate of $1.6 \cdot 10^{-6}$ s^{-1}, yields at ~200 Mpa (Kronenberg & Tullis 1984).

Broadly speaking, two deformation regimes are distinguished in the 'wet' deformed material (Green et al. 1970, Masuda & Fuijimura 1981): (i) at relatively low temperature, low water content, high strain rate, and high stress, the grains remain relatively small, become highly flattened with irregular grain boundaries, and

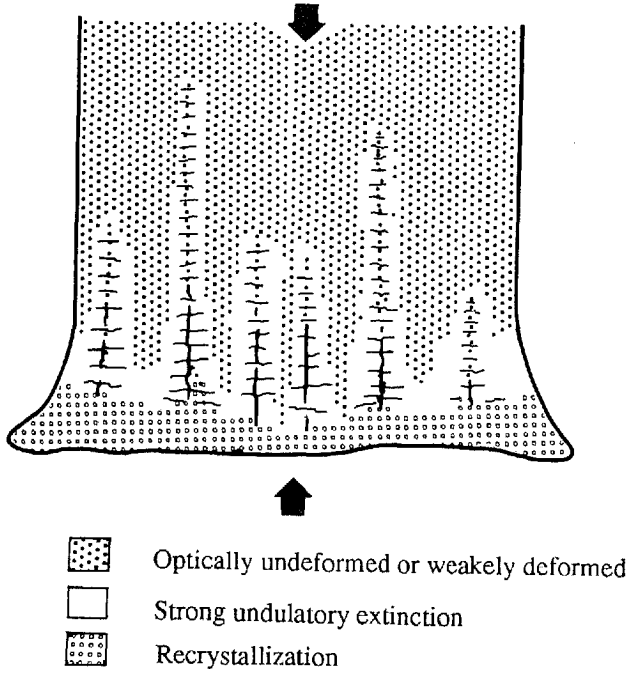

Fig. 2.5 *Schematically drawn section through a deformed water-added single crystal, showing distribution of optically deformed and undeformed parts. Horizontal cracks are interpreted to be unloading cracks. Arrows indicate loading direction. After Fitz Gerald et al. (1991). Temperature is 800°C, confining pressure is ~1640 Mpa, strain rate 10^{-5} s^{-1}.*

commonly contain deformation lamellae. Also a CPO develops with a maximum parallel to Z. (ii) At relatively high temperature, high water content, low strain rate, and low stress, the grains grow substantially during deformation, become equidimensional with straight grain boundaries, and show very few intracrystalline deformation features. A CPO develops, now consisting of a small circle distribution about Z with a half opening angle of ~50°.

In both regimes the deformation mechanisms remain improperly understood to date. Deformation may have occurred by dislocation glide and climb with water promoting the glide and/or recovery processes (e.g. Kronenberg & Tullis 1984). Alternatively, deformation may have occurred by solution transfer (e.g. Mackwell et al. 1989). The latter fits the observation that the grains grow substantially even when the samples are *hydrostatically* loaded with added water at high P-T conditions (typically T>500°C, P_c>1000 Mpa; Tullis & Yund 1982). Tullis & Yund (1982) proposed that the rate of (normal) grain growth was controlled by the rate of solution transfer across grain boundaries, which they assumed to contain water. SEM-observations of Mackwell et al. (1989) and Karato & Masuda (1989) show that fluid inclusions were indeed present in profusion at the grain boundaries in deformed fine-grained samples.

According to Green et al. (1970), the CPO's observed in these fine-grained rocks, were the result of strain-induced recrystallization at low temperature, and stress controlled selective (normal) grain growth at higher temperature. According to Tullis et al. (1973) and Kronenberg & Tullis (1984) the CPO's are caused by crystal-plastic deformation.

2.3.6 Experiments on natural quartzites

When natural quartzite is vacuum-dried at 800°C (<100 ppm H/Si) then its mechanical behaviour is similar to that of 'dry' single crystals and 'dry' fine-grained polycrystals. At T≈800°C, P_c≈1500 Mpa, and a strain rate of 10^{-7} s^{-1}, samples yield at a differential stress of 1000 to 1500 Mpa and develop abundant deformation lamellae, as well as fractures on the grain scale (Jaoul et al. 1984). By contrast, when deformed with ~0.4 wt% added water (at T=800°C, P_c-~1500 Mpa, and $\dot{\varepsilon}=10^{-6}$ s^{-1}; Jaoul et al. 1984) quartzites are 50 to 100 times weaker than the 'dry' material, and may be deformed ductilely up to high strains (50-70%).

As in the case of the fine grained quartz rocks, two broad types of behaviour are distinguished (Tullis et al. 1973; Jaoul et al. 1984):

(i) at low temperature, low water content, high strain rate, and high stress, large amounts of subbasal deformation lamellae and associated undulatory extinction are developed, as well as an *old-grain* CPO with a point maximum parallel to Z. The stress exponent for power law creep is commonly >2.

(ii) At high temperature, high water content, low strain rate, and low stress, large amounts of new, small equidimensional quartz grains and subgrains are formed, pre-

dominantly at the grain boundaries of the larger, original grains. The number of new grains increases with increasing strain. Deformation lamellae and undulatory extinction are relatively scarce or absent. An old-grain CPO develops, with maxima at 25 to 40° to Z depending on the exact experimental conditions. The stress exponent for power law creep commonly has a value between 1 and 2.

It is widely agreed that the water-weakening effect seen in experiments on quartzites is caused by promotion of glide and climb of dislocations by the added water, this being based on the presence of undulatory extinction, subgrains, recrystallized grains, deformation lamellae, and an original-grain CPO. There are, however, a number of observations that are inconsistent with this explanation, and these will be discussed below.

(i) In the experiments that show the water-weakening effect most clearly, and in which the quartzite samples are most ductile, the stress exponent for power law creep is very low (even as low as 1.2 according to Jaoul et al. 1981, and 0.89 according to Wang, Ord & Hobbs 1991, pers. comm.). This is not consistent with conventional dislocation glide and climb mechanisms being important, and points towards diffusional processes being responsible for the deformation.

(ii) As already mentioned, Kronenberg et al. (1986) have shown that diffusion of water into quartz is very slow (penetration rates were inferred to be less than 1-10 μm per day). Yet, in the experiments of Tullis & Yund (1985) quartzites with grain sizes up to 200 μm could be deformed ductilely (by addition of the water) in time spans less than 2 hr. This is inconsistent with a diffusion plus intragranular weakening process. It has been argued, that micro-cracking may be responsible for relatively rapid uptake during the experimental deformation of the quartzites (e.g. Tullis & Yund 1985); water could have diffused into the cracks and subsequently into the crystal lattice. Obviously, a very high micro-crack density would be required for such a mechanism (with spacings on the μm-scale), and no evidence for this has been reported yet. *Dislocation pipe diffusion* has also been put forward as a possible cause for the rapid penetration of the water (e.g. Tullis 1990), but calculations by Paterson & Luan (1990) have shown that this would require much higher dislocation densities than commonly observed in the starting materials. Alternatively, Fitz Gerald et al. (1991) proposed that *micro-cracking plus healing* could have been responsible for both *local* uptake of the water *and* for nucleation of abundant dislocations, with either bulk or dislocation pipe diffusion being responsible for further re-distribution of the water. However, such cracks have not been observed in the deformed quartzites.

(iii) Kronenberg & Wolf (1990) measured the intragranular water content (c_w) of experimentally deformed water-added quartzite using FTIR spectroscopy. The results showed that c_w for the deformed material was similar to the starting value, even though the samples were deformed in a ductile manner and were significantly weakened by the added water. This cannot be reconciled with the classic hydrolytic weakening concept since that requires easily measurable quantities of water to enter the lattice (several 1000 ppm H/Si at least) before weakening occurs. As an alternative explanation, Kronenberg & Wolf (1990) suggested that the added water could have

buffered the original c_w, so that the *original* intragranular water could have allowed the easy movement of the dislocations. They proposed that if no water had been added, then the original intragranular water would have diffused out of the grains, and the samples would have been stronger (Fig. 2.6). It is expected, however, that the diffusion of water *out* of the grains is several orders of magnitude slower than diffusion of water *into* the grains because the concentration gradient (Δc_w) is expected to be several orders of magnitude lower in the outward diffusion case. Kronenberg & Wolf's (1990) results are therefore inconsistent with a diffusion plus intragranular weakening process.

(iv) It appears that water-added quartz polycrystals are weaker at high pressure than at low pressure. This has been observed in quartzites (Kronenberg & Tullis 1984), but is better illustrated with their experiments on novaculite to which recourse is now made. With a grainsize of 3.6 to 4.9 μm, at a temperature of 800°C, a strain rate of $1.6 \cdot 10^{-6}$ s^{-1}, and with 0.5 wt% added water, samples deformed at a confining pressure of ~350 Mpa have a strength of ~700 Mpa, whereas samples deformed at a confining pressure of ~1500 Mpa have a strength of ~180 Mpa. The strength appears to be approximately inversely proportional to the confining pressure. The same behaviour is observed in experiments on the coarser-grained natural quartzites (see Kronenberg & Tullis 1984). It is widely assumed that the reason for this 'pressure effect' is that at higher pressure, more water can dissolve into the quartz (e.g. Kronenberg & Tullis 1984; Tullis 1990), but there is no experimental evidence for this. Moreover, a detailed model explaining the solubility increase with increasing pressure is lacking. However, Tullis & Yund (1982) reported that the rate of normal grain growth in water-added novaculite also increases with increasing pressure (at T=800°C), and correlated this increase in the rate of grain growth with the increase of solubility of quartz in a grain boundary solution. According to them, grain growth occurred by solution mass transfer across grain boundaries. Thus, the pressure effect on strength seen in the experiments on quartzite may also reflect a change in solubility of quartz and point towards deformation by solution transfer rather than a crystal-plastic deformation mechanism.

(v) The strength of water-added quartz polycrystals increases with slightly increasing grain size (Kronenberg & Tullis 1984). Combining data on various materials, the steady state flow stress is proportional to the grain size to the power 0.18. The effect of the grain size is also indicated by the fact that water-added fine grained quartz rocks may deform ductilely at relatively low confining pressures (300-500 Mpa; Green et al. 1970, Mainprice 1981) whereas coarse grained quartzites are still brittle at those pressures. Kronenberg & Tullis (1984) explained this grain size dependency of the strength by assuming that the finer grains would be saturated with water faster than the coarse grains. But they found no microstructural evidence for this mechanism (such as more deformation lamellae, or higher dislocation densities near the grain margins) nor did they find that samples progressively weaken with time (i.e., progressive diffusion of water in the grains). In fact, most of the water-added quartzites appeared to *strengthen* (rather than soften) slightly with progressive

A. Classical concept (e.g. Griggs 1967)

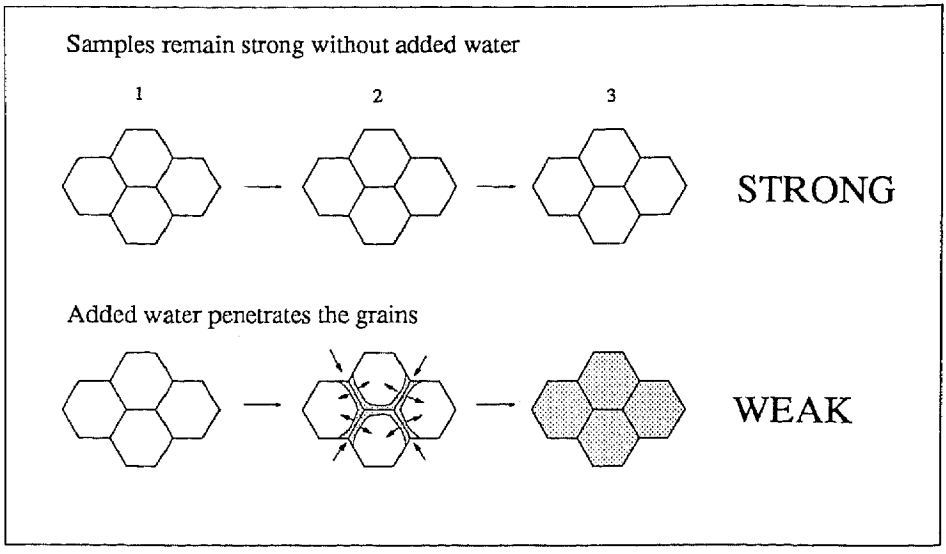

B. Concept of Kronenberg & Wolf (1990):

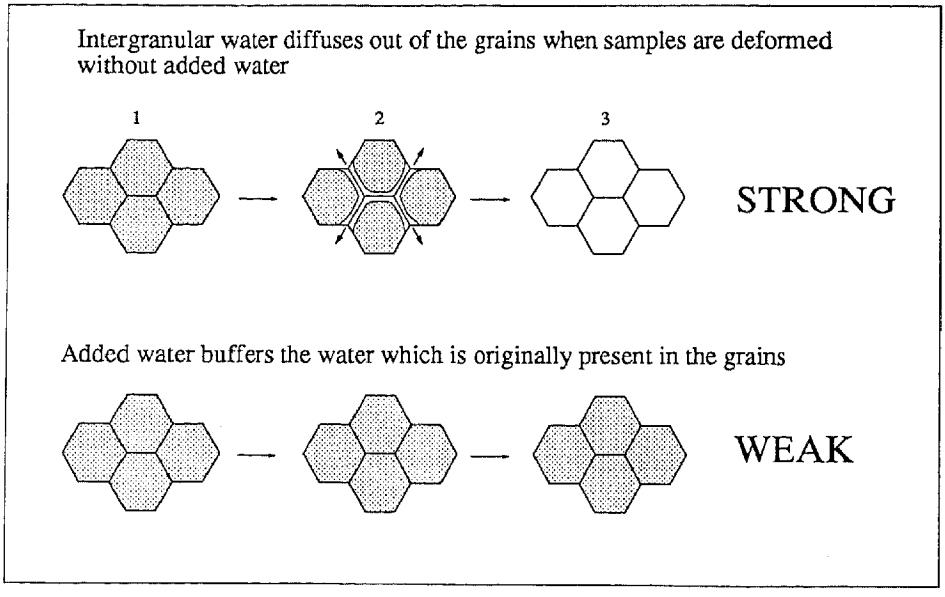

Fig. 2.6 *(Explanation see next page)*

deformation. Though the grain size dependency may point towards a role of solution transfer, its value (grainsize to the power 0.18) is rather low for that. Solution transfer models predict that the stress varies proportional with the grain size to the power 1 to 3 depending on the rate limiting process. When crystal-plastic mechanisms dominate, the flow strength generally decreases with increasing grain size due to phenomena such as the Hall-Petch effect (e.g. Nicolas & Poirier 1976).

2.3.7 Synthesis of previous experimental work

We will now synthesize and critically assess the evidence for crystal-plastic deformation provided by the experimental work reviewed above. The deformation experiments on quartz rocks have shown that the presence of water is essential for ductile deformation in the laboratory. Griggs & Blacic (1964, 1965) and Griggs (1967) assumed that this was caused by promotion of glide of dislocations by water-related point defects in the crystal lattice. Their assumption was based on the presence of deformation lamellae in the deformed single crystals which Christie et al. (1964a) had interpreted to be arrays of edge dislocations in 'dry' material. But these lamellae appear to consist of Brazil twins or glass in the 'dry' material, and probably formed by defectless yielding. Griggs & Blacic's (1964) experiments therefore do not provide evidence for dislocation-plastic deformation. This was confirmed by Kirby & Kronenberg (1984) and Kronenberg et al. (1986) who showed that single crystals with added water (such as in Griggs & Blacic's experiments) deformed predominantly by stable micro-cracking. On the basis of comparison between the dislocation microstructures observed in the deformed quartz with similar structures observed in crystal-plastically deformed metals and ceramics, Fitz Gerald et al. (1991) demonstrated that only very small amounts of crystal-plastic deformation (≤0.5 %) occurred in similar experiments, and only alongside axial sample-scale micro-cracks. In Fitz Gerald's (1991) samples, almost all of the deformation occurred in the fine-grained recrystallized sample ends. This may have occurred by crystal-plastic or by solution transfer processes. It is concluded therefore that the experiments on natural

Fig. 2.6 *Schematic diagram illustrating ideas of Kronenberg & Wolf (1990) about the weakening effect of added water on experimentally deformed quartzite. (a) Classical concept: water-added samples are weaker because the added water penetrates the original grains. (b) Kronenberg & Wolf's (1990) hypothesis: water-added samples are weaker because the added water buffers the water which is originally present in the grains. The samples deformed without added water are stronger because water diffuses out of the grains. Within the limits of resolution of* c_w*, both the classical hypothesis and that of Kronenberg & Wolf (1990) are inconsistent with the results of the present study.*

single crystals with added water provide no unequivocal evidence that crystal-plasticity was an important ductile strain producing mechanism. By contrast, there is substantial evidence that stable micro-cracking played an important role during deformation of these samples.

The experiments on 'wet' synthetic single crystals provide strong evidence that intragranular, dislocation-plastic processes occurred, but micro-cracking and/or solution-precipitation processes also appear to be involved in the nucleation of the dislocations in these samples, and the strains achieved were only very small (typically <5%) before the samples fractured or recrystallized. Furthermore, the observed crystal-plastic behaviour is due to the very specific way in which the water resides in the 'wet' synthetic material, namely, in tiny clusters containing water under very high pressure (McLaren et al. 1989). These clusters are conspicuously absent in natural quartz rocks (e.g. Kronenberg et al. 1990) so that the behaviour of the 'wet' synthetic material seems to be of little relevance to crystal-plastic deformation of quartz in the continental crust.

The experiments on fine-grained polycrystalline quartz rocks provided no conclusive evidence as to whether crystal-plastic or solution transfer processes were responsible for their deformation. The CPO's could be due to crystal-plastic mechanisms (Kronenberg & Tullis 1984) or due to oriented growth mechanisms (as suggested by Green et al. 1970) while the samples deformed by solution transfer.

Perhaps the strongest evidence for crystal-plastic deformation was provided by the experiments on natural quartzite by Tullis et al. (1973) who reported *old grain* CPO's in the deformed water-weakened samples. The samples also showed deformation microstructures that are consistent with crystal-plastic deformation (undulatory extinction, subgrains, recrystallized grains, deformation lamellae) but, on the other hand, the mechanical data (stress exponent for power law creep between 1 and 2) are not consistent with crystal-plastic deformation. Data on diffusion rates, and the effects of grain size and pressure in quartzites and novaculites are also inconsistent with crystal-plasticity. Whereas it is widely accepted that the experimentally deformed quartzites deformed by crystal-plastic mechanisms, it is concluded here that no firm statement can be made regarding the dominant deformation mechanisms.

It is inferred from the above that the evidence that crystal-plastic mechanisms are capable of producing large amounts of strain in experimentally deformed quartz materials is open to discussion. At least in some cases, solution transfer processes and micro-cracking may equally well have been responsible for water-weakening effects.

2.4 CONCLUSIONS

(i) The optical and TEM deformation microstructures observed in naturally and experimentally deformed quartz rocks such as undulatory extinction, subgrains, recrystallized grains and deformation lamellae, as well as the presence of CPO's, are

consistent with crystal-plastic deformation but do not provide unequivocal evidence for crystal-plastic mechanisms. Micro-cracking and solution-precipitation processes may, at least in some cases, also be responsible for such microstructures.

(ii) Deformation experiments on quartz have shown that water is needed to render quartz ductile and easily deformable. However, the mechanism of this water-weakening effect is not understood. It is widely assumed, though, that the weakening is an intracrystalline effect because the samples are believed to deform by crystal-plastic processes. However, this is based predominantly on optically observed and TEM 'crystal-plastic' deformation microstructures and at least in some cases, other processes may have been responsible for the weakening. Especially in experiments on quartzite, many findings are inconsistent with crystal-plastic deformation. More experimental work is clearly needed to assess the mechanism(s) by which water weakens quartz.

Chapter 3

EXPERIMENTS ON QUARTZITE

3.1 INTRODUCTION

As described in chapters 1 and 2, small amounts of water are known to have a large effect on the mechanical behaviour of quartz single crystals and rocks in experiments at high confining pressures (P_c) and temperatures (T), i.e., at T=600-1100°C, P_c=350-1650 MPa, and strain rates in the range 10^{-7}-10^{-5} s^{-1}. Under these conditions, the flow strength is considerably reduced (typically by 0.5 to 2 orders of magnitude), and macroscopic ductility is dramatically enhanced, in comparison with 'dry' deformation. As already explained, this 'water-weakening' effect is widely believed to result from *intracrystalline* effects such as a reduction in the Peierls stress for glide, promotion of climb, or enhanced dislocation multiplication, these being caused by water related defects penetrating the quartz lattice. However, in spite of the large amount of work done on the subject since 1964, the water-weakening effect is poorly understood (see also Paterson 1989; Koch et al. 1989; Tullis 1990). In particular, previous experimental investigations into the water-weakening effect in quartzites (e.g. Jaoul et al. 1984, Kronenberg & Tullis 1984) have yielded a variety of contradictory results. For example, the experiments by Jaoul et al. (1984) are characterized by mechanical data consistent with *diffusional creep* being the dominant mechanism associated with weakening, whereas the reported deformation microstructures and crystallographic preferred orientations (CPO's) suggest that *dislocation creep* was dominant. In addition, water-weakening of quartzites is known to occur in less than 2 hours (Tullis & Yund 1985) whereas water would need at least 10-100 days to diffuse into the grains (100-200 μm diameter) and to bring about an intracrystalline weakening effect. According to Tullis & Yund (1985), pervasive micro-cracking could be responsible for the rapid uptake of water and subsequent weakening of the quartzites, but no micro-cracks were observed by these and any other authors. Hence, clarification of the water-weakening effect in quartzites is needed.

The present paper reports a detailed study of natural quartzites, deformed experimentally in a Griggs solid-medium apparatus at a temperature of 800°C, at a confining pressure of ~1200 Mpa, at strain rates of 10^{-5}, 10^{-6} and 10^{-7} s^{-1}, with ~0.4 wt% of added water. The experiments are essentially a repeat of those of Jaoul et al. (1984), but, in contrast to the work of Jaoul et al. (1984), incorporate detailed optical, SEM, and TEM studies. The observations indicate that at the lowest strain rates, micro-cracking and solution-precipitation creep (SPC) are the dominant deformation mechanisms and cause a significant weakening effect. The results thus cast serious doubt on the widely accepted idea that water-weakening seen in experimental deformation of quartzites is an intracrystalline process.

3.2 DESCRIPTION OF STARTING MATERIAL

3.2.1 Optical microstructure

The present experiments (table 3.1) were performed on Dongelberg quartzite (Fig. 3.1) from the Cambrian of the Brabant Massif (Belgium). This is a very dense material (porosity <0.1%) consisting of ~97 vol% quartz with a mean grain size of 150-250 μm. The quartz grains are equant to irregular in shape and define a very weak grain shape preferred orientation parallel to the bedding. They show undulatory extinction in bands (in about 50% of the grains) oriented (sub)parallel to the c-axes. The material has a very weak CPO (Fig. 3.1a). Grain boundaries are irregular or serrated, showing grain boundary bulges characteristic of grain boundary migration. Locally, grain boundaries contain finer polygonal quartz grains (20-60 μm). These have straight boundaries and do not show undulatory extinction. Phengitic mica platelets (1-2 vol%), up to 30 μm long, are aligned parallel to the boundary. Fine-grained (<5 μm) Fe-hydroxides (1-2 vol%) at the grain boundaries give the bulk sample a brownish colour. Fluid inclusions occur along grain boundaries or deformation band boundaries but are of very minor volumetric importance (<2 μm diameter; <0.1 vol% in total). Healed micro-cracks are present but rare.

3.2.2 Water content

The water content of the starting material (see table 3.2) was determined using thermo-gravimetric analysis (TGA) and Fourier-transform infra-red (FTIR) spectroscopy preformed in carefully selected sequence to determine the location of the water. The details are given in appendix B, with only the results being quoted here. These showed that the bulk water content of the Dongelberg quartzite (pre-dried for ~12 hr at 150°C to remove the surface water) is ~0.3 wt%, corresponding to ~30000 ppm H/Si. The intragranular water content varies between 0 and 3000 ppm H/Si, most of which is present in optically visible fluid inclusions (>50% of this water is freezable). About 4000 ppm H/Si is present as *inter*granular water (in pores and at grain boundaries). Another ~4000 ppm H/Si is probably bound to Fe-hydroxides (FeOOH). This water is probably liberated during the present experiments since the Fe-hydroxides are far outside their stability field at 800°C and ~1200 MPa (e.g. Langmuir 1971) and will form hematite plus free water. Another 14000 to 15000 ppm H/Si is structurally bound to mica, and is probably not 'free' during the experiments, since large amounts of mica were still present after test termination. The source of about 6000 ppm H/Si could not be identified. This amount is assumed to be bound to some mineral *or* to be present in

Table 3.1. *Summary of experiments on Dongelberg quartzites. Wet = 0.4 wt% water added; dry = vacuum-heated at 800°C; as-rec = as-received; LTC = lower thermocouple temperature; UTC = upper thermocouple temperature; t_1 = elapsed time to reach PT-conditions; t_2 = time at PT-conditions before deformation; t_3 = elapsed time after deformation to reach room PT-conditions. + = control experiments on quartz single crystals.*

Sample Number		Strain rate (s^{-1})	Finite strain (%)	P_c (MPa)	LTC (°C)	UTC (°C)	t_1 (hr:min)	t_2 (hr)	t_3 (hr:min)	Yield stress (MPa)	Maximum stress (MPa)
GRU10	wet	$1.1x10^{-6}$	9	1060	786	810	8:10	38	5:00	150	150
GRU11	wet	$1.1x10^{-7}$	11	1040	784	800	2:20	19	2:40	---	<25
GRU13	wet	$1.1x10^{-5}$	12	1040	793	815	4:10	13	0:50	610	750
GRU14	wet	$1.1x10^{-5}$	6	1060	802	802	5:40	23	0:30	590	590
GRU15	wet	0	0	1100	805	800	1:50	113	0:40	---	---
GRU19	wet	0	0	1250	764	800	6:20	90	1:30	---	---
GRU20	wet	$1.1x10^{-6}$	12	1240	802	800	3:50	88	0:50	---	280
GRU21	wet	$1.1x10^{-6}$	6	1240	806	800	5:20	49	0:40	---	170
GRU23	wet	$1.1x10^{-7}$	11	1140	760	800	26:30	70	0:26	---	<25
GRU26	wet	$1.1x10^{-7}$	14	1130	798	800	4:30	144	0:20	---	<25
GRU29	wet	$1.1x10^{-6}$	40	1160	784	810	26:50	32	0:01	190	190
GRU31	as-rec	$1.1x10^{-7}$	10	1160	776	800	21:10	78	0:50	140	210
GRU35	wet	$1.1x10^{-7}$	46	1260	---	800	124:30	71	0:05	---	<25
GRU37 +	wet	$1.1x10^{-6}$	14	1200	795	820	23:50	75	2:10	---	---
GRU38 +	wet	$1.1x10^{-6}$	7	1160	800	---	99:45	19	0:10	---	<40
GRU39	as-rec	0	0	1170	774	815	34:45	133	1:50	---	---
GRU40	as-rec	$1.1x10^{-7}$	7	1190	788	815	30:20	324	0:17	225	225
GRU41	as-rec	$1.1x10^{-7}$	10	1200	816	800	25:55	17	0:22	---	---
GRU42 +	dry	$1.1x10^{-7}$	0	1220	790	815	53:45	44	0:22	---	700
GRU43 +	dry	$1.1x10^{-7}$	0	1200	780	808	29:15	23	0:60	---	1200
GRU46	dry	$1.1x10^{-7}$	3	1150	810	795	46:40	143	19:15	1220	1540

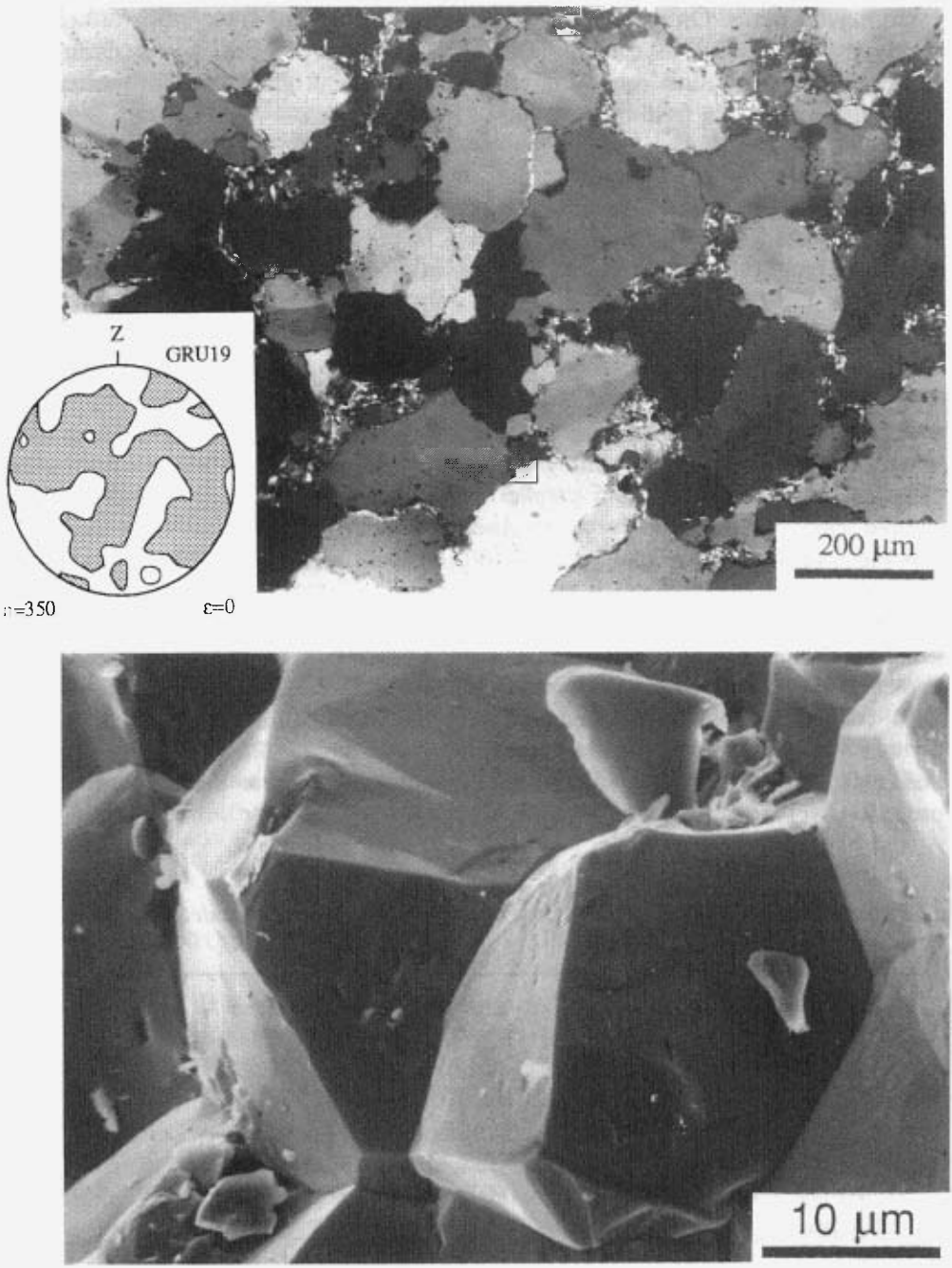

Fig. 3.1 *(a) Optical micrograph (crossed polars) of starting material (Dongelberg quartzite). CPO of undeformed sample GRU19 (hydrostatically loaded only) is indicated in lower left corner. (b) SEM micrograph of starting material.*

intergranular pores. On the basis of the above data, starting material deformed 'as-received' is believed to contain 8000-16000 ppm H/Si 'free' water during the present experiments, this consisting of originally present grain boundary water, and water made available from dehydration of Fe-hydroxides.

3.3 EXPERIMENTAL ASPECTS

3.3.1 Sample preparation

Cylindrical samples measuring 6 mm in diameter by 12±1 mm in length were cored from a single block of the Dongelberg quartzite at 45° to the bedding. This was done using a diamond coring tool with water as lubricant. The ends of the samples were ground flat and parallel to within 30 μm measured parallel to the sample length. The specimens were subsequently oven-dried at 150°C for 12 hours, and then weld-sealed in gold jackets (400 μm wall thickness; see further appendix A).

Samples were either deformed 'dry' (after vacuum heating at 800°C in nitrogen gas for 12 hours; bulk water content <200 ppm H/Si), 'as-received' (bulk water content ~30000 ppm H/Si; for distribution see table 3.2), or 'wet', i.e. with ~0.4 wt% (~40000 ppm H/Si) added water included within the jacket (bulk water content ~70000 ppm H/Si; for distribution see table 3.2). Note that samples deformed 'dry' contained abundant intergranular cracks after the vacuum heating procedure.

Table 3.2. *Water content (in ppm H/Si) of starting mate-rial determined with FTIR and TGA.*

	intra granular	inter granular	inter granular ??	bound to FeOOH	bound to mica	added water	diff stress (MPa)
"Dry"	<200						~1200
"As-received"	<200-3000	~4000	~6000	~4000	~15000		140-225
"Wet"	<200-3000	~4000	~6000	~4000	~15000	~40000	<25

3.3.2 Procedure and data processing

Deformation experiments were conducted in a Tullis-modified Griggs apparatus with NaCl as the confining medium (see appendix A). Temperature, pressure (in the confining pressure ram), axial load and displacement signals were continuously monitored during the experiments using a chart recorder and PC-based data logger.

In setting up each test, temperature and pressure were raised simultaneously in order to follow the water isochore of 1 gcm^{-3} as closely as possible. The experiments were performed in constant displacement rate mode at 800°C and at 1200 ± 100 MPa confining pressure. The imposed strain rates were $1.1x10^{-5}$, $1.1x10^{-6}$ and $1.1x10^{-7}$ s^{-1}. The total strains achieved fell in the range 5 to 46%. After deformation, the piston was moved upwards at maximum speed ($3x10^{-3}$ $mm{\cdot}s^{-1}$), and the temperature and pressure were lowered, once again following the water isochore of 1 gcm^{-3} as closely as possible. Cooling times varied from 1 to 50 minutes. Three samples were hydrostatically loaded only. These were maintained at 800°C and 1200 ± 100 MPa for 90 and 113 hours respectively. Seventeen experiments were carried out in all (see table 3.1). For comparison, four tests on single crystals were done.

With regard to the processing of the raw data it is important to note that the measured axial displacement and load were corrected for apparatus distortion (at 800°C and ~1200 MPa) and for friction respectively. Differential stresses were calculated using the initial cross section of the samples. Axial strain was computed with respect to the sample length at ambient (NPT) conditions. The resolution of the stress measurement is believed to be ~25 MPa, a figure which is closely comparable with that obtained in previous work using the Griggs apparatus (e.g. Jaoul et al. 1984). For further details see appendix A.

3.4 MECHANICAL RESULTS

The mechanical data are presented as differential stress versus strain curves in Fig. 3.2. The curves of samples deformed 'dry' at 10^{-7} s^{-1} (GRU46), and 'as-received' at 10^{-7} s^{-1} (GRU31 & 40) are shown in Fig. 3.2a; the curves of samples deformed 'wet' at 10^{-6} s^{-1} (GRU10, 20, 21 & 29) and 10^{-5} s^{-1} (GRU13 & 14) are shown in Fig. 3.2b. The 'wet' samples deformed at 10^{-7} s^{-1} (GRU11, 23, 26 & 35) were so weak that the differential stress could not be determined (which means that the stress must have been lower than ~25 MPa).

As illustrated by Fig. 3.2a, the presence of small amounts of water in the quartzite samples caused a significant mechanical weakening effect (see also table 3.1). At a strain rate of 10^{-7} s^{-1}, the 'dry' sample GRU46 (containing <200 ppm H/Si) yielded at ~1220 MPa, whereas the stresses supported by the 'wet' samples GRU11, 23, 26 & 35 (containing ~70000 ppm H/Si) were ≤25 MPa. The 'as-

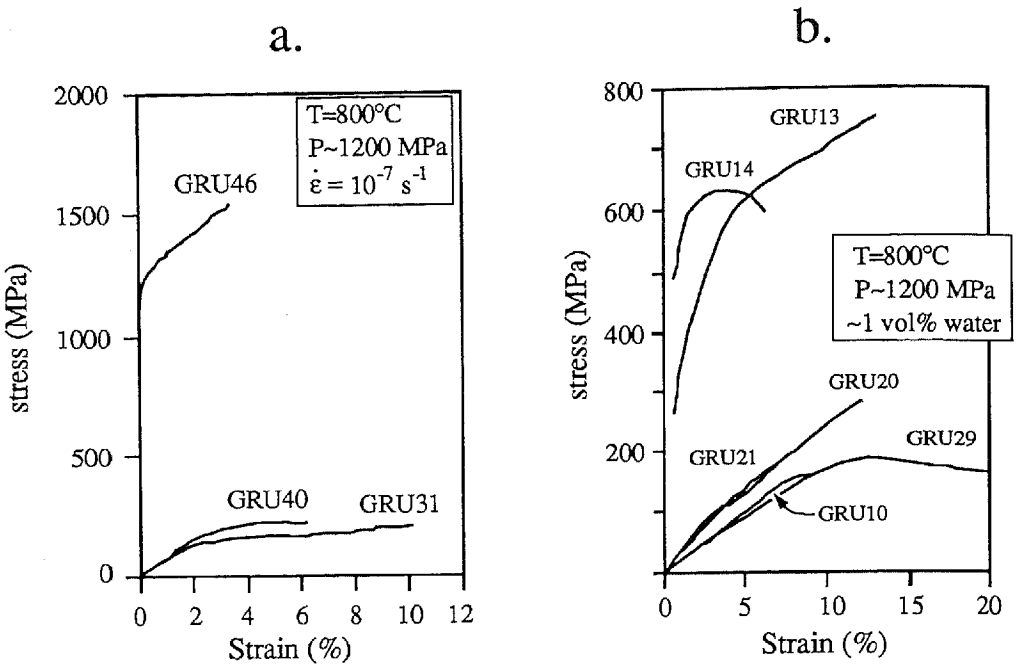

Fig. 3.2 *(a) & (b) Stress/strain curves obtained from the present experiments. The curves of samples deformed 'wet' at 10^{-7} s^{-1} could not be determined. The stresses were below the resolution limit of the Griggs apparatus, i.e. lower than ~25 MPa.*

received' samples GRU31 & 40 (containing ~30000 ppm H/Si) yielded at intermediate stresses (i.e. 140 and 225 MPa respectively). Hence, the 'dry' sample is at least 5 to 10 times stronger than the 'as-received' samples, and the 'as-received' samples are at least 5 to 10 times stronger than the 'wet' ones.

The effect of varying the strain rate on 'wet' samples is illustrated in Fig. 3.2b. Samples deformed at 10^{-5} s^{-1} (GRU13 and 14) yielded at 590 to 610 MPa, samples deformed at 10^{-6} s^{-1} (GRU10 and 29) yielded at 150 to 190 MPa, and samples deformed at 10^{-7} s^{-1} (GRU11, 23, 26, and 35) yielded at ≤25 MPa. This shows that the water-weakening effect is rate-dependent.

Most of the samples exhibited macroscopic yield behaviour followed by strain hardening in some cases (GRU13, 31, 40, and 46) and strain softening in others (GRU10, 14, and 29). Samples deformed 'wet' at 10^{-6} s^{-1} showed 8 to 11% strain hardening before macroscopic yielding.

Steady state deformation was not seen in any of the experiments. Nonetheless, the flow stresses measured after macroscopic yield (where observed) were plotted

versus strain rate in the log-log plot of Fig. 3.3. Focussing on the 'wet' samples, it shows that if power-law creep behaviour is assumed (regardless of mechanism, and assuming that the mechanical data reflect the sample behaviour), a stress exponent $n<1.3$ is implied for the region $\dot{\varepsilon}<10^{-6}$ s^{-1}.

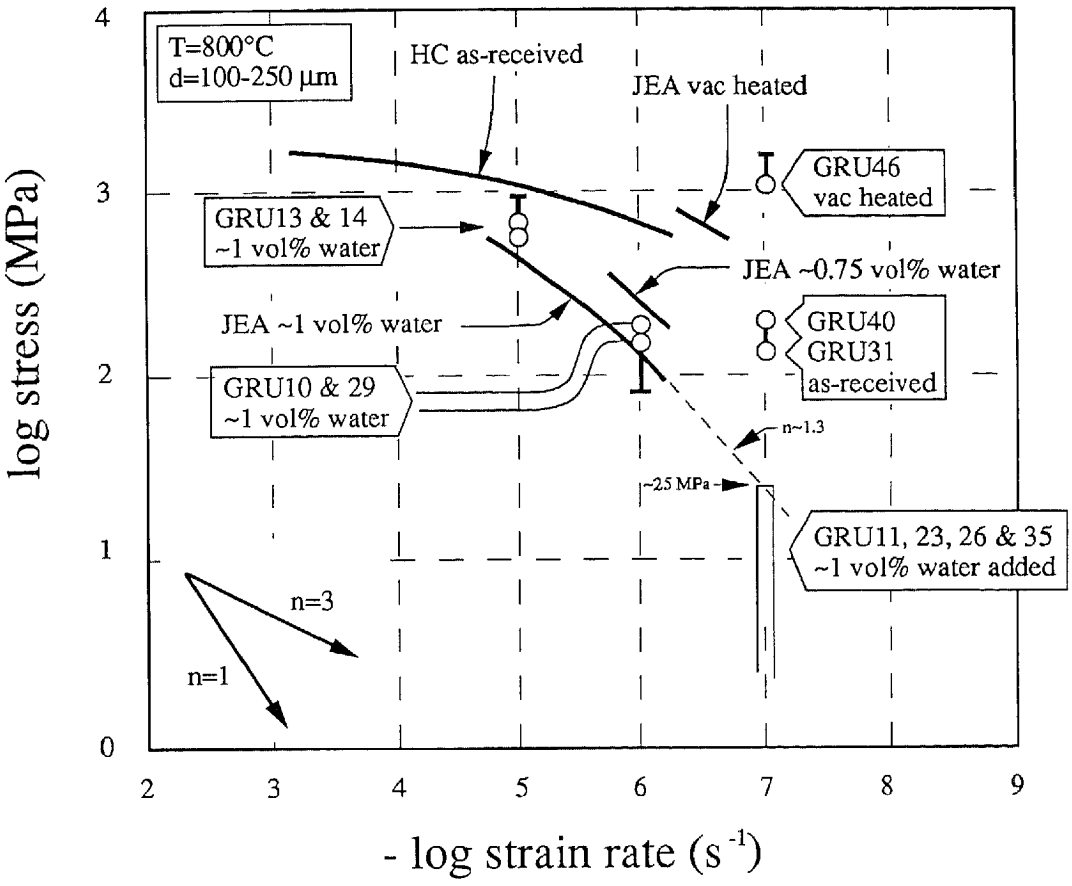

Fig. 3.3 *Log-log plot of differential stress versus strain rate constructed from the stress strain curves of Fig. 3.2. Solid circles and range bars refer respectively to the macroscopic yield points obtained in the present experiments (where observed) and the range of flow stresses recorded after yield. The differential stresses supported by samples deformed 'wet' at 10^{-7} s^{-1} lie within the indicated box or lower. Solid curves represent the data of Heard & Carter (1968; 800°C, 0.8 GPa confining pressure, deformed as received without added water in a gas apparatus) and of Jaoul et al. (1984; 800°C, 1.5 GPa confining pressure, deformed oven dried with and without 0.4 wt-% added water in a Griggs solid medium apparatus).*

3.5 MICROSTRUCTURAL OBSERVATIONS

In the following, the optical microstructure of the undeformed, hydrostatically loaded 'control samples' will first be described in order to characterize the microstructural damage introduced into the samples during the pressurization-heating cycle of the Griggs machine. The deformation microstructures observed in the single 'dry' sample deformed at 10^{-7} s^{-1} will then be described, followed by the microstructures observed in the 'wet' material deformed at 10^{-7} s^{-1}. The microstructures obtained under these two extreme conditions, i.e. 'dry' and 'wet' at 10^{-7} s^{-1}, contrast enormously, and represent two end-member microstructure signa-tures. Finally, the microstructures of the samples deformed under intermediate conditions will be described (i.e., 'wet' at 10^{-6} s^{-1} and 10^{-5} s^{-1}, and 'as-received' at 10^{-7} s^{-1}).

3.5.1 Hydrostatically loaded samples

Three hydrostatic loading experiments were carried out for microstructural control purposes. One of the three (GRU39) was loaded 'as-received', the other two (GRU15 & 19) were loaded 'wet' (see table 3.1). Broadly speaking, the starting microstructure was little modified. No microstructural change could be observed in the 'as-received' sample after the experiment, except for the presence of one single sample-scale unloading fracture oriented perpendicular to the sample axis. Similarly, the samples which were hydrostatically loaded 'wet' showed only minor microstructural changes. Those are at follows. Firstly, several through-going cracks were developed at 0-20° to the sample axis. Some of these cracks showed shear offsets up to 300 µm. Locally, these cracks are healed, or filled with very fine inequant quartz grains (<5 µm). Small numbers of healed, grain-scale (transgranular) micro-cracks were also observed. These micro-cracks are marked by fluid inclusions (<2 µm), and are oriented parallel to the sample axis. Locally they separate areas of slightly different optical extinction, i.e. there is a minor crystallographic mis-orientation developed across the crack walls. At the contact between the gold capsule and the quartzite in the 'wet' samples, the quartz was locally dissolved. The 'wet' samples also showed several through-going unloading fractures oriented perpendicular to the sample axis.

3.5.2 Material deformed 'dry' (10^{-7} s^{-1})

By contrast to the *hydrostatically* loaded samples, all *axially* loaded quartzite samples showed substantial modification of the starting microstructure. As listed in

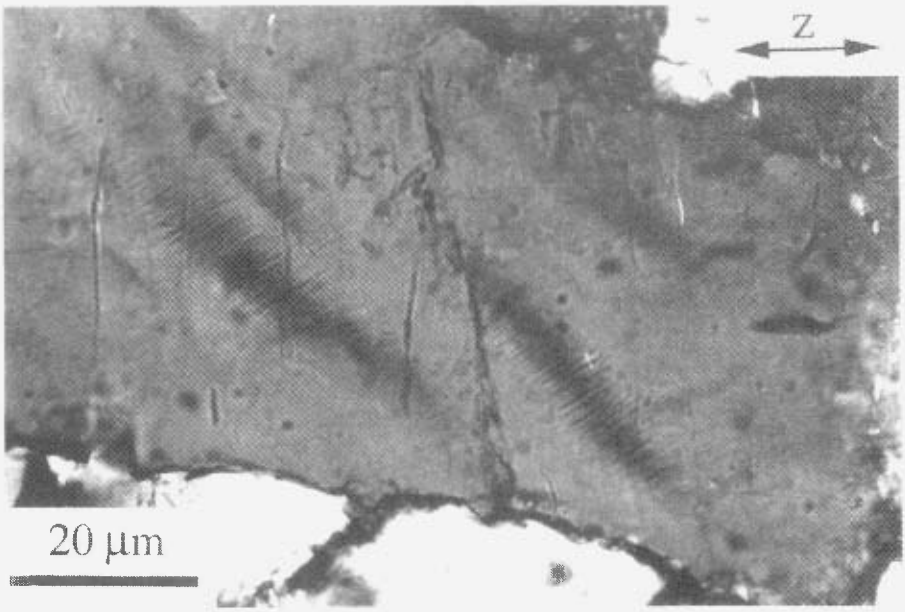

Fig. 3.4 *Optical micrographs (crossed polars) showing arrays of deformation lamellae developed in sample (GRU46) deformed 'dry' (<200 ppm H/Si) at T=800°C, Pc=~1200 MPa, and ε̇=10-7 s-1 to ~3% strain. Slight lattice rotation (<3°) where lamellae are present, causes banded undulatory extinction. Fractures oriented perpendicular to Z probably represent unloading fractures.*

table 3.1, the 'dry' sample (GRU46) was subjected to ~3% permanent strain at a strain rate of 10^{-7} s^{-1}. After this treatment ~80% of the original grains had developed subbasal deformation lamellae oriented at 30-60° to the shortening direction (Z). These lamellae are spaced 2-5 μm apart, and are 25-35 μm long. They occur mostly in en-echelon arrays, the arrays being inclined at 40-50° to Z (Fig. 3.4). Undulatory extinction was only observed where lamellae were present *and* curved. The sample also contains large amounts of intragranular (grain-scale) unloading fractures oriented perpendicular to Z. No further deformation features were observed, perhaps not surprisingly since the strain was very low.

3.5.3 Samples deformed 'wet' at 10^{-7} s^{-1}

3.5.3.1 Low finite strain (<15%)

The samples deformed 'wet' (i.e., with 0.4 wt% of added water) at a strain rate of 10^{-7} s^{-1}, and to 11-14% finite strain (GRU11, 23 & 26), show a completely different microstructure to that developed in the 'dry' test. In these samples very few grains contain deformation lamellae (<5%), and the frequency of deformation bands and undulatory extinction features only slightly exceeds that of the starting material.

Instead, the experimentally produced microstructure is characterized by conspicuous intergranular arrays of fine, new, polygonal to euhedral quartz grains (5-50 μm). These arrays are preferentially aligned parallel to Z (Fig. 3.5), and locally cross-cut the older grains (Figs 3.6 & 3.7a). No evidence was found for optical intracrystalline deformation features in these new grains (i.e. undulatory extinction, deformation lamellae, or deformation bands). The arrays contain abundant microcavities or voids (<10μm; ~1 vol% in all), intergranular channel structures and fluid inclusion trails (Figs 3.7b & 3.8). The void bounded surfaces of new grains are mostly euhedral, whereas new grain boundaries (i.e. grain-to-grain boundaries) are heavily decorated with fluid inclusions. Phengitic micas (1-50 μm) and fine-scale (<1μm) Fe-bearing crystalline efflorescences also grow within the new grain arrays.

Old grain boundaries oriented *parallel* to Z are often dilated and show (sub)euhedral, syntaxial overgrowth structures (Fig. 3.9). These frequently appear pinned by micas, and fluid inclusion trails separating distinct (syntaxial) overgrowth cells are common. The cells are of similar size as the (sub)euhedral new grains (5-50 μm) and have a cubic shape (determined by rhombic crystal faces). SEM-kathodoluminescence (unfortunately) revealed no difference in luminescence between the overgrowths and the original grains (Fig. 3.10). Some old grains appear to be slightly flattened and exhibit mica 'beards' growing perpendicular to Z. The old grains also show numerous straight, as well as irregular, healed intra- and transgranular micro-cracks aligned parallel to Z.

Fig. 3.5 *(a) Optical micrograph of sample GRU11 ('wet', 10^{-7} s^{-1}, ~11 % strain) showing intergranular arrays of fine new quartz grains developed parallel to the shortening direction (Z). (b) Distribution of arrays of new grains (in black) in sample GRU11. Note preferential orientation parallel to Z. Black areas do not necessarily represent sites of precipitation only, but also sites of micro-cracking. Note also that apparently wide black areas probably reflect oblique sectioning (30 μm section). Horizontal cracks are (un)loading cracks. Location of (a) is indicated in (b).*

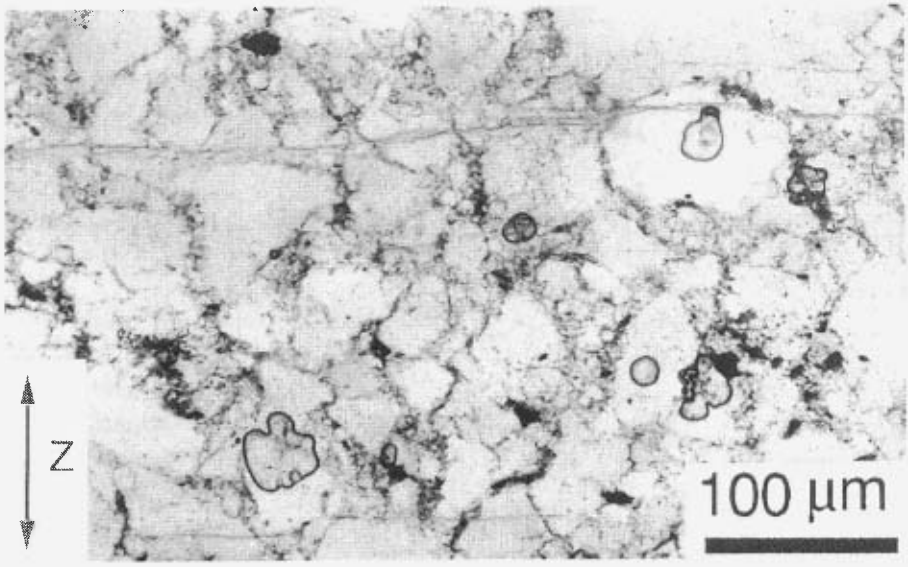

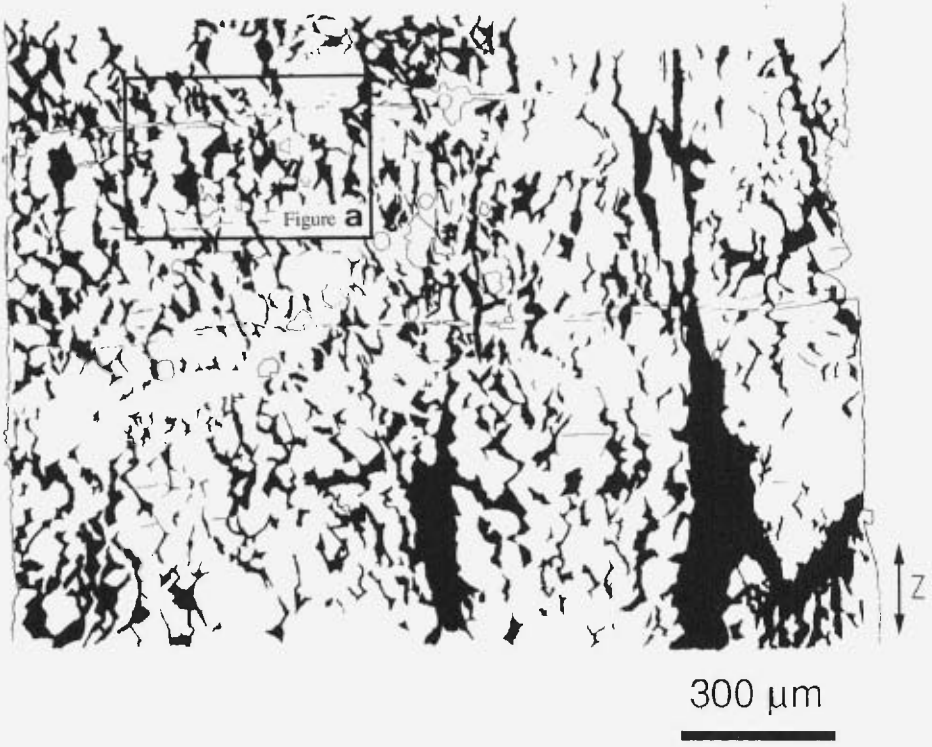

Fig. 3.5 *(Explanation see previous page)*

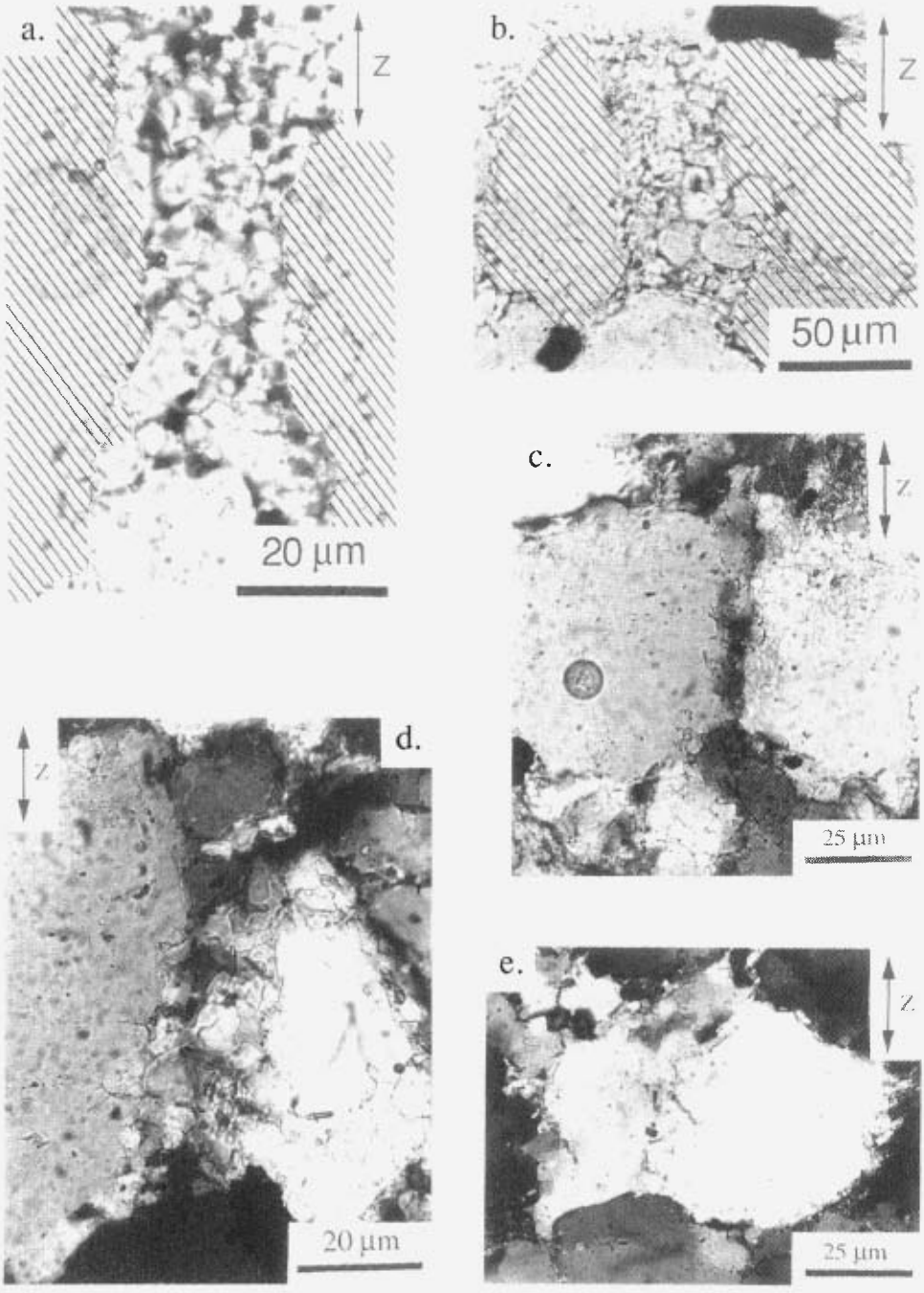

Fig. 3.6 *(Explanation see next page)*

Locally, the walls of these micro-cracks show euhedral crystal morphology, again resembling syntaxial overgrowths. Irregular intragranular microfractures along which a few degrees of rotation has taken place give the impression of (blocky) undulatory extinction (Fig. 3.11). It should be noted that most of the undulatory extinction that was observed in the original grains was associated with such intragranular micro-cracks, or with the presence of abundant, irregularly shaped fluid inclusions, suggestive of healed, irregular micro-cracks (Fig. 3.11b, c & d).

Old grain boundaries oriented *perpendicular* to Z show abundant fluid inclusions occupying up to 25% of the boundary surface. But the overgrowth features seen on dilated grain boundaries oriented parallel to Z are conspicuously absent. In experiment GRU23, the originally polished surface of a quartz single crystal spacer, placed in the sample capsule between sample and piston, revealed well developed indentations (50-200 μm in diameter) corresponding to grains in the quartzite sample. These indentations are characterized by irregular channel structures and abundant fluid inclusions similar to those seen on grain boundaries oriented perpendicular to Z in the bulk sample (Fig. 3.12). In the quartz spacer, numerous healed micro-cracks were visible as fluid inclusion trails oriented parallel to Z. The intervening regions are slightly misoriented (<3°). Frequently, the irregular channel structures seen at the indented surface of the single crystal occur at the intersection of micro-cracks with the surface. The channel spacing measures 1-20 μm. Optically, the single crystal spacer showed no evidence for crystal-plastic deformation.

In samples GRU11 & 26, the homogenization temperatures of respectively 12 and 15 fluid inclusions were determined on a heating-freezing stage (see appendix C). The fluid densities thus obtained agreed well with optically estimated densities of the fluid, i.e. around 0.8 (volume of liquid divided by the total volume of the inclusion). The results indicate that the fluid pressure during formation of the inclusions was close to the applied confining pressure in most of the cases, i.e. 800 to 1000 MPa. The *effective* confining pressure was therefore 100 to 300 MPa in these samples.

Fig. 3.6 *Optical micrographs of inter- and intra-granular arrays of fine new quartz grains, the arrays being preferentially aligned parallel to Z. The arrays contain abundant microcavities or voids, intergranular channel structures, and fluid inclusion trails. Sample: GRU11 deformed with 0.4 wt% added water at* 10^{-7} s^{-1} *to ~11% strain. Note the abrupt transition from old to new grains and the sub-euhedral shape of many of the new quartz crystals. (a) & (b) plane polarized light; (c) to (e) crossed polars. Old grains in (a) & (b) as identified on the optical microscope rotation stage are hatched.*

Fig. 3.7 *(a) & (b) Optical micrographs of sample GRU11, deformed with 0.4 wt% added water at 10^{-7} s^{-1} to ~11% strain. (a) Intergranular array of new grains, oriented parallel to Z. Same location as Fig. 3.6a. The original grains are almost free of intragranular deformation features except for healed axial micro-cracks. Note abrupt transition from old grains to new grains indicating that the new grains did not result from rotation recrystallization. Note also overgrowth features on grain boundaries oriented parallel to Z. (b) Close-up of new-grain array showing euhedral shape of new grains and of overgrowth features. Note square cross-section of new grains; most of the crystal faces are parallel to rhombic planes. (c) & (d) Optical photomicrographs of sample GRU35 deformed 'wet' at 10^{-7} s^{-1} to ~46% strain, showing intragranular axial arrays of new grains. The new grain aggregates show much less euhedral grains, and lower porosity than at low finite strain. Location of Figs (c) and (d) is indicated in Fig. 3.17. SEM pictures of such aggregates are shown in Fig. 3.18. Note that the original grains themselves are still relatively free of internal deformation features apart from the presence of fluid inclusions. (e) Optical photomicrographs of sample GRU35. Flattened small new grains showing irregular grain boundaries and large amounts of voids at grain boundaries. Compare with undeformed euhedral new grains of sample GRU11 (~11% strain) in fig. b. Note that the original grain is almost strain-free and contains fibre-like overgrowth features at grain boundary oriented parallel to Z. Transition between flattened small new grains and large original grain is abrupt. (All photo-micrographs: crossed polars plus gypsum plate.)*

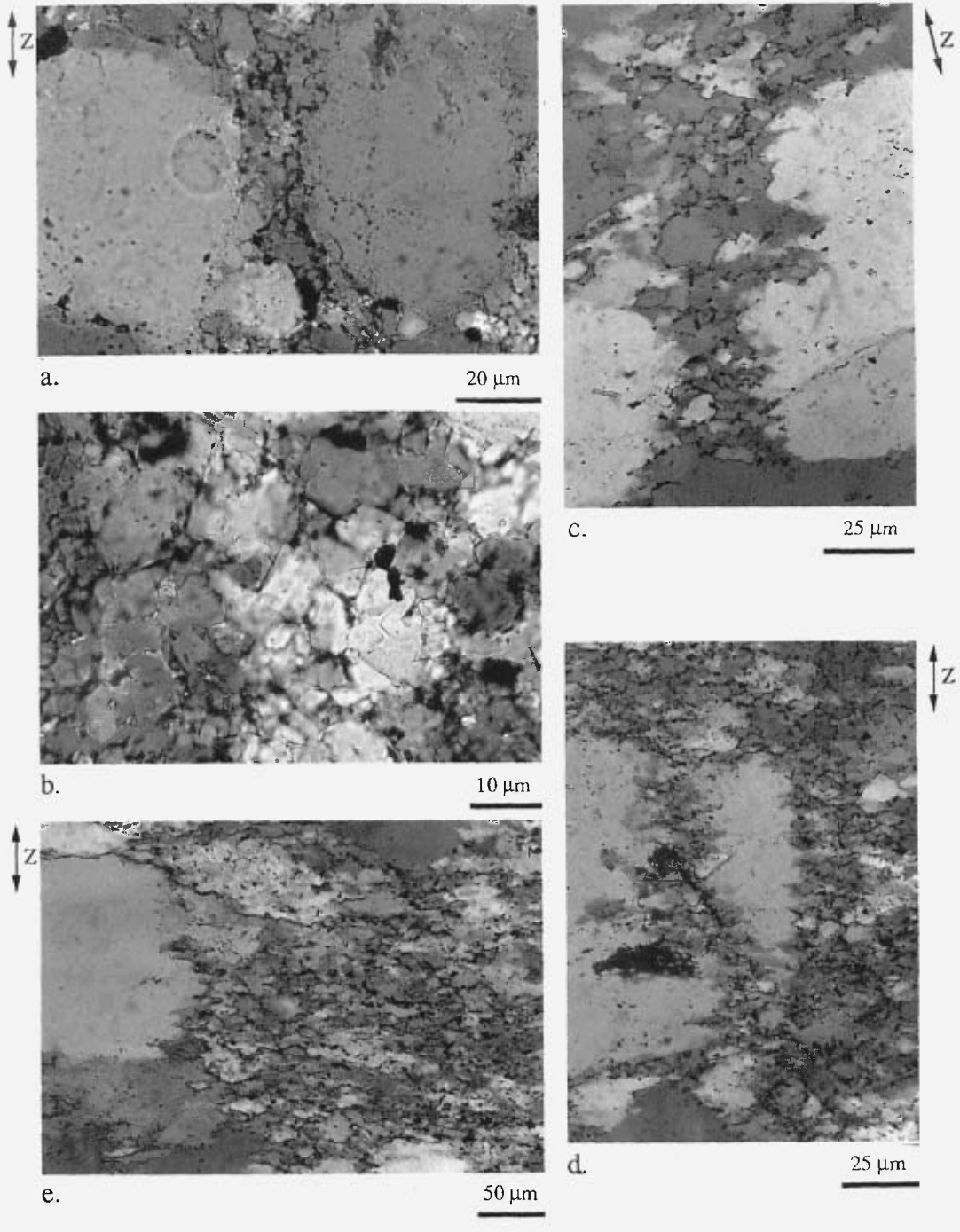

Fig. 3.7 *(Explanation see previous page)*

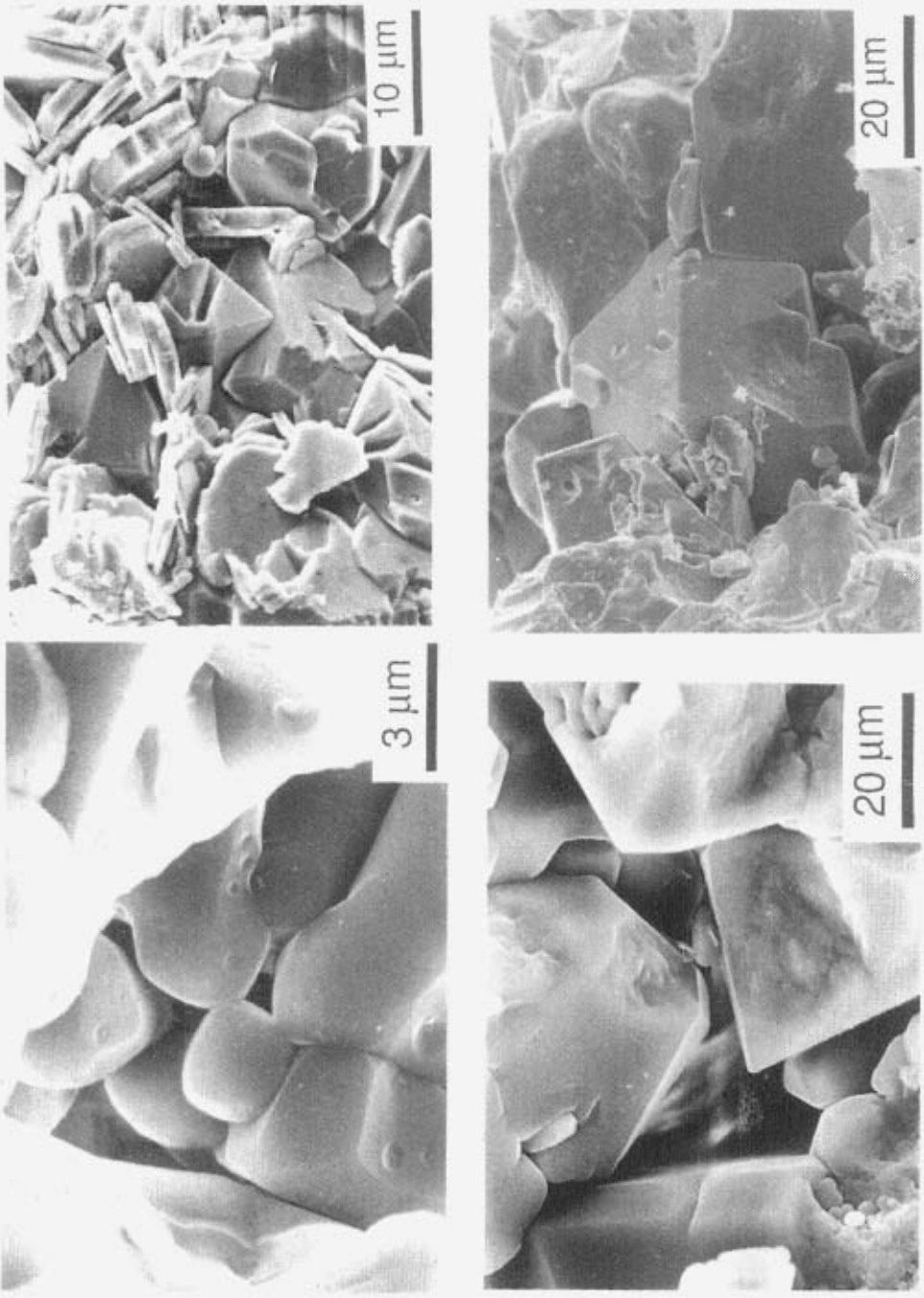

Fig. 3.8 *SEM micrographs of new grains in axial arrays of quartz grains in sample GRU11 ('wet', 10^{-7} s^{-1}). Note sub- to euhedral morphology and voids. Note also mica platelets included in the quartz. Note also absence of glass.*

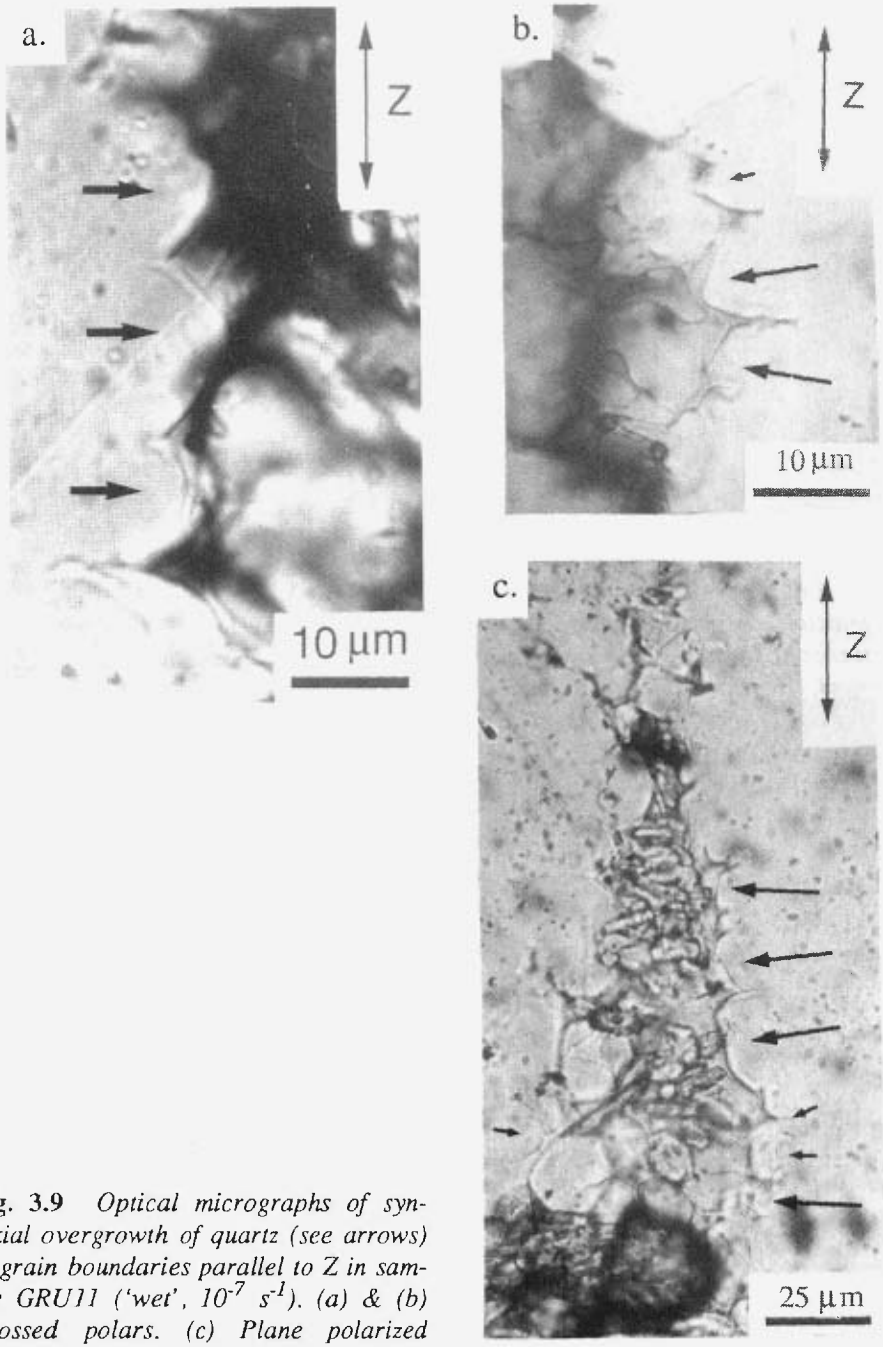

Fig. 3.9 *Optical micrographs of syntaxial overgrowth of quartz (see arrows) at grain boundaries parallel to Z in sample GRU11 ('wet', 10^{-7} s^{-1}). (a) & (b) Crossed polars. (c) Plane polarized light.*

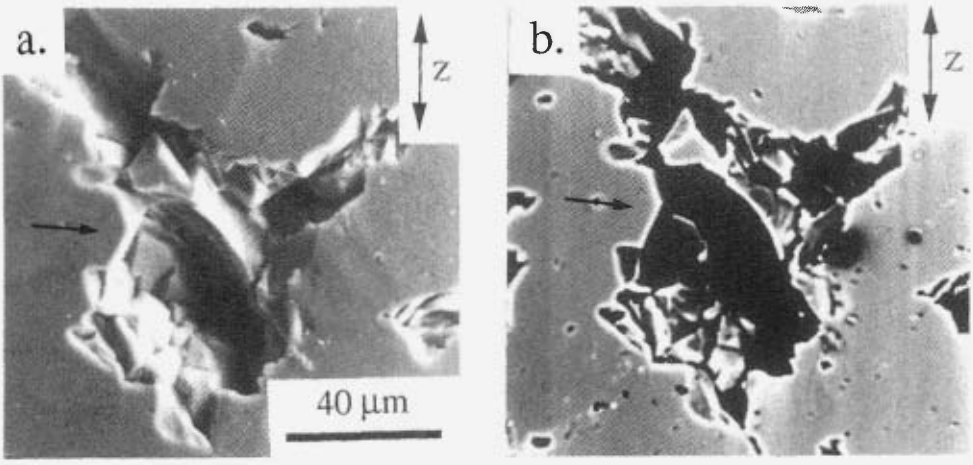

Fig. 3.10 *(a) SEM micrograph of sample GRU11 showing axially oriented micro-crack with syntaxial overgrowth feature (see arrow). (b) Same location but now cathode luminescence (CL) image. The overgrowth structure has the same luminescence as the background. Hence, it was not possible to distinguish overgrowth quartz from the original grains with CL.*

Fig. 3.11 *Optical micrographs (crossed polars) of sample GRU11, deformed with added water at 10^{-7} s^{-1}. (a) Irregular transgranular micro-cracks with euhedral overgrowth features at the crack walls and development of fine new grains. Slight rotation of the fractures blocks give the impression of undulatory extinction. (b), (c) & (d) Undulatory extinction in original grains, associated with the presence of large amounts of mostly irregularly shaped fluid inclusions, suggesting slight rotation along irregular intragranular micro-cracks. (c) & (d) are of similar grain but with slightly different position w.r.t. the polars.*

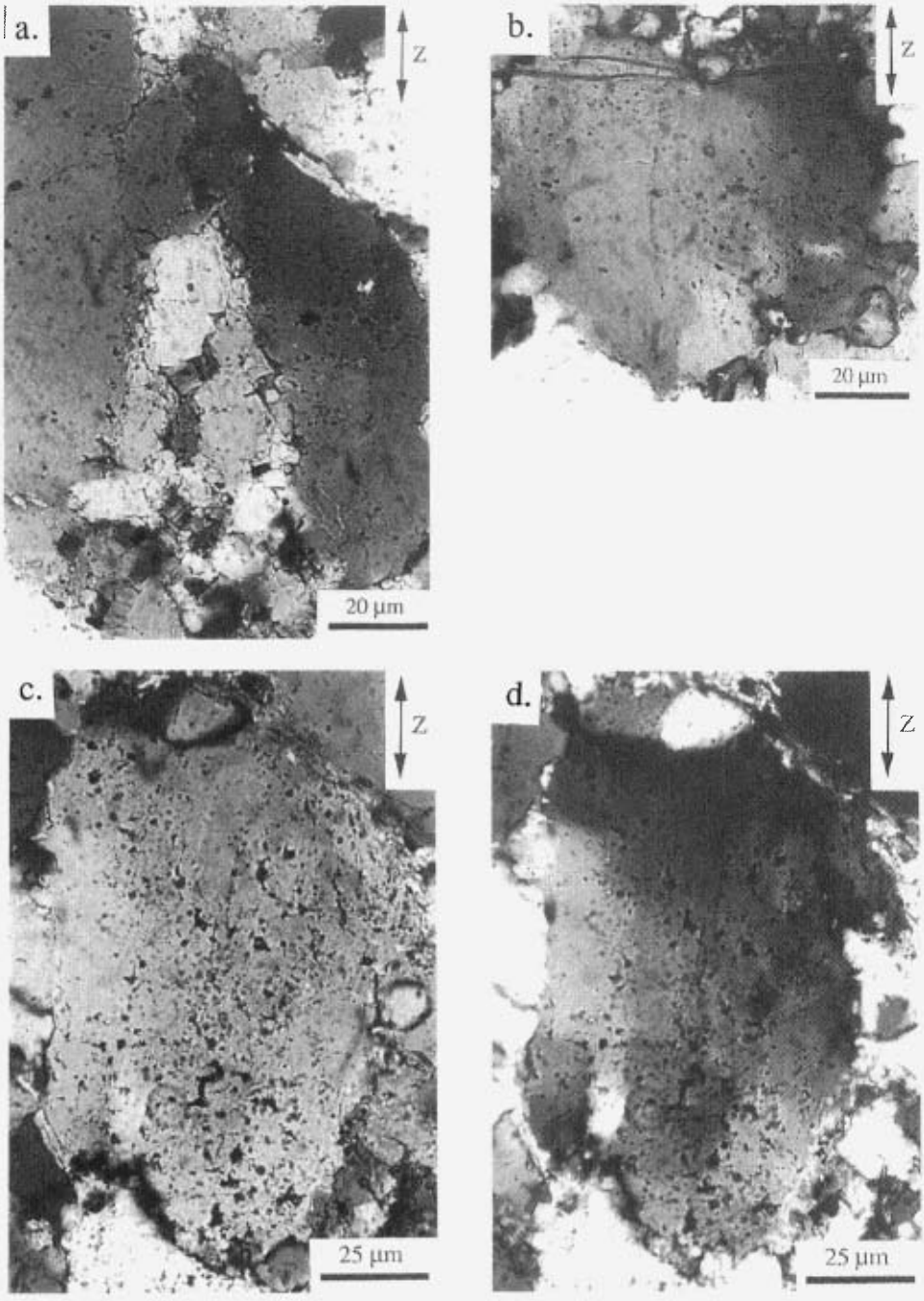

Fig. 3.11 *(Explanation see previous page)*

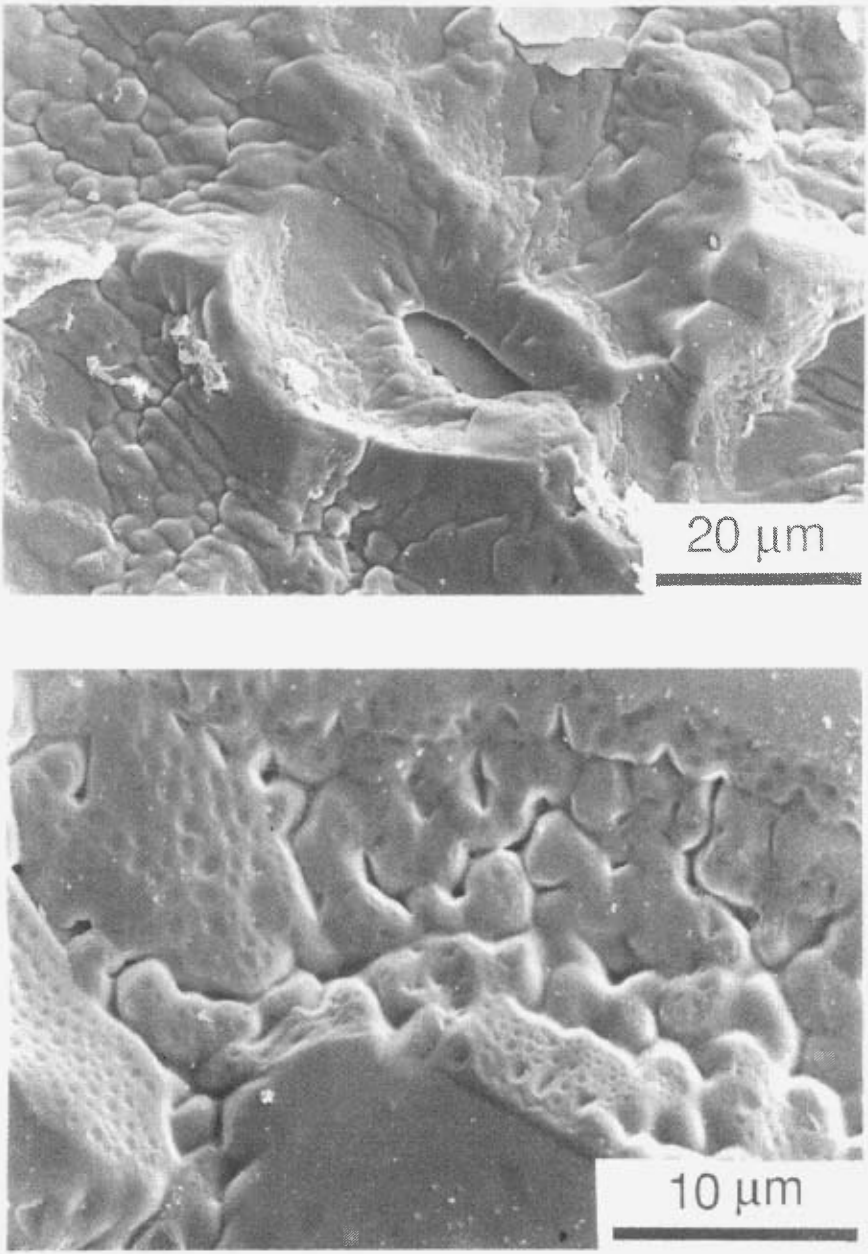

Fig. 3.12 *SEM micrographs of originally polished surface of quartz single crystal spacer oriented perpendicular to Z in experiment GRU23 ('wet', 10^{-7} s^{-1}). Note the well-developed indentations with fluid inclusions and irregular channel structures.*

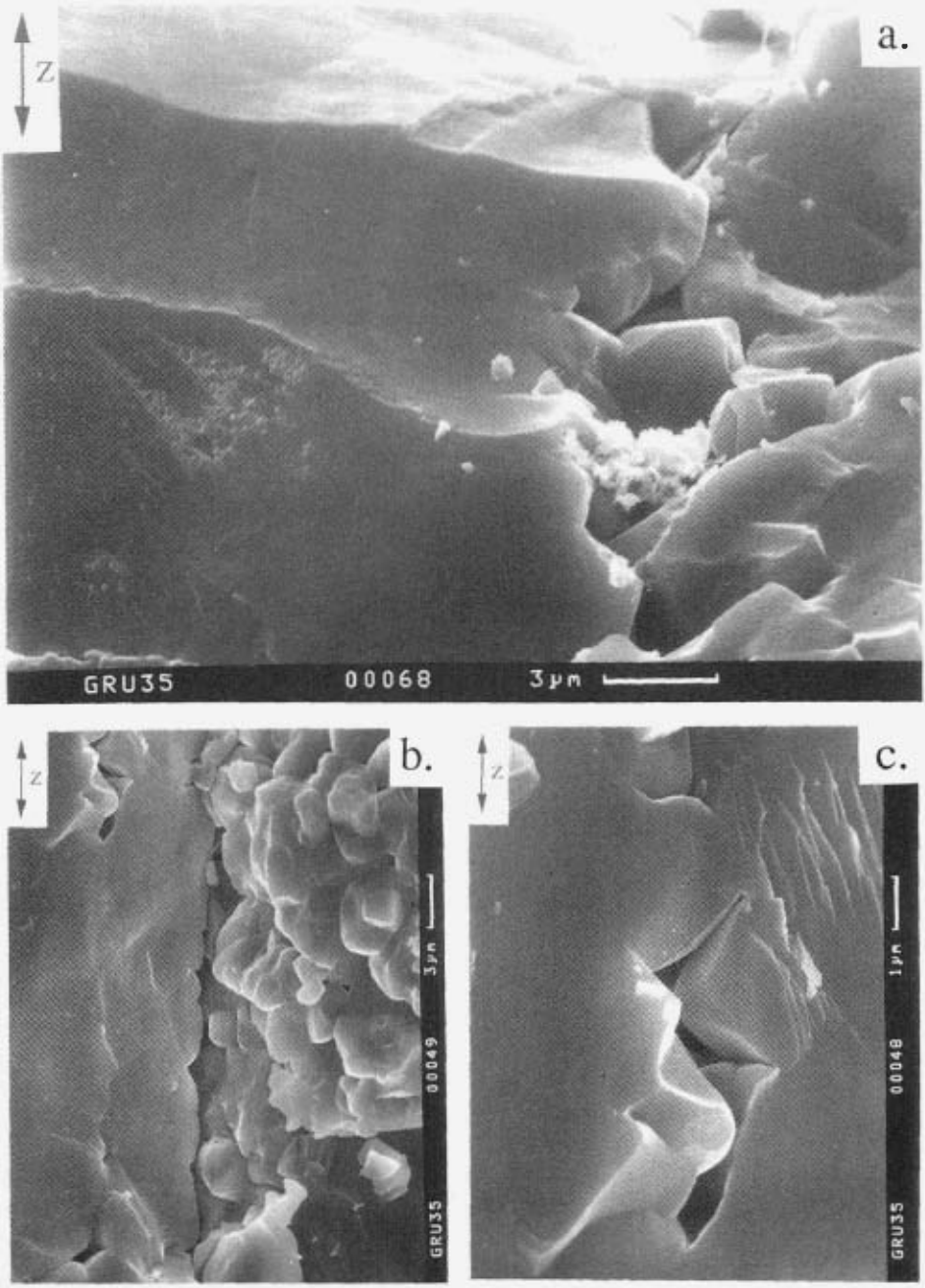

Fig. 3.13 *SEM micrographs showing axial micro-cracks in original grains in sample GRU35 deformed 'wet' at 10^{-7} s^{-1} to ~46% strain. (a) Note presence of fine euhedral grains within the partially healed micro-cracks. (b) Micrograph showing two cracks. The left one is partially healed; the right one is open. The right half of the micrograph is the surface of the micro-crack, consisting of sub-euhedral new grains plus overgrowth structures. (c) Enlargement of upper part of the crack on the left size of (b).*

3.5.3.2 *High finite strain (~46%)*

One sample (GRU35) was deformed to a bulk finite strain (ε_b) of 46±1 %. This sample shows slightly more (subbasal) deformation lamellae (in ≤12% of the original grains). A significant number of original grains now show undulatory extinction, again mostly associated with the presence of small new grains, or subgrains, with numerous fluid inclusions (1-15 μm in diameter) at the new-(sub)grain boundaries, often arranged in irregular arrays suggestive of partially healed cracks such as depicted in Fig. 3.11. SEM pictures of such cracks are shown in Fig. 3.13. The original grains contain much more (irregularly shaped) fluid inclusions. The fluid density of the inclusions was estimated from the relative size of included gas bubbles. A value of 0.8-0.9 was obtained, which corresponds to a fluid pressure of 900-1000 MPa, and an effective pressure of 260-360 MPa during the formation of the inclusions. This figure is similar to that obtained at low strain.

The original grains are significantly flattened, having an average ellipsoidity ($\bar{R}$) of 1.68±0.03 (measured in the plane of the thin-section, which was cut parallel to Z; 470 grains were measured; Fig. 3.15). The $\bar{R}$-value of the starting material is 0.96±0.02 (Fig. 3.15a). By assuming axial-symmetric shortening, the average finite *grain* strain ($\bar{\varepsilon}_g$) of the original grains corresponding to $\bar{R}$ is obtained by (see Fig. 3.16):

$$\bar{\varepsilon}_g\,[\%] = 100\left(1 - \bar{R}^{-2/3}\right) \qquad (3.1)$$

which yields $\bar{\varepsilon}_g$ = 29±1 % for GRU35. The difference between $\bar{\varepsilon}_g$ and ε_b may be

Fig. 3.14 *Optical photomicrographs (crossed polars plus gypsum plate) of sample GRU29 ('wet', 10^{-6} s^{-1}, ~40% strain) showing intergranular axial micro-cracks and deformation lamellae. Crack walls show euhedral crystal morphology indicating that solution-precipitation processes operated and gave the fracture an irregular form. (a) Micro-cracks do not cross-cut the grain entirely. (b) Micro-crack cross-cuts deformation lamellae. Note slight rotation of fractured blocks. (c) Original grain containing several axial micro-cracks developed sub-parallel to deformation lamellae. Note relatively large amounts of rotation of the fractured blocks giving the impression of undulatory extinction and subgrains. East-west trending extinction bands are developed perpendicular to slightly bended deformation lamellae. (d) Micro-cracks (see arrows) cross-cutting deformation lamellae. Note euhedral habitus of fracture walls. (e) Bended deformation lamellae plus undulatory extinction in bands. Yellow grain is fractured.*

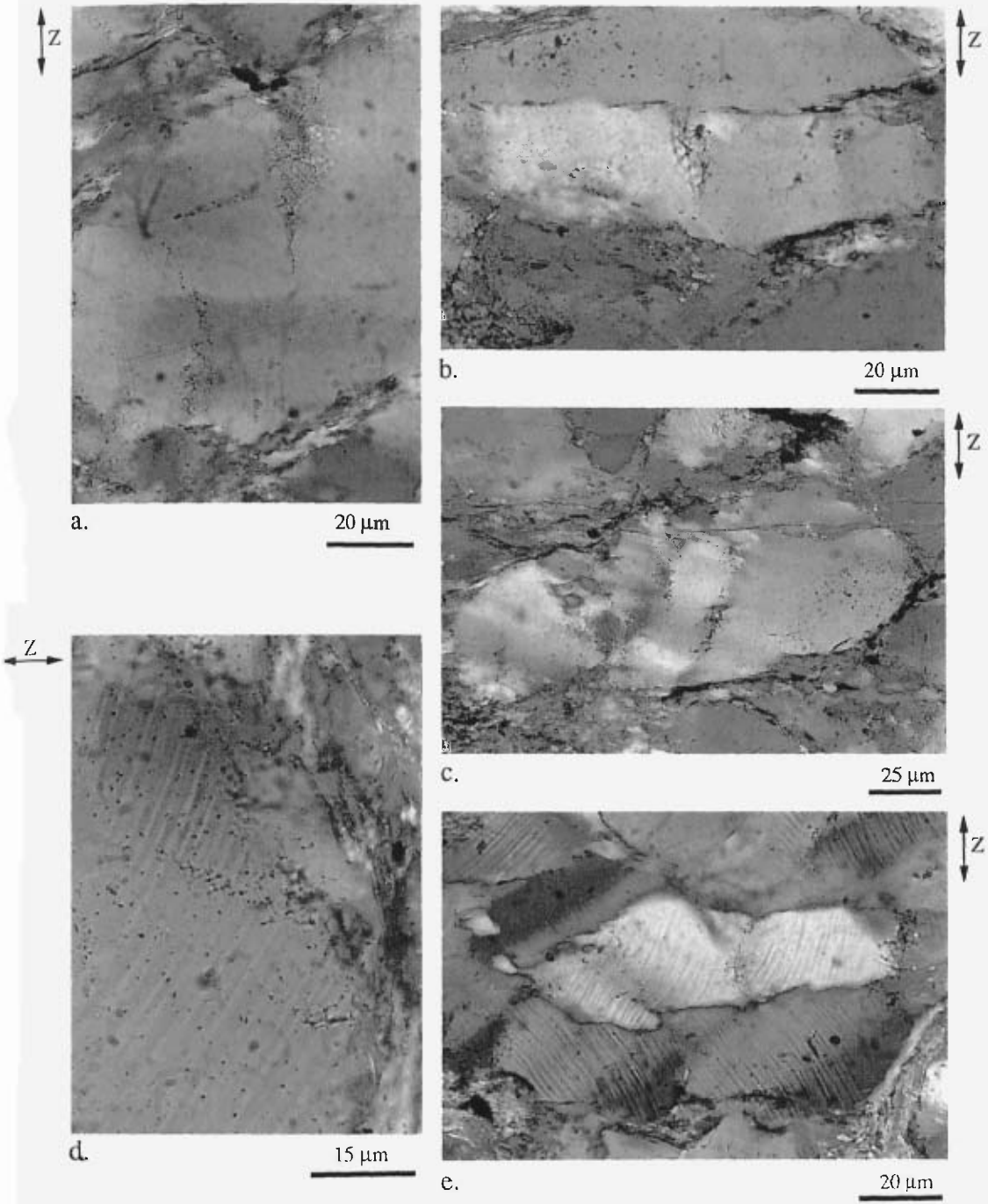

Fig. 3.14 *(Explanation see previous page)*

either due to grain boundary sliding, which does *not* contribute to $\bar{\varepsilon}_g$, *or* due to solution mass transfer, which does *partly* contribute to $\bar{\varepsilon}_g$, depending on whether precipitation occurred by syntaxial overgrowth *or* by nucleation of small new grains (Fig. 3.17). Some grains are flattened more than others, depending on the angle between the c-axis and Z (Fig. 3.15b).

As at low strain, the original grains are commonly split into two or more parts (or 'sub' grains) with an open fracture or an axial array of smaller new grains in between (Fig. 3.7c & d). Original-grain grain boundaries oriented parallel to Z are commonly serrated, showing well developed regular intergrowth or interfingering structures, with individual 'fibres' of 1 to 5 μm wide and 2 to 25 μm long. Locally these structures resemble growth fibres, and are conspicuously absent at grain boundaries oriented perpendicular to Z.

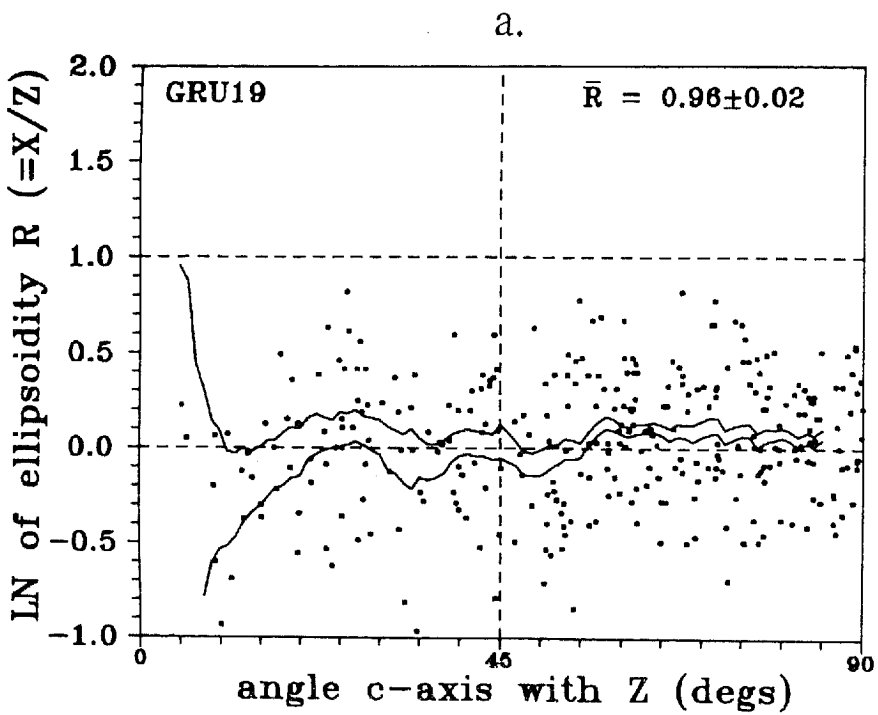

Fig. 3.15 *Natural logarithm of ellipsoidity ($\bar{R}$) versus angle of c-axis with Z for (a) sample GRU19 which was hydrostatically loaded only, (b) sample GRU29, and (c) sample GRU35. Each point refers to one grain. The average ellipsoidity $\bar{R}$ plots between the lines; the upper line is $\bar{R}$ plus its error; the lower line is $\bar{R}$ minus its error. Note that in the deformed samples, grains with a certain orientation of the c-axis with Z are flattened more than others. R-values are indicated in upper right corner.*

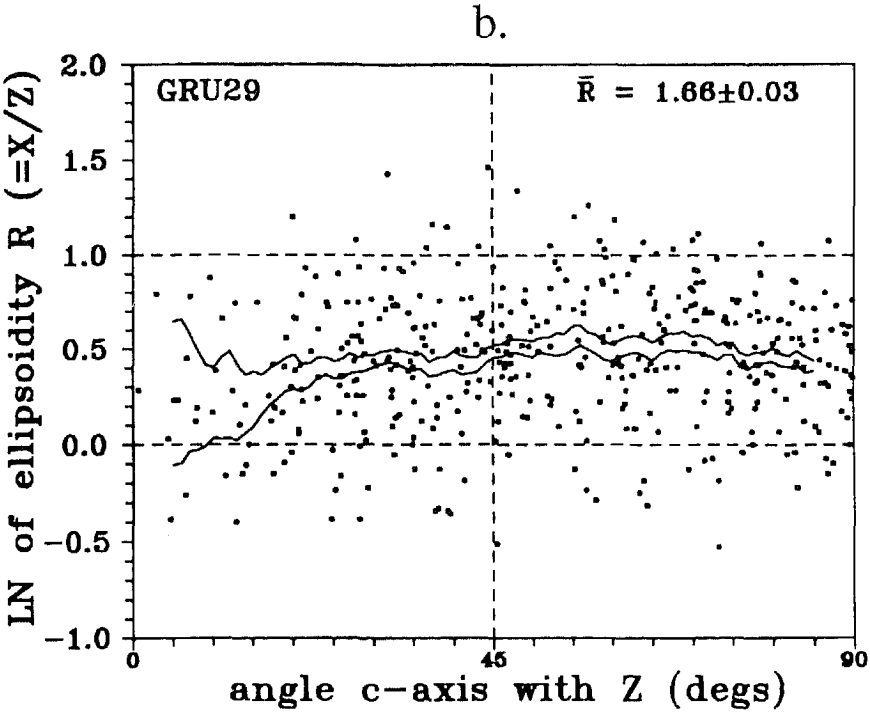

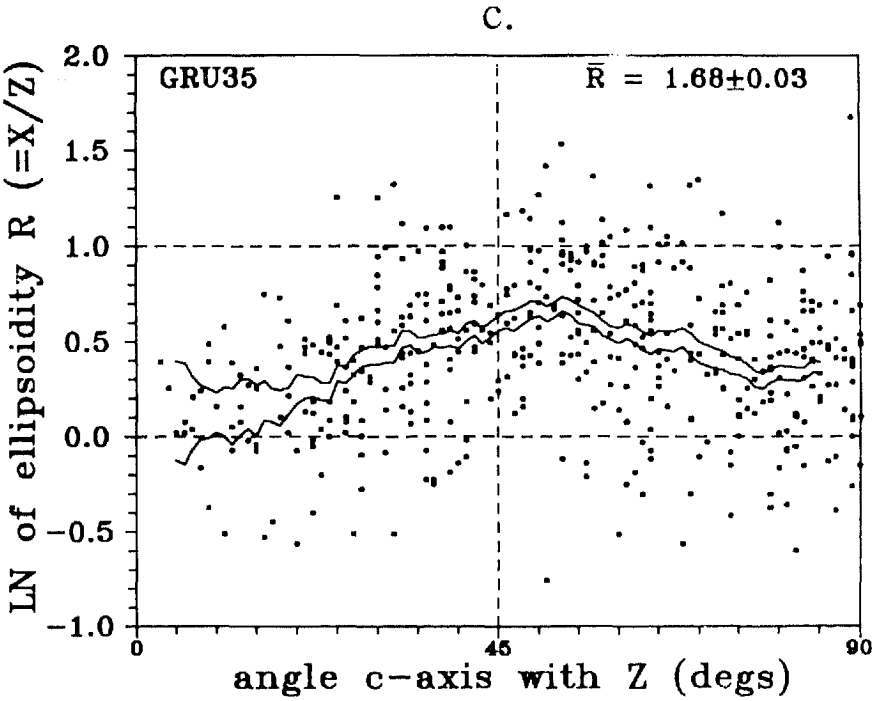

Fig. 3.15 *(Continued)*

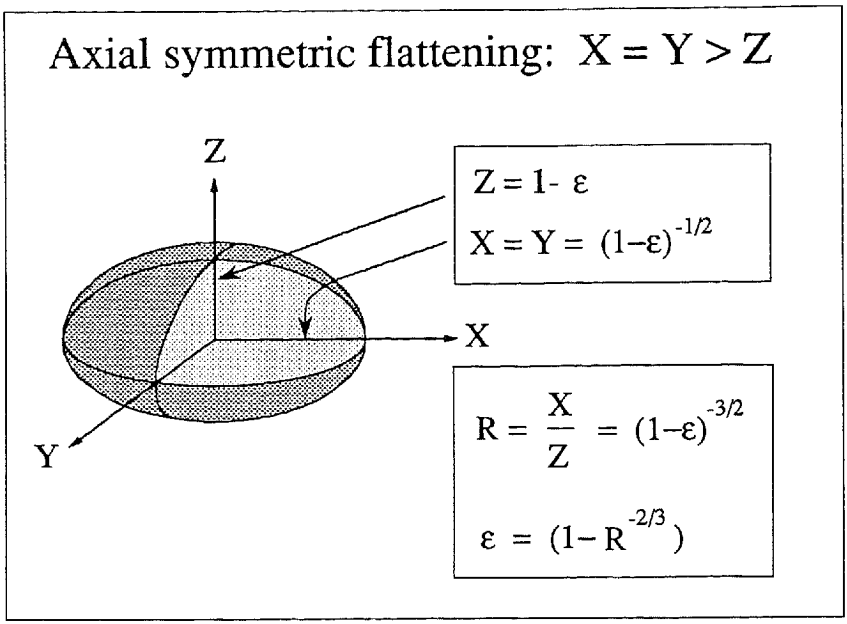

Fig. 3.16 *Diagram illustrating the relationship between the ellipsoidity R (=X/Z; measured in a section parallel to Z) and the strain (ε) of an initially spherical grain with unit radius, assuming constant volume, axial symmetric flattening.*

Fig. 3.17 *Schematic illustration of how SPC and crystal-plastic deformation contribute to the ellipsoidity, or grain-strain, of the original grains. (a) Original grain before deformation. (b) When the deformation is entirely crystal-plastic, then the grain strain (ε_g) of the original grains is equal to the bulk strain (ε_b). (c) When the deformation is entirely due to SPC, and when precipitation of the dissolved material occurs entirely in the form of small new grains at grain boundaries oriented parallel to Z (dark grey area) then the grain strain (ε_g) of the original grains is smaller than the bulk strain (ε_b), and equal to $1-(1-\varepsilon_b)^{2/3}$. (d) & (e) illustrate the contribution of respectively syntaxial overgrowth and of crystal-plastic deformation to ε_g.*

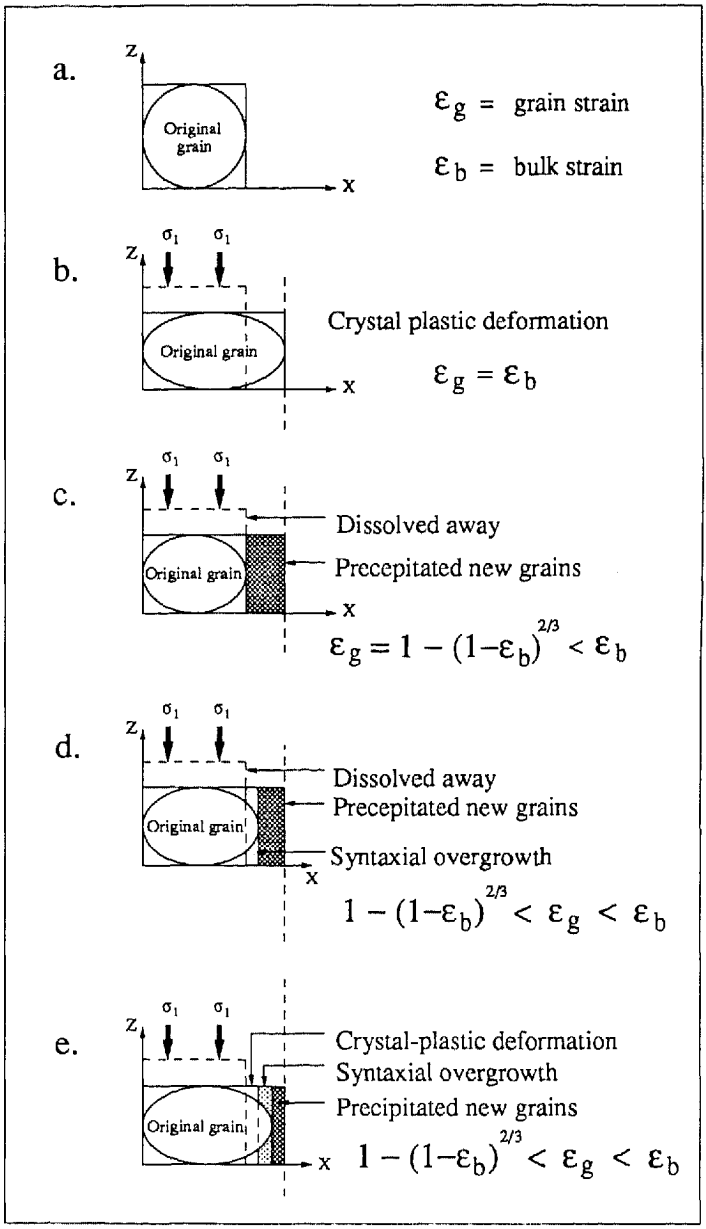

Fig. 3.17 *(Explanation see previous page)*

Small, equidimensional as well as irregularly shaped new grains, preferentially developed in numerous 15 to 100 μm wide arrays oriented subparallel (0-20°) to Z (Fig. 3.18), are much more abundant than at low strain. (The width of the arrays is measured in the plane of the thin-section, which may not be the true width of the arrays, as they probably intersect the thin-section plane obliquely; the thin-section contains 15 to 20% new grains). As at low strain, the new-grain arrays contain

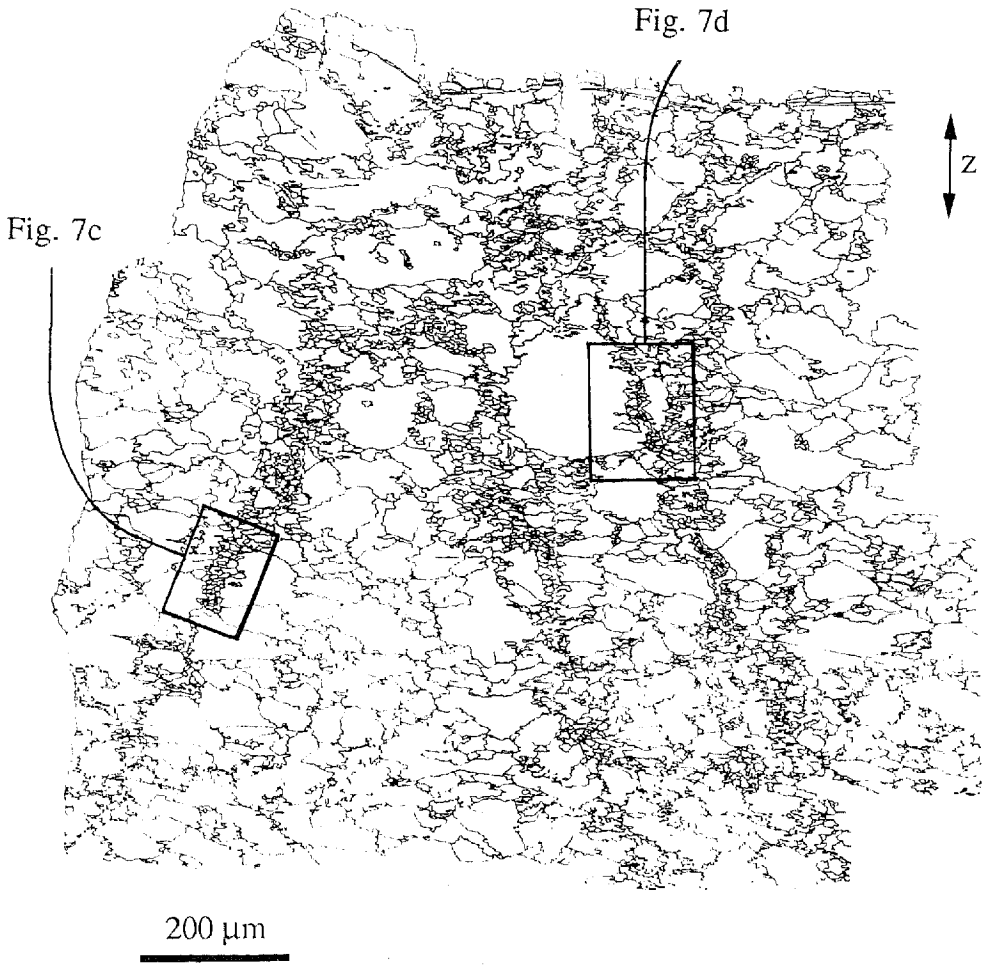

Fig. 3.18 *Traced micrograph of part of sample GRU35 showing flattening of original grains and the distribution of new grains in arrays sub-parallel to Z.*

abundant microcavities (or voids) and intergranular channel structures (1-5 μm diameter) located both at grain triple junctions and on grain boundaries (commonly occupying up to 25% of the grain boundary surface). But the voids are smaller, and the number of euhedral crystal faces is lower (Fig. 3.19).

Locally, new grains are strongly flattened (grain size 5-15 μm by 15-100 μm) and have irregular grain boundaries (Fig. 3.7d). In areas where the sample was curled around the piston (where the sample had moved outside the differential stress field), the new grains are larger (≤60 μm), mostly equidimensional, and have straight grain boundaries.

A TEM study of this sample showed that the dislocation density of the original grains, as well as of the new grains was of the order of 5 to 10 times 10^8 cm^{-2}. The small new grains generally have the lowest dislocation densities, and locally are even completely free of them. The dislocations have irregular orientations, both in the original grains (Fig. 3.20a & b) as in the new grains (Fig. 3.20c & d). Some of the dislocations are straight and occur in regular arrays, whereas others are curved and locally tangled. In the original grains dislocation networks and loops were observed (Fig. 3.20b), suggestive of dislocation glide (see arrow in Fig. 3.20a).

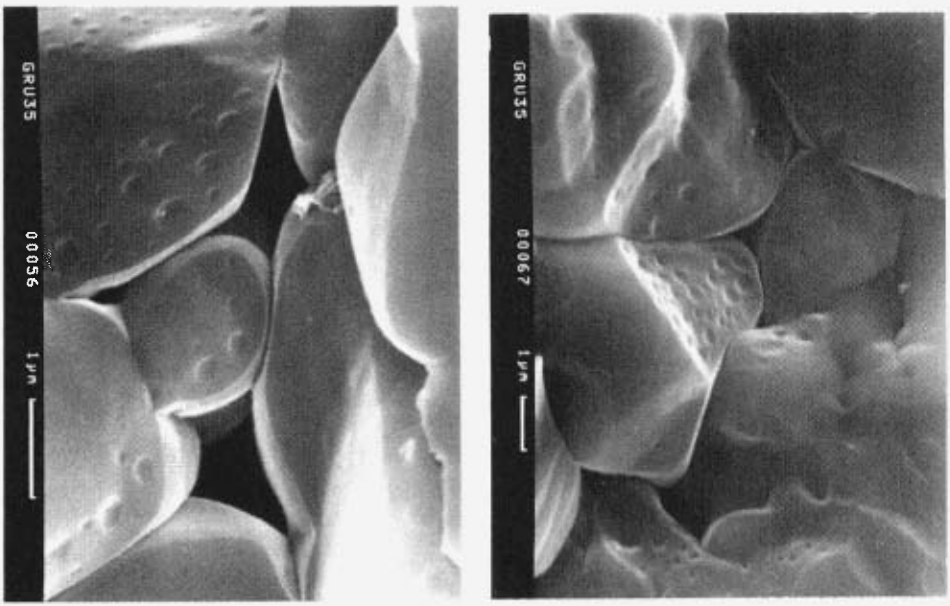

Fig. 3.19 *SEM micrographs of sample GRU35 showing microstructure within new grain arrays. The arrays contain large amounts of voids and channels at grain triple junctions. New-grain grain-boundaries contain large amounts of fluid inclusions. Euhedral crystal planes are much less frequent than at low finite strain. Note absence of glass.*

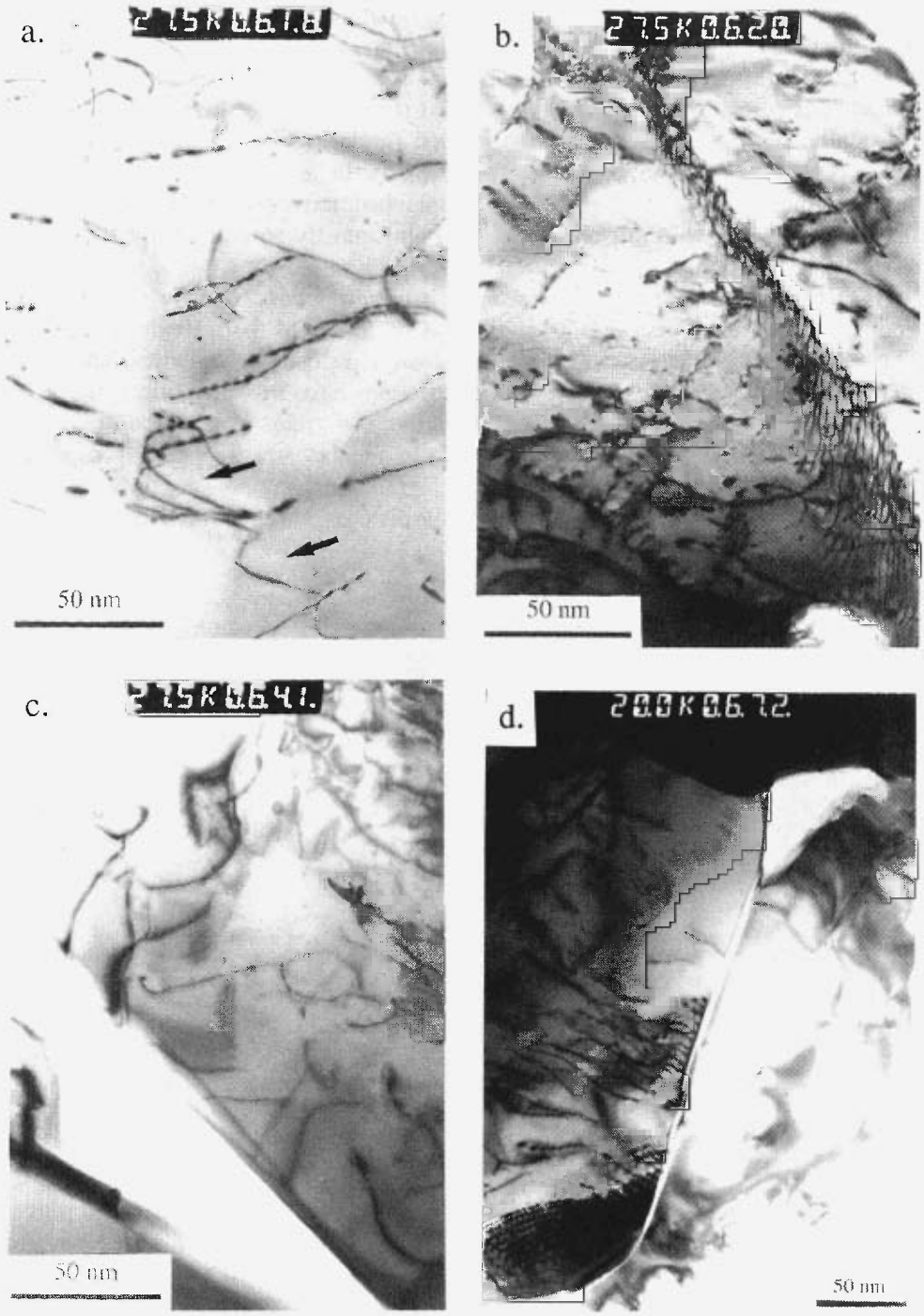

Fig. 3.20 *(Explanation see next page)*

3.5.4 Microstructures developed under intermediate conditions

3.5.4.1 Low finite strain (6-12%)

At low finite strain (6-12%), samples deformed 'wet' at 10^{-6} (GRU10, 20 & 21) and at 10^{-5} s^{-1} (GRU13 & 14), and 'as-received' at 10^{-7} s^{-1} (GRU31, 40 & 41), all show deformation microstructures characteristic of the 'dry' as well as of the 'wet' material deformed at 10^{-7} s^{-1}. Deformation lamellae are abundant (in 30-55% of the grains), as well as transgranular and grain boundary micro-cracks with overgrowth features on the crack walls. By contrast to the 'dry' material, the lamellae do not occur in en-echelon arrays, but cross-cut the grains completely. New grains occur, but are less frequent, and smaller (≤20 μm) than in the samples deformed at 10^{-7} s^{-1}.

The samples deformed 'wet' at 10^{-5} s^{-1} (GRU13 & 14) show also several through-going axial fractures. These fractures are filled-in with very fine (1-5 μm) subeuhedral quartz and mica grains (in a zone ≤50 μm wide). The fracture walls locally show fine (1-5 μm) overgrowth features.

3.5.4.2 High finite strain (~40%)

Sample GRU29, deformed 'wet' at 10^{-6} s^{-1} to a bulk finite strain (ε_b) of 40±1 %, shows significantly more axial intragranular micro-cracks (Fig. 3.14), subbasal deformation lamellae plus associated undulatory extinction (in ~65% of the original grains; see also Fig. 3.14), and small new grains, than the LFS samples (GRU10, 20, & 21) deformed under similar conditions. These micro-cracks (along which commonly 3-10° rotation has taken place) frequently follow deformation lamellae that are oriented subparallel to Z (Fig. 3.14a & c). Micro-cracks that cross-cut lamellae are also common (Fig. 3.14b, d & e). As at low strain, the crack walls mostly show euhedral crystal morphology, resembling syntaxial overgrowths. Irregular, partly healed micro-cracks, along which minor amounts of rotation has taken place, give the impression of undulatory extinction. The *volume* percentage

Fig. 3.20 *TEM micrographs of sample GRU35. (a) & (b) Dislocation configuration of deformed original grains. Note dislocation loop structure indicative of dislocation glide in (a) (see arrows), and dislocation wall in (b). (c) & (d) Dislocation configuration of new grains. Note curved dislocations in (c) (consistent with climb), and parallel arrays of straight dislocations in (d) (consistent with glide). Note presence of large voids, as also shown in the SEM-pictures.*

of new grains to old grains could not be established, but measured in the thin-section, 10 to 15 % of the area consisted of new grains (compared to <5% in the LFS samples).

The R-value of the original grains is 1.66±0.03 corresponding to $\bar{\varepsilon}_g$=29±1 % (equation 1; 435 grains were measured; Fig. 3.15c). Some grains are flattened more than others, depending on the angle between the c-axis and Z. On average, grains with c-axes oriented at 50-70° to Z are flattened more ($\bar{\varepsilon}_g$=32±2 %) than the other grains ($\bar{\varepsilon}_g$=28±1 %). Grains with c-axes at 0-20° to Z are flattened the least ($\bar{\varepsilon}_g$=19±4 %).

The sample contains two very thin, sample scale shear zones, one making an angle of ~37° with Z, and another making an angle of ~60° with Z. Locally the grain long axes are bent into these shear zones. The absolute displacement measured in the thin-section was less than ~50 μm on the steep shear zone, and less than 25 μm on the other one. Therefore, the shear zones only have accommodated <1% of ε_b.

3.6 INTERPRETATION OF RESULTS

Though of relatively poor quality, the mechanical data reported above demonstrate that samples deformed with small amounts of added water are significantly weaker than those deformed 'dry'. This weakening is of the order of 2 to 100 times at a strain rate of 10^{-7} s^{-1} and with ~0.4 wt% water added. Furthermore, the weakening effect is rate dependent, such that for $\dot{\varepsilon} \leq 10^{-6}$ s^{-1} the stress exponent, assuming a power-law formulation is ≤1.3.

Let us now consider the influence of water on deformation mechanisms. The optical deformation microstructures observed in the single 'dry' sample (GRU46) deformed at 10^{-7} s^{-1} consisted of en-echelon arrays of deformation lamellae, which (optically) looked like crystallographically controlled shear fractures. Deformation bands were also present. Almost identical microstructures were observed in a 'dry' single crystal deformed under similar conditions (GRU43). I did no TEM work on these materials, but Christie & Ardell (1974) observed in samples deformed at broadly similar conditions (T=750°C, $\dot{\varepsilon}=10^{-6}$-$10^{-4}$ s^{-1}) that lamellae of the type observed consisted of glass. The mechanisms by which such lamellae form is not well understood. Though widely believed to reflect dislocation-plastic activity, they may also have originated by defectless yield on crystallographically controlled shear fractures (chapter 2).

In contrast to these features, the samples deformed 'wet' at 10^{-7} s^{-1} (GRU11, 23, 26 & 35) show microstructures which are clearly related to the presence of the added water. This is inferred from the numerous microcavities, fluid inclusions and intergranular channel structures present in the observed arrays of new (sub) euhedral quartz and mica grains. These axially aligned arrays of new grains are not

present in the quartzite deformed 'dry'. They are interpreted to result from precipitation from solution in grain boundary and transgranular micro-cracks aligned parallel to Z. In addition, indentations (without plastic deformation) into the polished surface of the quartz single crystal included in experiment GRU23 provide strong evidence that pressure solution took place in the 'wet' tests at 10^{-7} s^{-1} (note also the absence of overgrowth features on the grain boundaries oriented normal to Z). In all samples deformed under these conditions, the old grains are more or less free of subgrains, deformation lamellae, and CPO. These observations indicate that crystal-plastic deformation did not significantly contribute to the development of the microstructure. The possibility that melt-assisted diffusional transfer processes (e.g. Koch et al. 1989) were important, seems unlikely since no evidence whatsoever was found for a melt-glass phase. The relative importance of different deformation processes such as dislocation activity, grain boundary sliding and SPC has been inferred from the microstructures seen in samples deformed to high strains making use of measured ellipticity of grains and of volume of precipitated grains (see appendix D). The results are given in table 3.3 and indicate that SPC and grain boundary sliding were dominant. The dislocation density observed in TEM may be consistent with minor plastic deformation but could also be introduced by growth.

Table 3.3 *Relevant data concerning the contribution of the different deformation processes to the bulk strain of samples GRU29 & 35.*

	GRU29	GRU35
Bulk strain	40 ± 1 %	46 ± 1 %
Average grain strain	29 ± 1 %	29 ± 1 %
Percentage of new grains	10 - 15 %	15 - 20 %
Contribution of Solution mass transfer	19 - 28 %	28 - 36 %
Contribution of Grain boundary sliding	4 - 8 %	7 - 12 %
Contribution of Crystal plasticity and/or solution mass transfer with syntaxial overgrowth	4 - 17 %	0 - 11%

Because the *effective* confining pressure was very low, it can be argued that the presently observed water-weakening effect might have been caused by fracturing plus an accompanying loss of cohesion of the sample. However, the rate dependence of the weakening effect indicates that this was not the case; rather a *rate dependent* process, such as stress corrosion cracking or SPC, must have controlled the deformation. It is concluded that micro-cracking and SPC were indeed responsible for most of the observed water-weakening effects. The very low stress exponent ($n<1.3$) inferred from Fig. 3.3 for 'wet' samples at $\dot{\varepsilon} \leq 10^{-6}$ s^{-1} is consistent with this conclusion, though more reliable mechanical data are clearly desirable.

3.7 COMPARISON WITH PREVIOUS EXPERIMENTAL RESULTS

Comparison of experimental data obtained in different laboratories is complicated by the use of different starting materials, deformation apparatus, sample assemblies, water fugacities, fluid pressures and chemistries, confining pressures, temperatures and strain rates. Also the present study is the first in which the water was sealed into the capsules by welding the capsule 'tight'. In previous studies the water was either simply enclosed in the capsules without real sealing (e.g. Jaoul et al. 1984, Kronenberg & Tullis 1984, Ralser et al. 1991), or water was made available from the dehydrating talc confining medium (e.g. Tullis et al. 1973, Koch et al. 1989). Notwithstanding the difference in sample sealing, the present study essentially repeats and is therefore more or less directly comparable to that of Jaoul et al. (1984). It is important to note, however, that the microstructures and weakening behaviour reported by Jaoul et al. (1984) are broadly similar to those observed in other experimental studies on quartzites (e.g. Tullis et al. 1973; Parrish et al. 1976; Kronenberg & Tullis 1984; Koch et al. 1989; Ralser 1990; Wang, Ord & Hobbs 1991 pers. comm.), so that comparison with these seems justified too.

3.7.1 The experiments of Jaoul et al. (1984)

Jaoul et al. (1984) used Heavitree quartzite (grain size ~150 μm) as a starting material with varying amounts (≤0.5 wt-%) of added water. Their tests were performed at 1500 Mpa confining pressure, temperatures of 1073 K to 1373 K and strain rates varying from 10^{-4} to 10^{-7} s^{-1}. The steady state rheological data obtained by Jaoul et al. (1984) at 1073 K, with an H_2O content of 0.4 wt-%, seem broadly consistent with the flow stress versus strain rate data reported in this study (Fig. 3.3), and likewise show water-weakening at low strain rates with power-law stress exponents reaching values as low as 1.4 or even 1.2 (Jaoul et al. 1981). The microstructures reported by Jaoul et al. (1984) for water weakened material also seem to

be very similar to the SPC plus infilled crack microstructure seen in the present experiments on 'wet' material at 10^{-7} s^{-1} (see Fig.3E, Jaoul et al. 1984, cf. present Fig. 3.5). But, as explained above, Jaoul et al. (1984) interpret this microstructure as indicative of crystal-plasticity plus dynamic recrystallization (core and mantle structure). They correlate their water-weakening effect with the onset of this latter process and suggest that weakening is actually caused by intracrystalline enhancement of climb and glide by dissolved water defects ('classical' hydrolytic weakening argument). It was also mentioned above, that this interpretation would imply that water-weakening should be time dependent due to progressive penetration of water into the original grains (≤1 μm per day after Paterson & Luan 1990), but no progressive change in creep behaviour with time has been observed (Jaoul et al. 1984; Kronenberg & Tullis 1984). Furthermore, Kronenberg & Wolf (1990) report that the intergranular water content of water-weakened Heavitree quartzite appears unchanged before and after experimental deformation (see also chapter 5).

On the basis of the above information, it is proposed here that the water-weakening effect reported by Jaoul et al. (1984) was very probably due to the same process as that inferred for the present experiments, i.e. due to coupled micro-fracture plus solution-precipitation transfer. Since Jaoul et al. (1984) do report the presence of a minor amount (<3 vol%) of glass in their samples, the possibility of melt-assisted SPC cannot be ruled out in their experiments (see Koch et al. 1989). Melting was presumably caused by the breakdown of muscovite plus quartz. Notably, the water-added experiments of Mainprice & Paterson (1984), Jaoul et al. (1984), and those of the present study were indeed performed outside the stability field of muscovite plus quartz (in the presence of 20-30 wt% added water). Nevertheless, in the present study, the water-added samples GRU11 & 26 still contained micas after deformation, as was optically verified and indicated by FTIR-spectra (see chapter 5). No glass was observed, neither optically, nor with the SEM. This may be because the stability field referred to above was determined with 20-30 wt% added water, whereas only ~0.4 wt% water was added to the 'wet' samples, almost 2 orders of magnitude less. The development of melt in the test of Jaoul et al. (1984), but not in the present one, may also reflect compositional differences.

3.7.2 Other experiments

Additional support for the operation of a micro-cracking plus SPC mechanism under the present or similar conditions (probably with minor melting), is widespread in the literature. For example, extensional pockets of 'recrystallized' grain boundaries parallel to Z are also reported by Dell'Angelo & Tullis (1989). These pockets contain segregations of impurities plus very small amounts of melt and were interpreted as an extensional crenulation cleavage (though as pointed out by the authors, they do not appear to crenulate a foliation). In addition, ample

evidence has been reported in the literature for the existence of interconnected grain boundary fluids, microvoids, and channel structures under similar conditions to those investigated here (for hydrostatic experiments see Watson & Brenan 1987, Mackwell & Weathers 1987, Mackwell et al. 1989; for non-hydrostatic experiments see Den Brok 1989, Karato & Masuda 1989, Mackwell et al. 1989).

In the case of experiments on single crystals, there can be little doubt that a truly intracrystalline water-weakening effect occurs in 'wet' synthetic quartz, but in experiments on 'dry' natural crystals tested with added water, substantial evidence has been reported for a correlation between weakening and micro-cracking (Kirby & Kronenberg 1984; Kronenberg et al. 1986; Fitz Gerald et al. 1987, 1991). In these cases, however, it still remains unclear whether micro-cracking itself is associated with the weakening (possibly in association with SPC processes), or that it simply reduces the diffusion path for water into the crystal, thus allowing intracrystalline weakening effects to take place (Ord & Hobbs 1987).

Recently, Fitz Gerald et al. (1991) demonstrated that sample-scale fracturing (plus healing) produced dislocations in single crystals of natural quartz deformed with added water. These dislocations became mobilized by the differential stress and caused ~0.5% strain in a ~100 μm wide zone on each side of the *healed* sample-scale fractures. Most of the bulk sample strain took place in the healed or 'recrystallized' zones. In the present study, micro-cracking plus healing processes also occurred and may, following Fitz Gerald et al., have produced dislocations allowing glide and climb. But the microstructural and mechanical data reported in the present study are inconsistent with these processes being dominant.

3.8 CONCLUSIONS

The present experiments indicate that at a temperature of 800°C, a confining pressure of ~1200 MPa, and at a strain rate of 10^{-7} s^{-1} (and to a lesser extent also at 10^{-6} s^{-1}), water-weakening of Dongelberg quartzite is achieved by micro-cracking and solution-precipitation creep, rather than by any intracrystalline effect. The results cast serious doubt on the widely accepted idea that water-weakening of quartzites seen in experiments is due to an intracrystalline hydrolytic weakening mechanism (see also Den Brok 1989; Mackwell et al. 1989).

Chapter 4

PREFERRED ORIENTATION DEVELOPMENT

4.1 INTRODUCTION

The mechanical data and microstructures reported in chapter 3 provide evidence that quartzites deformed at 800°C and ~1200 MPa, in the presence of ~0.4 wt% added water, deform predominantly by micro-cracking plus solution transfer. As mentioned previously (chapter 3), this sharply contradicts the widely held view that deformation of quartzite under these conditions occurs by crystal-plastic mechanisms, facilitated by a 'classical' intracrystalline hydrolytic weakening effect (e.g. Koch et al. 1989, Paterson 1989, Tullis 1990). One of the principal lines of evidence presented in the literature in support of crystal-plastic deformation mechanisms is the development of (strong) c-axes preferred orientations (CPO's) in old grains (e.g. Tullis et al. 1973). Recently, however, the optical methods generally used to measure CPO's in the experimentally deformed quartzites have been shown to introduce a certain degree of systematic bias (Dell'Angelo & Tullis 1986; see also Starkey & Sutherland 1978), so caution is needed in interpretating existing CPO-data.

The present chapter documents work on the c-axes and deformation lamellae orientation distributions developed in the experiments on quartzites documented in chapter 3, focussing attention on samples deformed to high strains (≥40%). Measurements were performed optically, but taking special care to use techniques which would avoid artificial biasing of the data. In contrast to previous work, the results show little or no CPO development in the old-grain populations. This finding more or less rules out crystal-plasticity as the dominant deformation mechanism in these samples, but is fully consistent with coupled micro-cracking plus solution transfer creep.

4.2 SAMPLES STUDIED AND METHOD USED

The present preferred orientation work was performed on samples of Dongelberg quartzite subjected to the following treatments as described in chapter 3 (see table 3.1):

(i) Sample GRU19, hydrostatically loaded to a temperature (T) of 800°C and a confining pressure (P_c) of ~1250 MPa, with ~0.4 wt% added water for ~90 hr.

(ii) Sample GRU29, deformed to 40±1 % strain at T=800°C, $P_c \approx 1160$ MPa, a strain rate ($\dot{\varepsilon}$) of $\sim 10^{-6}$ s^{-1}, with ~0.4 wt% added water.

(iii) Sample GRU35, deformed to 46±1 % strain at T=800°C, $P_c \approx 1260$ MPa, $\dot{\varepsilon} \approx 10^{-7}$ s^{-1}, with ~0.4 wt% added water.

C-axes orientation data were obtained for all samples by means of optical study of thin sections using a universal stage. Orientations were measured in old grains only (newly grown grains were omitted). Since Starkey & Sutherland (1978) have shown that orientation distribution data becomes systematically biased when no precautions are taken to ensure that *all* grains in a representative area are measured, maps were made of each thin-section studied, by tracing grain boundaries from micrographs. In this way, *all* old grains (i.e., grains ≥50 μm) in the central part of the sample could be measured, so that any sampling bias was minimized. Some 350 grains were measured up in sample GRU19, 435 in GRU29, and 470 in GRU35.

At this point it is useful to note the consequences of failure to measure *all* grains in a given area. As documented by Starkey & Sutherland (1978) and Dell'Angelo & Tullis (1986), this leads to (unintentional) selection of *those* grains that display the highest birefringence (because these are optically most outstanding). These grains have their c-axis oriented sub-parallel to the thin-section plane, at high angles (i.e., 30-45°) to the principal polarization directions. Thus, for example, measurement of a truly random fabric results in a CPO showing strong peripheral maxima at 30-60° to the N-S and E-W directions (assuming N-S and E-W polarization; see Fig. 3 of Starkey & Sutherland 1978). Therefore, the true strength and the true location of maxima in such improperly measured fabrics remain essentially obscure.

4.3 RESULTS

4.3.1 C-axes data

The old-grain c-axes data obtained for samples GRU19 (hydrostatically loaded only), GRU29, and GRU35 are presented in the pole figures of Fig. 4.1. The preferred orientations are clearly very weak (maximum concentrations are ~2 times uniform), with those of the deformed samples (GRU29 & 35) being hardly different from the undeformed hydrostatically loaded sample (GRU19). All samples show a tendency towards slight orthorhombic symmetry, with small, very weak maxima at 20-25°to Z in the thin-section plane. In the deformed samples, very weak maxima are also present in the plane perpendicular to Z.

4.3.2 Data on deformation lamellae

Deformation lamellae are developed in deformed samples only. They occur in ~65% of the original grains in sample GRU29 and in ≤12% of the original grains in sample GRU35. The lamellae are sub-basal, making on average an angle of 12±1° with the

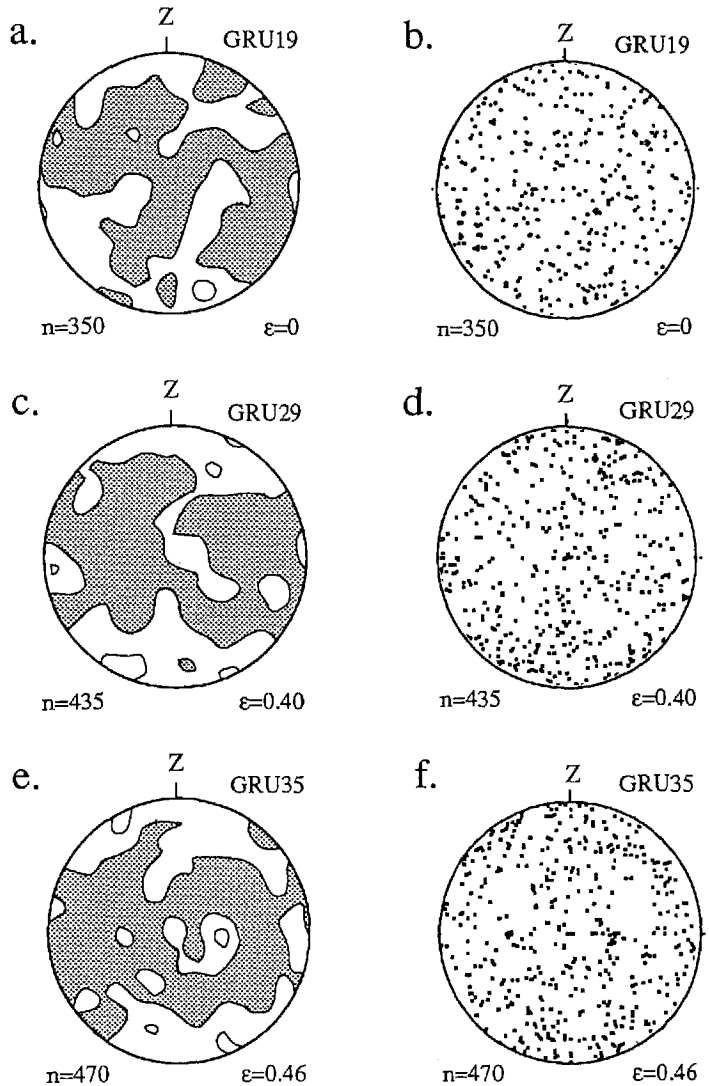

Fig. 4.1 *(a) & (b) Old-grain CPO of undeformed sample GRU19 hydrostatically loaded to T=800°C and $P_c \approx 1200$ MPa. (c) & (d) Old-grain CPO of sample GRU29 deformed to ~40% strain with ~0.4 wt% added water at T=800°C, $P_c \approx 1200$ MPa, and $\dot{\varepsilon} \approx 10^{-6}$ s^{-1}. (e) & (f) Old-grain CPO of sample GRU35 deformed to ~46% strain with ~0.4 wt% added water at T=800°C, $P_c \approx 1200$ MPa, and $\dot{\varepsilon} \approx 10^{-7}$ s^{-1}. Contours in equal area plots are 1 and 2 times uniform. Shortening direction Z is indicated.*

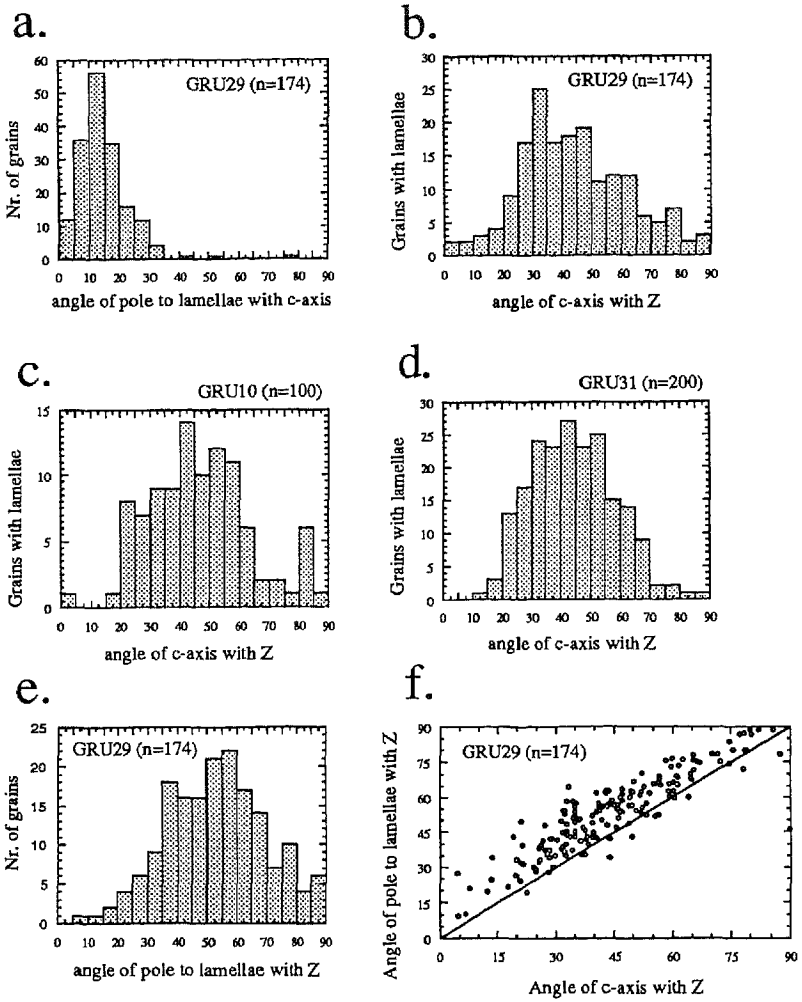

Fig. 4.2 *(a) Histogram showing distribution of angles between c-axis and poles to lamellae in grains with lamellae in sample GRU29. Average angle is 12±1°, hence, the lamellae are sub-basal. (b) Histogram showing distribution of angles between c-axes of grains with lamellae and Z in sample GRU29. (c), & (d) Same as (b) for respectively sample GRU10 (deformed to ~9% strain with ~0.4 wt% added water at T=800°C, P_c≈1200 MPa, and $\dot{\varepsilon}$≈10^{-6} s^{-1}) and sample GRU31 (deformed 'as-received' to ~11% strain at T=800°C, P_c≈1200 MPa, and $\dot{\varepsilon}$≈10^{-7} s^{-1}). (e) Histogram showing distribution of angles between poles to lamellae and Z in sample GRU29. (f) Diagram showing that the angles of c-axes with Z are mostly smaller than the angles of poles to lamellae with Z, i.e., looking perpendicular to Z, lamellae are oriented steeper than the basal planes.*

basal plane in sample GRU29 (Fig. 4.2a). Too few lamellae were present in sample GRU35 to measure their orientation in a statistically significant manner.

The presence of lamellae in original grains correlates with the grain's c-axis orientation with respect to Z. This is illustrated for sample GRU29 in Fig. 4.2b. About 75% of the grains with lamellae have their c-axis at 25 to 65° to Z. For comparison, the distribution of c-axes of grains with lamellae in sample GRU10 (~9% strain; conditions further as GRU29; see chapter 3) and sample GRU31 (~10% strain, deformed 'as-received'; conditions further as GRU35; see chapter 3) are also shown (Fig. 4.2c & d). These distributions are broadly similar to the one of GRU29.

The poles to lamellae (only measured in GRU29) also show a preferred orientation (Fig. 4.2e). These are oriented at 35 to 80° to Z in ~80% of the grains with lamellae. Looking perpendicular to Z, the lamellae are oriented steeper than the basal planes, almost without exception (Fig. 4.2f). In other words, the angle between the pole to the lamellae and Z is larger (by ~12° on average) than the angle between the c-axis and Z.

4.4 INTERPRETATION

The Present results show that little or no old-grain CPO developed in the experiments reported in chapter 3, for strains up to 46%. The slight orthorhombic symmetry, also present in the undeformed sample GRU19, is most likely inherited from the starting material.

From studies on other materials (e.g. metals, calcite, salt) and from computer simulation work using methods such as the Taylor-Bishop-Hill model, it is well-established that deformation by crystal-plastic mechanisms produces relatively strong preferred orientations, even after strains of only ~15%. It is therefore inferred that crystal-plastic mechanisms cannot have been of more than minor importance in the experiments considered in this chapter (as far as old grains are concerned). This seems superficially contradictory to the fact that deformation lamellae are abundant in the deformed sample GRU29, since the presence of these is commonly regarded as strong evidence for crystal-plastic deformation (e.g. Tullis et al. 1973, Ralser et al. 1991). Recall, however, that the physical significance of deformation lamellae is not understood (chapter 2). The presence of lamellae does not necessarily indicate that crystal-plastic deformation occurred or was important.

Shear displacement along lamellae (Christie et al. 1964a, Heard & Carter 1968), regardless of the detailed mechanism, should in principle produce a preferred orientation if sufficient strain is accommodated, *and* when the lamellae have a strong preferred orientation, such as in sample GRU29 (Fig. 4.2e). In the case of GRU29, where the lamellae are sub-basal, a small-circle distribution of c-axes about Z with a half-angle <45° is expected to develop, the half-angle decreasing in value with increasing strain. However, the absence of a significant CPO rules out that this process

was significant in the experiments considered.

In contrast, the present results are consistent with deformation by micro-cracking plus solution transfer since these mechanisms very unlikely produce old-grain preferred orientations. Only if the solution transfer were interface-reaction controlled and when reaction/growth kinetics would be highly anisotropic, then an old-grain CPO would develop. But the anisotropy in reaction/growth kinetics of quartz is probably not strong enough to produce a significant old-grain CPO at 40-46% strain (see values given by, e.g., Chernov & Dimitrov 1989 and Gratz et al. 1990). Thus, the conclusion drawn in chapter 3 that deformation of quartzite, under the conditions studied, occurs by micro-cracking and solution transfer creep is strongly supported by the present findings.

4.5 COMPARISON OF RESULTS WITH PREVIOUS DATA

The results presented in this chapter show that little or no old-grain preferred orientation develops in quartzites deformed with ~0.4 wt% of added water at P_c=1160-1260 MPa, T=800°C, $\dot{\varepsilon}=10^{-6}$ and 10^{-7} s^{-1}, to 40 and 46% strain. This result is quite different from previous reports of Tullis et al. (1973), Jaoul et al. (1984), Dell'Angelo & Tullis (1986) and Den Brok & Spiers (1991) which showed relatively strong CPO's developed under broadly similar experimental conditions. Data presented by Den Brok & Spiers (1991) was for sample GRU29 (Fig. 4.3) re-measured in the present work. The previous fabric was 2-3 times stronger (maximum density 5-6 times uniform). The difference is caused by the above-mentioned improper measurement technique. In the present study *all* the grains were measured, whereas Den Brok & Spiers (1991) unintentionally selected grains with the highest birefringence because these were optically most outstanding.

The same improper measurement technique was documented by Dell'Angelo & Tullis (1986). They wanted to explain why *peripheral* maxima were obtained in *axially* flattened samples. They therefore measured old-grain CPO's of two mutually perpendicular thin-sections both taken parallel to Z in one and the same axially deformed sample. In both cases a similar pattern with peripheral maxima was obtained (see their Fig. 3). This indicates that the maxima were indeed caused by the measurement technique.

The difference in strength between the old-grain CPO's reported by Tullis et al. (1973), Jaoul et al. (1984) and Dell'Angelo & Tullis (1986) on the one hand, and those reported in the present study on the other hand, is of the same magnitude as the difference in strength between the improperly measured (Fig. 4.3a) and the properly measured (Fig. 4.3b) old-grain CPO of GRU29. The strength of the old-grain CPO's of the above authors is ≤6 times uniform, and these all show *peripheral* maxima whereas the samples are *axially* flattened. Therefore, the difference in strength can be explained entirely by the improper measurement technique.

In one example, additional support for improper measurement is provided by x-ray measurements. Fig. 9a of Tullis et al. (1973) shows an optically measured old-grain CPO of a quartzite deformed to ~60% strain at T=1000°C, $P_c \approx 1500$ MPa, $\dot{\varepsilon} \approx 10^{-5}$ s^{-1}, in dehydrating talc. The pattern is very weak, the maximum density being ~3% per 1% area. But x-ray measurements indicated that the fabric in the same sample was still weaker, the maximum density being less than 2% per 1% area (see their Fig. 9b). This is even lower than the maximum density of fabrics of the present study (~2 times uniform for ~40% strain). Tullis et al. (1973) reported that the x-ray measurements resulted *always* in weaker fabrics than the optical measurement technique. This, again, shows that the difference in strength between the optically measured CPO's reported by Tullis et al. (1973), Jaoul et al. (1984) and Dell'Angelo & Tullis (1986) on the one hand, and those of the present study on the other hand, can be explained entirely by the above mentioned improper optical measurement technique. Therefore, *and* because the deformation microstructures observed in the samples deformed by these authors look broadly similar to those observed in the samples of the present study (see chapter 3), it is proposed that these samples also deformed probably predominantly by solution transfer creep and micro-cracking.

It should be noted, however, that not all the optically measured CPO's can be attributed entirely to improper measurement. Optically measured CPO's of samples

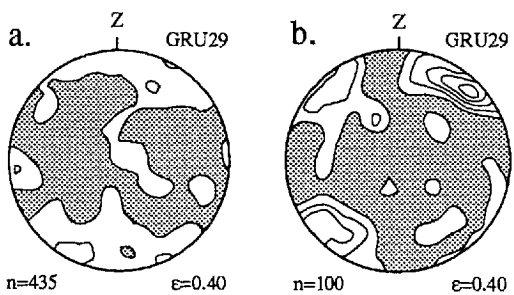

Fig. 4.3 *Optically measured old-grain CPO's of sample GRU29. (a) Properly measured fabric of present study. All old grains were measured. (b) Improperly measured fabric of Den Brok & Spiers (1991); those grains were selected (unintentionally) that displayed the highest birefringence and hence were optically most outstanding. Note that the figure caption of Den Brok & Spiers' (1991) figure 14 should read: 'contours were taken at 2% per 1% area', instead of 1% per 1% area.*

deformed 'as-received' at T=800-900°C, P_c≈1500 MPa, and $\dot{\varepsilon}$≈10^{-6} s^{-1} (Dell'Angelo & Tullis 1986) show a decrease in angle between the peripheral maxima and Z with increasing strain (from ~30° at ~20% strain to 15-20° at ~60% strain). Improper measurement, cannot explain the development of maxima so near to Z. However, the fact that the maxima in these CPO's are peripheral indicates that they resulted at least partly by improper measurement, so that they are too strong.

It is important to note that the samples that show this behaviour are characterized by large amounts of sub-basal deformation lamellae (Dell'Angelo & Tullis 1986, Tullis et al. 1973). Shear displacements along these lamellae, regardless of the mechanism (cf. Christie et al. 1964, Heard & Carter 1968), are expected to result in weak maxima making an angle of ≤45° with Z, this angle decreasing with increasing strain. This is expected to be the case especially when the lamellae have a preferred orientation such as in sample GRU29 (see also Heard & Carter 1968 for samples deformed 'as-received'). It is therefore suggested here that these weak CPO's with maxima at ≤45° to Z are possibly caused by glide along lamellae.

The CPO's determined with x-ray analysis are not affected by improper measurement. However, they may include an unknown contribution of recrystallized grains. Recrystallization can produce strong CPO's (probably by stress-induced oriented grain growth; Green et al. 1970). Experiments have shown that for similar strains CPO's of recrystallized quartz rocks are much stronger than the old-grain CPO's measured in the quartzites. They consist of small-circle girdle distributions about Z, with half opening angles of ~50°. X-ray measurements of c-axes in heavily recrystallized samples would consequently result in a superposition of a 'recrystallization' fabric on the 'old-grain' fabric. Therefore, as long as the contribution of the recrystallized grains to the total fabric is unknown, caution is needed in interpreting these fabrics. These CPO's cannot be regarded as old-grain CPO's. The same is true for CPO's measured with the photometric method (e.g. Ralser et al. 1991).

4.6 CONCLUSIONS

C-axes and deformation lamellae orientations have been measured in old grains in quartzite samples deformed experimentally to ~40 and ~46% strain with ~0.4 wt% added water at P_c=1160-1260 MPa, T=800°C, and strain rates of 10^{-6} and 10^{-7} s^{-1}. Measurements were made using a technique which ensures that all grains in a selected area are measured with minimal bias. Results have shown no significant preferred orientation development in comparison with the starting material. This excludes crystal-plastic mechanisms as dominant deformation process but is fully consistent with solution transfer creep and micro-cracking. The results provide additional support for the idea that water-weakening seen in experiments on natural quartzites occurred by solution transfer creep and micro-cracking.

The results differ from previous findings (Den Brok & Spiers 1991), mainly because

special care was taken to avoid artificial biassing of the data. Optically measured old-grain CPO's reported in the literature (Tullis et al. 1973, Jaoul et al. 1984, Dell'Angelo & Tullis 1986) are probably affected by improper measurement as well and may be as weak as those measured in the present study. The experimental evidence (found in the literature) that crystal-plastic deformation mechanisms (glide and climb of dislocations) are capable of producing strong CPO's in quartz is based almost entirely on the work of Tullis et al. (1973), who reported that quite strong old-grain CPO's could be produced in quartzites. The present work shows, however, that these old-grain CPO's are probably very weak. This means that the experimental evidence for crystal-plastic deformation as an important CPO-producing mechanisms is very weak as well. Further experiments are desirable in order to investigate whether crystal-plastic mechanisms are indeed capable of producing CPO's in quartz.

Chapter 5

FTIR-DETERMINATION OF INTRAGRANULAR WATER CONTENT

5.1 INTRODUCTION

In chapter 3 it was shown that water-weakening in quartzites experimentally deformed at a temperature of 800°C, a confining pressure of ~1200 MPa, and a strain rate of $\leq 10^{-6}$ s^{-1}, and with ~0.4 wt% added water, is probably due to micro-cracking and solution transfer rather than by any intracrystalline water-weakening effect. This explanation is in shap contrast to most previous work (e.g., Jaoul et al. 1984, Koch et al. 1989, Hirth & Tullis 1992; see also chapter 2).

The present chapter reports a Fourier-transform infrared (FTIR) spectroscopy micro analysis study of quartzites deformed at T=800°C, $P_c \approx 1200$ MPa, $\dot{\varepsilon} \approx 10^{-7}$ s^{-1}, and both with and without ~0.4 wt% added water. The aim was to determine whether or not the water-weakening effects observed in chapter 3 are associated with any changes in intragranular water content (c_w), and hence to test the validity of the solution transfer versus classical hydrolytic (intragranular) weakening hypothesis further.

5.2 DEFORMATION EXPERIMENTS AND CONDITIONS

All of the experiments reported in the present chapter were carried out on the Dongelberg quartzite, used and described in chapter 3 (see also Den Brok & Spiers 1991). It will be recalled that this is a very dense material (porosity < 0.1%) consisting of ~97 vol-% quartz with a grain size of 150-250 μm. The quartzite contains ~2 vol% white micas (probably phengitic) and ~1 vol% Fe-(hydr)oxides. The bulk water content, determined by thermogravimetry (measuring the weight loss of samples heated for 30 hours in nitrogen gas at 800°C), is about 0.3 wt%. This figure includes the water made availble from dehydration of micas and Fe-hydroxides (see further appendix B).

Cylindrical test pieces of this material, measuring 6 mm in diameter by 12 ± 1 mm in length, were cored from a single block at 45° to the bedding. This was done using a diamond coring tool with water as lubricant. The ends of the sample were then ground flat and parallel to within 30 μm measured parallel to the sample length. The samples were subsequently oven-dried at 150°C for 12 hours.

As described in appendix A, the samples were deformed using a Tullis-modified Griggs apparatus with NaCl as the confining medium. In setting up each test, temperature and pressure were raised simultaneously in order to follow the water isochore of 1 g/cm^3 as closely as possible. The experiments were performed at

constant displacement rates corresponding to strain rates of ~10^{-6} and ~10^{-7} s^{-1}. The total strains achieved fell in the range 5 to 15%. After deformation, the piston was moved upwards at maximum speed (3 x 10^{-6} m/s), and the temperature and pressure were lowered, once again following the water isochore of 1 g/cm^3 as closely as possible. Cooling times varied from 30-50 minutes.

With regard to the processing of the raw data (see appendix A) it is important to note that the measured axial displacement and load were corrected for apparatus distortion (at 800°C and 1200 MPa) and friction respectively. Differential stresses were calculated with respect to the initial cross section of the samples. Axial strain was computed with respect to the initial sample length at ambient (NTP) conditions. As discussed in apendix A, the resolution of the stress measurement is believed to be approximately 25 MPa, a figure which is closely comparable with that obtained in previous work using the Griggs apparatus (e.g. Jaoul et al. 1984).

5.2.1 Experiments with added water

No new experiments on 'wet' samples are reported in this chapter. To determine any changes in c_w during experimental deformation with added water, intragranular FTIR-spectra were measured in quartzite samples GRU11 & 26 (see chapter 3 and Den Brok & Spiers 1991). In the corresponding experiments, these samples were weld-sealed in Au-capsules together with ~0.4 wt% of added water, and were deformed at a temperature of 800°C, a confining pressure of ~1200 MPa, and a strain rate of ~10^{-7} s^{-1}. The samples were ~9 times weaker than samples deformed without added water under similar P-T conditions (see chapter 3 and table 5.1).

Table 5.1 *Summary of experimental data. Wet: 0.4 wt% (~1 vol%) water added; as-rec: as-received; LTC, lower thermocouple temperature; UTC, upper thermocouple temperature; t_1, elapsed time to reach PT-conditions; t_2, time at PT-conditions before deformation; t_3, total time at PT-conditions; t_4, elapsed time after deformation to reach room PT-conditions; c_w: intragranular water content.*

Sample Number		-log strain rate (s^{-1})	Finite strain (%)	P_c (MPa)	LTC (°C)	UTC (°C)	t_1 (hr:min)	t_2 (hr)	t_3 (days)	t_4 (hr:min)	Yield stress (MPa)	Max. stress (MPa)	Average c_w (ppm H/Si)
DBQ16	as-rec	0	0	0	0	0	0	0	0	0	—	—	1250 ± 300
GRU11	wet	7.0	11	1040	784	800	2:20	19	13.5	2:40	?	<25	1900 ± 500
GRU26	wet	7.0	14	1130	798	800	4:30	144	22.2	0:20	?	<25	1200 ± 300
GRU39	as-rec	0	0	1170	774	815	34:45	133	5.5	1:50	—	—	2000 ± 500
GRU31	as-rec	7.0	10	1160	776	800	21:10	78	14.8	0:50	140	210	2450 ± 900
GRU41	as-rec	7.0	10	1200	816	800	25:55	17	12.3	0:22	?	?	1400 ± 400
GRU40	as-rec	7.0	7	1190	788	815	30:20	324	21.6	0:17	225	225	1850 ± 400

5.2.2 Experiments without added water

To determine whether intragranular water would diffuse *out* of the original grains in samples deformed without added water, intragranular FTIR spectra were measured in samples subjected to the following treatments (see table 5.1):

(i) Sample GRU39. This was jacketed in gold without added water, and held at a temperature of 800°C and a confining pressure of ~1200 MPa for ~5.5 days.

(ii) Sample GRU31 & 41. These were also jacketed in gold without added water, but experimentally *deformed*, at a temperature of 800°C, a confining pressure of ~1200 MPa, a strain rate of ~10^{-7} s^{-1}, and a finite strain of 10 (±1) %. The duration of the test was ~12.3 and ~14.8 days respectively.

(iii) Sample GRU40. This was again jacketed in gold without added water, but first held at 800°C and ~1200 MPa for ~13.5 days (without deformation). It was then deformed to 7 (±1) % strain at 10^{-7} s^{-1} for a further ~8.1 days before termination of the test.

5.3 MECHANICAL DATA

The relevant mechanical data are presented as axial stress versus strain graphs in Fig. 3.2 (see also table 5.1). Due to failure of the force measurement system, no stress/strain curve was produced for experiment GRU41. Experiment GRU31 shows macroscopic yielding at ~140 MPa and ~2% strain followed by strain hardening. After ~10% strain the differential stress was ~210 MPa. Sample GRU40, which was deformed after a preheating stage of ~13.5 days yielded at ~225 MPa, after which the sample appeared to approach steady state flow. Sample GRU11 & 26 had strengths that remained below the stress resolution of the Griggs apparatus, i.e. <25 MPa (appendix A).

5.4 OPTICAL MICROSTRUCTURES

The microstructure of sample GRU39, hydrostatically loaded without added water for ~5.5 days, was similar to that of the starting material, except for the presence of a single sample-scale fracture oriented perpendicular to the sample axis. This was presumably introduced during depressurization.

Sample GRU41, which was deformed to ~10% strain without added water, showed (subbasal) deformation lamellae developed in 30-60% of the grains. Deformation bands were also present, and mostly associated with bending of the lamellae. Abundant axially oriented microfractures were also observed on the sample scale. These appeared to propagate from a sample-scale shear fault oriented at ~30°

to the shortening direction (Z). Many finely spaced (presumably) unloading fractures oriented perpendicular to Z were also present. The deformation microstructures seen in samples GRU31 & 40 were closely similar to those observed in sample GRU41, except that no sample-scale axial or shear fractures were observed, and that the number of unloading fractures was few.

The microstructures of samples GRU11 & 26 were described in detail in chapter 3 and by Den Brok & Spiers (1991). In these samples the most conspicuous microstructural feature was the presence of abundant fine, new polygonal to euhedral quartz grains, developed in axially oriented microfractures and grain boundaries. The original grains were almost free of intracrystalline deformation features. Deformation lamellae were present in less than ~5% of the original grains.

5.5 FTIR-MEASUREMENTS

The samples in which the intragranular water content (c_w) was measured are listed in table 5.1. These include samples GRU11, 26, 31, 39, 40, 41, and sample DBQ16 (the starting material).

5.5.1 Techniques

The FTIR-spectra were obtained using a IFS-46 Bruker spectroscope (see table 5.2 for apparatus specifications) with IR-microscope (Bruker), so that the samples could be observed microscopically. This allowed accurate selection of grains and localities where we wanted to measure the spectra. It also allowed the estimation of

Table 5.2 *FTIR-spectroscope apparatus specifications*

Wave number resolution: 4 cm^{-1}
Apodisation function: Blackman-Harris (3-term)
Zero-filling: 2
Infrared source: globar (SiC)
Michelson-Interferometer: Beam splitter KBr, Germanium coated
Mirror objective: magnification 15x, aperture 0.28
IR-detector: HgCdTe with ZnSe window, N_2-cooled

the amount of optically visible (>~0.5 μm) fluid inclusions present. We used a measurement spot of ~70 μm, which was small enough to focus on single grains in the Dongelberg quartzite (grain size 150-250 μm).

The sections used for the FTIR-spectroscopy were 50-240 μm thick, longitudinal sections through the cylindrical samples. They were polished on both sides using SiC powder with grit sizes down to 0.3 μm. The thickness of the samples allowed only measurement of the largest grains (diameter >200 μm). For this reason only 2-20 grains could be measured per sample.

FTIR-spectra of each grain examined (128 scans per spectrum) were measured in the range 5000 to 1700 cm^{-1}, both at low temperature (~77 K) and at room temperature (~295 K). Raw spectra were obtained (Fig. 5.1a), from which c_w was estimated. In order to do this, a base-line correction was carried out to correct for scattering and other effects (Fig. 5.1b). The intragranular water content then was obtained by numerically calculating the integral absorption of the room temperature spectra between 2850 and 3740 cm^{-1} (according to Paterson 1982), and assuming that the absorption was isotropic (i.e. independent of crystallographic orientation). The accuracy of determinations is of the order of ~100 ppm H/Si. Water contents could be measured down to ~200 ppm H/Si in samples of ~200 μm thick, and down to ~500 ppm H/Si in samples of ~100 μm thick.

5.5.2 Results

67 spectra were measured in 63 grains located in 7 samples studied. The c_w's of the different samples are shown in table 5.1 & 5.3 and in Fig. 5.2. The base-line corrected spectra are shown in Fig. 5.3.

The room temperature spectra all show broad band absorption between 3000 and 3700 cm^{-1} with a peak value at approximately 3400 cm^{-1}. This is characteristic for absorption by molecular water (cf. Fig. 5.4). Some of the room temperature spectra also show a narrow band absorption at ~3650 cm^{-1}. This is probably due to absorption by micas, which were present on the μm-scale in fluid inclusions. The amount of water structurally bound to micas (assumed to be the absorption between 3570 and 3675 cm^{-1}) was estimated (again assuming isotropic absorption) and indicated in Fig. 5.2 (see also table 5.3). Note that in this chapter the c_w refers to the bulk c_w *minus* the water believed to be present in micas. The reason for this is that the mica-bound water is not believed to play a significant role during deformation because micas were still present after deformation. Very weak absorption by quartz (Si-O bonds) near 3200 and 3300 cm^{-1} (e.g., Kats et al. 1962) was neglected. In sample GRU11 (grains 8, 11 & 12) moderately narrow peaks are present around 2850 to 2950 cm^{-1}. These peaks are most likely due to organic material, notably araldite used in thin-section preparation.

The low temperature spectra also show broad band absorption between 3000 and

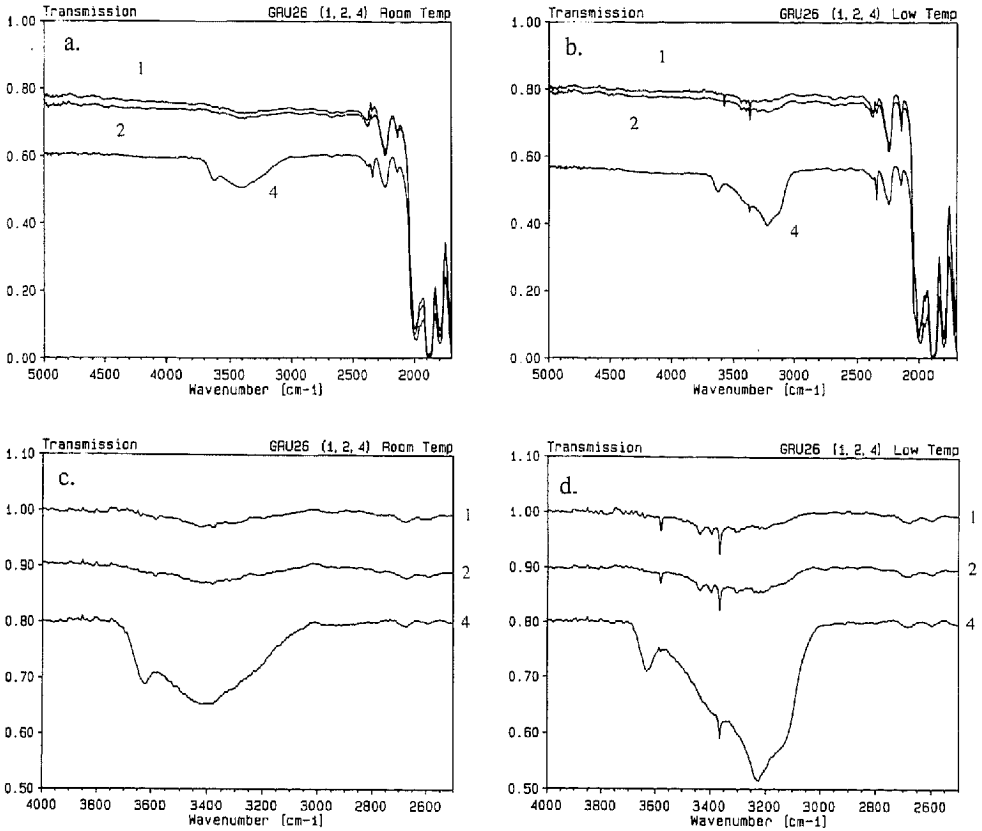

Fig. 5.1 *Examples of typical FTIR-spectra, before (a & b), and after (c & d) base-line correction. (a & c) are room temperature spectra, (b & d) are low temperature spectra. The spectra were measured at localities 1,2 and 4 in sample GRU26 (see Fig. 5.5a & b). Sample thickness is indicated in table 5.3. In order to compare the different base-line corrected spectra, they were shifted by 0.1, together with the zero. Therefore, the y-axis units apply only for the spectrum that intersects the y-axis at 1. Very weak peaks in the base-line corrected spectra at approximately 2600 and 2680 cm^{-1} are due to absorption by quartz. Quartz peaks at approximately 3200 and 3300 cm^{-1} are too weak to recognize. Therefore, spectra are believed to be entirely due to absorption by O-H bonds.*

Table 5.3 *Summary of c_W determinations. +: presence of (non)freezable water is indicated by IR-spectrum; (+): only small amounts of (non)freezable water indicated by IR-spectrum; further explanation see text.*

sample nr	grain nr	Sample thickness (μm)	ppm H/Si (bulk)	ppm H/Si (mica)	ppm H/Si (quartz)	freezable	non freezable
DBQ16	1	200	500	<200	300-500	+	+
	2	200	<200		<200	+	
	3	200	600		600	50%	50%
	4	200	700	<200	500-700	+	+
	5	200	1700	200	1500	40%	60%
	6	200	1900	200	1700	40%	60%
	7	200	2300	500	1800	+	
	8	200	800	100	700	+	
	9	200	11000	7800	3200	+	+
	10	200	700	<100	600-700	+	+
	11	200	200		200		+
	12	200	5600	2700	2900	+	(+)
	13	200	3500	1500	2000	+	
GRU11	1	90	<500		<500		
	2	90	4600		4600	60%	40%
	3	90	500		500	+	
	4	90	6100		6100	+	(+)
	5	90	3000	200	2800	+	
	6	90	<500		<500		
	7	270	1100		1100	+	
	8	270	1800		1800	+	
	9	270	2200		2200	+	
	10	270	500	<100	400-500	+	
	11	270	1400	700	700	+	
	12	270	2900	1300	1600	+	
GRU26	1	220	400		400	+	
	2	220	300		300	+	
	3	220	1300	<200	1100-1300	+	+
	4	220	2100	200	1900	+	
	5	220	800		800	+	+
	6	220	1700		1700	+	
	7	220	3000	<200	2800-3000	+	
	8	220	900	<200	700-900	+	
GRU39	1	140	4300		4300	30%	70%
	2	140	700		700		
	3	240	800		800	+	
	4	240	5700	1900	3800	+	
	5	240	3900	1700	2200	+	
	6	240	1200	100	1100	+	
	7	240	1900	100	1800	+	
	8	240	1300	<100	1200-1300	+	
GRU31	1	110	3700		3700	+	(+)
	2	110	800		800	+	
	3	50	1600		1600	+	
	4	50	6200		6200	60%	40%
	5	50	<1000		<1000		
	6	50	1400		1400		

Table 5.3 *Continued*

Sample nr	grain nr	Sample thickness (μm)	ppm H/Si (bulk)	ppm H/Si (mica)	ppm H/Si (quartz)	freezable	non freezable
GRU41	1	240	3000		3000	+	
	2	240	4300	2300	2000	+	(+)
	3	240	200	100	100	+	(+)
	4	240	2100	1000	1100	+	(+)
	5	240	800		800	+	(+)
	6	240	4200	2800	1400	+	(+)
GRU40	1	180	2900	<200	2700-2900	40%	60%
	2	180	600	<200	400-600	+	
	3	180	1100		1100	+	
	4	180	1700		1700	+	
	5	180	4700	200	4500	+	
	6	180	400	<200	200-400	+	
	7	180	4000		4000	+	
	8	180	2100	<200	1900-2100	70%	30%
	9	180	400	<200	200-400	60%	40%
	10	180	1300		1300	+	(+)
	11	180	2300	700	1600-2300	+	
	12	180	2000		2000	+	
	13	180	1500	100	1400	+	(+)
	14	180	2100	1000	1100	+	
	15	180	3500		3500	+	+

3700 cm^{-1}, but now in most cases with a peak value at ~3200 cm^{-1} characteristic for absorption by ice (Fig. 5.4). In addition, most of the low temperature spectra show sharp peaks, the strongest of which is located at ~3370 cm^{-1}, and a weaker at ~3580 cm^{-1}. This is charcteristic of most quartz spectra determined at low temperatures, and is believed to be due to absorption by hydrogen-related crystal point and line defects (e.g. Aines & Rossman 1984). The absence of sharp peaks in the room temperature spectra but especially in the low temperature spectra indicates that the amount of water that is structurally bound to quartz (i.e., as X-O-H point defects) is only of the order of several ppm H/Si (e.g. Aines & Rossman 1984). By comparing the spectra with that of pure ice, the total amount of freezable water could be estimated (table 5.3). In all but one of the grains >40% of the water was freezable.

The variation in c_w is remarkably large, both in the starting material and in the deformed samples. For instance, there are 'dry' grains containing <200 ppm H/Si and 'wet' grains containing >3000 ppm H/Si (e.g. Fig. 5.5a & b). The c_w's vary also within single grains. In one grain in the deformed sample GRU40 (Fig. 5.5c) a 'dry' part contained ~600 ppm H/Si whereas a 'wet' part contained ~2900 ppm H/Si. Differences in c_w appeared to correlate with differences in the amount of

optically visible fluid inclusions: the 'wet' grains contain abundant optically visible fluid inclusions whereas the 'dry' grains are virtually free of optically visible fluid inclusions. Optical estimates of the total water held in fluid inclusions indicate that fluid inclusions may account entirely for the c_w determined from the IR-spectra.

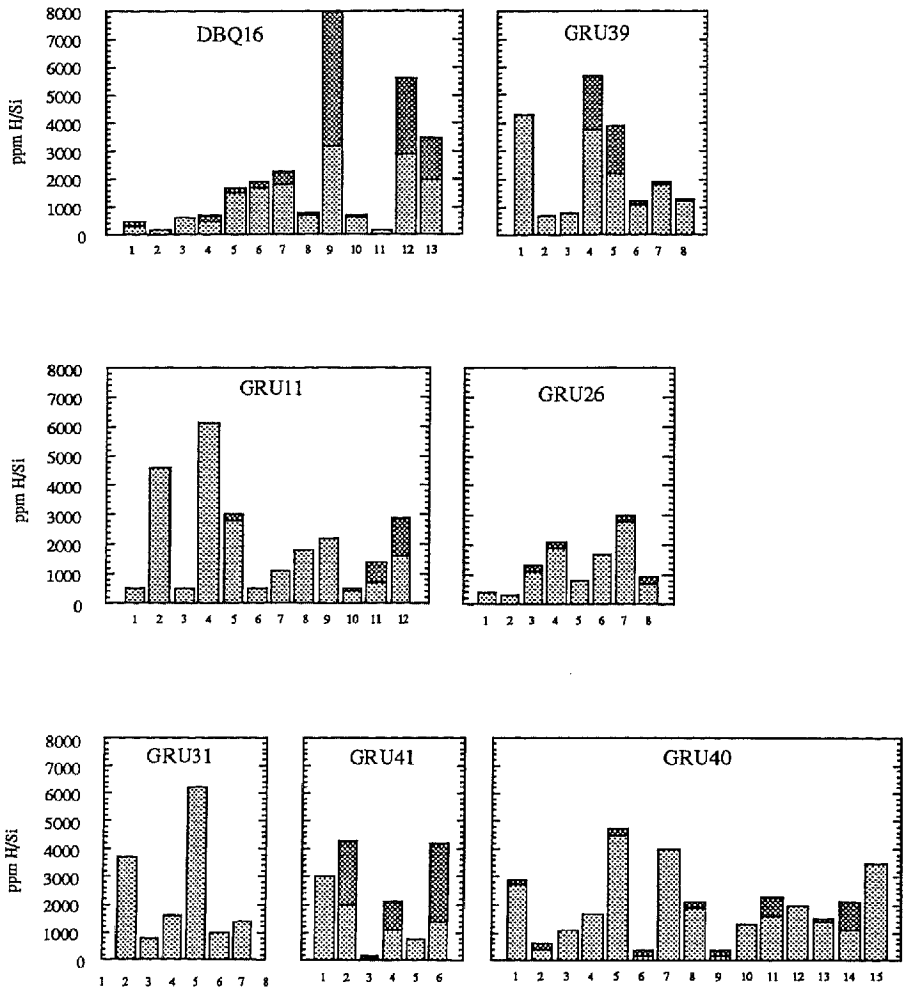

Fig. 5.2 *Histograms showing intragranular water content (c_w). Each histogram refers to one sample (number indicated). Each column refers to one grain. The darker shaded part of the columns is the contribution of absorption by mica.*

The non-freezable portion of the water probably resides in the smaller fluid inclusions in which water can exist metastably in the fluid state (e.g. Aines & Rossman 1984). Grains without optically visible fluid inclusions contain generally less than ~500 ppm H/Si.

Unfortunately, insufficient grains were measured in each samples to enable a well-balanced average c_w to be obtained per sample. For the 2 to 20 grains per sample, the spread in c_w was simply too large. Nevertheless, all of the samples broadly showed the same average c_w (of the order of 2000±500 ppm H/Si; table 5.1), and all contained relatively 'dry' grains (<200 ppm H/Si) and relatively 'wet' grains (>3000 ppm H/Si).

In a few cases we were able to measure the c_w of grains containing deformation lamellae (Fig. 5.5d). These grains appeared to be relatively 'dry'.

5.6 DISCUSSION

5.6.1 Samples deformed with added water

The FTIR measurements show that the average c_w of the samples GRU11 (1900 ± 500 ppm H/Si) and GRU26 (1200 ± 300 ppm H/Si) is broadly similar to that of the starting material DBQ16 (1250 ± 300 ppm H/Si).The spread in c_w is also similar. This indicates that no equilibration of c_w occurred, and that on average the ~0.4 wt% of added water (equivalent to ~40000 ppm H/Si) did not penetrate into the original grains in amounts greater than 100-500 ppm H/Si. Original grains with c_w's of <200-300 ppm H/Si were still present after exposure to the added water at 800°C and ~1200 MPa for ~3 weeks, just as in the starting material. Yet, the differential stress required to deform these water-added samples (i.e. <25 MPa) was at least 9 times lower than the stress required to deform the samples without added water (140-225 MPa; see chapter 3). Apparently, then, the water-weakening effect reported in chapter 3 occurred without penetration of more than 100-500 ppm H/Si into the quartz grains. It cannot be excluded that larger amounts than 100-500 ppm H/Si diffused into single grains while others lost water, the average c_w remaining the same. However, it is difficult to think of any reason *why* this would be the case.

It is now argued that penetration of amounts of water of the order of 100-500 ppm H/Si or lower (the resolution of the spectroscope) are unlikely to have caused the weakening effect. An indication of the amount of water needed to weaken quartz may be obtained by comparing the flow law obtained by Balderman (1974) on 'wet' synthetic single crystals of quartz containing ~4300 ppm H/Si, with the flow law obtained by Linker & Kirby (1981) on 'wet' synthetic single crystals containing ~370 ppm H/Si (the flow parameters are listed by Blacic & Christie

1984, table 2, page 4235). For a temperature of 800°C, and a strain rate of 10^{-7} s^{-1}, the single crystal containing ~4300 ppm H/Si is predicted to have a steady state flow stress of ~160 MPa, and the crystal containing ~370 ppm H/Si, a flow stress of ~300 MPa. Hence, increasing the water content by a factor ~12 (from 370 to 4300 ppm H/Si) causes a decrease in strength by a factor ~2. The average water content of the starting material (DBQ16) was 1250±300 ppm H/Si; addition of 100-500 ppm H/Si, i.e., an increase in water content by a factor <0.5, would accordingly cause a decrease in strength by a factor ~0.1. This is approximately only 1% of the observed decrease by a factor ≥9. Note further that Griggs (1974) predicted that variations in flow stress of a factor of 2 would be caused by varying the water contents by a factor of 100. Hence, an increase in the c_w of the starting material (1250 ± 300 ppm H/Si) by adding 100-500 ppm H/Si, is expected to have almost no effect on the strength.

The weakening by a factor ~9 was caused by addition of ~40000 ppm H/Si, a figure which compares well with the results of Jaoul et al. (1984) who measured a weakening effect of a factor ~10 by adding ~30000 ppm H/Si (at T=800°C, P_c= ~1500 MPA, and $\dot{\varepsilon}=10^{-6}$ s^{-1}; see their fig. 7). Jaoul et al (1984) further showed that addition of 0.12 wt% water (equivalent to ~12000 ppm H/Si) resulted in a weakening by a factor of ~4. This indicates that the weakening effect of the size of that observed in the present experiments is caused by large amounts of water (of the order of several 10000 ppm H/Si), which significantly exceeds the spectroscopic resolution of 100-500 ppm H/Si.

Fig. 5.3 *Base-line corrected FTIR-transmission spectra. Sample numbers are indicated above, and grain numbers at the right side of each graph. These numbers correspond to numbers in table 5.3. Sample thicknesses are also indicated in table 5.3. Spectra at the left side are room temperature spectra, and at the right side low temperature spectra. In order to compare the different base-line corrected spectra, they were shifted by 0.1, together with the zero. Therefore, the y-axis units apply only for the spectrum that intersects the y-axis at 1. Note layer thickness interference in sample GRU11 (grains 1 to 6).*

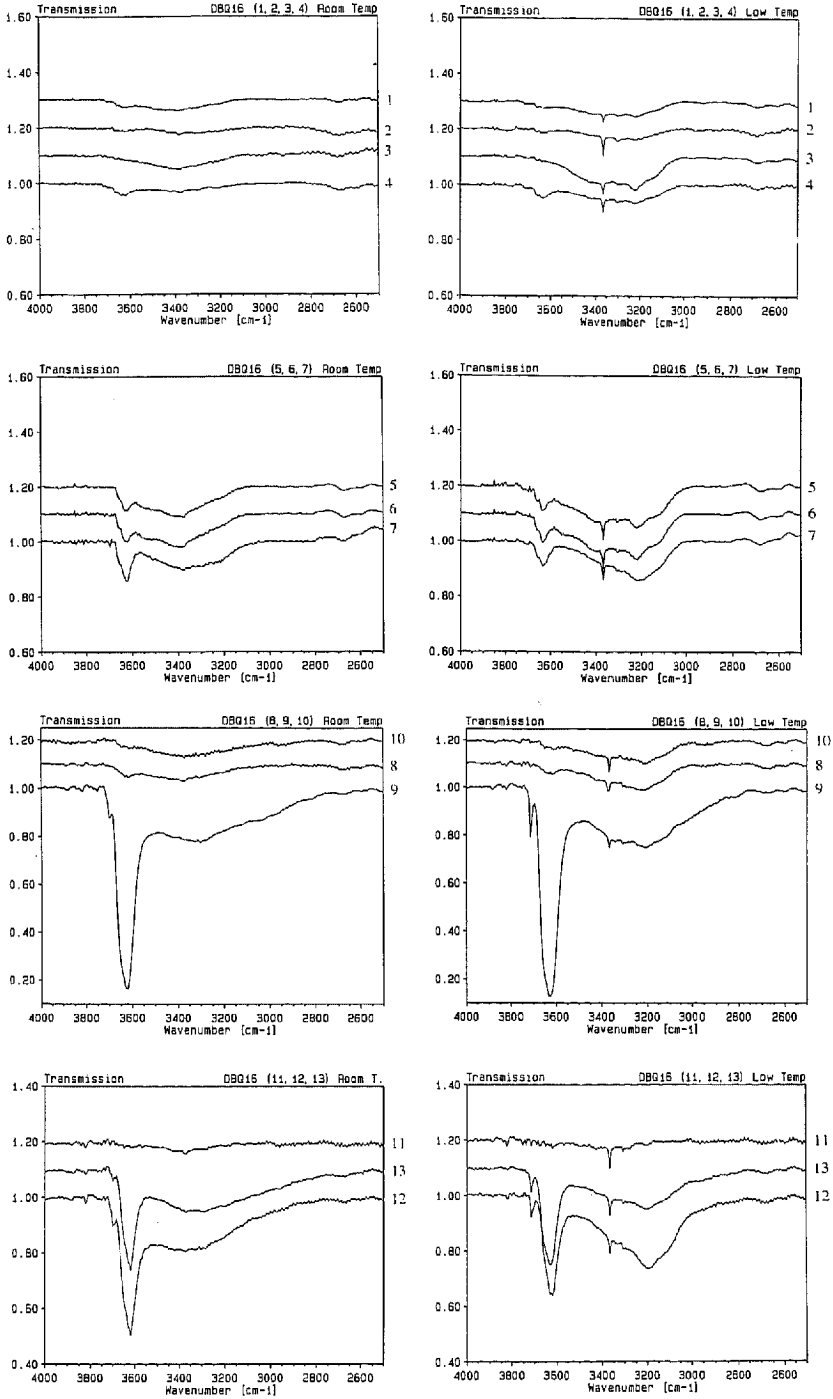

Fig. 5.3 *(Explanation see previous page)*

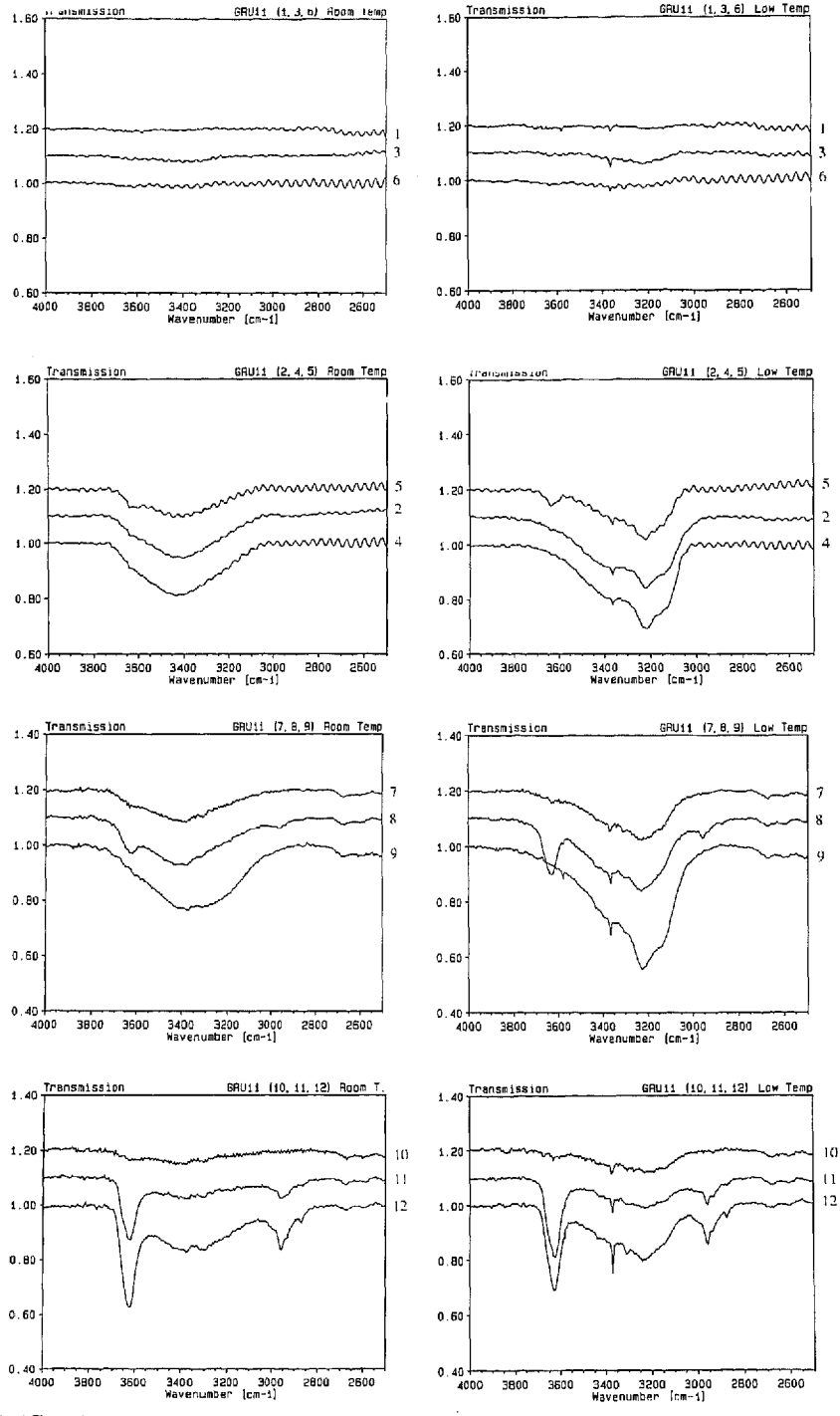

Fig. 5.3 *(Continued)*

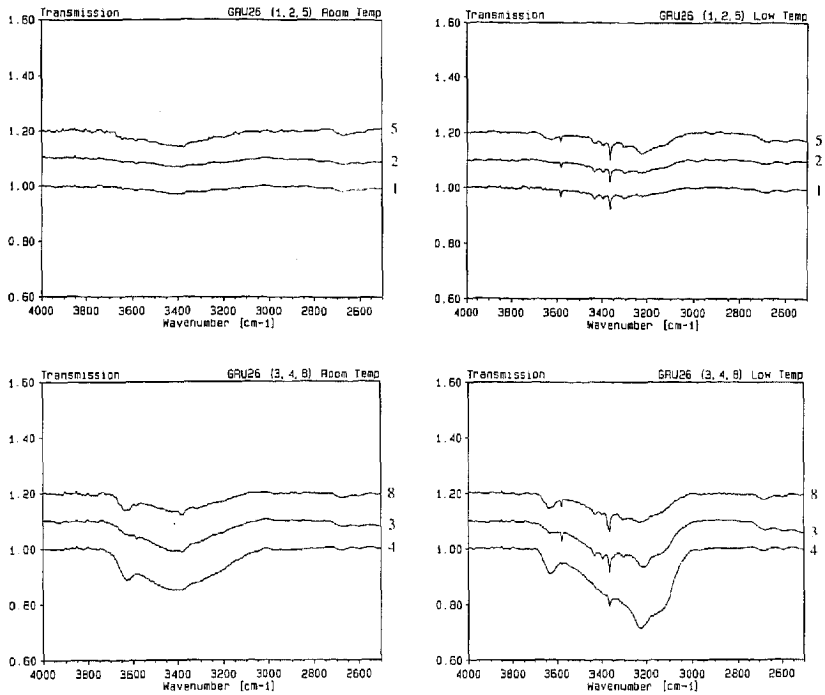

Fig. 5.3 *(Continued)*

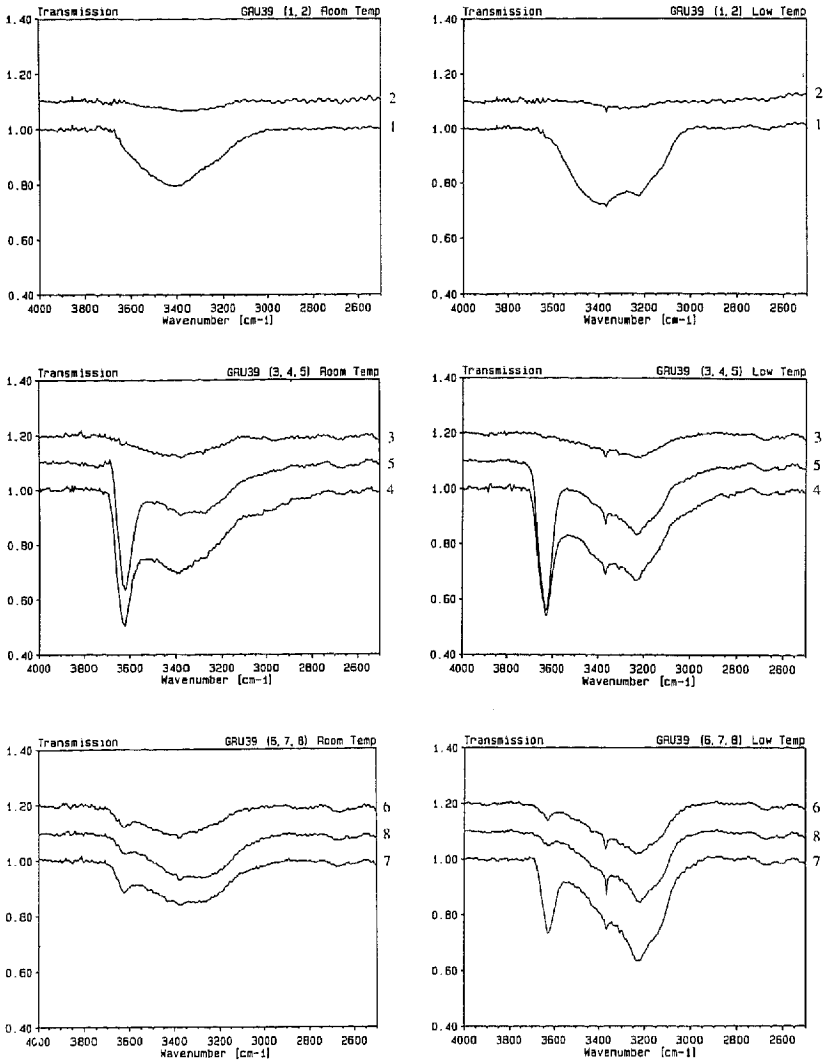

Fig. 5.3 *(Continued)*

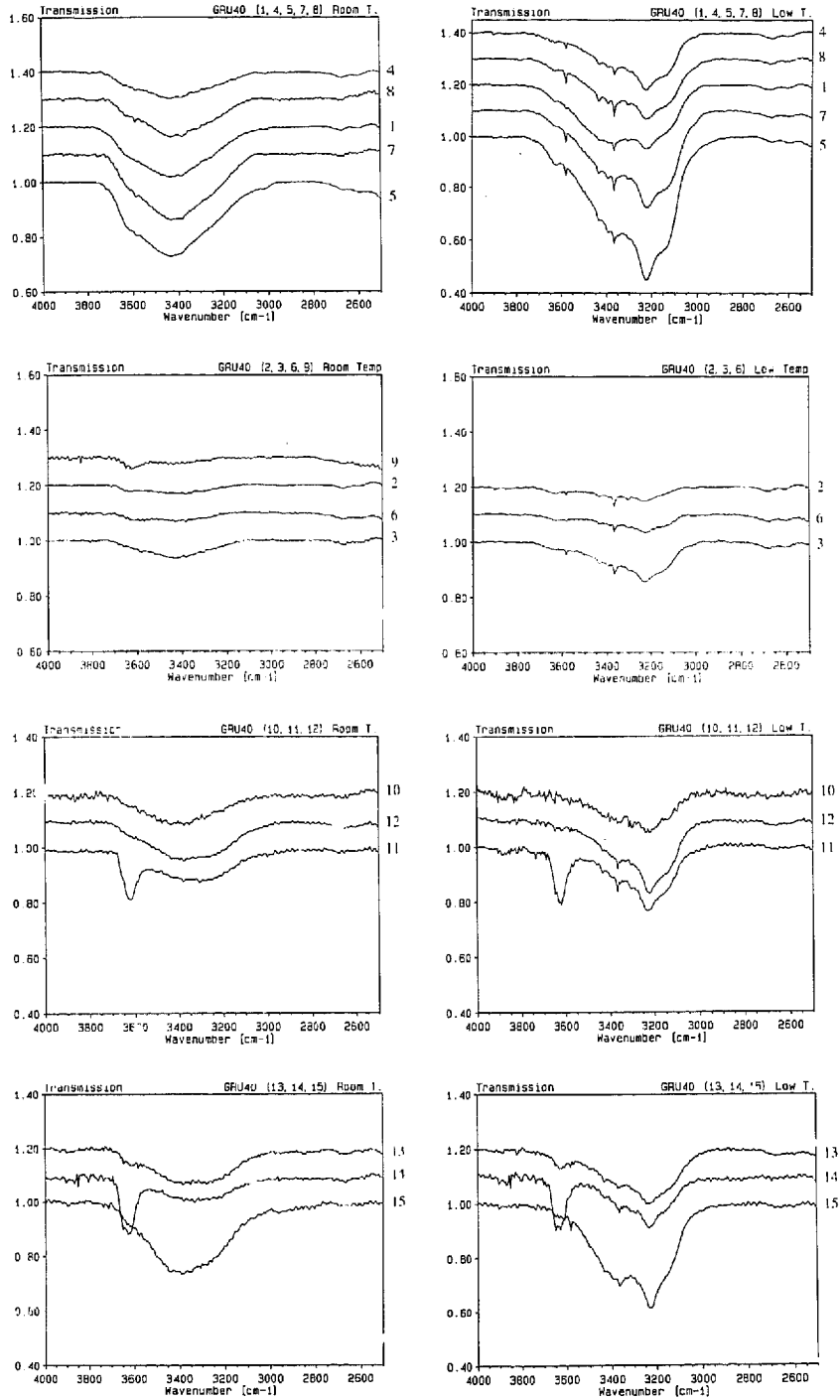

Fig. 5.3 *(Continued)*

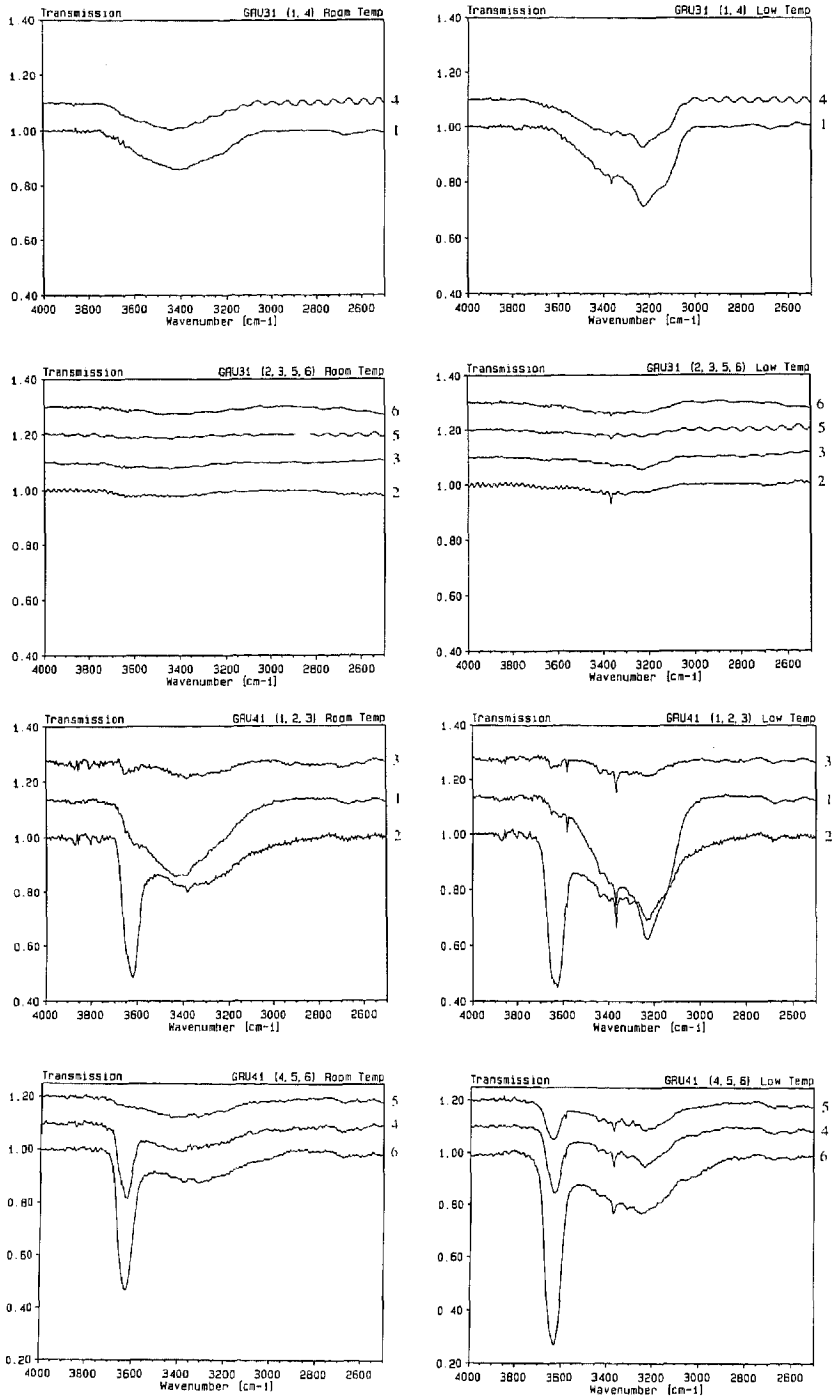

Fig. 5.3 *(Continued)*

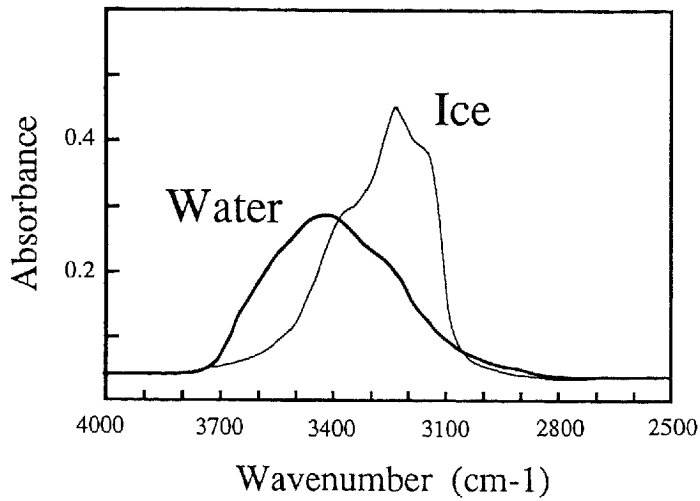

Fig. 5.4 *IR-spectra of water and ice (after Aines & Rossman 1984)*

5.6.2 Samples deformed without added water

As described above, the average c_w of all samples deformed without added water (GRU31, 39, 40 & 41) was found to be broadly similar to that of the starting material (DBQ16), and also to that of the samples deformed with added water (GRU11 & 26; see table 1). Relatively 'dry' (<1000 ppm H/Si), as well as relatively 'wet' grains (>2000 ppm H/Si) were still present in these samples after having been exposed for 6-22 days to a temperature of 800°C, a pressure of ~1200 MPa, and a differential stress of 0 to 210 MPa, without added water. Therefore, within present resolution limits, the difference in strength between the samples deformed with added water and those deformed 'as-received' cannot be attributed to differences in c_w. Similarly, the present findings are also inconsistent with the suggestion by Kronenberg & Wolf (1990) that the original intragranular water would diffuse out of the grains when the samples are deformed without added water (see chapter 2).

5.6.3 Origin of water-weakening in the quartzites

The present study has shown that quartzites can be mechanically weakened by a factor ~9 by adding ~0.4 wt% water (at T=800°C, P_c=~1200 MPa, $\dot{\varepsilon}=10^{-7}$ s^{-1}), but *without* penetration of significant amounts of water into the original quartz grains. Yet, the samples have been held for 5.5 to 22.2 days at these high P-T conditions. As discussed above, this is inconsistent with the classical *hydrolytic weakening* theory which is widely believed to explain the water-weakening effects commonly observed in experiments on quartzites (e.g. Tullis et al. 1973, Mainprice & Paterson 1984, Jaoul et al. 1984, Koch et al. 1989, Kronenberg et al. 1990, Tullis 1990).

On the other hand, the FTIR-results on c_w are qualitatively consistent with the solution transfer hypothesis of water-weakening proposed in chapter 3 and by Den Brok & Spiers (1991). In this mechanism, diffusion of water in or out of the original grains is not required to produce a significant weakening effect. Since Mackwell & Weathers (1987) have shown that water may penetrate grain boundaries in quartzite within an hour under hydrostatic conditions (P_c=300 MPa, T=500°C), a solution transfer mechanism also offers an explanation why samples are weakened relatively fast. The present FTIR-results are also consistent with a weakening process involving melt-assisted diffusional creep. However, as discussed in chapter 3, no evidence was found for melting in the present 'wet' samples.

Finally, it should be noted that our observations do not rule out that on average small amounts of added water (<100-500 ppm H/Si) may have penetrated the quartz grains by bulk lattice, or dislocation pipe diffusion, and may thus have to some extent affected the dislocation substructure (cf. Tullis & Yund 1989).

Fig. 5.5 *Optical photomicrographs of samples used in FTIR-spectroscopy. (a) 'dry' grain in sample GRU26; measurements 1 and 2 indicated. (b) 'wet' grain in sample GRU26; measurement 4 indicated. (c) Measurements 1 & 2 in sample GRU40 showing 'dry' and 'wet' parts. (d) Measurements 6 & 9 in sample GRU40 showing deformation lamellae in relatively 'dry' parts. Diameter of spotsize ≈70 μm.*

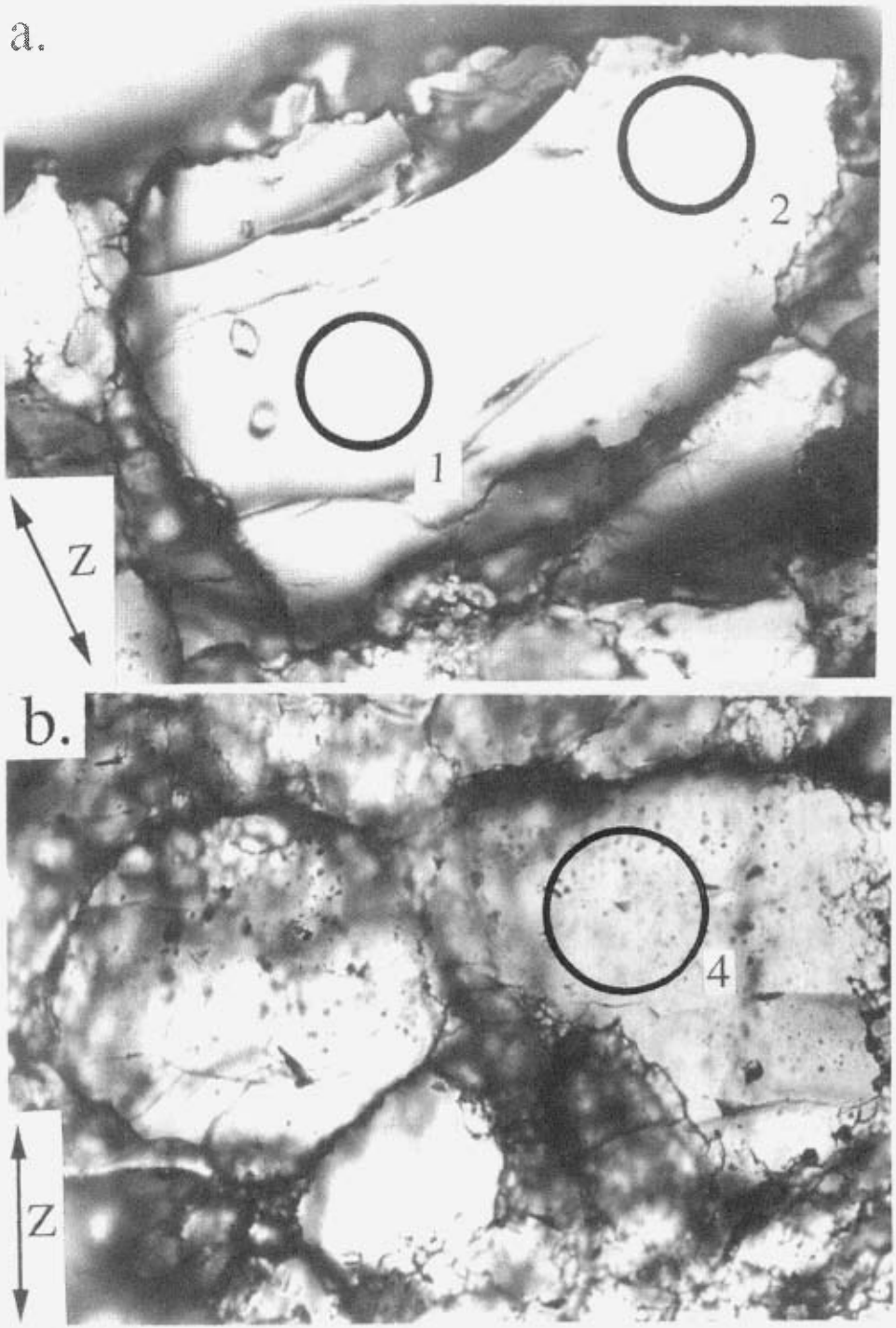

Fig. 5.5 *(Explanation see previous page)*

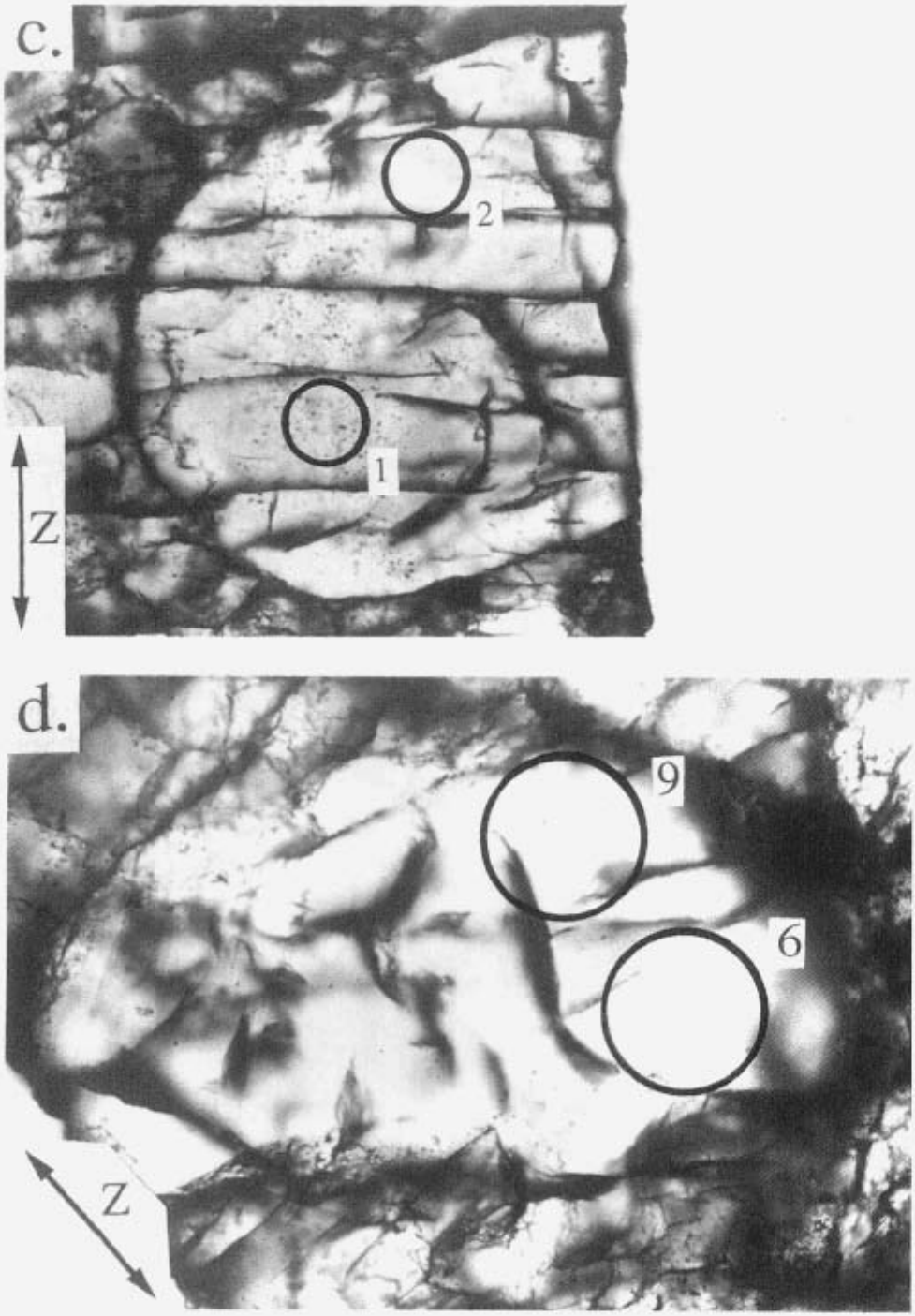

Fig. 5.5 *(Continued)*

5.7 CONCLUSIONS

It appears that on average, and within measurement resolution (100-500 ppm H/Si), added water does not diffuse into the quartz grains of Dongelberg quartzite experimentally deformed with ~0.4 wt% of added water, at a temperature of 800°C and a confining pressure of ~1200 MPa. The samples have been under these P-T conditions for 13.5 to 22.2 days. Nevertheless, the flow stress of the water-added samples was ≥9 times lower than that of samples deformed *without* added water. Based on flow laws obtained on 'wet' synthetic single crystals, an intracryastalline weakening effect by a factor ~10 is expected to be caused by an increase in c_w by a factor ~100. The average c_w of the starting material is 1250±300 ppm H/Si, hence, an increase of c_w by 100-500 ppm H/Si (i.e. an increase by a factor <0.5) is not expected to cause a significant weakening effect. It is concluded that water-weakening of quartzite by addition of water occurs without diffusion of water into the original grains.

On average and within measurement resolution, intragranular water present in the starting material does not diffuse out of the original grains during experiments of 6 to 22 days at a temperature of 800°C, a pressure of 1200 MPa, and differential stresses of 0 to 225 MPa, and when added water is absent. It therefore appears unlikely that the water-weakening effect is caused by a buffering effect of added water on the intragranular water, as suggested previously by Kronenberg & Wolf (1990).

Apparently, intragranular water plays no significant role in the water-weakening of quartzite. Taking the absence of glass in the present 'wet' samples into account, this supports the explanation given in chapter 3 and by Den Brok & Spiers (1991), that water-weakening in quartzite is caused predominantly by stable micro-cracking plus solution transfer.

Given the large spread in c_w of the starting material, and the relatively small number of measurements per sample, it is desirable to verify the conclusions of this chapter using a starting material with less variation in c_w.

Chapter 6

EXPERIMENTAL RESULTS VERSUS MICROPHYSICAL MODELS FOR SOLUTION-PRECIPITATION CREEP

6.1 INTRODUCTION

The previous chapters list mechanical, microstructural, and microchemical evidence that the quartzites, deformed experimentally with ~0.4 wt% of added water at a temperature (T) of 800°C, a confining pressure (P_c) of ~1200 MPa, and strain rates ($\dot{\varepsilon}$) of 10^{-6} and 10^{-7} s^{-1}, deform predominantly by solution-precipitation creep (SPC) plus micro-cracking. However, the mechanical data presented in chapter 3 were compared only in a rough qualitative sense with models for SPC (i.e., only the strain rate sensitivity of stress was considered). In this chapter I will examine in more detail to what extent the observed behaviour is consistent with SPC-models derived for various rate controlling steps. If such consistency can be demonstrated, then insight can be gained into the detailed rate controlling solution-precipitation processes and most appropriate theoretical creep equation. The latter is essential for extrapolating laboratory data to predict the mechanical behaviour of quartzites in nature.

The present discussion will be limited to the mechanical behaviour of the quartzites deformed 'wet', i.e., with ~0.4 wt% of added water. These samples show the clearest microstructural evidence for deformation by SPC. The others showed evidence for at least some deformation by intragranular processes as indicated by the presence of deformation lamellae. The 'wet' samples showed a stress versus strain-rate relationship characterized by a power law n-value of ≤1.3 at a strain rate in the range 10^{-6} to 10^{-7} s^{-1} (Fig. 6.1). This is consistent with a diffusional creep mechanism such as SPC, but not with dislocation mechanisms. Note, however, that as already reported in chapter 3, the stresses plotted in Fig. 6.1 are not *steady-state* values, but macroscopic *yield* stresses with the error bars indicating the recorded range of post-yield stresses. Nonetheless, the values are closely similar to the steady-state stresses reported by Jaoul et al. (1984) in creep experiments conducted under broadly similar conditions. I therefore assume throughout this chapter that the stress versus strain-rate data reported in chapter 3 can be treated as sufficiently representative of steady-state values to justify comparison with steady-state SPC-models.

In chapter 3 it was shown from microstructural studies of samples deformed to large strains at 10^{-6} and 10^{-7} s^{-1} (GRU29 to ~40%, and GRU35 to ~46% strain) that SPC was the dominant strain accumulating mechanism, accounting generally for 40-90% of the total deformation. It is therefore reasonable to assume that the strain rate contribution attributable to SPC alone lies within a factor of ~0.5 of the experimentally imposed strain rates. This uncertainty in the strain rate contribution,

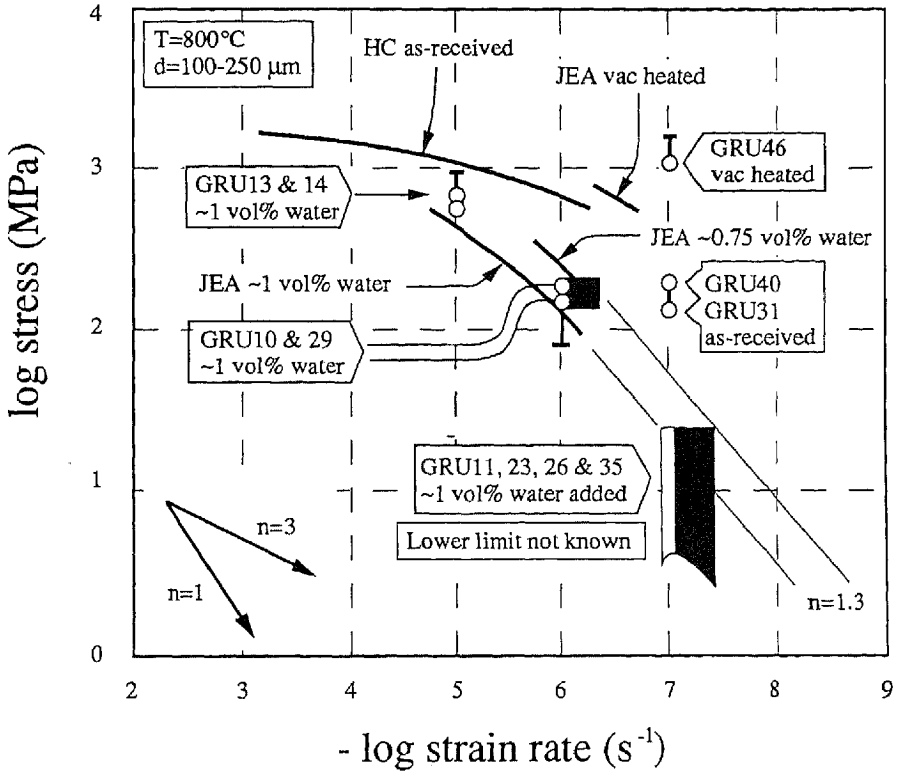

Fig. 6.1 *Mechanical data of experiments reported in this thesis (open circles, and open rectangular; error bars indicate range of post-yield stresses), and of Jaoul et al. (1984; JEA) and Heard & Carter (1968; HC)(heavy lines). Data of HC were obtained at 800 to 1000 Mpa confining pressure and 800°C in a gas-confined apparatus, data of JEA were obtained at ~1500 MPa and 800°C in a Griggs solid medium apparatus. The mechanical behaviour of the samples deformed with ~0.4 wt% added water follows an approximately linear stress-strain rate relationship, indicative of diffusional creep (n-value ≤1.3). The black rectangles indicate stress versus strain-rate conditions inferred for the contribution of SPC to the total deformation.*

attributable to solution-precipitation processes in the present experiments is indicated in Fig. 6.1 by means of the black 'error boxes'.

In the following, I will first shortly review various SPC-models, making a few simple extensions. I shall then consider the microstructure and grain boundary structure of the deformed samples, and finally compare the mechanical behaviour with predictions based on a microstructurally appropriate SPC-model. It is concluded that the observed behaviour is best described by a model assuming a static island-crack (SIC) grain boundary structure, where stresses are supported by μm-scale crack-bound islands with channels being located where the (intragranular) micro-cracks intersect the grain boundary, and that the rate of deformation is controlled by diffusion at the crack-bound island-island contacts, either (i) by water-assisted solid-state grain boundary diffusion, or (ii) by diffusion through a fine, fluid containing nanometer-scale dynamically stable island-channel (DIC) structure.

6.2 MICROPHYSICAL MODELS FOR SOLUTION-PRECIPITATION CREEP

Several models have been derived to mathematically describe SPC in polycrystalline materials. Broadly speaking, these fall in two classes of mechanisms, namely grain boundary diffusional mechanisms, versus dissolution-coupled or marginal dissolution mechanisms (see e.g. Spiers & Brzesowsky 1992). In the case of quartz rocks, it is widely agreed that the latter is of negligible importance (see Rutter 1983, Lehner 1990). For this reason attention is restricted here to grain boundary diffusional models. These models (Weyl 1959, Rutter 1976, Raj 1982, Lehner 1990, Spiers & Schutjens 1990) all have in common that material is assumed to *dissolve* in some kind of grain boundary solution phase at grain boundaries under high mean normal stress, is subsequently *transported by diffusion* through this grain boundary phase, and finally *precipitated* out of solution at grain boundaries (or other interfaces) under low mean normal stress. Different models have been derived, depending on assumptions made regarding the grain boundary structure, and depending on whether the interface reactions (i.e., the dissolution and precipitation steps) or the diffusion process control the rate of deformation. In the following, the various models will be briefly described according to the assumed grain boundary structure.

6.2.1 Dynamically stable island-channel (DIC) model

The DIC-model (Raj 1982, Lehner & Bataille 1984, Spiers & Schutjens 1990) is based on the assumption that the grain boundaries contain free liquid in channel-like structures on a scale which is fine compared to the grain size. The channels form an interconnected network, separated by islands of solid-solid contact (Fig. 6.2). This network represents a non-equilibrium structure assumed to be *dynamically stable*, i.e., the islands and channels are considered to continuously change position during deformation, but the area fraction of islands within the grain boundary zone, and the thickness of the zone remain unchanged. Meanwhile there is a net flux of dissolved material through the channels, out of the grain boundaries under high normal stress, towards the grain boundaries under low normal stress. This is driven by gradients in the chemical potential of the solid developed between grain boundaries under high normal stress and grain boundaries under low normal stress. Neglecting surface energy, the corresponding potential difference ($\Delta\mu$) between source and sink sites can be written:

$$\Delta\mu = \Delta f + P\,\Delta V_m \qquad (6.1)$$

where f is the Helmholz free energy of the solid (consisting of elastic and defect stored energy terms), P is the pressure, and V_m is the molar volume of the solid (e.g. Spiers & Schutjens 1990). To a first approximation, however, $\Delta\mu \approx \Delta\sigma_n V_m$ where $\Delta\sigma_n$ is the difference in grain boundary normal stress (see Lehner 1990).

It has recently been argued that the DIC-structure would be an unstable structure, apt to smooth out, because the islands are preferentially dissolved away and the fluid mechanically expelled or trapped in inclusions by surface energy driven healing of the grain boundary (e.g. Hickman & Evans 1991). This is acknowledged by Spiers & Schutjens (1990), Lehner (1990), and Schutjens (1991) for conditions approaching equilibrium. However, for the non-equilibrium conditions corresponding to SPC, these authors argue that the island-channel structure can be treated as quasi stationary because of the presence of defects in the solid, because of heterogeneities in solid deformation, and because of crystallographically controlled interface kinetics, all of which may continuously perturb the rate of dissolution and precipitation along the phase boundary.

Within the framework of the DIC grain boundary model, two different 'flow laws' have been derived for dense polycrystals, depending on whether the *interfacial* reactions, or the *diffusion* process control the deformation rate (Raj 1982, Lehner 1990, or Spiers & Schutjens 1990). Following Lehner (1990) and Spiers & Schutjens (1990), these models are given in table. 6.1 (equations i and ii). Both show a linear dependence of strain rate ($\dot{\varepsilon}$) on applied stress (σ). The *interface-controlled* SPC equation (equation i in table 6.1) predicts that the strain rate is

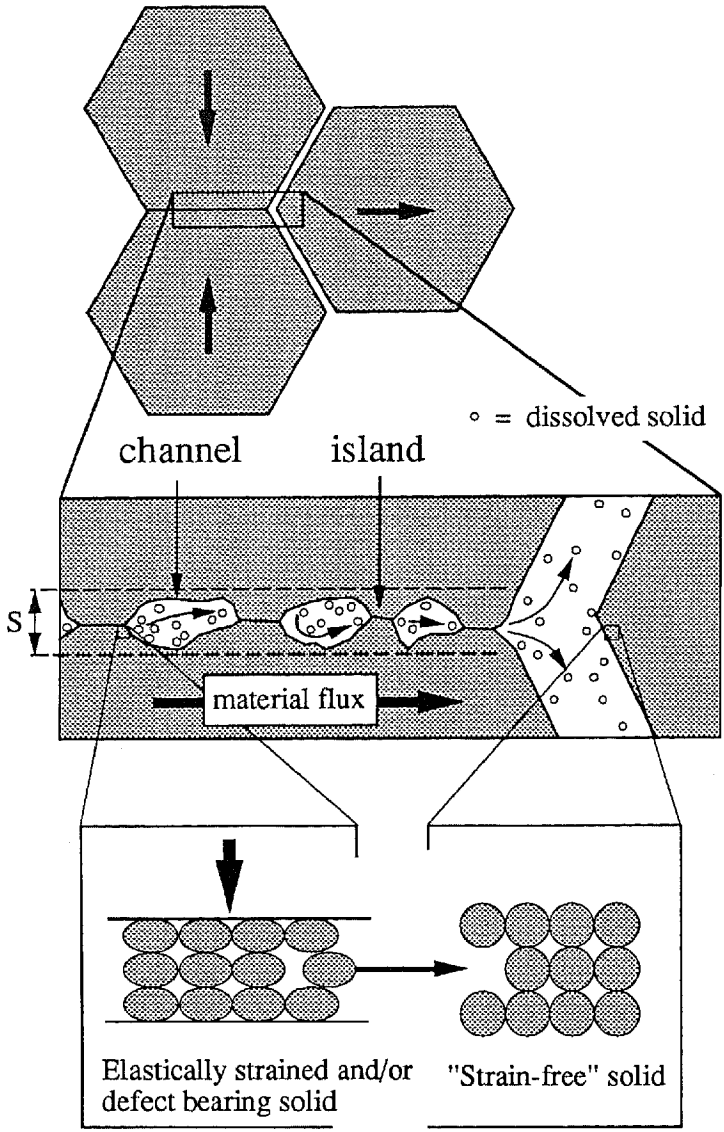

Fig. 6.2 *Schematic representation of grain boundary under high normal stress according to the dynamically-stable island-channel (DIC) model. The islands and channels are believed to continuously change position during the deformation, but the effective grain boundary width (S) and the fraction of islands are believed to remain constant. Grain-to-grain contacts at the islands are assumed to be solid. Driving force for mass transport is the difference in elastic and/or defect stored energy between the grain boundaries under high normal stress and the grain boundaries under low normal stress.*

proportional to the interfacial reaction rate coefficient (I), and inversely proportional to the grain size (d). The *diffusion-controlled* SPC equation (equation ii in table 6.1) predicts that the strain rate is proportional to the effective diffusivity of the grain boundary zone (product D_fC_fS; see table 6.2 for meaning of variables) and inversely proportional to the cube of the grain size.

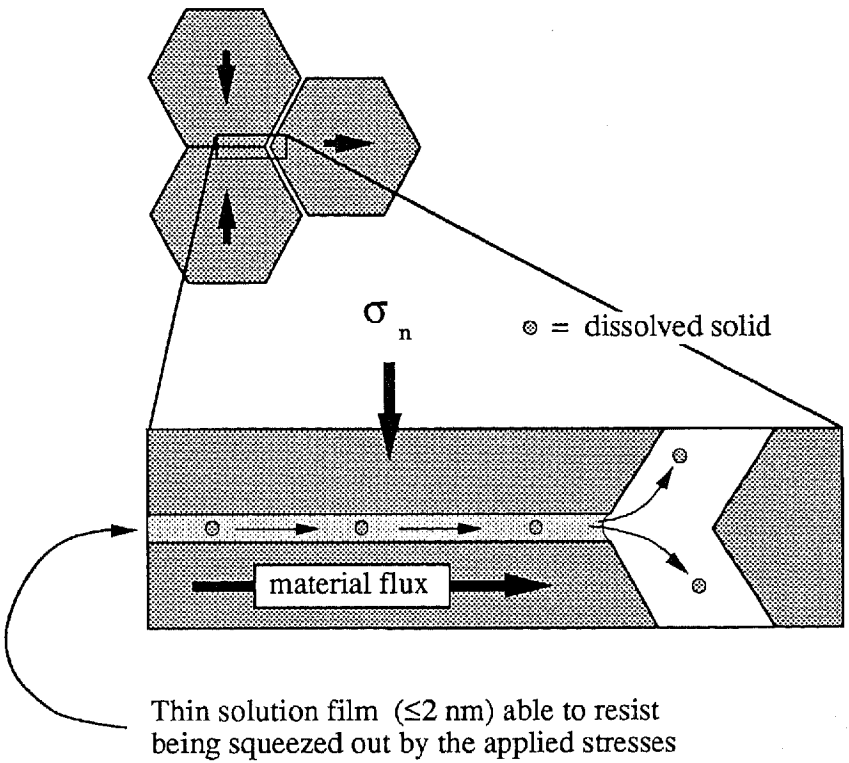

Fig. 6.3 *Thin-film model of Rutter (1976). The grain boundaries under high normal stress are believed to contain a ≤2 nm thin continuous water film with fluid properties, but strong enough to resist being squeezed out by the applied stresses. Rutter (1976) assumed that the diffusivity through the thin film is so small, that diffusion rather than interface reactions (dissolution-precipitation) control the rate of deformation.*

6.2.2 Thin-film model

Another SPC-model was derived by Rutter (1976) using the driving force equation $\Delta\mu \approx \Delta\sigma_n V_m$. The final mathematical description is identical to equation (ii) in table 6.1 for the diffusion-controlled DIC-model, but the grain boundary is assumed to consist of a continuous thin solution film adsorbed or bonded onto the solid grain surfaces (Fig. 6.3). Such films are believed to be several molecules thick (≤2 nm), and to posses sufficient shear strength to resist being squeezed out by the applied stresses (e.g., Rutter 1976, 1983, Sharma et al. 1980, Clarke 1987, 1989, Kwon & Messing 1991). Within the thin film, the diffusivity is assumed to be lower than in the bulk solution. Should interface reaction rates be slow in comparison with mass transport by diffusion through the thin grain boundary film, then equation (i) (Table 6.1) would apply for the thin-film model, as well as for the DIC-model.

Experimental evidence for the existence of ≤2 nm thin films in stressed grain boundaries is found in hot-pressing and deformation experiments on siliceous ceramics (Sharma et al. 1980, Wang & Raj 1984, Clarke 1987, 1989, Hwang & Chen 1990). These films consist of siliceous glass, believed to be melt during deformation. In superplastic SiAlON ceramics deformed at 1550°C and atmospheric pressure there is evidence that thin films are able to resist a differential stress of ~20 MPa (independent of the strain rate) before being squeezed out completely (Chen & Hwang 1992).

Surface force measurements by Peschel et al. (1982), Israelachvili (1986, 1992) and Horn et al. (1988, 1989) have shown that thin *aqueous solution* films, squeezed between mica, alumina, or silica, are also capable of withstanding shear stresses. Peschel et al (1982) and Horn et al. (1989) found that at NPT-conditions, a 1-2 nm aqueous solution film squeezed between silica plates was able to resist a stress of ~0.1 Mpa, whereas ~1 Mpa was needed to squeeze out these films completely.

6.2.3 Static island-crack (SIC) model

Gratz (1991) proposed an SPC-model based on a grain boundary structure consisting of *static* islands separated by cracks or crack-controlled channels, the scale being somewhat coarser (i.e., on a μm-scale) than the DIC-model (Fig. 6.4). He assumed that the grain-to-grain contacts at the crack-bound islands contained a thin fluid film of the type assumed by Rutter (1976), and that the diffusivity in the film was at least several orders of magnitude lower than the diffusivity in the channels. Thus, the rate of mass removal from the grain boundaries under high normal stress to the micro-cracks, or through the channels towards grain boundaries parallel to the shortening direction (Z), would be determined by diffusion rates within the thin fluid films at the crack-bound island-island contacts. As a result, the rate of

Table 6.1. *Scalar solution-precipitation creep equations written for axisymmetric compressional deformation of dense polycrystals. For definition of terms see Table 6.2.*

(*i*)	$\dot{\varepsilon} = A_I \left[\frac{V_m I}{RT d}\right] \sigma$	(i) Interface-controlled SPC-model. When dissolution is rate controlling $A_I = 1$ and I is the dissolution velocity for a driving force of 1 RT. When precipitation is rate controlling $A_I = -A_p/A_s$ and I is the precipitation velocity for a driving force of 1 RT.
(*ii*)	$\dot{\varepsilon} = A_D \left[\frac{\rho^f}{\rho^s}\right] \left[\frac{V_m D_f S C_f}{RT d^3}\right] \sigma$	(ii) Diffusion-controlled SPC-model assuming dynamically stable island-channel (DIC) structure (Lehner 1990) or continuous thin-film (Rutter 1976)
(*iii*)	$\dot{\varepsilon} = B \left[\frac{\rho^f}{\rho^s}\right] \left[\frac{V_m D_f S C_f}{RT d a^2}\right] \left[\frac{1}{\alpha}\right] \sigma$	(iii) Static island-crack (SIC) model with grain boundary diffusion control at the islands (Gratz 1991) and $D_{isl} << D_{channel}$
(*iv*)	$\dot{\varepsilon} = A_I \left[\frac{V_m I}{RTd}\right] \left[\frac{1}{\alpha}\right] \sigma$	(iv) SIC-model with interface reaction control.
(*v*)	$\dot{\varepsilon} = B \left[\frac{\rho^f}{\rho^s}\right] \left[\frac{V_m D_f S C_f}{RT d [a']^2}\right] \left[\frac{1}{\alpha}\right] \sigma$	(v) SIC-model as (iii) but when $D_{isl} \approx D_{channel}$. When all dissolved material precipitates in the cracks then a'=a, when all dissolved material is transported to grain boundaries parallel to Z then a'=d; else, a<a'<d.
(*vi*)	$\dot{\varepsilon} = B \left[\frac{V_m D_s S}{RT d a^2}\right] \left[\frac{1}{\alpha}\right] \sigma$	(vi) SIC-model with solid-state diffusion at the islands.

Table 6.2. *Definition of terms appearing in equations of tables 1 to 5*

Symbol	Definition	Units
$\dot{\epsilon}$	Axial strain rate	s^{-1}
σ	Axial differential stress	Pa
V_m	Molar volume of solid phase	m^3mol^{-1}
ρ^f	Density of fluid phase	kg m^{-3}
ρ^s	Density of solid phase	kg m^{-3}
D_f	Fluid phase grain boundary diffusivity (either thin-film or in channels of DIC-structure)	m^2s^{-1}
D_s	Solid phase grain boundary diffusivity	m^2s^{-1}
C_f	Solubility of solid in grain boundary solution	mole fraction
I	Dissolution and/or precipitation velocity for a driving force of 1 RT.	ms^{-1}
A_I	Dimensionless factor. $A_I=1$ when dissolution is rate controlling, and $A_I=A_p/A_s$ when precipitation is rate controlling	
A_p	Area fraction of surface where precipitation takes place	
A_s	Area fraction of surface where dissolution takes place	
A_D	Dimensionless factor depending on grain shape: A=44 for spherical grains; A=32 for disk-shaped grains	
B	As A_D, but B=11 for spherical grains, and B=8 for disk shaped grains	
S	Average fluid thickness in thin-film or fine-scale DIC grain boundary, *or* effective solid-state grain boundary width	m
R	Gas constant	$JK^{-1}mol^{-1}$

Table 6.2. *(Continued)*

Symbol	Definition	Units
T	Absolute temperature	K
d	Grain size	m
a	Island diameter (in SIC-model)	m
a'	Apparent island diameter (SIC-model); a'=a when precipitation occurs in the cracks only; a'=d when precipitation occurs at grain boundaries parallel to Z only	m
α	Area fraction of islands occupying grain boundary zone (SIC-model)	

deformation would depend on the size (a) of the crack-bound islands, as well as on the grain size (d) and the stress (σ).

The rate equation derived by Gratz (1991) is given in equation (iii) of table 6.1. Note that the geometric factor has the value 8 instead of the incorrect value of 32 reported by Gratz (1991) in case of disk-shaped (cylindrical) grains, and 11 in case of spherical grains. In contrast with the other diffusion-controlled models, Gratz' model predicts that the strain rate is inversely proportional to the grain size, and inversely proportional to the square of the island diameter.

6.2.4 Extension of the SIC-model

Clearly, there is no *a-priori* reason to limit the SIC-model to the thin-film diffusion controlled case. For example, if the dissolving islands or precipitation sites become sufficiently small in area, dissolution or precipitation could become rate controlling. The corresponding creep equation is easily derived from equation (i) of table 6.1, and is given in (iv). Furthermore, Gratz (1991) assumed that the diffusivity on the crack-bound island-island contacts was several orders of magnitude lower than in the crack-bound channels. In that case it does not matter whether dissolved material precipitates directly in the cracks or is transported to the grain boundaries parallel to Z. But when the diffusivity on the island-island contacts is *not* much different from the diffusivity in the larger, crack-bound channels, then it is very important whether the dissolved material is precipitated

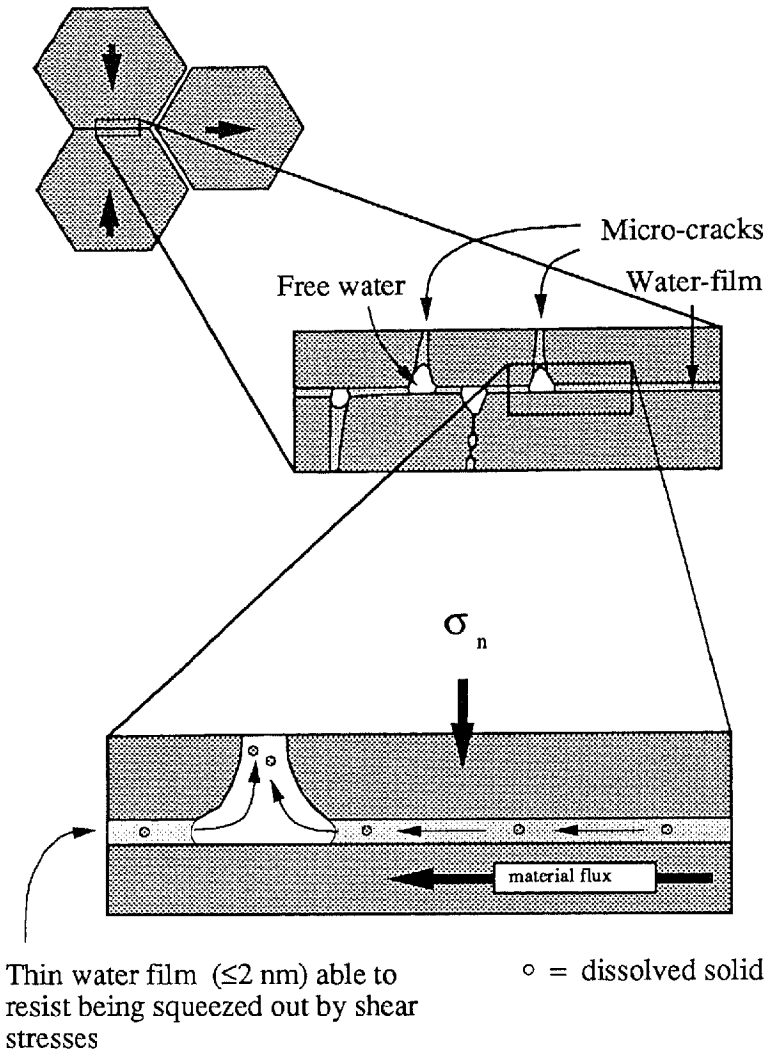

Fig. 6.4 *Static island-channel (SIC) model of Gratz (1991). Mass transfer is assumed to take place through a thin water film (of the type assumed by Rutter 1976) at the crack-bound island-island contacts, with either direct precipitation of dissolved material into the cracks, or with further transport through channels which are located at the intersection of micro-cracks with the grain boundary to grain boundaries oriented parallel to Z. The diffusivity in the thin water film is assumed to be several orders of magnitude lower than in the channels, so that in addition to the grain size, the size of the islands also determines the rate of deformation.*

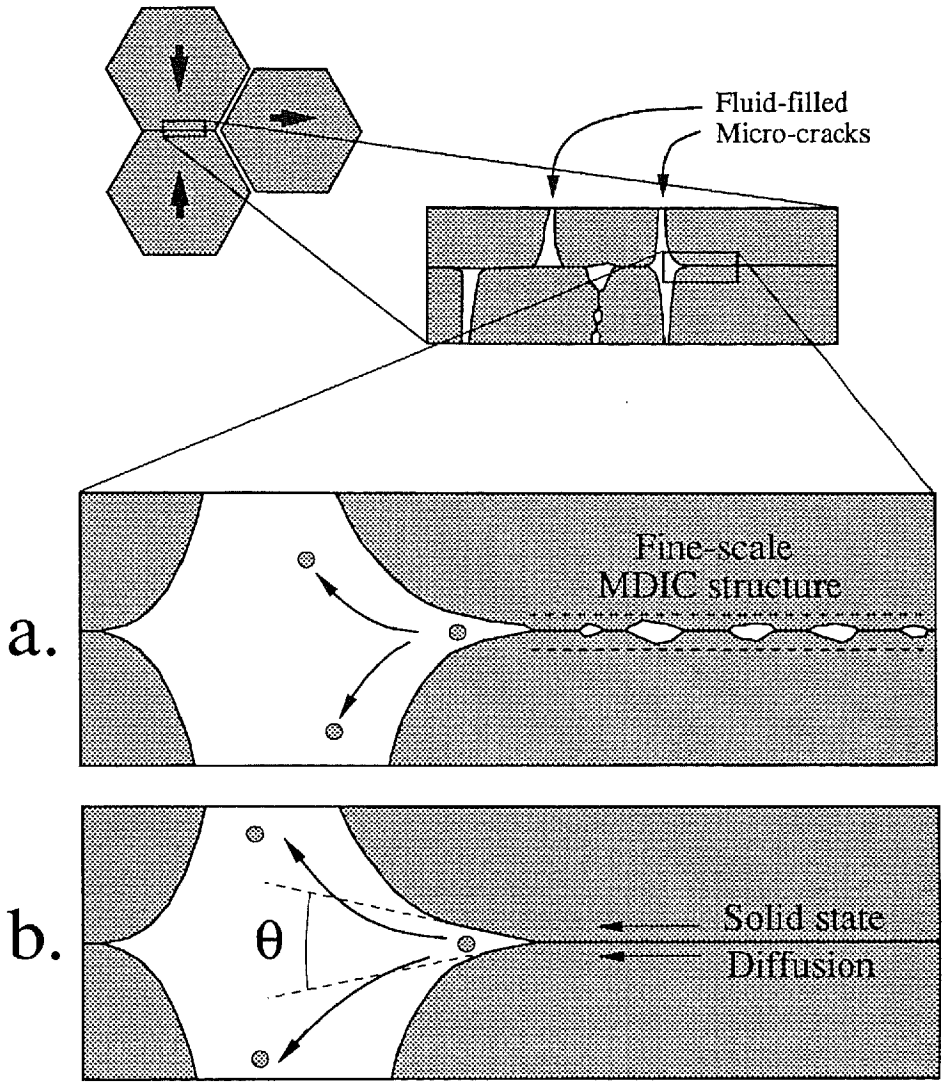

Fig. 6.5 *Extension of the SIC-model. (a) The crack-bound island-island contacts of the SIC grain-boundary consist of a fine-scale dynamically stable island-channel (DIC) structure. (b) The island-island contacts of the SIC grain boundary are solid. Diffusion occurs through the solid-state (Coble creep). At the widening island-island contact dissolution occurs in order to keep the dihedral angle (θ) at a near equilibrium value. Dissolved material is further assumed to be transported through the channels, located where micro-cracks intersect the grain boundary, and precipitated either in the cracks or at grain boundaries parallel to Z.*

directly *in* the cracks, or is transported to the grain boundaries parallel to Z. In this case, the corresponding creep equation is given in (v; table 6.1) where the apparent island size (a') is equal to the 'true' island size (a) when all of the dissolved material is precipitated in the cracks, and equal to the grain size (d) when all of the dissolved material is transported through the crack-bound channels to the grain boundaries parallel to Z. Here α represents the area fraction of grain boundaries occupied by the larger crack-bound islands. Equation (v) is expected to apply when the crack-bound island-island contacts themselves contain a fine-scale DIC-structure and the diffusivity in the fine-scale channels on the islands is not much different from the diffusivity in the larger crack-bound channels.

An additional possibility, is that the crack-bound island-island contacts have a solid-state character. Following the model of Cooper & Kohlstedt (1984), deformation could then occur by solid-state grain boundary diffusional deformation at the contacts (Coble creep), *coupled* with interfacial energy driven dissolution at the contact margins (Fig. 6.5). Assuming that solid-state diffusion would be rate controlling and several orders of magnitude lower than diffusion through the crack-bound channels, and applying Coble's model to the islands, results in equation (vi) in Table 6.1.

6.3 MICROSTRUCTURAL OBSERVATIONS VERSUS MICROPHYSICAL MODELS

An attempt is now made to assess which of the above models is most consistent with the microstructure, observed in the quartzite samples deformed with ~0.4 wt% added water at T=800°C, $P_c \approx 1200$ Mpa, and $\dot{\varepsilon} \approx 10^{-6}$ and 10^{-7} s^{-1}, as reported in chapter 3.

It will be recalled, that these samples showed a microstructure characterized by abundant axially oriented intra- and intergranular grain-scale micro-cracks, commonly filled with small new subeuhedral quartz grains. These new grains were interpreted to be precipitated out solution.

6.3.1 Grain boundary microstructure *after* experiments

Whereas grain boundaries oriented parallel to Z commonly showed subeuhedral overgrowth features, these were conspicuously absent on grain boundaries oriented perpendicular to Z. These grain boundaries were instead relatively smooth on the grain-scale, and contained abundant fluid inclusions (0.1 to 1 μm in diameter) and channel-like structures (0.5-1 μm diameter; see e.g. Fig. 6.6a). The originally polished surface of the quartz single crystal spacer, added in line with the quartzite

sample in experiment GRU23 (see chapter 3; T=800°C, $P_c \approx 1200$ Mpa, $\dot{\varepsilon} \approx 10^{-7}$ s^{-1}, with ~0.4 wt% added water) showed large amounts of indentations pits of 50 to 150 μm diameter, indicative of removal of material by solution transfer. The indented surface also showed densely spaced grain boundary fluid inclusions and a channel network (Fig. 6.6b & c). The channels were located where (partially healed) micro-cracks separated 3-10 μm apart intersected the grain boundaries. These were also detected locally, in thin-sections cut parallel to Z, of both the single crystal spacer, as well as in the original grains of the water added quartzite samples (e.g. Fig. 6.6c). In many cases, the fluid inclusion arrays on the grain boundaries perpendicular to Z followed a pattern indicative of (partial) healing of these micro-cracks.

6.3.2 Grain boundary microstructure *during* experiment

From the above, it is inferred that during deformation, grain boundaries perpendicular to Z had a structure consisting of islands separated by crack-bound channels, with matter being transported from island contacts into the intervening cracks or channels where it was either precipitated, or transported to the grain boundaries oriented parallel to Z. The overall structure could have been essentially static (cracks early) or dynamic (ongoing cracking plus healing). However, the fine-scale structure of the island-island contacts *during* deformation, and the origin of the fluid inclusion arrays, remain problematic, since the microstructure on this scale may have been corrupted during cooling and/or depressurization of the sample (cf. Hickman & Evans 1991). Several possibilities are considered below:

(i) The islands may have had a fine-scale DIC-structure, a thin film, or a solid-state contact *during* deformation, that was disrupted during unloading. Subsequent healing could have resulted in the grain boundary fluid inclusion arrays. This possibility is supported by the presence of partially healed sample-scale unloading fractures oriented perpendicular to Z, indicating that extensional forces existed during unloading, tending to pull apart grain boundaries perpendicular to Z.

(ii) The island-island contacts may have consisted of a fine-scale DIC-structure which may have been healed during or after the experiment, resulting in the grain boundary fluid inclusion arrays. It is unlikely that the contacts consisted of a thin water film which was healed during or after the experiments, since on average the amount of water present in the fluid inclusions on the grain boundaries would account for a film of 100-200 μm thick (about 2 orders of magnitude too thick for a thin film).

(iii) The islands may have had a fine-scale DIC-structure, a thin water film, or a solid-state contact *during* deformation, while the fluid inclusions were already present on the grain boundary as well. These may have been left behind, either after smoothing of an originally rougher grain boundary during the initial stages of

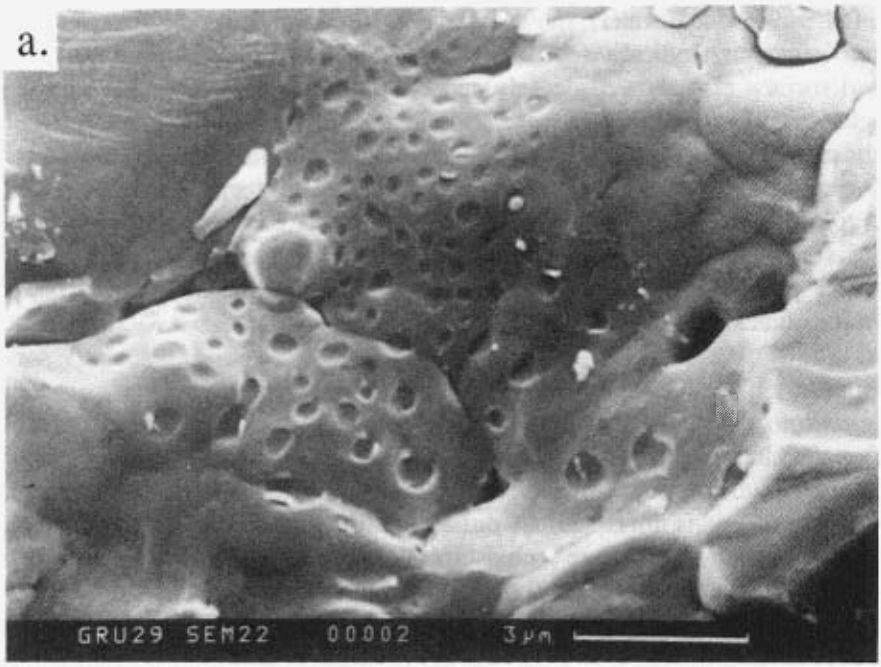

Fig. 6.6 *(a) SEM micrograph of sample GRU29 ($\dot{\varepsilon}=10^{-6}$ s^{-1}, T=800°C, P≈1200 MPa, and ~0.4 wt% water added) showing old-grain grain boundary oriented perpendicular to Z with fluid inclusion arrays, and channels where micro-cracks intersect the grain boundary. (b) SEM micrograph of originally polished surface of single crystal spacer added in line with quartzite sample in experiment GRU23 (see chapter 3) (T=800°C, P=~1200 MPa, $\dot{\varepsilon}=10^{-7}$ s^{-1}, ~1 vol% added water, ~10% finite strain). The surface is oriented perpendicular to Z, and shows a regular channel pattern, the channels being located where micro-cracks intersect the grain boundary. The c-axis of the single crystal spacer is oriented perpendicular to Z, sticking out of the paper. The hexagonal pattern of the micro-cracks indicates that these followed the prismatic planes. The channels are typically 3 to 10 μm spaced apart. Note large amounts of fluid inclusions on the islands. (c) Optical micrograph of quartzite sample GRU23 showing densely spaced, healed micro-cracks parallel to Z. (Crossed polars.)*

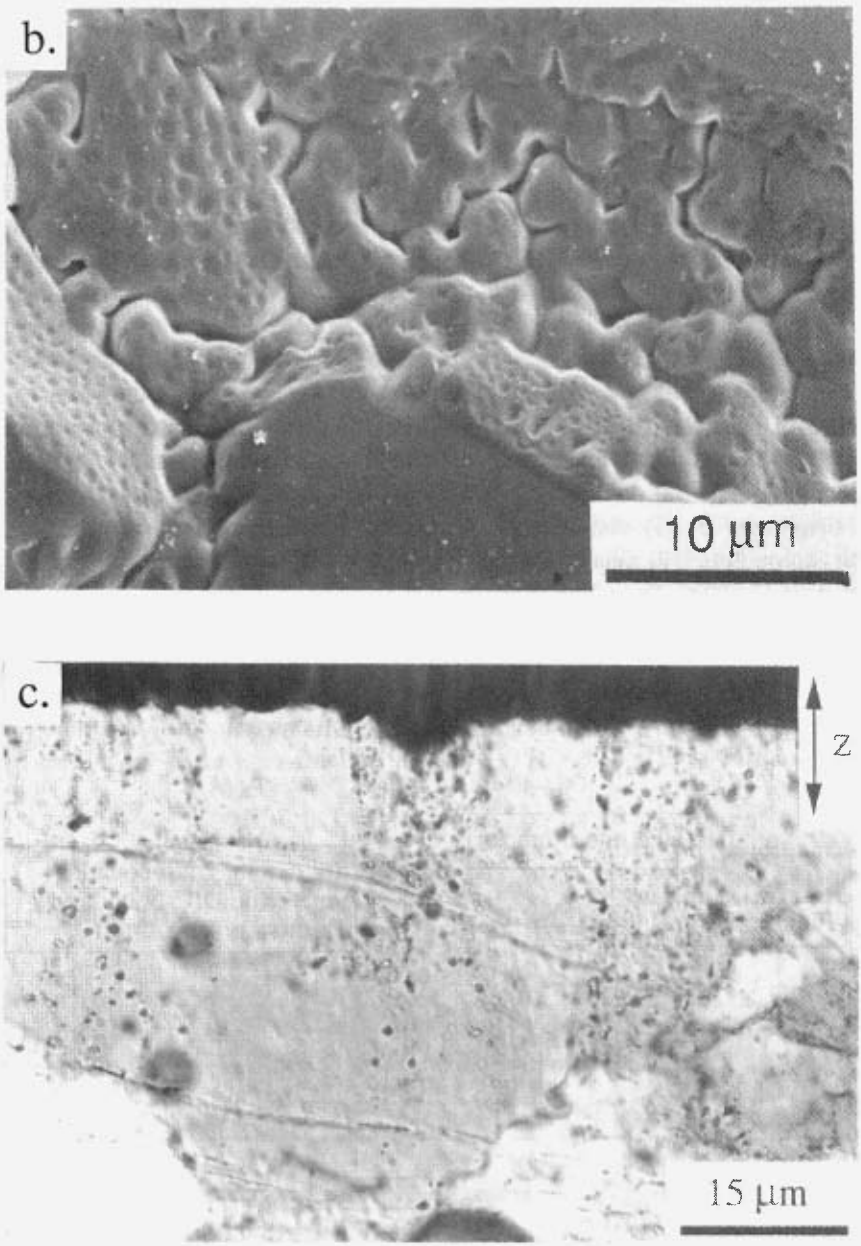

Fig. 6.6 *(Continued)*

the deformation, *or* by the healing of the crack-bound channels during deformation. The latter finds local support in the regular arrangement of fluid inclusions, but mostly the fluid inclusions on the boundary do not show patterns suggestive of healed cracks.

(iv) The island-island contacts may have been solid while the fluid inclusions resulted by precipitation from water that was originally dissolved in the grain boundary region. It is not known how much water can be dissolved into a (elastically disturbed) grain boundary lattice, but it seems unlikely that a coverage of 25% of the islands by (0.1 to 1 μm diameter) fluid inclusions could be explained by that, since approximately 1H/2Si would need to have been dissolved in that case in the lattice next to the grain boundary to a depth of ~1 μm, which seems much too much.

On the basis of the above, it is concluded that the most microstructurally appropriate SPC-model would appear to be the SIC-model coupled with axial micro-cracking, though no definite statement can be made regarding the fine-scale structure of the island-island contacts during deformation. These may have had a fine-scale DIC-structure, a thin (<2 nm) water film, or they may have been solid (not wetted). The fluid inclusions on the crack-bound island-island contacts may have originated by (i) disruption of the grain boundaries and subsequent healing during unloading, (ii) healing of a fine-scale DIC-structure during or after the experiment, or (iii) by smoothing out of an initially rough grain boundary, or locally, by healing of the micro-cracks.

The possibility cannot be excluded that the island-crack structure was to some extent dynamic (on-going cracking plus healing). Even in this case, however, the time averaged structure would be similar to the SIC-model.

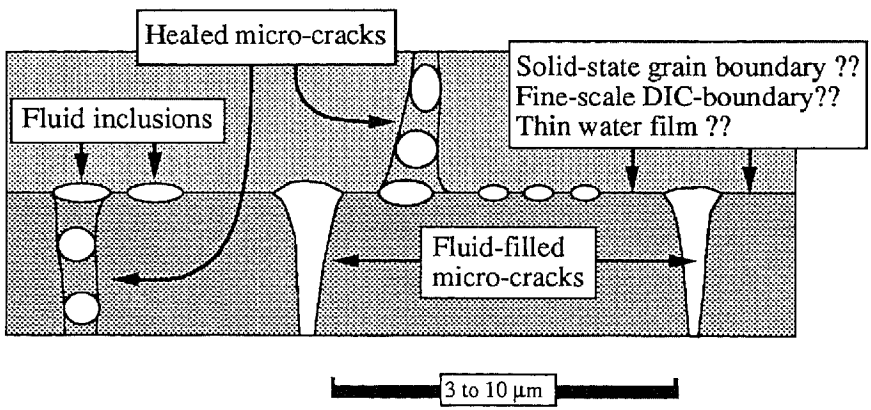

Fig. 6.7 *Schematic representation of grain boundary structure as observed in water-added samples such as depicted in Fig. 6.6.*

6.4 PREDICTIONS OF THE SIC-MODEL VERSUS MECHANICAL DATA

Having inferred that the SIC-model (with intergranular micro-cracking) is the most consistent with the microstructures observed in the quartzite samples deformed with ~0.4 wt% added water at T=800°C, $P_c \approx 1200$ Mpa, and $\dot{\varepsilon} \approx 10^{-6}$ and 10^{-7} s^{-1} the mechanical predictions of the SIC-model are now considered and compared with the corresponding data obtained in the quartzite experiments. The following variants of the SIC-model can be distinguished and are considered:

(i) SIC-model with fine-scale DIC-structure at the crack-bound island-island contacts, and with *dissolution* or *precipitation* controlling the deformation rate. This case is represented by equation (iv) in Table 6.1.

(ii) SIC-model with a fine-scale DIC-structure at the crack-bound island-island contacts, and with grain boundary *diffusion* controlling the deformation rate. This case is represented by equations (iii) or (v) in Table 6.1, depending on whether the diffusion rate on the crack-bound islands is significantly different from that in the crack-bound channels.

(iii) SIC-model with solid-state diffusion at contacts controlling the deformation rate. This case is represented by equation (vi) in Table 6.1.

The thin-film model is rejected for the present case, since the differential stresses during the experiments (chapter 3) were well above the ~1 MPa required to squeeze out a thin water film between silica plates at NPT conditions, i.e., the differential stresses were 150-190 MPa at 10^{-6} s^{-1} (GRU10, 20, 21 & 29) and very probably ≥10 MPa at 10^{-7} s^{-1} (GRU11, 23, 26 & 35).

Note that the possible effects of the isolated fluid inclusions present within contact regions during deformation is not accounted for in the models/equations referred to above. Their area fraction is only ~0.25 so that their influence can be neglected.

6.4.1 Estimation of parameters

In order to apply the above models (equations (iii), (iv), (v) and (vi) in Table 6.1) in a quantitative way enabling comparison with experimental stress versus strain-rate data, the various phenomenological coefficients and variables must be assigned values which are appropriate for the experiments considered. This is done below.

6.4.1.1 Experimental, microstructural, and state variables

The experiments in quartzites of present interest were carried out at temperature (T) of 1273 K, confining pressure (P_c) of ~1200 Mpa and strain rates ($\dot{\varepsilon}$) of ~10^{-6}

and ~10^{-7} s^{-1}. At the same time the microstructure of the material tested was characterized by a grain size (d) of 150-250 μm, an island size (a) of 3-10 μm, an area fraction of static, crack-bound island-island contacts (α) of 0.5-1, an area fraction of grain boundary surface where dissolution occurs (A_s) of 0.05-0.35, and where precipitation occurs (A_p) of 0.65-0.95. Note also that the molar volume of the solid phase (V_m) is $2.6 \cdot 10^{-5}$ $m^3 mol^{-1}$, the density (ρ^s) of the solid (quartz) is $2.2\text{-}2.5 \cdot 10^3$ kgm^{-3}, and of the liquid (ρ^f) is 0.8-0.9 kgm^{-3}.

6.4.1.2 Interfacial rate coefficient I

The most recent estimate of the dissolution-precipitation velocity coefficient for the quartz-water system can be obtained from Gratz et al. (1990). These authors report a value of I≈1 to 4·exp (-90000/(RT)) ms^{-1}, determined at a temperature of 106 to 236°C, a pressure of 1 atmosphere, and pOH≈6. Reaction rates do not appear to be influenced significantly by pressure (at least up to 700 Mpa; Wood & Walther 1983), so that their I-value is extrapolated to ~1200 Mpa. By further extrapolating their results to 250°C, $I \approx 3 \cdot 10^{-9}$ ms^{-1}, while at 800°C, I≈4 to $17 \cdot 10^{-5}$ ms^{-1} is obtained.

6.4.1.3 Diffusivity in >2 nm diameter channels

At NPT conditions, the diffusivity of silica in films and channels of more than ~2 nm wide is equal to the diffusivity in bulk solution (e.g. Israelachvili 1986, 1992, Horn et al. 1988, 1989, Israelachvili et al. 1990). Only below ~2 nm (i.e., ~6-10 molecular diameters) the diffusivity is expected to be lower than in the bulk. This is believed to be due to increased hydrogen-bonding, resulting in a structured layer with lower density near the silica surface in very narrow pores (e.g. Etzler 1988) or thin films (Israelachvili 1986, 1992, Israelachvili et al. 1990). During the present experiments at 800°C and 1200 Mpa, the width of such a structured layer is believed to be ≤2 nm wide, since both the temperature, as well as the pressure, are expected to work against formation of a structured layer with a lower density.

The diffusivity of silica in bulk water at a temperature of 800°C and a pressure of ~1200 Mpa has not yet been experimentally determined. At a temperature of 298.15 K and a pressure of 1 atmosphere, a value of $1.09 \cdot 10^{-9}$ $m^2 s^{-1}$ was obtained by Wollast & Garrels (1971). There are two papers that report the diffusivity at intermediate temperatures and pressures. Balashov et al. (1983) measured the diffusivity of silica in a porous TiO_2 aggregate (grain size ~1 μm; ~63% porosity) at 250°C and 100 Mpa, and obtained a value of $4.1 \cdot 10^{-9}$ $m^2 s^{-1}$. Ildefonse & Gabis (1976) determined the diffusivity of silica in a porous graphite aggregate (50 to

60% porosity) at 550°C and 100 Mpa, and obtained a value of $2.4 \cdot 10^{-8}$ $m^2 s^{-1}$. To obtain the diffusivity at 800°C and 1200 Mpa, I have extrapolated these values, assuming that silica diffusion follows Einstein-Stokes behaviour so that $D \sim 1/\eta$, where η is the viscosity of the fluid. I further assumed that η varies linearly with the density of the fluid (see e.g. Dudziak & Farnck 1966; Walton 1960). The diffusivity may then be estimated from the density of the fluid. The density of water at 250°C and 100 Mpa is ~0.85 $g \cdot cm^{-3}$, at 550°C and 100 Mpa ~0.5 $g \cdot cm^{-3}$, and at 800°C and 900 to 1200 Mpa ~0.90 $g \cdot cm^{-3}$ (Fisher 1976). This yields $D = \sim 0.4 \cdot 10^{-8}$ $m^2 s^{-1}$ by extrapolation of Balashov et al.'s (1983) results, and $D = \sim 1.4 \cdot 10^{-8}$ $m^2 s^{-1}$ by extrapolation of Ildefonse & Gabis' (1976) results. The diffusivity of silica in bulk water and channels of > 2 nm diameter was therefore assumed to be of the order of 0.4 to $1.4 \cdot 10^{-8}$ $m^2 s^{-1}$. (For comparison, Fletcher & Hofmann (1974) and Rubie (1986) assume $D \approx 10^{-8}$ $m^2 s^{-1}$ for most metamorphic conditions.)

The effective diffusivity ($D_f C_f S$) in ≥2 nm films and channels at T=800° and $P_c \approx 1200$ MPa, with $C_f \approx 0.02$ (Anderson & Burnham 1965), and S=2-1000 nm is therefore estimated to be $1.6 \cdot 10^{-19}$ to $2.8 \cdot 10^{-16}$ $m^3 s^{-1}$.

6.4.1.4 Diffusivity in ≤2 nm diameter channels

Rutter (1976) assumed that the diffusivity in ≤2 nm thin solution films and channels was decreased compared to the bulk value due to the electro-viscous effect. In a 2 nm thin film the viscosity would be increased by ~5 orders of magnitude due to this effect. Assuming Stokes-Einstein behaviour (i.e., $D \sim 1/\eta$), the diffusivity would be decreased by ~5 orders of magnitude. More recently it appeared, however, that the viscosity increase due to the electro-viscous effect in thin solution films is very small (considerably less than a factor 10; e.g. Rubie 1986). Again assuming $D \sim 1/\eta$ this means that the diffusivity decrease by the electro-viscous effect would consequently be significantly less than a factor ~10 (Rubie 1986).

Molecular dynamics based computer simulations (Magda et al. 1985, Vanderlick & Davis 1987, Schoen et al. 1988, Bitsanis et al. 1990) predict that the self-diffusivity in molecularly thin films is decreased by a factor ≤2. Measurements with the Israelachvili surface force apparatus on molecularly thin solution films have shown that the viscosity of aqueous solutions remains equal to the bulk value even down to the last molecular layer (Israelachvili 1986, 1992, Horn et al. 1989, Israelachvili et al. 1990). The diffusivity of silica in ≤2 nm films and channels is therefore assumed to fall in the range 0.5 to 1 times the bulk value (i.e., 0.2 - $1.4 \cdot 10^{-8}$ $m^2 s^{-1}$ at 800°C and 1200 Mpa). It should be noted, however, that this holds only as long as the diffusion rate of *silica* in thin films is not slowed down *more* than the self-diffusion rate of water.

With $C_f \approx 0.02$ and S=0.6-2 nm, an effective diffusivity of $5.6 \cdot 10^{-19}$ to $2.4 \cdot 10^{-20}$ $m^3 s^{-1}$ at T=800°C and $P_c \approx 1200$ MPa is obtained.

6.4.1.5 Diffusivity of solid-state grain boundaries

An indication of the solid-state grain boundary diffusivity in quartz in the presence of water may be obtained from the work of Farver & Yund (1991b). These authors determined the effective grain boundary diffusivity of *oxygen* in novaculite (Grain size 1.2 and 4.9 μm). The measurements were carried out in the presence of water at 100 Mpa in the range 450 to 800°C. At NPT conditions, before and after the experiment, the grain boundaries were *physically* less than 1 nm wide, they were not wetted, and no interconnected grain triple junction network was observed.

According to Farver & Yund (1991b), the diffusion occurred most likely through a grain boundary physically <1 nm but effectively ≤10 nm wide. According to them, added water would have been dissolved in the grain boundary crystal lattice, and have enhanced the diffusivity of oxygen, much like the way water enhances the *bulk lattice* diffusivity of oxygen in quartz (Farver & Yund 1991a), perhaps by replacing Si-O bonds by weaker hydrogen bonds and effectively reducing the energy of the activated state as suggested by Rubie (1986).

Farver & Yund (1991b) measured an effective diffusivity (D_0S) of 2.6 to $3.4 \cdot 10^{-17}$ $m^3 s^{-1}$, and an activation energy Q≈113 kJ/mol. With

$$D = D_0 \exp(-Q/RT) \qquad (6.2)$$

a D_sS-value for oxygen of $\sim 8 \cdot 10^{-23}$ $m^2 s^{-1}$ is obtained for a temperature of 800°C at P_c=100 Mpa. For our purposes, this effective solid-state diffusivity needs to be extrapolated to ~1200 Mpa. This will be done with the help of a study on the pressure dependency of the *bulk lattice* diffusion of oxygen in silica (with added water) by Farver & Yund (1991a). They showed that the lattice diffusivity increased with increasing water pressure. Their data are plotted in Fig. 6.8 together with two data points of Elphick et al. (1986). Extrapolation of these values to ~1200 Mpa shows that an increase of 100 to ~1200 Mpa at 800°C, causes an increase in the lattice diffusivity by one order of magnitude. If the *grain boundary* diffusion in Farver & Yund's (1991b) experiments occurred by solid-state diffusion through a grain boundary physically less than ~1 nm but effectively ≤10 nm wide, then it is reasonable to expect that this grain boundary diffusion rate would also increase by one order of magnitude when the pressure is increased from 100 to 1200 Mpa. If so, then the effective grain boundary diffusivity is increased to

$D_sS \approx 8 \cdot 10^{-22}$ $m^2 s^{-1}$. It is important to note that this is the effective grain boundary of *oxygen*, which may be different from that of silicon.

6.4.2 Predicted stress versus strain-rate behaviour

Armed with values of the various parameters plus variables needed, it is possible to apply the various SIC-models to predict the corresponding stress versus strain-rate relations expected for the experimental conditions considered. The results obtained

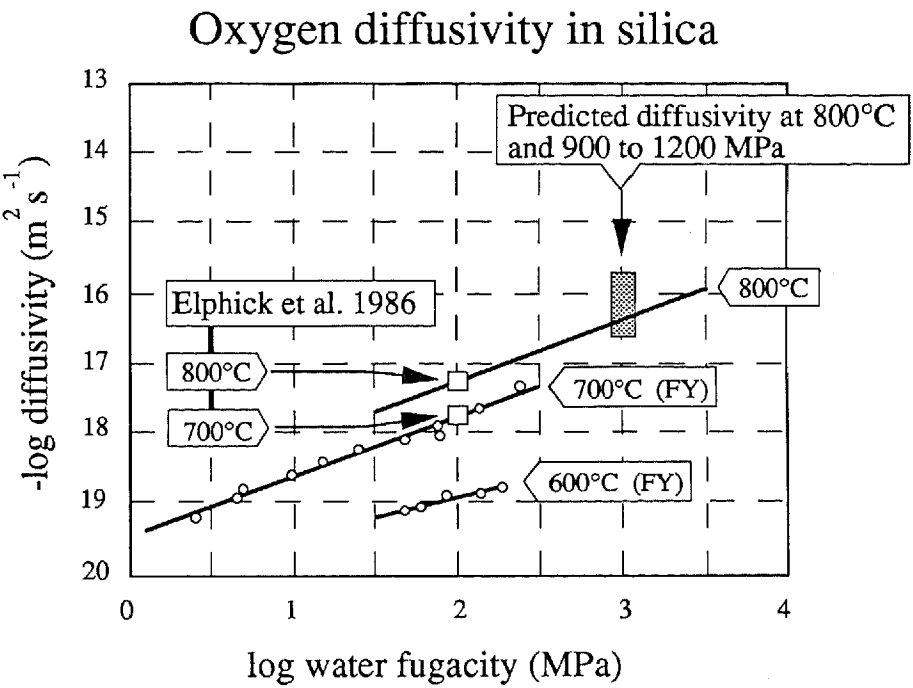

Fig. 6.8 *Diagram showing bulk lattice oxygen diffusivity data of Farver & Yund (1991a) and Elphick et al. (1986) as a function of water fugacity. Data are plotted as log water fugacity versus minus-log diffusivity, and show that the diffusivity increases with increasing water pressure at 600 and 700°C. By assuming similar behaviour at 800°C, extrapolation of the 800°C data point of Elphick et al. (1986) predicts that the bulk lattice diffusivity increases ~1 order of magnitude by increasing the water fugacity from 100 MPa to 1200 MPa. It is assumed in the text that the water-enhanced solid-state grain boundary diffusion follows a similar behaviour.*

are described below and presented in Figures 6.9-6.12.

(i) The results of the SIC-model with fine-scale DIC-structure on the crack-bound islands, controlled by the rate of dissolution and/or precipitation (equation iv in table 6.1) are shown in Fig. 6.9. The interface velocity is assumed to be the same in *all* cases. The strain rates predicted at constant stress are many orders of magnitude faster than the experimental data. Even when it is assumed that the interface-reaction rate at 800°C and ~1200 MPa is equal to that measured by Gratz et al. (1990) at 250°C an 1 atmosphere, no good fit is obtained.

(ii) The results of the SIC-model with a fine-scale DIC-structure and diffusion control at the larger crack-bound island-island contacts are shown in Fig. 6.10, 6.11 & 6.12. Because the difference between the diffusivity in the DIC-structure *on* the crack-bound islands is less or equal to 0.5 times the diffusivity in the crack-bound channels the rate of deformation depends on whether material is precipitated directly in the cracks or is transported towards grain boundaries parallel to Z. Therefore, equation (v) of table 6.1 was applied. Figure 6.10 illustrates the case for a grain boundary width (S) of 2-1000 nm where all dissolved material precipitates directly in the cracks (a'=a). No good fit is obtained. Figure 6.11 illustrates the other extreme, where for a grain boundary width (S) of 2-1000 nm all the dissolved material is transported to grain boundaries parallel to Z. Good fit is obtained in this case when the effective grain boundary width of the DIC-structure on the crack-bound islands is of the order of 25 nm. It is also inferred from Fig. 6.11 that for intermediate apparent island sizes ($a<a'<d$) good fit is obtained for $2<S<25$ nm. The results for an effective DIC grain-boundary width in the range 0.6-2 nm are shown in Fig. 6.12, both for a'=a and for a'=d. Good fit is obtained between the two extremes: S=0.6 nm with a'=a, and S=2 nm with a'=d.

(iii) The results of the SIC-model with water enhanced solid-state diffusion at grain boundaries (equation vi in table 6.1) following diffusion data of Farver & Yund (1991b) are shown in Fig. 6.13. There is good agreement with the experimental data assuming $D_sS \approx 8 \cdot 10^{-22}$ m^3s^{-1}, d=175 μm, α=0.8, and a=3-10 μm.

6.4.3 Discussion

The above results show that at T=800°C, $P_c \approx 1200$ Mpa, $\dot{\varepsilon} \approx 10^{-6}$ and 10^{-7} s^{-1}, and with ~0.4 wt% added water, the interface controlled SIC-model can be safely rejected, whereas different diffusion controlled SIC-models produce good results. Two possibilities are considered:

(i) The crack-bound island-island contacts of the SIC-model consist of a fine-scale DIC-structure with channels having a diameter of ≤25 nm, and with $a<a'<d$. It is emphasized here that no such ≤25 nm diameter channels were observed in SEM-micrographs of the crack-bound islands, but they may be too small to detect.

Unfortunately, it is difficult to judge from the microstructure whether the dissolved material actually precipitated in the intragranular micro-cracks or whether it was transported to grain boundaries parallel to Z. However, as most of the micro-cracks appear to be open (at least at NPT conditions after deformation) it seems most likely that the material precipitated in the cracks, so that a'≈a. In that case a SIC-model with an effective DIC grain-boundary width of ≤1 nm (i.e., ~1-3 molecular diameters wide) shows good fit with the mechanical data (Fig. 6.12).

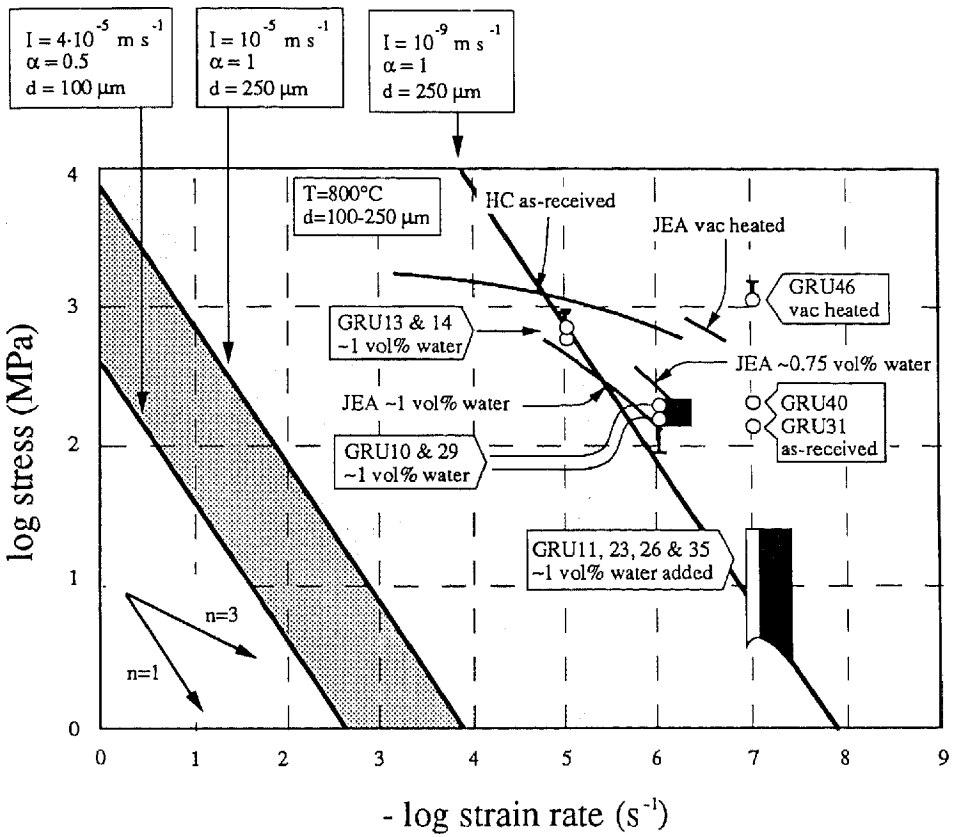

Fig. 6.9 *Log stress versus minus-log strain rate diagram comparing the interface-controlled SPC law (equation iv in table 6.1) with the mechanical behaviour of the samples deformed with ~0.4 wt% added water at 800°C, ~1200 MPa, and 10^{-6} and 10^{-7} s^{-1} (black rectangles). Strain rates at constant stress predicted by equation (iv) are many orders of magnitude too fast to explain the mechanical data obtained in the present experiments (darkest dotted area). Even when the interface velocity (I) is assumed to be as low as that measured by Gratz et al. (1990) at 250°C and 1 atmosphere, the predicted strain rate at constant stress is too fast.*

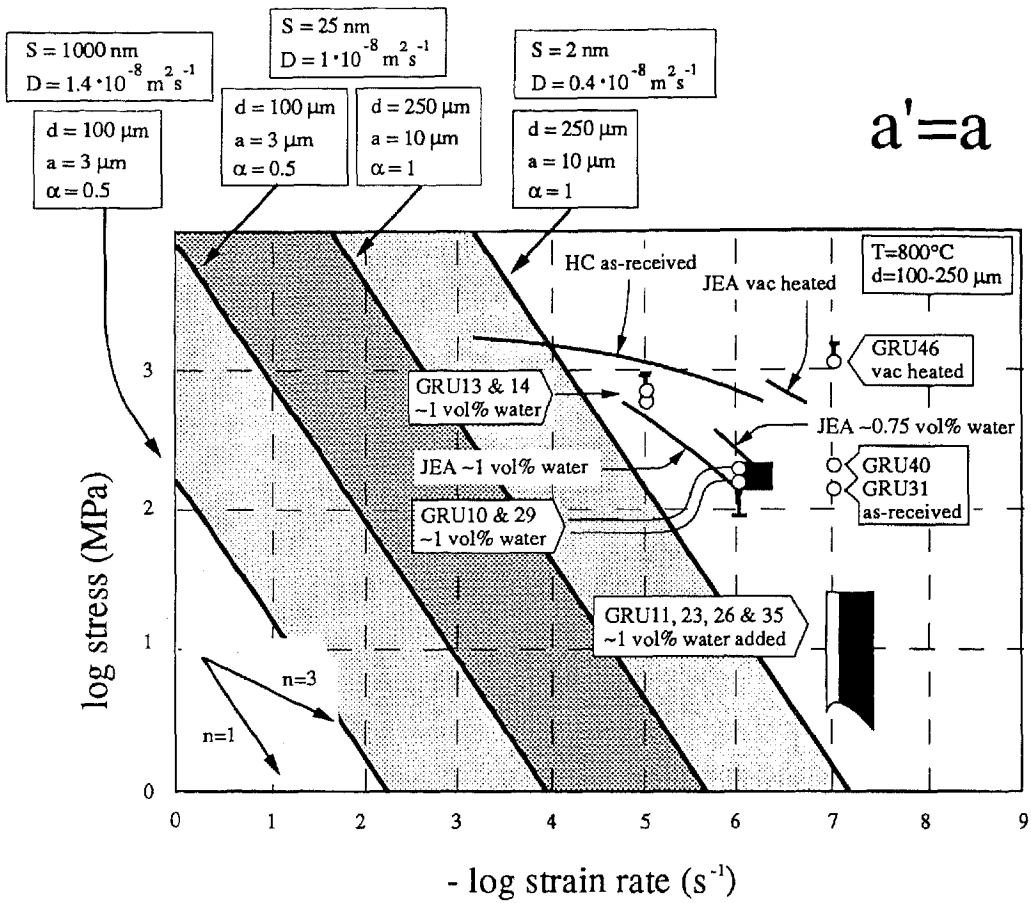

Fig. 6.10 *Log stress versus minus-log strain rate diagram comparing the SIC-model with fine-scale dynamically stable island-channel (DIC) structure at the larger, crack-bound island-island contacts (equation v table 6.1 with a'=a) for S=2-1000 nm. Strain rates at constant stress predicted for a'=a are at least one order of magnitude too fast, even for the smallest channel size (2 nm).*

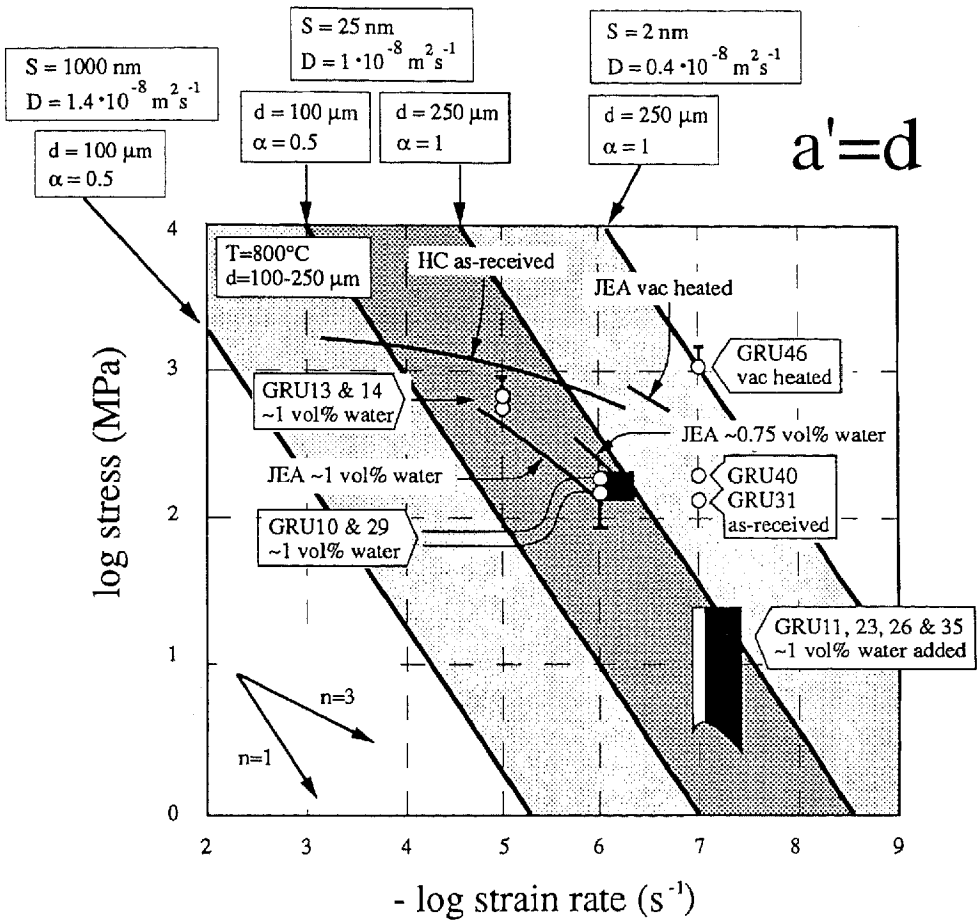

Fig. 6.11 *As Fig. 6.10 but now a'=d, i.e., no precipitation occurred in the cracks, but all dissolved material is transported to the grain boundaries parallel to Z. There is good agreement between the SIC-model and the experimental data when S≈25 nm. Good fit is also obtained for S≤25 nm with a<a'<d, i.e., when some material is precipitated in the cracks and some material is transported to grain boundaries parallel to Z.*

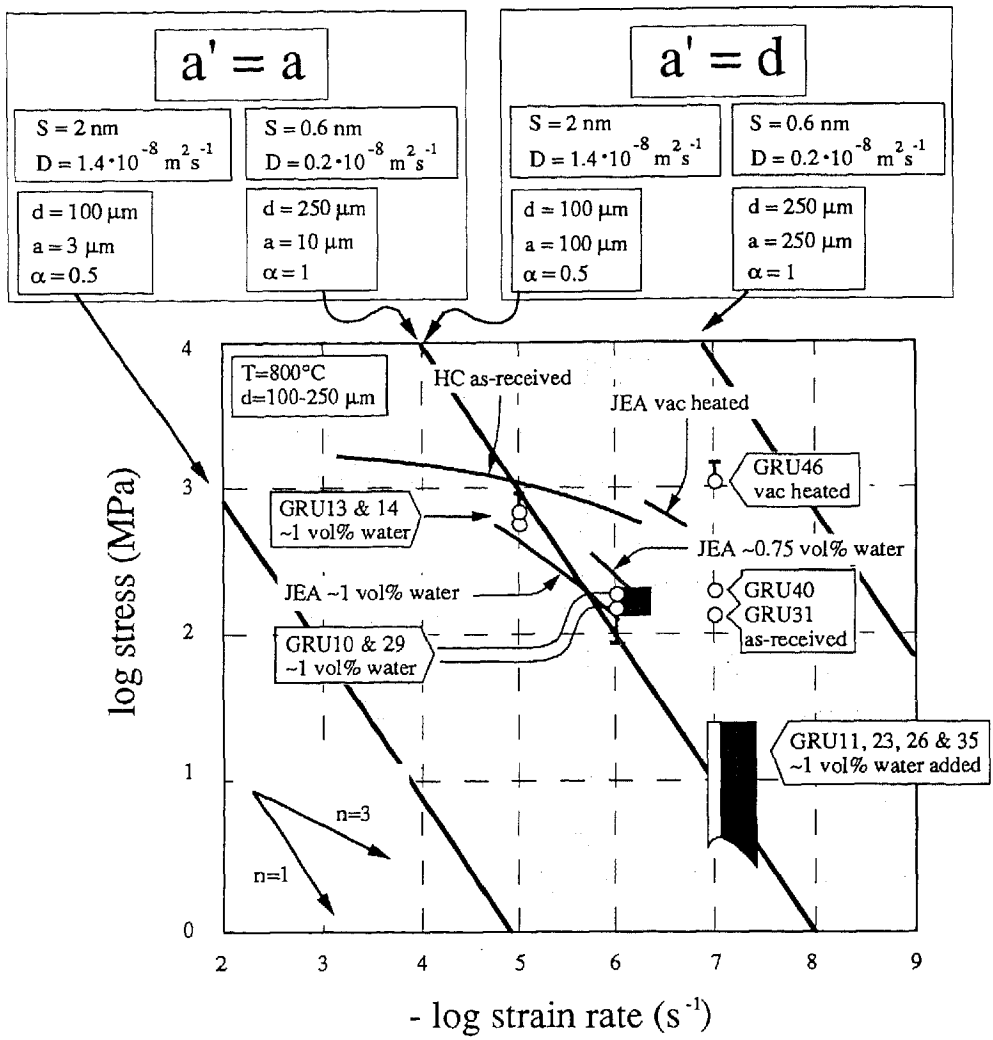

Fig. 6.12 *As Fig. 6.10 & 6.11 but now for S=0.6-2 nm and both a'=a and a'=d. In this case, the grain boundary diffusivity may be 0.5-1 times the bulk diffusivity. There is good agreement between the SIC-model and the experimental data between the two extremes: a'=a with S=0.6, and a'=d with S=2 nm.*

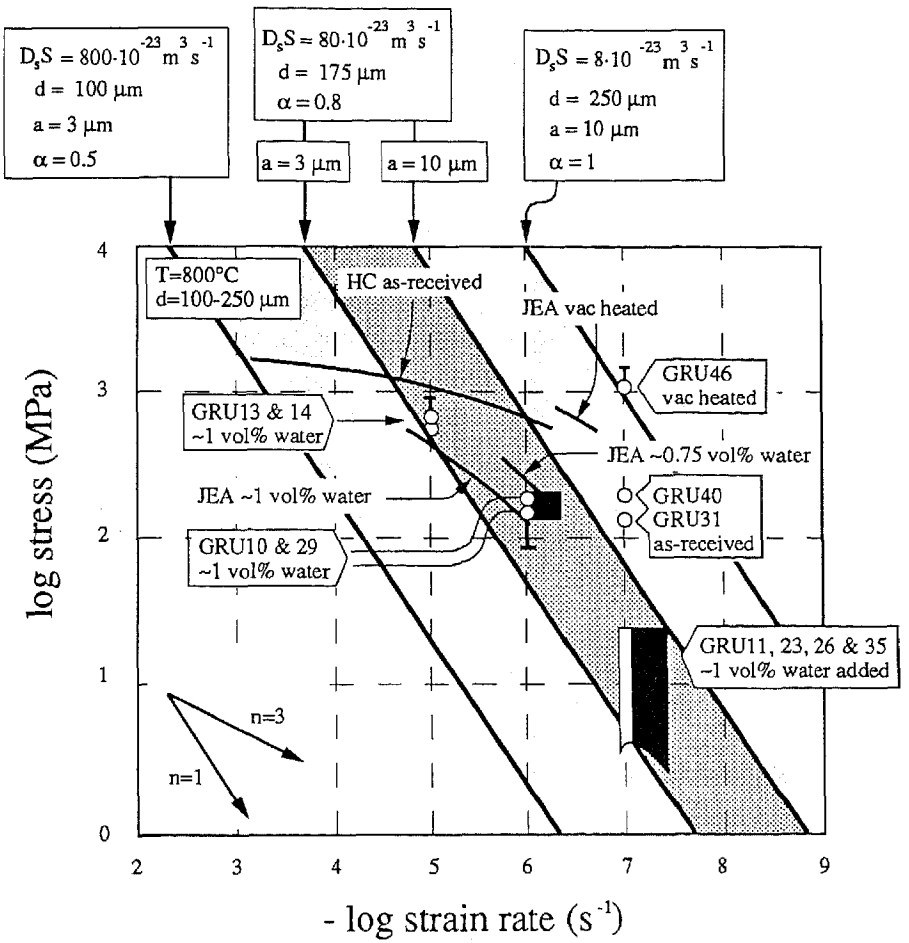

Fig. 6.13 *Comparison of mechanical data with predictions based on the SIC-model, in which the rate of deformation is controlled by water-enhanced crack-bound solid-state diffusion through the grain boundary crystal lattice at the island-island contacts (as depicted in Fig. 6.5) and following experimental diffusion data of Farver & Yund (1991b), with further mass transport through grain boundary channels located where micro-cracks intersect the grain boundary or direct precipitation in the cracks. There is good agreement between the mechanical data and the predictions. Darkest spotted area indicates most likely conditions.*

This is much like the DIC-structure on the molecular scale proposed by Raj (1982).

(ii) The crack-bound island-island contacts of the SIC-model are solid, and diffusion on the crack-bound islands occurred through the solid-state, with further transport through the liquid-filled crack-bound channels and cracks. Material is precipitated either in the cracks or at grain boundaries parallel to Z. Good fit is obtained when applying water-assisted solid-state grain boundary diffusion data of Farver & Yund (1991b). However, the way in which water would promote the solid-state grain boundary diffusion rate in quartz is not yet understood.

It cannot be excluded that possibilities (i) and (ii) are in fact similar processes, i.e., that water-enhanced solid-state grain boundary diffusion such as reported by Farver & Yund (1991b) was in fact diffusion through a 1-3 molecules thick DIC-structure. They reported that their grain boundaries were physically ≤1 nm thick.

6.5 CONCLUSIONS

The microstructure and grain boundaries seen in quartzites deformed experimentally at T=800°C, $P_c \approx 1200$ MPa, $\dot{\varepsilon} \leq 10^{-6}$ s^{-1} and with ~0.4 wt% added water (chapter 3) are most consistent with a static island-crack (SIC) grain boundary model, i.e., a grain boundary consisting of μm-scale islands bounded by intragranular micro-cracks coupled with intergranular micro-cracking. Comparison of the mechanical data with SIC-models of solution-precipitation creep shows good fit when the rate of deformation is controlled by diffusional processes at the crack-bound island-island contacts. These may either (i) have a fine-scale dynamically stable island-channel structure with channels of ≤1 nm diameter when dissolved material is precipitated directly in the cracks, or ≤25 nm when material is not only precipitated in the cracks but transported to grain boundaries parallel to Z, *or* (ii) the crack-bound island-island contacts may be solid, with mass transfer occurring by water-assisted solid-state grain boundary diffusion (following diffusion data of Farver & Yund 1991b).

The present results support the conclusions given in chapters 3, 4, and 5, that the water-weakening effect seen in experiments on quartzite at T=800°C, $P_c \approx 1200$ MPa, $\dot{\varepsilon} \leq 10^{-6}$ s^{-1}, with ~0.4 wt% added water, are caused by solution-precipitation processes plus micro-cracking rather than by an intracrystalline, dislocation-plastic effect. The results further show that the grain boundary structure, determined by the micro-crack spacing, exerts a very significant role in the mechanical behaviour of quartz rocks.

Chapter 7

GENERAL CONCLUSIONS AND SUGGESTIONS FOR FURTHER WORK

The purpose of this chapter is to assemble the information presented in the preceding chapters in order to draw general conclusions and to assess the geological implications of the results obtained. Finally, questions left unanswered are identified and suggestions are made for further research.

7.1 ASSESSMENT OF PREVIOUS WORK

From the literature survey presented in chapter 2, it is evident that crystal-plastic deformation is widely accepted as the most important ductile deformation mechanism in quartz rocks in the continental crust. This view is based largely on the abundance of optical deformation and TEM microstructures which are known to be associated with crystal-plastic deformation in metals (such as undulatory extinction, subgrains, recrystallized grains, core-and-mantle structures), and the widespread occurrence of crystallographic preferred orientations (CPO's). Experiments have shown, that such 'crystal-plastic' deformation microstructures and CPO's can only be produced in quartz deformed *'wet'*, i.e., in the presence of small amounts of (added) water. Furthermore, 'wet' quartz is ductile, and can be easily deformed. In contrast, 'dry' quartz is exceedingly strong, and when deformed experimentally, rather unnatural lamellar deformation features are formed consisting of glass. Extrapolating laboratory data to natural conditions, water has therefore been assumed to be responsible for ductile deformation of the continental crust, by facilitating intracrystalline crystal-plastic deformation processes, i.e., glide, climb, and multiplication of dislocations. The mechanism by which this water-weakening occurs is poorly understood. Indeed, it has been a source of controversy for almost 30 years with the literature remaining full of awkward inconsistencies.

However, in chapter 2 it was concluded, however, that the above 'crystal-plastic' deformation microstructures and CPO's should not be viewed as definitively diagnostic for crystal-plastic deformation. Other water-assisted deformation processes, such as solution-precipitation transfer and micro-cracking plus healing, may also be responsible for the observed microstructures, at least in some cases. This implies that the assumed preponderance of crystal-plastic deformation mechanisms in quartz rocks in the continental crust is, in principle, open to discussion. In addition, it was concluded, that the *experimental* evidence that crystal-plastic mechanisms are capable of producing large amounts of ductile strain in quartz and that water-weakening occurs by facilitating dislocation glide plus climb, is also open to discussion, since in most reports this evidence is also based on the above-mentioned 'crystal-plastic' micro-

structures and CPO's. In particular, it was shown that the following experimental observations are inconsistent with a dislocation-plastic origin for the water-weakening effect:

(i) Optical 'crystal-plastic' deformation microstructures and an old-grain CPO characteristic of experimentally deformed, water-added, natural quartzite suggest that ductile deformation and water-weakening occurred by crystal-plastic mechanisms, whereas the mechanical data (stress exponent for power law creep around 1, Wang et al. 1991 pers. comm., Jaoul et al. 1981) are inconsistent with crystal-plastic deformation, and point towards diffusional mechanisms being responsible for the deformation.

(ii) Natural quartzite with a grain size of ~200 μm can be ductilely deformed within periods of less than 2 hours, whereas diffusion experiments on single crystals have shown that water can only be diffused into quartz at a rate of <1 to 10 μm per day. This is much too slow to explain the relatively rapid weakening effect in terms of a 'classical' diffusion plus dislocation-plastic intracrystalline weakening effect.

This thesis has aimed to investigate these observations further in order to understand how water renders natural quartzite both weak and ductile.

7.2 DEFORMATION BEHAVIOUR OF QUARTZITE IN THE PRESENT EXPERIMENTS

The present investigation has focussed on experiments on natural quartzite with an average grain size of 150 to 250 μm, deformed with different water contents in a Griggs-type solid-medium apparatus at $P_c \approx 1200$ MPa, T=800°C, and strain rates ($\dot{\varepsilon}$) of 10^{-5}, 10^{-6}, and 10^{-7} s^{-1}.

In summary, the experiments showed that at constant strain rate the strength of the quartzite decreased with increasing water content. At $\dot{\varepsilon} \approx 10^{-7}$ s^{-1}, 'dry' samples (<200 ppm H/Si) flowed at a differential stress of ~1220 Mpa, 'as-received' samples (~30000 ppm H/Si) at 140-225 Mpa, and 'wet' samples (~70000 ppm H/Si, i.e., with ~0.4 wt% added water) at <25 Mpa. The strength of the water-added material was also strain rate dependent. With ~0.4 wt% added water, samples deformed at 10^{-5} flowed at a differential stress of 590-610 MPa, those deformed at 10^{-6} s^{-1} yielded at 150-190 MPa, and those at 10^{-7} s^{-1} at <25 MPa. The corresponding stress exponent assuming power law creep was ≤1.3.

Broadly speaking, two classes of optical deformation microstructures were recognized in the deformed samples.

(i) At high differential stress, high strain rate, and low water content, samples showed abundant subbasal deformation lamellae, with undulatory extinction visible in bands associated with bending of the lamellae.

(ii) At low differential stress, low strain rate (≤10^{-6} s^{-1}), and high water content (~0.4 wt% water added), the samples showed abundant small new grains. Very few

deformation lamellae developed under these conditions, and only in the relict old grains. The small new grains had subeuhedral crystal shapes and occurred in axially aligned, intra- or intergranular arrays, characterized by inclusions, voids and channel structures which were presumably water filled during the experiment. The new grains were thus interpreted to be precipitated out of solution in axially aligned intragranular, transgranular, and grain boundary micro-cracks. Old-grain boundaries oriented parallel to the shortening direction (Z) showed subeuhedral overgrowth features, conspicuously absent on grain boundaries oriented perpendicular to Z. Abundant grain-scale pits and indentations developed in the originally polished surface (oriented perpendicular to Z) of a single crystal spacer added in line with the quartzite sample in one experiment provided evidence for dissolution on Z-normal faces. No significant old-grain CPO was developed in the water-added samples, even at 46% finite strain, whereas the grains were significantly flattened. This was also found true for a sample (GRU29), deformed 'wet' to 40% finite strain at intermediate strain rate. Though this sample contained large amounts of deformation lamellae, the absence of CPO indicates that crystal-plastic deformation processes were insignificant.

Aside from the microstructural and CPO work reported in chapters 3 and 4, FTIR measurements were also performed (chapter 5). FTIR measurements of intragranular water contents showed that on average, and within the resolution of the spectroscope (100-500 pm H/Si), the water content of the starting material was similar to that of the 'wet' and 'as-received' deformed material. This indicates that the water-weakening and ductile deformation seen in samples deformed at T=800°C, P_c≈1200 MPa, and $\dot{\varepsilon}=10^{-7}$ s^{-1}, occurred without diffusion of significant amounts of water into the grains. This is difficult to reconcile with an intracrystalline water-weakening mechanism, since this would require diffusion of easily measurable amounts of water into the grains.

Drawing together the above information, it was concluded that the mechanical data (chapter 3), the optical deformation microstructures (chapter 3), the absence of significant original-grain CPO's after 40-46% strain (chapter 4), and the lack of measurable diffusion of water into, or out of the original grains during 'wet' or 'as-received' deformation (chapter 5), are all best explained by a coupled solution-precipitation creep (SPC) and micro-cracking mechanism. This is supported by a comparison of the microstructural observations and mechanical data with SPC-models (chapter 6). Good agreement was obtained with a model which assumes that grain boundaries oriented perpendicular to Z consist of a static μm-scale island-crack structure (stresses across the boundary being supported by the micro-crack bound island-island contacts) and that the rate of deformation is governed by diffusional processes within the island-island contacts. This diffusion may have occurred either (i) in the solid-state, by water-assisted solid-state grain boundary diffusion (Coble creep) following grain boundary diffusion data of Farver & Yund (1991b), or (ii) through a fine-scale fluid-filled, dynamically stable island-channel structure within the crack-bound island contacts, with channels of ≤1-25 nm diameter.

7.3 CPO'S IN QUARTZ ROCKS: MEASUREMENT ERRORS AND IMPLICATIONS

In the present experiments, no significant old-grain CPO's were developed at T=800°C, P_c≈1200 Mpa, strain rates of 10^{-6} and 10^{-7} s^{-1} and with 0.4 wt% added water, even in samples deformed to 40-46% strain. However, Tullis et al. (1973), Dell'Angelo & Tullis (1986), and Den Brok & Spiers (1991) reported quite strong old-grain CPO's developed in quartzites deformed under broadly similar conditions. Notably, these old-grain CPO's provide the strongest experimental support cited in the literature for the hypothesis that dislocation-plastic processes are dominant in experiments on quartz rocks.

In chapter 4 of this thesis, it was shown that errors in the optical measurement technique (artificial biassing by improper grain selection such as reported earlier by Starkey & Sutherland 1978) caused the difference between the present results (no CPO) and those of Den Brok & Spiers (1991; quite strong CPO). The original-grain CPO's measured by Tullis et al. (1973) and Dell'Angelo & Tullis (1986) were also improperly measured (Dell'Angelo & Tullis 1986). Therefore, these original-grain CPO's may also be very weak or non-existent, just as in the present study. If so, then the principal piece of *experimental* evidence that dislocation plastic processes dominate the ductile deformation of quartz is completely absent. As a corollary, experimental evidence for a correlation between CPO and crystal-plastic deformation in quartz is also removed. Clearly then, great care is needed both in the measurement and interpretation of CPO's developed in deformed quartz rocks. In cases where CPO's are reliably measured, it should be recognized that while consistent with crystal-plastic mechanisms they can also be related to solution-precipitation and recrystallization processes (e.g., Green et al. 1970, Hobbs 1968, Cox & Etheridge 1983, Power & Tullis 1989).

7.4 DIAGNOSTIC POTENTIAL OF QUARTZ MICROSTRUCTURES

The present experiments have shown that SPC and micro-cracking can produce optical deformation microstructures which are very similar to those commonly attributed to crystal-plastic deformation. In chapter 3, a few examples were shown of fractured grains where slight rotation of the resulting fragments, together with the irregularity of the presumably corroded fractures and local growth of small new grains, give the impression of subgrain development and rotation, recrystallization, and undulatory extinction. The same is illustrated more spectacularly in control experiments performed on single natural crystals of quartz deformed with ~10 vol% added water at a strain rate of 10^{-6} s^{-1}, a temperature of 800°C, a pressure of ~1200 MPa to ~7% finite strain (sample GRU38; see table 3.1). The deformed sample contains an axially oriented zone consisting of axially elongated subgrains separated by irregularly and

partially healed fractures, and small numbers of sub-euhedral new grains (Fig. 7.1). The sample further contains numerous axial arrays of fluid inclusions. A 200 μm thick section (Fig. 7.2) cut parallel to the section shown in Fig. 7.1 but ~1 mm removed, illustrates more clearly that the elongated subgrains are separated by fractures, and that solution-precipitation processes occurred within the cracks to produce sub-euhedral overgrowth structures and irregularity of the crack walls. Here, the observed subgrains are actually slightly rotated, fractured blocks. These findings support the interpretation of such optical micro-structures in terms of cataclasis plus solution transfer processes, for example as reported by Sederholm (1895), Sander (1911), or Griggs & Bell (1938). The reader is also referred to Nyman et al. (1992) who recently re-interpreted core-and-mantle structures seen in deformed amphiboles, and previously thought to be indicative of crystal-plastic deformation, in terms of cataclasis.

It is concluded, that microscopic deformation features such as undulatory extinction, subgrains, recrystallized grains, and core-and-mantle structures seen in both naturally and experimentally deformed quartz rocks should be interpreted with caution. They should *not* be viewed as exclusively diagnostic of dislocation-plastic mechanisms (see also White 1973a). As in the present experiments, they may also originate by micro-cracking and solution transfer processes. In the authors view, several quartz tectonites classically believed to have deformed mainly by dislocation mechanisms, may in fact have deformed mainly by SPC plus micro-cracking. This is also in good agreement with characteristics of many shear zones, including, for example, the abundance of fluid inclusions and/or fluid inclusion trails (healed micro-cracks) (e.g., Kronenberg et al. 1990), the abundance of new minerals in the deformed rocks and a different chemistry compared to the host, indicative of mass transfer (e.g., Beach 1976, Kerrich et al. 1980, Crevola 1987, Bell & Cuff 1989, Kano 1991), the abundance of pressure shadows (indicative of solution transfer), and the abundance of quartz-filled fractures (e.g., De Roo & Williams 1990).

Note further, that ribbon quartzes, common features in many shear zones, often look like growth fibres (e.g., fig. 10 of Simpson 1983). The mylonites in that case actually resemble slicken sides or fibrous shear veins. In respect of this, it is illustrative to compare, for example, the microstructure observed in fibrous veins (e.g., fig. 2b & c of De Roo 1989) with that observed in mylonites (e.g., in fig. 2i of Schmid & Casey (1986). Also fibrous intragranular microstructures such as depicted by Cox & Etheridge (1989, their fig 5a & b) resemble 'crystal-plastic' microstructures. Many shear zones indeed have 'pull-apart' geometries, indicative of addition of material (see, e.g., detailed maps by Mitra 1979, his fig. 15; or fig. 1a by Phillips 1965).

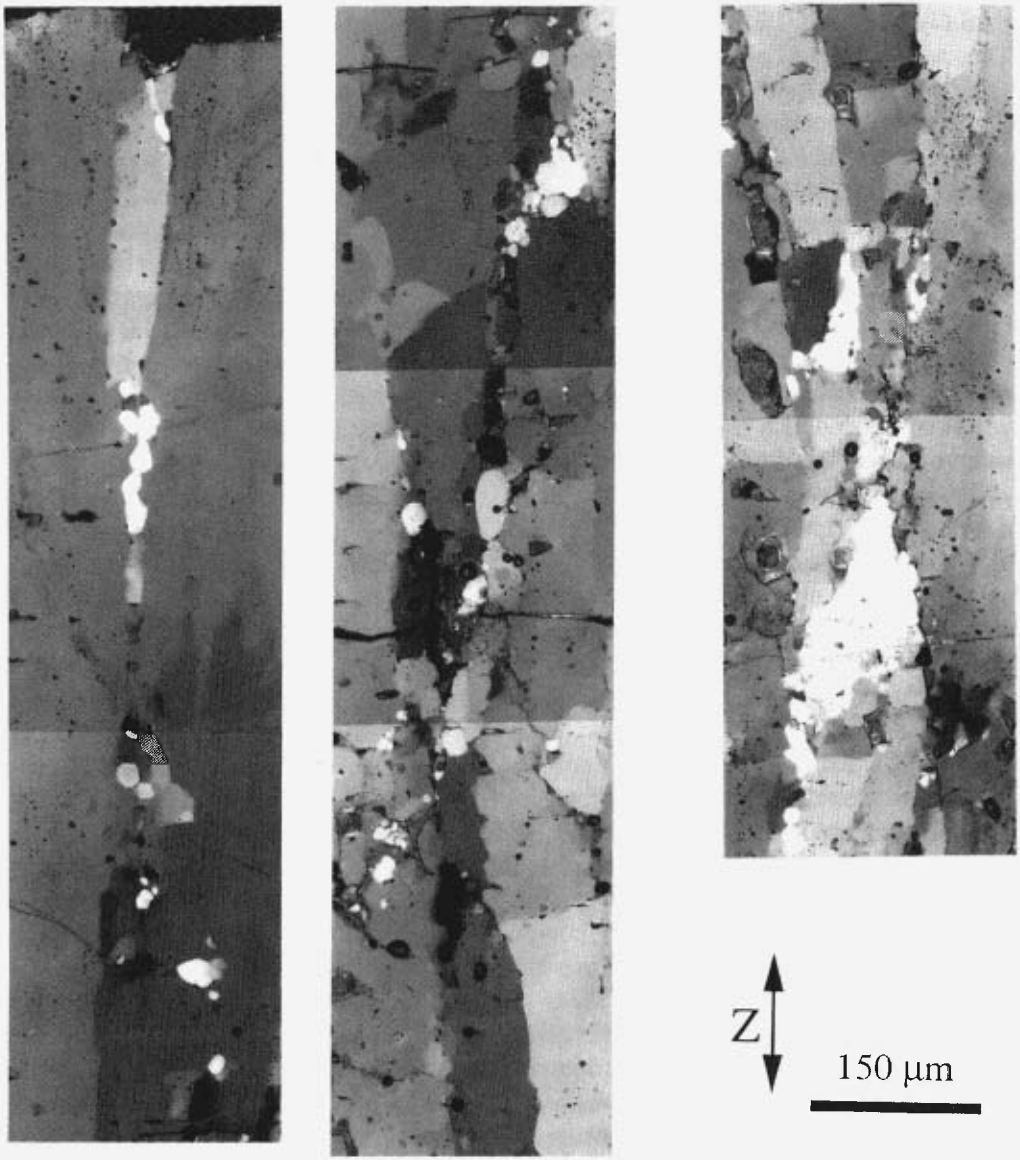

Fig. 7.1 *Optical micrograph of natural single crystal (GRU38), experimentally deformed at T=800°C, P_c=~1200 MPa, $\dot{\varepsilon}=10^{-6}$ s^{-1}, ~7% strain, and with ~10 vol% added water, showing axial zone of axially elongated subgrains plus smaller equidimensional subgrains, separated by partially healed fractures. Locally, fractures are healed perfectly, leaving behind no trace of fluid inclusion trails. Open fractures are very irregular as a consequence of dissolution-precipitation processes, either by precipitation plus overgrowth of material dissolved elsewhere (e.g., at the sample ends) or by local solution-redeposition processes. (Crossed polars.)*

Fig. 7.2 *(Explanation see next page)*

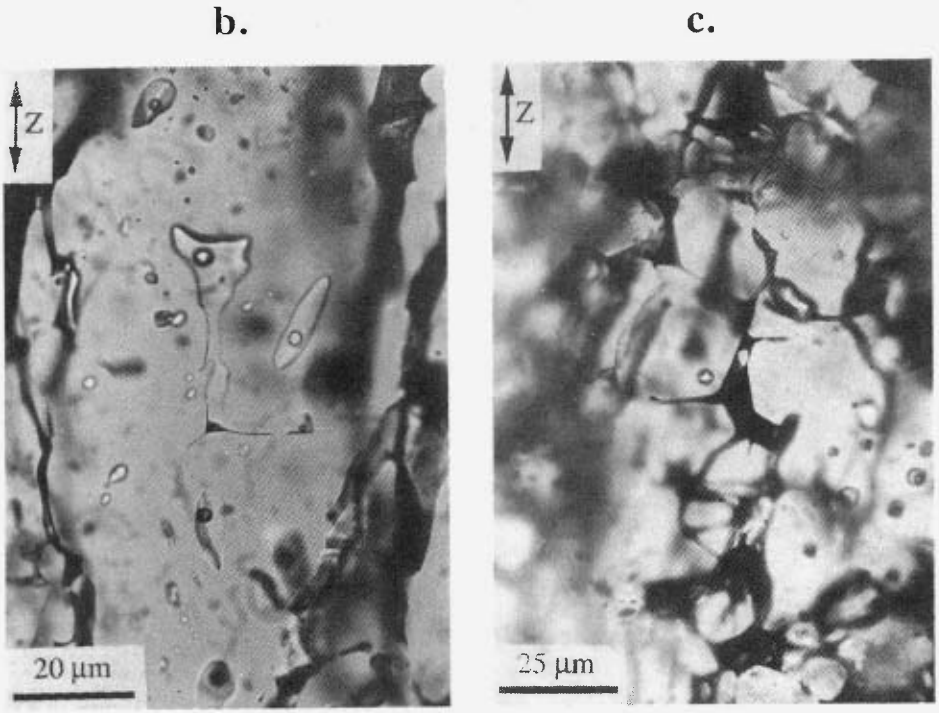

Fig. 7.2 *Same sample as in Fig. 7.1 (section is parallel to Fig. 7.1) but now ~200 µm thick. Due to the thickness of the section, it is clearer that the subgrains are really fractured and slightly rotated blocks. (a) Upper half of micrograph shows open fractures parallel to the shortening direction (Z) with crystal-growth features visible at crack walls. Lower part is healed and illustrates that healing often leaves behind both planar as well as irregular arrays of fluid inclusions. (b) & (c) Details of partially healed fractures showing evidence for solution-precipitation processes being responsible for irregularity of the crack walls.*

7.5 IMPLICATIONS OF RESULTS FOR CRUSTAL STRENGTH

Strength profiles of the continental crust have been calculated by various authors by extrapolating the previous existing experimental data and assuming that the underlying mechanisms are crystal-plastic ones (e.g., Kirby 1985, Carter & Tsenn 1987, Ord & Hobbs 1989). It is interesting to consider whether water-assisted diffusional creep plus micro-cracking mechanisms, as seen in present experiments are expected to occur under (realistic) crustal conditions (especially since this has been shown to be broadly consistent with commonly observed natural optical microstructures) and whether the present data would modify previously predicted strength profiles.

Unfortunately, extrapolation of the present results to natural conditions is problematic, because the effects of pressure, temperature, and strain rate have not been systematically investigated, since the differential stress could not be measured accurately in the Griggs machine, and because the dependence of micro-crack spacing on such variables is not understood. However, a rough attempt at estimating the effect of SPC in nature can be made using the diffusion controlled SIC model found to match the present experiments best (chapter 6, equation vi in table 6.1). This model assumes water-assisted solid state grain boundary diffusion occurring at the crack-bound island-island contacts (refer section 6.2.4). It can be used to estimate upper bound flow stresses at constant strain rate and constant grain size by assuming that the island size (a) is less or equal to the grain size (d), making use of Farver & Yund's (1991b) determination of the water-assisted, solid-state grain boundary diffusion properties to estimate the absolute rate and its temperature dependence. No corrections were made for the effect of pressure on the grain boundary diffusion rate. Assuming that an increase in the pressure causes an increase of the grain boundary diffusivity in the same way as it does with the lattice diffusion (Farver & Yund 1991a), at 800°C, an increase from 100 to 1000 MPa would cause an increase by a factor ~10 at most. At lower temperatures, the pressure effect is significantly less, e.g., at 600°C a factor of ~5. Hence, by disregarding the pressure effect, upper-bound stresses are obtained. The strength profiles thus obtained for strain rates of 10^{-12} s^{-1} (possibly equivalent to localized deformation rates in shear zones, cf. Carter & Tsenn 1987) and 10^{-14} s^{-1} (average bulk geological strain rate) for temperature gradients of 20 and 30°C per kilometer and grain sizes of 10 and 100 μm are given in Fig. 7.3. Brittle deformation is included assuming Byerlee's relation (Byerlee 1978; see, e.g., Ord & Hobbs 1989), and assuming *hydrostatic* pore fluid pressure. The depth in the continental crust at which the fluid pressure becomes approximately equal to the lithostatic pressure varies between 6 and 10 km, as indicated by deep drilling data and theoretical considerations (Norris & Henley 1976; Sibson 1983; Kozlovsky 1984, Walther & Wood 1986; Fyfe et al. 1978; Connolly & Thompson 1989). Consequently, at depths <6-10 km Byerlee's relation is expected to apply well, whereas below the transition, it predicts maximum stresses. The results show the following:

(i) SPC is possible in the continental crust under realistic conditions, i.e., temperature gradient 20-30°C/km, strain rates of 10^{-12}-10^{-14} s^{-1}, grain sizes in the range 10-100 μm, and differential stresses up to 400 MPa, as long as water is present.

(ii) At constant grain size, constant grain boundary structure, constant temperature gradient, constant water content, and constant strain rate, the strength profile has a shape similar to the profiles based on crystal-plastic flow laws reported by most others (cf. Kirby 1985, Carter & Tsenn 1987, Ord & Hobbs 1989), and likewise predicts a brittle-ductile transition between 5 and 25 km depth and very low stresses (<1 MPa) only several kilometers below the brittle-ductile transition. The similarity to previous profiles is due to the fact that earlier work is based on the extrapolation of flow laws based on experiments similar to those described in the present study (chapter 3) but interpreted to be due to crystal-plastic processes (e.g., flow law by Jaoul et al. 1984).

(iii) The depth at which the brittle-ductile transition occurs, or at which SPC is possible, depends not only on the temperature gradient, the strain rate, and the presence of water, but also on the grain size and the grain boundary structure (crack/channel spacing). The dependence of the strength on the last two parameters is so strong, that a single, well-constrained profile cannot be drawn since both the grain size and particularly the grain boundary structure during deformation are unknown in most cases and probably vary strongly in space and time. However, on the basis of the present results, it can be inferred that mechanically very weak, *or* very strong zones may occur in quartz rocks anywhere below 5 km, depending on spatial and temporal variations in the grain size and the grain boundary structure. For example, the strength of a coarse-grained quartz tectonite in the middle of the crust may be several hundreds of MPa's, while the strength of a fine-grained quartz mylonite at the same location may be less than 1 MPa. Hence, the present data and model lead to the expectation that the brittle-ductile transition and the base of the seismogenic zone will be 'smeared-out' over a substantial depth range (e.g., 5-25 km) in response of active tectonism. Thus, for example, the SPC-models predict that earthquakes could easily be generated by brittle deformation of relatively coarse-grained quartz rocks in the middle crust (if fluid pressures are maintained high) while SPC plus stable micro-cracking processes may occur in fine-grained quartz rocks at the same depth. Clearly, the behaviour occurring at any particular depth can be expected to be severely influenced by time-dependent grain growth, healing and/or micro-cracking effects.

It is concluded that whereas SPC plus micro-cracking, as seen in the present experiments, can easily occur at most crustal conditions and can explain most of the observed deformation microstructures, reliable strength profiles are location specific and cannot yet be ideally constructed. Further study of the mechanical behaviour in experiments and of natural deformation microstructures, also focussing on the inter-play of grain growth and micro-cracking, and on grain boundary structure, is required for that.

7.6 UNANSWERED QUESTIONS AND SUGGESTIONS FOR FURTHER WORK

Whereas some questions regarding the water-weakening effects seen in experiments on natural quartzite have been answered, many others are left unanswered and require further experimental, theoretical, microstructural, and field work.

(i) First of all, it is desirable to repeat the experiments reported in this thesis but with different starting materials, with different grain sizes, at different pressures, temperatures, water-contents, and preferably in a deformation apparatus in which the stresses can be measured accurately, and the water pressure controlled (e.g. gas-confined 10 kb Paterson-type apparatus). This should be done not only in order to

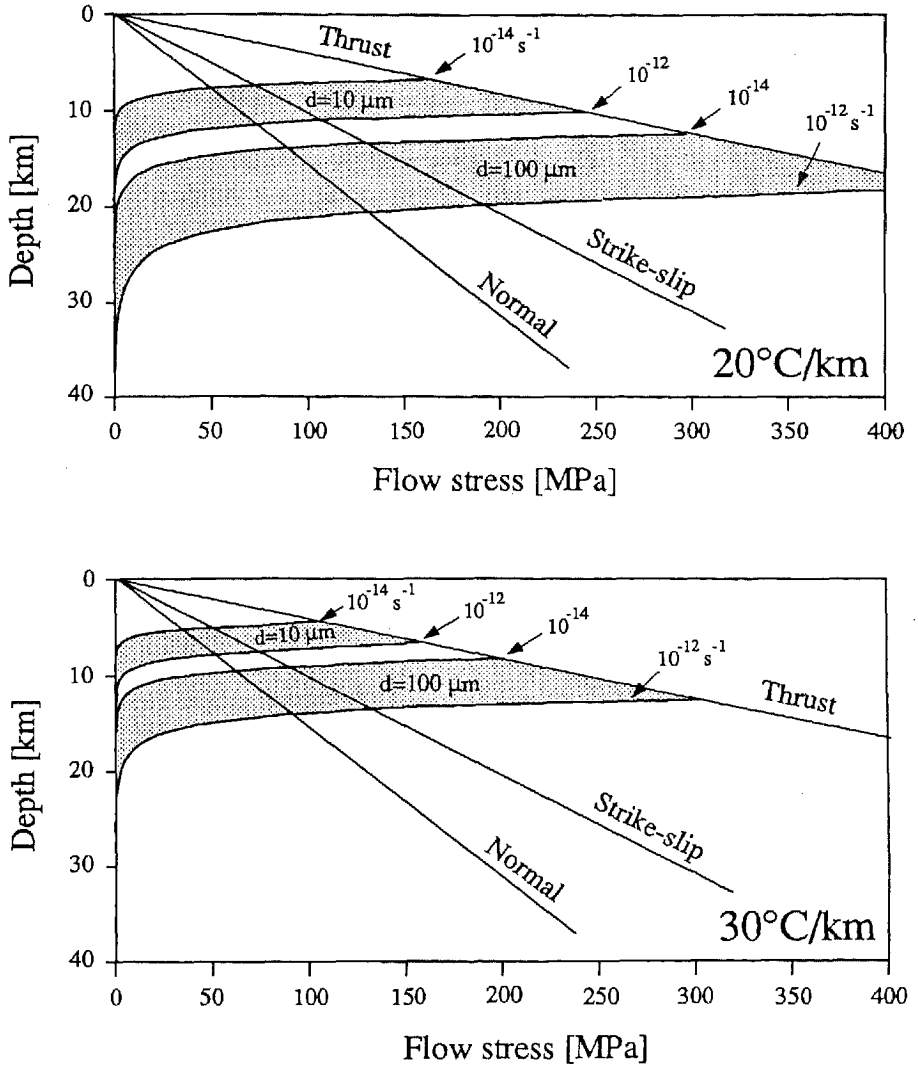

Fig. 7.3 *Flow stress (MPa) versus depth (km) predicted for the diffusion-controlled SIC-model (equation vi table 6.1; chapter 6) assuming water-assisted solid-state diffusion at the crack-bound island-island contacts, for two different grain sizes (10 and 100 μm), for temperature gradients of 20 and 30° per kilometer, and for strain rates of 10^{-12} and 10^{-14} s^{-1}. In all cases, the crack-bound island size (a) was assumed to be less or equal to the grain size (d) so that the strength profiles are upper bound. Stresses predicted for thrust, strike-slip, and normal faulting are based on Byerlee's (1978) equation assuming the pore fluid pressure to be determined by the hydrostatic load.*

verify the present experiments, but to improve understanding of the effect of the above parameters on the water-assisted diffusional processes, and the microphysical processes themselves. It is also very important to study in detail the grain boundary structure under the different conditions, since this is predicted to strongly influence the mechanical behaviour. Similarly the effect of grain growth on mechanical behaviour should be investigated thoroughly (cf. Rutter et al. on calcite).

(ii) Very little TEM-work has been done in the present study, mainly because the experiments were not well-suited to obtain conclusive answers in this way. Certainly, dislocation substructures have been and will be found (e.g. Ardell et al. 1973) but may be very difficult to interpret. Are they the result of small amounts of dislocation-plastic deformation as generally accepted, or can they also be the result of crystal growth processes and/or stable micro-cracking? Experiments should be designed in such a way that unambiguous answers can be obtained with TEM to these questions. This could be done, for example, via a TEM study of dislocation structures resulting from high P-T crack-healing experiments in samples hydrostatically loaded only (i.e. without deformation), to study the influence of crystal growth processes on the development of dislocation structures (cf. low P-T work of McLaren & Phakey 1965, Carstens 1969, or Grant & White 1978 on natural, and Bakker 1992 on experimental material). Alternatively, experimentally produced syntaxial overgrowth structures on elastically stressed quartz could be investigated using TEM to see what dislocation structures would actually result, again at high P-T conditions. In addition, TEM-work could be done on samples deformed exclusively by stable micro-cracking (i.e. without bulk crystal-plastic deformation) or solution-precipitation processes, to study the effect of micro-cracking on the dislocation structures. The significance of dislocation substructures in quartz could be substantially clarified by such experiments.

(iii) There is convincing evidence in the literature that water affects the dislocation motion in 'wet' synthetic single crystals (e.g., McLaren et al. 1989) and in natural polycrystals (e.g., Tullis & Yund 1989), but how? This question is still not resolved and basic experiments are needed. One way to improve our understanding would be to anneal and deform single crystals of quartz with a well-defined starting dislocation-microstructure in the presence of added water and study the change in dislocation structure. Synthetic quartz would be a good starting material. The dislocation structure of this material commonly consists of regular arrays of long and straight growth dislocations. If deformed carefully, so that the effects of deformation, recovery, and recrystallization can be separated, then one could possibly find out whether water would actually promote dislocation glide, or climb, and what kind of substructures would develop by these processes.

(iv) The origin of deformation lamellae both in experiments and nature remains enigmatic, as well as how water promotes their development. Are the lamellae Brazil twins, or crystallographically controlled shear fractures? Does water promote their propagation by stress corrosion cracking? Why are the lamellae *sub*-basal? Especially TEM work on experimentally produced deformation lamellae is required to answer these questions. A good start would be to repeat the experiments of Carter et al.

(1964) and Christie & Green (1964) and study in detail the deformation microstructures (optically and with TEM) as a function of temperature, pressure, and crystallographic orientation.

(v) Careful optical and TEM microstructural study of naturally deformed quartz rocks (especially mylonites) is needed to ascertain the dominant deformation mechanisms occurring in the nature, taking into account that the significance of the optical deformation microstructures such as undulatory extinction, subgrains, recrystallized grains, core & mantle structures and deformation lamellae, as well as the presence of CPO's, may be able to form by SPC plus micro-cracking in addition to dislocation mechanisms.

(vi) New theoretical and experimental work is needed to asses whether the CPO's seen in natural quartz tectonites can arise as a result of recystallization and/or oriented crystal growth during SPC.

Appendix A

EXPERIMENTAL APPARATUS AND METHODS

A.1 THE GRIGGS SOLID MEDIUM APPARATUS

The experiments described in this thesis were carried out using a Griggs solid medium deformation apparatus (or 'Griggs rig'; Fig. A.1 & A.2). The apparatus was originally developed by D.T. Griggs in the early sixties (Griggs 1967) and later modified together with J.D. Blacic (see Green et al. 1970). The version present in Utrecht is a Tullis modified variant (see e.g. Tullis & Tullis 1986) purchased from UCLA in 1978. It is capable of simultaneously generating pressures up to 1300 MPa and temperatures up to 1000°C, and allows cylindrical samples to be deformed at constant displacement rates in the range 0.001-10 mm hr^{-1}.

Unfortunately, considerable uncertainty is associated with the differential stress measurement in the Griggs type machine. The main reason for this is that the axial force on the sample is measured externally to the high pressure cell. Consequently, the strength of the solid confining medium, and the friction felt by the deformation piston introduces significant errors. Frictional forces acting on the confining pressure piston also introduce significant errors. Therefore, the rig is not well-suited to accurately measuring differential stresses. However, it is the only type of apparatus currently available in which sufficiently high pressures and temperatures can be achieved to deform quartz in a ductile manner, and much insight into deformation mechanisms may be gained from detailed microstructural analysis of the deformation microstructures.

A.1.1 The confining pressure system

The Griggs machine (Fig. A.1 & A.2) is basically a piston-cylinder apparatus utilizing a solid pressure medium such as rocksalt, calcite, talc, or copper. The sample assembly is embedded in the solid confining medium and the whole is contained by a compound pressure vessel (heigth 50.8 mm) made of an outer vessel of relatively soft steel and an inner vessel of hardened steel or other super hard alloy (e.g. hardened stainless steel, DIN Werkstoff Nr 1.4122, X35CrMo17, Rc 55). The inner vessel has an internal bore of 25.4 mm. Pressure is applied to the solid confining medium from the top via a hydraulic ram (Fig. A.3). Both the vessel and the solid confining medium are supported by a hardened steel base plate. The oil in the hydraulic ram system can be pressurized up to ~70 MPa using an Enerpac hand pump. The intensifying action of the hydraulic ram (Fig. A.3) transmits a maxi-

mum vertical stress of ~1300 MPa to the solid confining medium. A lead disk inserted between the piston and the solid confining medium ensures uniform transmission of pressure. The lead is prevented from extruding past the confining piston by a stainless steel (1.4122 Rc 28) packing ring (Fig. A.4 & A.5a).

The oil pressure is measured using both a 10000 psi (~70 MPa) pressure transducer (STD-type from BLH Electronics, Massachusetts USA), and a mechanical (dial) pressure gage. There is no servo control system nor any oil/gas accumulator attached to the pressure system. Consequently, variations in oil pressure due to diurnal temperature variations, variations in cooling capacity of the cooling system, and oil leaks, may cause a ±0.5 MPa variation in the oil pressure. This corresponds to ±10 MPa pressure variation in the solid confining medium. Note that the pressure vessel, the steel base plate, and the hydraulic ram are cooled by water to maintain integrety of the steel when the assembly is heated. To minimize the effect of the room temperature variations, a case made of isolation material was built around the rig (Fig. A.2) to thermally isolate it. Temperature within the case was controlled at 32±1°C using a thermostat to control a flow switch regulating the water flow of the cooling system.

In the Utrecht machine, compressed NaCl-powder (75-225 μm grain size) is used as the confining medium (Fig. A.4). This material has a very low strength at elevated temperatures, and even melts locallu at T≈800°C. Further, it can be pressed with ease into the shape required to fit into the vessel. The powder was compacted dry in special dies. Application of ~150 MPa yields a porosity of 3-4%. Friction between the salt confining medium and and the pressure vessel was minimized by inserting a 20 μm layer of teflon tape between them. Nonetheless, the friction was still very high. 20-30 kN was needed to force the assembly out of the vessel after an experiment. This level of friction implies that, at room temperature, the pressure in the solid medium deviates by at least 7% from the value indicated by the pressure of the oil. Note further that the magnitude of resulting pressure gradients within the solid pressure medium and the degree to which the pressure is truely hydrostatic, is not known. This is one of the major drawbacks of the Griggs machine.

A.1.2 Sample assembly and heating system

The sample assembly used in the Utrecht machine (Figs. A.4 & A.5) was designed by J.L. Urai (cf. Green & Borch 1989). The assembly is internally heated utilizing a cylindrical graphite resistance furnace (length 29.7 mm, inner diameter 12.85 mm, wall thickness 750 μm) which surrounds the sample (Fig. A.4 & A.5). A soft-fired pyrophyllite sleeve (700 μm thick) on each side isolates the furnace from the salt. Two copper rings (each 1 mm thick) on top of the furnace and the salt provide electrical contact between the top end of the furnace and the vessel. The

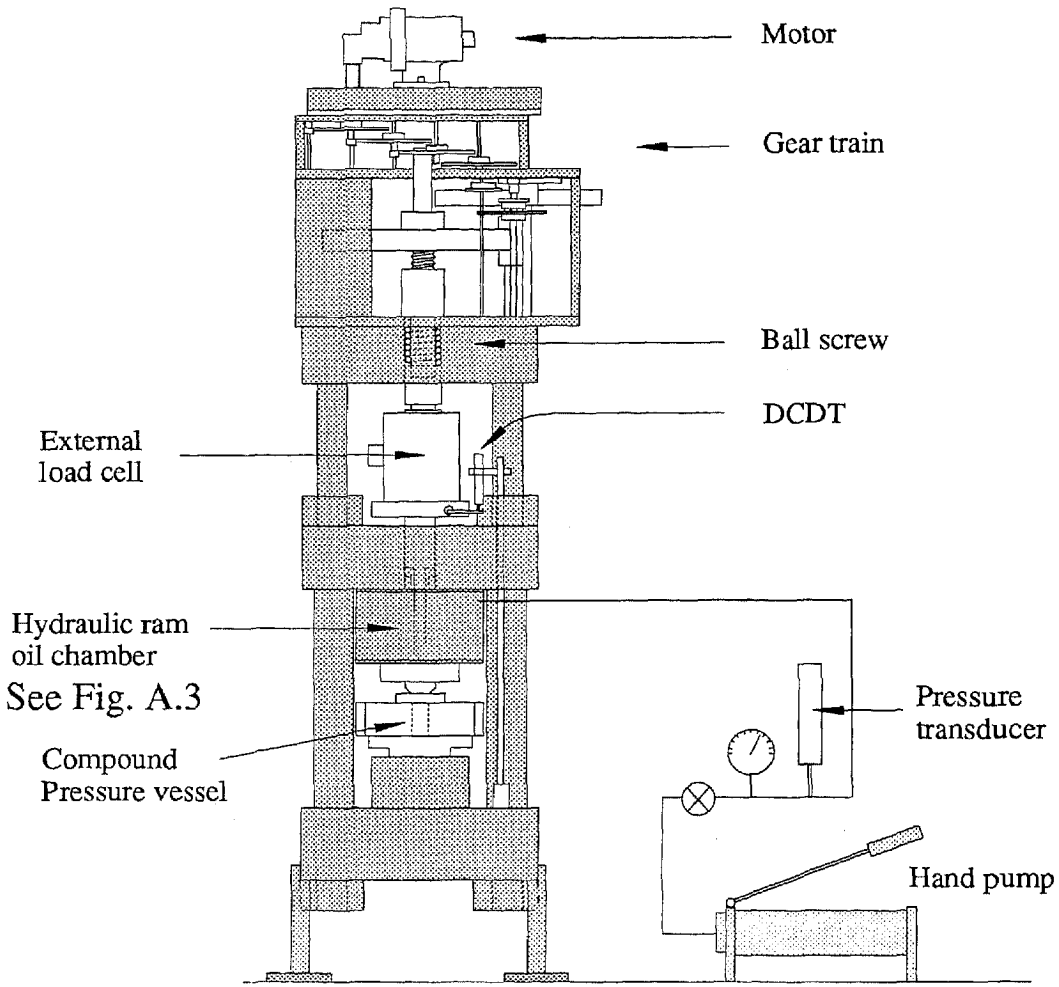

Fig. A.1 *Schematic drawing of the Tullis-modified Griggs machine (after Tullis & Tullis 1986).*

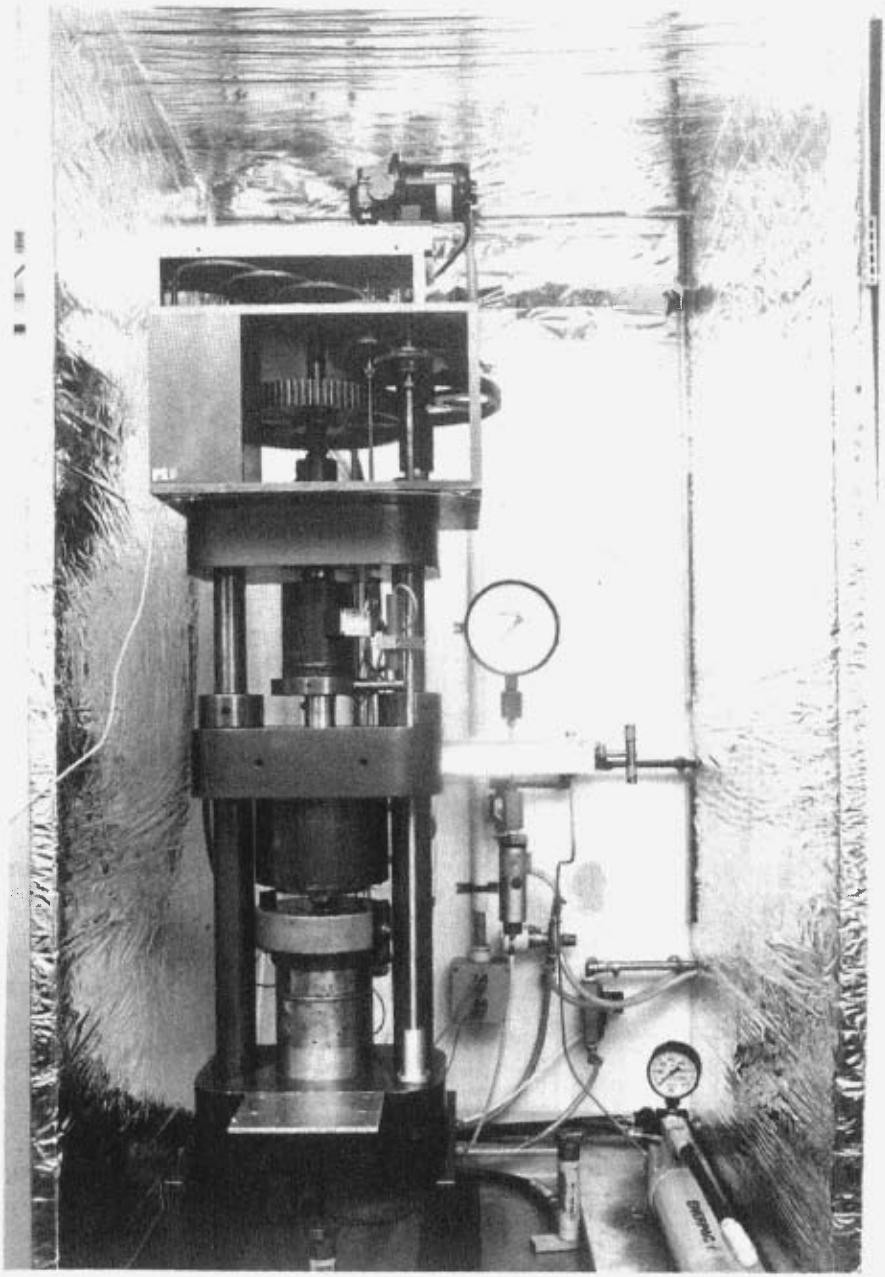

Fig. A.2 *Photograph of the Tullis-modified Griggs machine in the HPT-lab at Utrecht University. Note that it is built into an insolation box (coated with aluminium foil) in which the temperature is controlled to ~32°C. This serves to eliminate daily variations in temperature which strongly affect stress measurement.*

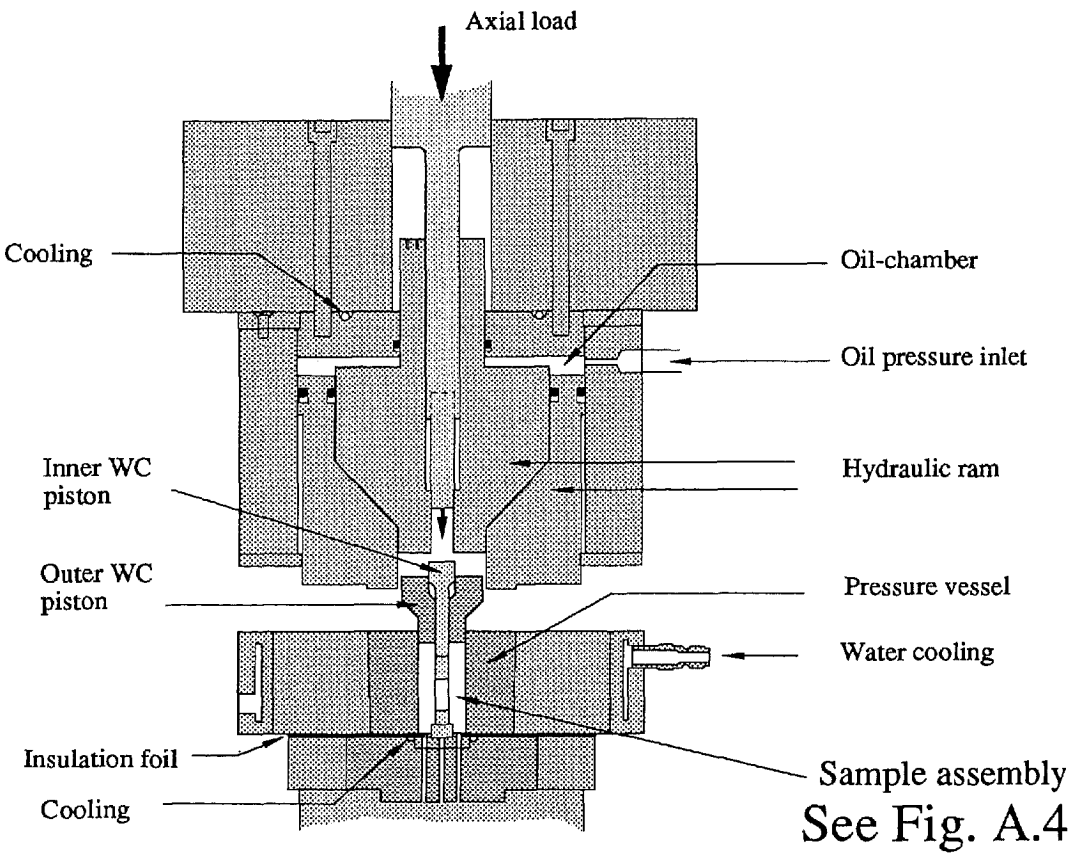

Fig. A.3 *Schematic drawing of part of the Griggs apparatus showing the hydraulic ram, pressure vessel and sample loading system. For scale, pressure vessel diameter is ~20 cm.*

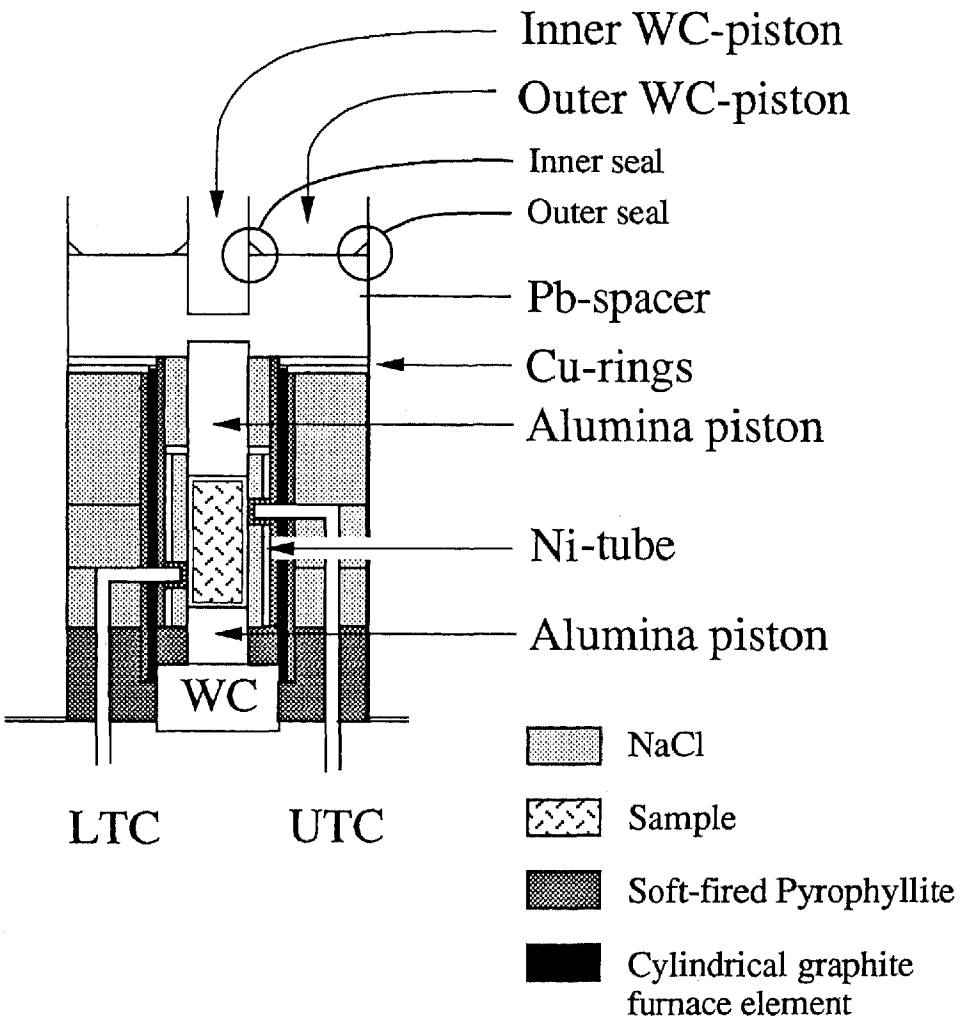

Fig. A.4 *Schematic diagram of sample assembly. Upper and lower thermocouples denoted UTC and LTC. Assembly is 1 inch in diameter*

steel bottom plate and the lower tungston carbide (WC) piston provide the bottom connection to the furnace. The vessel and the base plate are insulated from each other by 3-4 sheets of 10 μm thick polyester drawing film (Mylar). The furnace is separated from the vessel by the salt confining medium (Fig. A.5). During operation, the voltage across the furnace can reach up to ~6V, and the current ~300A. Power is supplied by a Eurotherm 470 (240V/75A) power unit connected in series with a 6V/300A transformer (step-down ratio of 40).

Temperature within the furnace assembly is monitored by a lower and an upper Pt-Pt10%Rh thermocouple (LTC and UTC respectively; Fig. A.4 & A.5). The thermocouple wires (0.35 mm diameter) are isolated from the salt confining medium using crushable mullite tubes (1.6 mm outer diameter). Temperature is controlled using a Eurotherm 820 Temperature Controller and one of the two thermocouples to regulate the power unit mentioned above. A Ni-tube (700 μm wall) between the furnace and the sample helps minimize temperature gradients. Temperature differences measured between the two thermocouples were commonly 0-8°C.

A.1.3 The axial loading system

Axial loading of the sample assembly is accomplished by an upper 'inner' piston made of tungsten carbide (WC); see Figs A.3 & A.4. This piston moves through a central hole in the confining pressure ram and in the 'outer' confining pressure piston (Fig. A.3). The inner piston is driven by a motor and gear train assembly via a low friction ball screw and thrust bearing. Interchangeable gears allow the piston to be advanced at different, constant displacement rates of the order of 0.001 to 10 mm hr^{-1}. This corresponds to strain rates of ~$2x10^{-8}$ to $2x10^{-4}$ s^{-1}, for an initial sample length of ~12 mm and strains less than ~10%.

Inside the furnace, the temperatures are so high that the tungsten carbide will not support the stresses needed to plastically deform dry quartz. Therefore the axial load is passed from WC pistons to alumina pistons at top and bottom (Fig. A.4). The alumina is polycrystalline, has a purity of 99.9% Al_2O_3, and a porosity of ≤0.5%. The ends of both the upper and lower alumina pistons are ground flat to within 30 μm measured parallel to the piston length (i.e., the error ≤0.5% for the shortest piston). A lead spacer is inserted between the upper WC- and alumina pistons so that the sample cannot be axially loaded during the initial pressurization and heating stage. As mentioned above, the lead is prevented from extrusion by a stainless steel (1.4122) packing ring. The axial load is measured outside the pressure vessel, with a BLH-Electronics C2P1-type load cell (resolution after signal conditioning ~5 N; non-linearity is ±0.05%). A Hewlett Packard DCDT (direct current displacement transducer) is mounted on a cross arm on the axial load column below the load cell and measures the displacement with respect to the steel base plate (resolution after signal conditioning ~0.2 μm; non-linearity is ±0.5%).

A.2 SAMPLE PREPARATION AND JACKETING

the experiments reported in this thesis were performed mostly on Dongelberg quartzite plus a few on single crystals of Brazilian quartz. These materials are described in chapter 3. Right cylindrical samples measuring 6 mm in diameter by 12 ± 1 mm in length were prepared from these materials using a diamond coring tool with water as lubricant. The ends of the samples were manually ground flat and parallel to within 30 μm to the sample length (i.e., error ≤0.25%) using silicon carbide powders and abrasive paper. All samples were subsequently oven-dried at 150°C for 12 hours.

Most samples were weld-sealed in gold jackets (400 μm wall thickness) together with the desired amounts (~0.4 wt% or ~1 vol%) of distilled water. In the jacketing procedure, one end of the tubular jacket was first formed into a cone-shaped closure (Fig. A.6) by turning on a lathe. The tip of the resulting cone was then sealed with an argon precision arc welder. The water was then placed in the capsule (i.e. into the cone-shaped pit), followed by the sample. While the water was immobilized by freezing in a stream of liquid nitrogen played onto the sealed cone, the open end of the capsule was formed into a second cone, using the lathe, and subsequently weld-sealed. Both ends were then carefully flattened using a hand-press. Lastly, the capsules were tested for leaks by immersion in oil at 120°C. The following more convenient way to machine the second cone was practicized in later experiments. This method employed a 4-jaw chuck made of Delrin (Poly Oxy Methylene), which has a very low thermal conductivity (0.23 $Wm^{-1}K^{-1}$). The chuck and the sealed cone containing the water and the sample were first cooled in liquid nitrogen and then mounted in the lathe. Due to the low thermal conductivity of the Delrin, the water remained frozen for 5-10 minutes, which was enough to machine the second cone.

Samples deformed 'dry' or 'as-received' were not weld-sealed in their capsules; the capsules were simply slid over the alumina pistons.

A.3 MECHANICAL TESTING PROCEDURE

All deformation experiments reported in this thesis were performed in constant displacement rate mode. The temperatures fell in the range 800° ± 30°C, and the pressures in the range 1.2 ± 0.1 GPa. The imposed strain rates were $1.1\pm0.1\times10^{-5}$, $1.1\pm0.1\times10^{-6}$, and $1.1\pm0.1\times10^{-7}$ s^{-1}.

a.

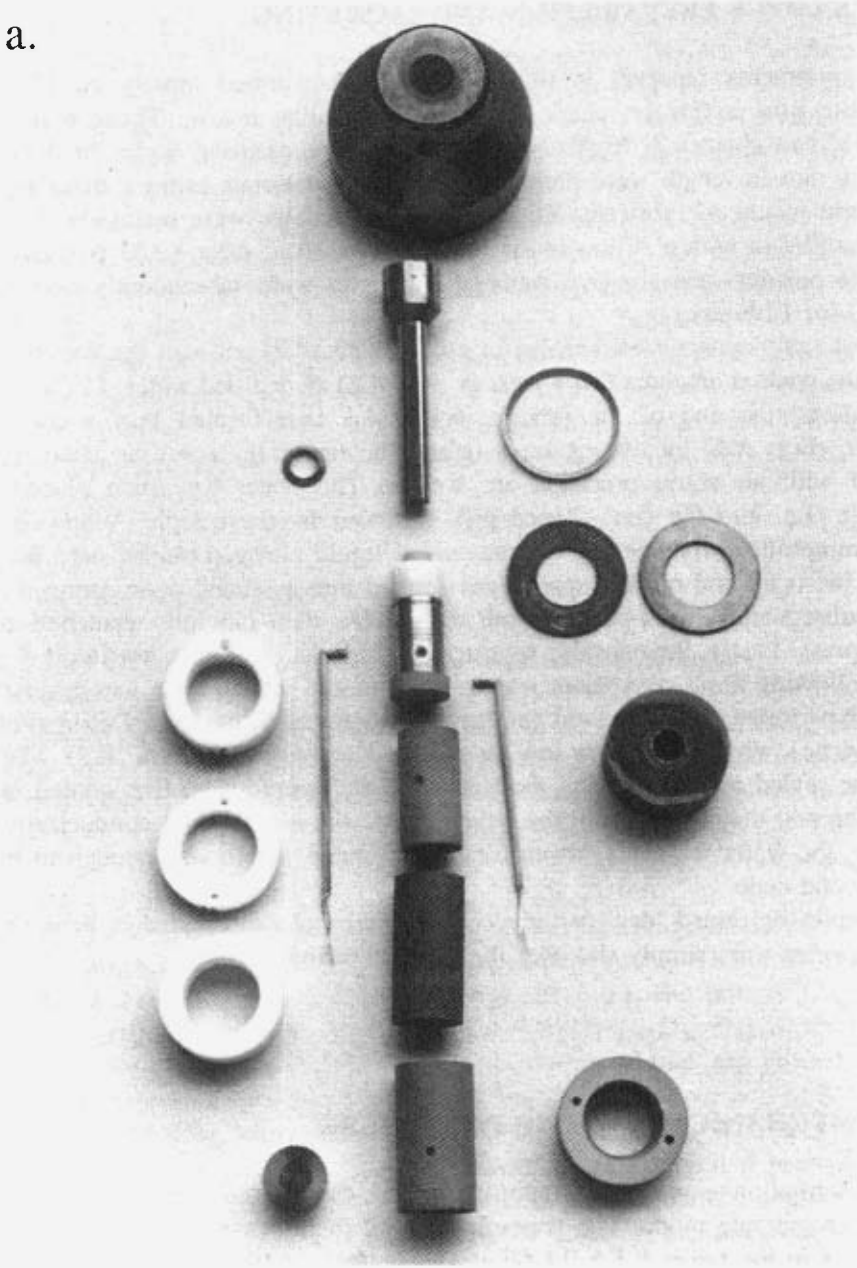

Fig. A.5 *Photographs of (a) loose components of the sample assembly, and (b) all components assembled before mounting the assembly into the vessel. Note that except for the inner and outer upper WC-pistons, and the lower WC-piston, all pieces are non re-usable and must be machined for each experiment.*

Fig. A.5 *(Continued)*

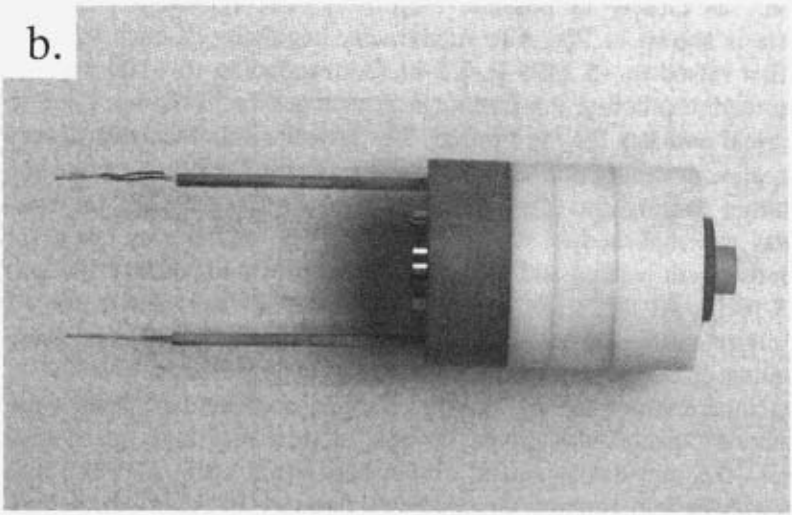

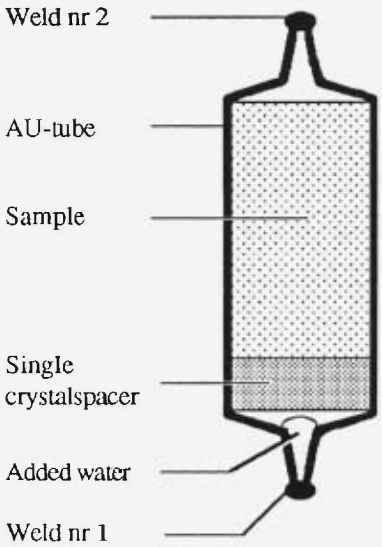

Fig. A.6 *Schematic diagram of encapsulated sample prior to deformation. The single crystal spacer was added in special experiment only. Sample diameter is ~6 mm.*

In setting up each deformation test (both wet *and* as-received samples), temperature and pressure were raised simultaneously in order to follow the water isochore of 1 gcm^{-3} as closely as possible (Fig. A.7). The typical P-T history followed in all tests is shown in Fig. A.8. At the very beginning of each test, the oil pressure was first raised to ~5 MPa in 2-5 hr (corresponding to ~100 MPa in the solid confining medium) before the furnace was switched on. This was done to provide good electrical contacts for the furnace. The pressure was then raised very slowly, in order to prevent destruction of the sample as well as the furnace and the thermocouples. Further heating and loading to 100°C and ~200 MPa (in the confining medium) was accomplished in ~5 hr, after which no action was taken for another 8-12 hr. Subsequent heating and loading to and 800°C and ~1200 MPa was accomplished in 5-10 hr. At this stage, the apparatus was left to stabilize for ~1 day, so that the oil pressure and axial load could settle down, both increasing slowly due to warming up and thermal expansion of the loading frame.

As soon as the temperature of the rig, the oil pressure, and the axial load, were stablilized, the inner WC-piston was driven inwards at relatively high speed (1-5 mm hr^{-1}) and, after ~0.5 mm displacement, driven backwards again for ~0.2 mm (Fig. A.9). This was done to determine the confining pressure in the solid medium independently from the value calculated from the pressure of the oil. In addition, the frictional force acting on the inner WC-piston could be determined in this way. Figure A.9 schematically illustrates how reversal of the inner piston movement direction, from an inwards to an outwards direction, causes an axial-load drop. This load drop consists of the sum of the friction acting on the inner piston when moving inward, plus the friction acting when moving outward. Assuming that the friction in both directions is similar, then its value is half the load drop. In a typical experiment, the friction determined in this way was 1-3 kN (30-90 MPa). The axial load needed to advance the inner piston through the upper lead plate, minus the friction, is equal to the load that is needed to push against the pressure in the solid medium, from which the confining pressure in the solid medium may be calculated. The confining pressures determined in this way were systematically 50-80 MPa lower than the pressures calculated using the pressure of the oil. This difference is caused by friction between the confining pressure piston and the pressure vessel. It corresponds to a friction of 22-35 kN.

After determining the pressure in the manner described above, the inner piston was advanced at a relatively high speed (1-5 mm hr^{-1}) to locate the sample, i.e. the 'hit point' between the WC-piston and the upper alumina piston (Fig. A.4 & A.9). The piston was then retracted (by 0.1 to 0.3 mm) to allow for a 'take-off run' at the desired experimental displacement rate. A 'take-off run' (Fig. A.10) is needed to determine the background load, i.e. the load needed to push against the pressure plus the friction. This load must be subtracted from the total load signal to calculate the load supported by the sample (see section A.2). After all above preliminaries, the 'take-off run' was executed and the sample deformed at the desired strain rate.

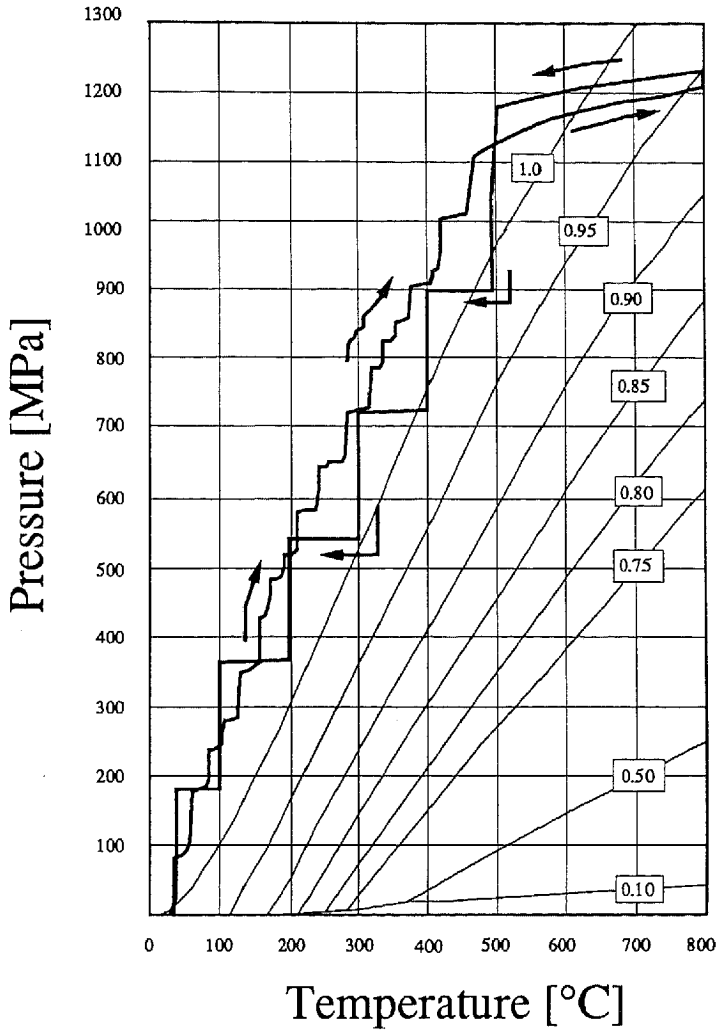

Fig. A.7 *Diagram showing typical PT-path for pressurization/heating stage of individual experiment. Density of water as a function of PT also shown (after Fisher 1976). Pressure and temperature were raised (and lowered) simultaneously in order to follow the water isochore of 1 gcm^{-3} as closely as possible.*

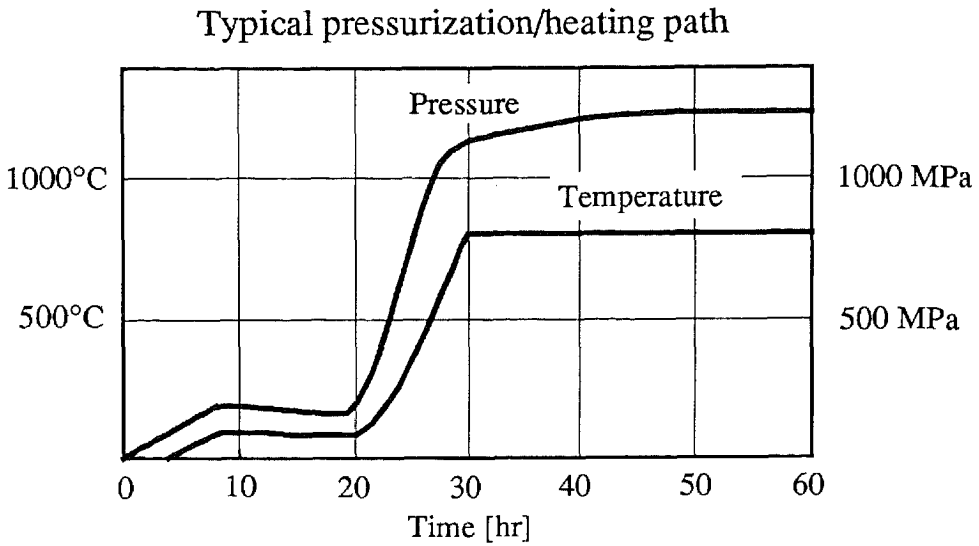

Fig. A.8 *Schematic diagram showing typical pressurization & heating history for experiment performed in the Griggs apparatus. First, the pressure is raised slowly, before the furnace is switched on, to provide a good contact between (i) the furnace and the copper rings and (ii) the rings and the vessel respectively. Further heating and pressurization to ~100°C and ~200 MPa is accomplished in ~5 hr, after which no action is taken for another 8 to 12 hr. Subsequent heating plus loading to 800°C and ~1200 MPa is accomplished in 5 to 10 hr.*

In terminating each test, the piston was retracted at maximum speed (~10 mm hr^{-1}), and the temperature and pressure were then lowered, once again following the water isochore of 1 gcm^{-3} as closely as possible (Fig. A.7). Cooling/depressurization times varied from 1 to 50 minutes. Finally, the sample assembly was forced out of the vessel and mechanically disaggregated to take out the sample. Concentrated nitric acid was used to dissolve the gold-encapsulated sample out of the Ni-tube, and the gold capsule was subsequently cut along its length using a 100μm diamond saw with water as a lubricant. In this way, four to six thin-sections could be prepared from each sample.

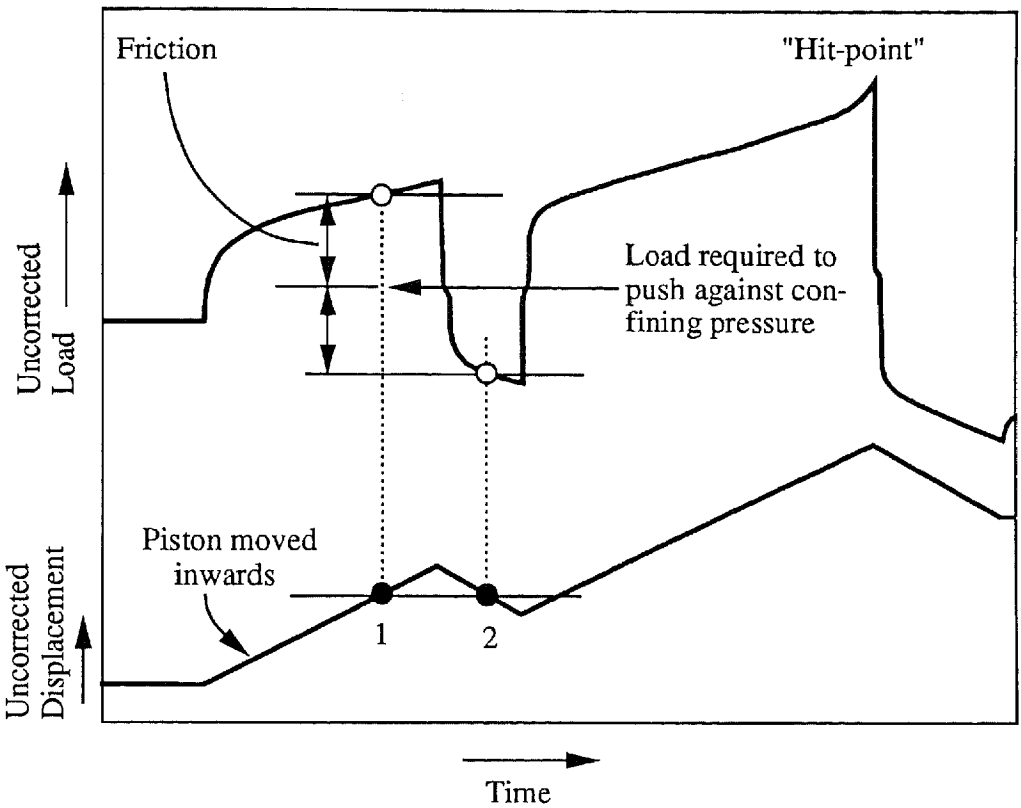

Fig. A.9 *Schematic diagram illustrating the procedure employed for determining (i) the confining pressure from the axial load signal, and (ii) the friction at the inner piston. The piston is first moved inwards, and after ~0.5 mm displacement driven backwards again for ~0.2 mm. The reversal in movement direction causes a load-drop. The difference between the load signals at two similar piston positions on either side of the reversal (e.g. positions 1 & 2) is assumed to be equal to twice the frictional force. The mean load between the two load levels (open circles) is hence equal to the load required to push against the confining medium. From this value the confining pressure may be calculated. After reversal, the piston is moved inwards again at high speed to find the 'hit point'. When this is found, the piston is reversed once again to allow for a 'take-off run' (see text and Fig. A.10).*

A.4 DATA ACQUISITION AND PROCESSING

A.4.1 Aquisition

After signal conditioning, the voltage output of the load cell, the pressure transducer, the DCDT, the thermocouples and the furnace power unit were recorded on a chart recorder and simultaneously logged onto 5¼-inch diskettes using an Olivetti M24 Personal Computer, equipped with a PC-30 AD-conversion board. The AD574-converter has 12-bit resolution, producing an error of 1:4096 (0.0002%). This is entirely negligible compared to errors introduced in applying the various corrections in data-processing, and introduced by the non-linearity of the load cell (±0.05%), the DCDT (±0.5%), the pressure transducer (±0.5%), and the temperature measurement (±1°C, or 0.001% at 800°C).

The signals logged on diskette were subsequently reduced to the (uncorrected) physical quantities that they respectively represent; the load cell output to force (kN), the pressure transducer output to pressure (MPa), the DCDT output to length (mm), and the temperature transducer outputs to temperature (°C).

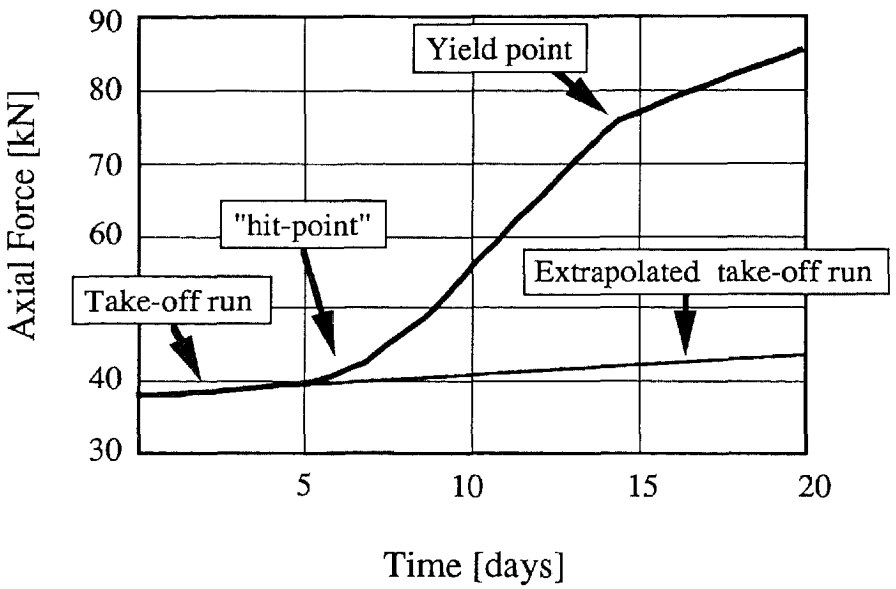

Fig. A.10 *Raw load versus time data for experiment GRU46 (P_c~1200 MPa, T=800°C, $\dot{\varepsilon}=10^{-7}$ s^{-1}; vacuum dried Dongelberg quartzite). Diagram serves to illustrate the 'take-off run' and that the 'hit point' is not sharp.*

A.4.2 Reduction of differential load data

Raw axial load versus displacement data is shown in Figure A.11a. During the 'take-off run', i.e., as the inner piston is advanced through the upper lead disk, the axial load required to push against the pressure plus friction increases linearly with displacement. This reflects the increase in confining pressure (10 ± 5 MPa per mm displacement), which occurs because no compensation is made for penetration by the inner piston. The friction is also increased by the increasing confining pressure. As soon as the WC-piston touches the upper alumina piston, which is in direct contact with the sample, the load rises until the sample begins to yield. The 'hit point' is not sharp, because the lead and the gold have to be squeezed out from between the pistons and the sample.

To determine the axial load supported by the sample, it was assumed that the above-mentioned 'take-off run' could be linearly extrapolated (Fig. A.11a). The extrapolation would thus give an estimate of the load required to push against the pressure plus the friction, while the sample is axially loaded. The load supported by the sample is obtained by subtracting the extrapolated values from the total measured load. It should be noted, however, that load or displacement variations in confining pressure, as well as variations in friction between the inner and the outer piston, may cause deviations in the linearity of the extrapolated run.

For example, a small underestimation of the load supported by the sample is caused by the fact that the axial loading system as well as the confining pressure system are yoked in series. Both the inner piston and the confining pressure ram push downwards against the steel base plate. Therefore, application of an axial load causes stretching of the yokes around the confining pressure ram, which is consequently unloaded slightly. This results in an oil pressure drop, and hence, in a drop of the pressure in the solid medium. Straight extrapolation of the take-off curve would thus correspond to an overestimation of the pressure and the friction, consequently resulting, in an underestimation of the stress supported by the sample. Considering the pressure effect alone, at ~1200 MPa hydrostatic pressure and 800°C, a superimposed axial stress of ~1000 MPa causes the oil pressure to drop by ~1 MPa, which corresponds to ~18 MPa in the solid confining medium, hence leading to an underestimation of the axial stress by ~2 %. Probably the largest error may be caused, however, by variation in the level of the friction at the inner piston (30-90 MPa) as well as at the outer confining piston (30-80 MPa). There is no way to monitor the level of these frictional forces during the experiment. Nonetheless, independently of these errors, several experiments on very weak samples, in which no sign of a 'hit point' could be seen, showed the axial load to increase linearly and in line with the take-off run. On this basis it was inferred that the deviations from the 'take-off run' were, in general, less than ~25 MPa, independently of the load-related errors.

After applying the above-mentioned 'take-off' correction, the differential stress supported by the samples (Fig. A.11b) was calculated by dividing the corrected

A.4 DATA ACQUISITION AND PROCESSING

A.4.1 Aquisition

After signal conditioning, the voltage output of the load cell, the pressure transducer, the DCDT, the thermocouples and the furnace power unit were recorded on a chart recorder and simultaneously logged onto 5¼-inch diskettes using an Olivetti M24 Personal Computer, equipped with a PC-30 AD-conversion board. The AD574-converter has 12-bit resolution, producing an error of 1:4096 (0.0002%). This is entirely negligible compared to errors introduced in applying the various corrections in data-processing, and introduced by the non-linearity of the load cell (±0.05%), the DCDT (±0.5%), the pressure transducer (±0.5%), and the temperature measurement (±1°C, or 0.001% at 800°C).

The signals logged on diskette were subsequently reduced to the (uncorrected) physical quantities that they respectively represent; the load cell output to force (kN), the pressure transducer output to pressure (MPa), the DCDT output to length (mm), and the temperature transducer outputs to temperature (°C).

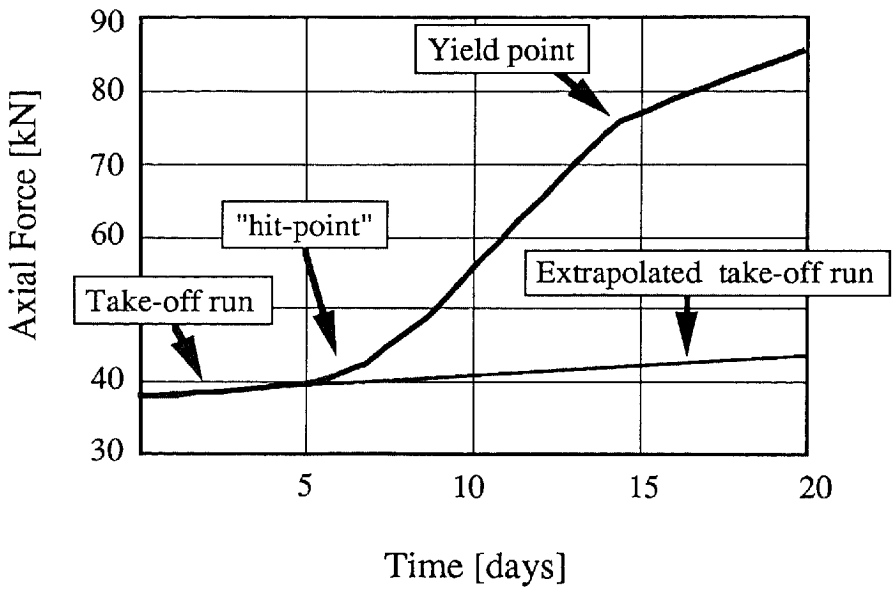

Fig. A.10 *Raw load versus time data for experiment GRU46 (P_c~1200 MPa, T=800°C, $\dot{\varepsilon}=10^{-7}$ s^{-1}; vacuum dried Dongelberg quartzite). Diagram serves to illustrate the 'take-off run' and that the 'hit point' is not sharp.*

A.4.2 Reduction of differential load data

Raw axial load versus displacement data is shown in Figure A.11a. During the 'take-off run', i.e., as the inner piston is advanced through the upper lead disk, the axial load required to push against the pressure plus friction increases linearly with displacement. This reflects the increase in confining pressure (10 ± 5 MPa per mm displacement), which occurs because no compensation is made for penetration by the inner piston. The friction is also increased by the increasing confining pressure. As soon as the WC-piston touches the upper alumina piston, which is in direct contact with the sample, the load rises until the sample begins to yield. The 'hit point' is not sharp, because the lead and the gold have to be squeezed out from between the pistons and the sample.

To determine the axial load supported by the sample, it was assumed that the above-mentioned 'take-off run' could be linearly extrapolated (Fig. A.11a). The extrapolation would thus give an estimate of the load required to push against the pressure plus the friction, while the sample is axially loaded. The load supported by the sample is obtained by subtracting the extrapolated values from the total measured load. It should be noted, however, that load or displacement variations in confining pressure, as well as variations in friction between the inner and the outer piston, may cause deviations in the linearity of the extrapolated run.

For example, a small underestimation of the load supported by the sample is caused by the fact that the axial loading system as well as the confining pressure system are yoked in series. Both the inner piston and the confining pressure ram push downwards against the steel base plate. Therefore, application of an axial load causes stretching of the yokes around the confining pressure ram, which is consequently unloaded slightly. This results in an oil pressure drop, and hence, in a drop of the pressure in the solid medium. Straight extrapolation of the take-off curve would thus correspond to an overestimation of the pressure and the friction, consequently resulting, in an underestimation of the stress supported by the sample. Considering the pressure effect alone, at ~1200 MPa hydrostatic pressure and 800°C, a superimposed axial stress of ~1000 MPa causes the oil pressure to drop by ~1 MPa, which corresponds to ~18 MPa in the solid confining medium, hence leading to an underestimation of the axial stress by ~2 %. Probably the largest error may be caused, however, by variation in the level of the friction at the inner piston (30-90 MPa) as well as at the outer confining piston (30-80 MPa). There is no way to monitor the level of these frictional forces during the experiment. Nonetheless, independently of these errors, several experiments on very weak samples, in which no sign of a 'hit point' could be seen, showed the axial load to increase linearly and in line with the take-off run. On this basis it was inferred that the deviations from the 'take-off run' were, in general, less than ~25 MPa, independently of the load-related errors.

After applying the above-mentioned 'take-off' correction, the differential stress supported by the samples (Fig. A.11b) was calculated by dividing the corrected

A.4 DATA ACQUISITION AND PROCESSING

A.4.1 Aquisition

After signal conditioning, the voltage output of the load cell, the pressure transducer, the DCDT, the thermocouples and the furnace power unit were recorded on a chart recorder and simultaneously logged onto 5¼-inch diskettes using an Olivetti M24 Personal Computer, equipped with a PC-30 AD-conversion board. The AD574-converter has 12-bit resolution, producing an error of 1:4096 (0.0002%). This is entirely negligible compared to errors introduced in applying the various corrections in data-processing, and introduced by the non-linearity of the load cell (±0.05%), the DCDT (±0.5%), the pressure transducer (±0.5%), and the temperature measurement (±1°C, or 0.001% at 800°C).

The signals logged on diskette were subsequently reduced to the (uncorrected) physical quantities that they respectively represent; the load cell output to force (kN), the pressure transducer output to pressure (MPa), the DCDT output to length (mm), and the temperature transducer outputs to temperature (°C).

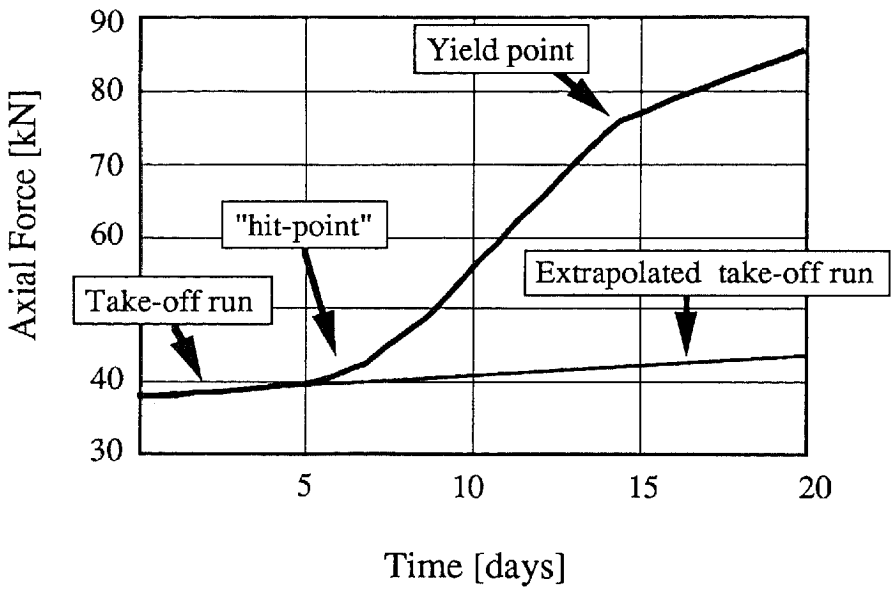

Fig. A.10 *Raw load versus time data for experiment GRU46 (P_c~1200 MPa, T=800°C, $\dot{\varepsilon}=10^{-7}$ s^{-1}; vacuum dried Dongelberg quartzite). Diagram serves to illustrate the 'take-off run' and that the 'hit point' is not sharp.*

A.4.2 Reduction of differential load data

Raw axial load versus displacement data is shown in Figure A.11a. During the 'take-off run', i.e., as the inner piston is advanced through the upper lead disk, the axial load required to push against the pressure plus friction increases linearly with displacement. This reflects the increase in confining pressure (10 ± 5 MPa per mm displacement), which occurs because no compensation is made for penetration by the inner piston. The friction is also increased by the increasing confining pressure. As soon as the WC-piston touches the upper alumina piston, which is in direct contact with the sample, the load rises until the sample begins to yield. The 'hit point' is not sharp, because the lead and the gold have to be squeezed out from between the pistons and the sample.

To determine the axial load supported by the sample, it was assumed that the above-mentioned 'take-off run' could be linearly extrapolated (Fig. A.11a). The extrapolation would thus give an estimate of the load required to push against the pressure plus the friction, while the sample is axially loaded. The load supported by the sample is obtained by subtracting the extrapolated values from the total measured load. It should be noted, however, that load or displacement variations in confining pressure, as well as variations in friction between the inner and the outer piston, may cause deviations in the linearity of the extrapolated run.

For example, a small underestimation of the load supported by the sample is caused by the fact that the axial loading system as well as the confining pressure system are yoked in series. Both the inner piston and the confining pressure ram push downwards against the steel base plate. Therefore, application of an axial load causes stretching of the yokes around the confining pressure ram, which is consequently unloaded slightly. This results in an oil pressure drop, and hence, in a drop of the pressure in the solid medium. Straight extrapolation of the take-off curve would thus correspond to an overestimation of the pressure and the friction, consequently resulting, in an underestimation of the stress supported by the sample. Considering the pressure effect alone, at ~1200 MPa hydrostatic pressure and 800°C, a superimposed axial stress of ~1000 MPa causes the oil pressure to drop by ~1 MPa, which corresponds to ~18 MPa in the solid confining medium, hence leading to an underestimation of the axial stress by ~2 %. Probably the largest error may be caused, however, by variation in the level of the friction at the inner piston (30-90 MPa) as well as at the outer confining piston (30-80 MPa). There is no way to monitor the level of these frictional forces during the experiment. Nonetheless, independently of these errors, several experiments on very weak samples, in which no sign of a 'hit point' could be seen, showed the axial load to increase linearly and in line with the take-off run. On this basis it was inferred that the deviations from the 'take-off run' were, in general, less than ~25 MPa, independently of the load-related errors.

After applying the above-mentioned 'take-off' correction, the differential stress supported by the samples (Fig. A.11b) was calculated by dividing the corrected

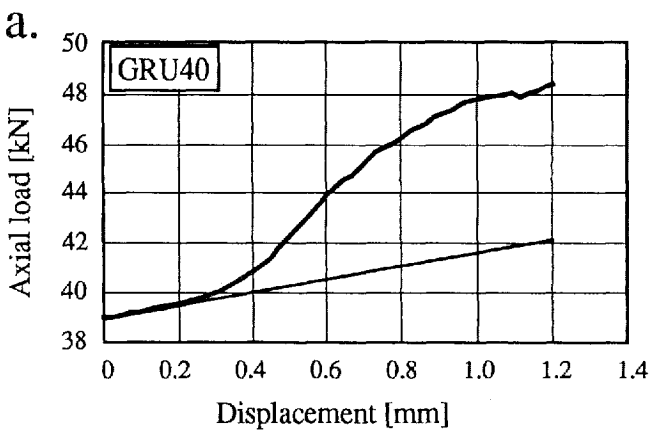

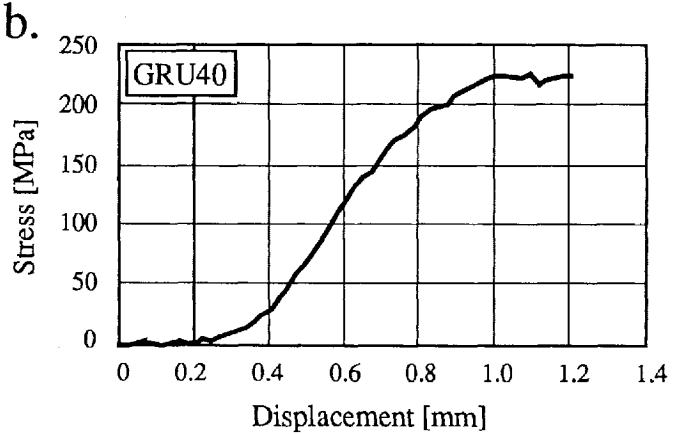

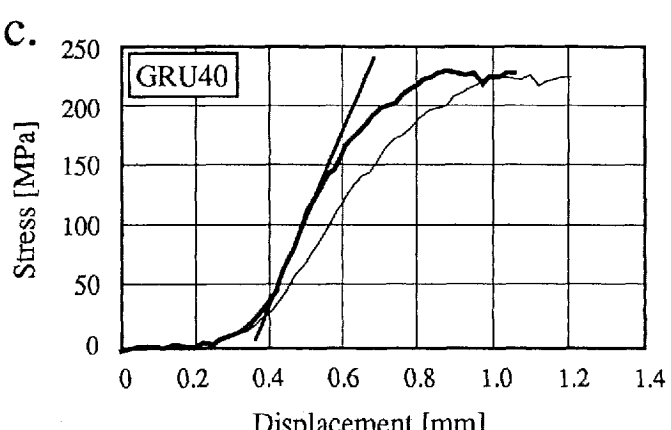

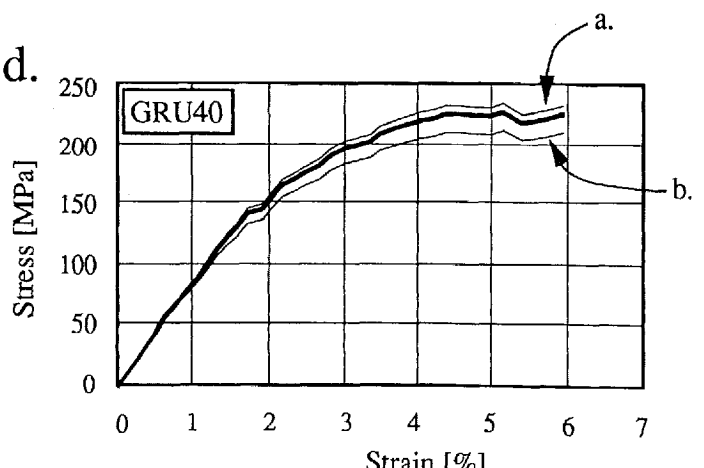

Fig. A.11 *(Explanation see next page)*

axial load (in kN) by the original cross-sectional area of the samples. In this way the stress was systematically overestimated, because the cross-sectional area of the samples increases during an experiment. No corrections were made, however, since the true increase in cross-section is not known. In some cases, samples were barrelled. In others, deformation was more intense at one end of the sample, and at relatively high strain (40-50%) the piston was punched into the samples. Division by the original cross-sectional area can introduce an error (in % of the stress) equal to the strain (in %) as long as the piston is not punched into the samples. Given that the finite axial strain was <15% in most experiments, the stresses are consequently ≤15% overestimated. Most of the yield stresses are determined at 2-6% strain so that these are presumably up to 2-6% overestimated. Together with variations in the capacity of the water cooling system daily temperature variations may cause variations in the axial stress of ~10 MPa.

Taking all of the above mentioned errors into account, it is estimated that the maximum error in the axial stress determineation is 15-20% and the typical error is ≤10%.

A.4.3 Reduction of displacement data

The apparatus stiffness was determined in calibration runs on dry quartz single crystals (Fig. A.12). Microscopical study of the samples and accurate measurement of the length after the calibration runs showed that these crystals were *elastically* deformed only. The stiffness correction determined in this way incorporates elastic distortion of the quartz as well. At a confining pressure of ~1200 MPa, and a temperature of 800°C, the elastic stiffness of the rig plus quartz is 22.0 ± 0.1 μm kN^{-1}, with the contribution of quartz calculated at 6 μm kN^{-1}.

Fig. A.11 *Example of data-processing (experiment GRU40, P_c~1200 MPa, T=800°C, $\dot{\varepsilon}=10^{-7}$ s^{-1}; as-received Dongelberg quartzite). (a) Raw data, showing extrapolated 'take-off run', and that the 'hit point' is not sharp. (b) Data after subtraction of the 'take-off run', and determination of the axial stress from the load signal (using the initial cross-section of the sample). (c) Data after stiffness correction. The stiffness-uncorrected curve is indicated by the thin line. Straight line is best-fit to the linear first part of the loading curve. (d) Final result after 'hit point' correction; maximum errors due to errors in the 'take-off' correction plus to change in cross-sectional area are indicated a and b respectively.*

In reducing the data obtained from individual experiments, the stiffness correction was applied to the raw displacement data taking the so-called 'hit point' as the position of zero true displacement. To find the 'hit point', i.e. the imaginary point of zero stress and zero strain, a straight line was fitted to the initial linear part of the loading curve, between the 'hit point' and the yield point (Fig. A.11c). This line was then extrapolated to the zero stress. The error in displacement introduced in this way may be substantial in cases where the loading curve was significantly non-linear, or where gold was found between the sample and the piston after deformation. In the first case, the error is caused fitting error. In the

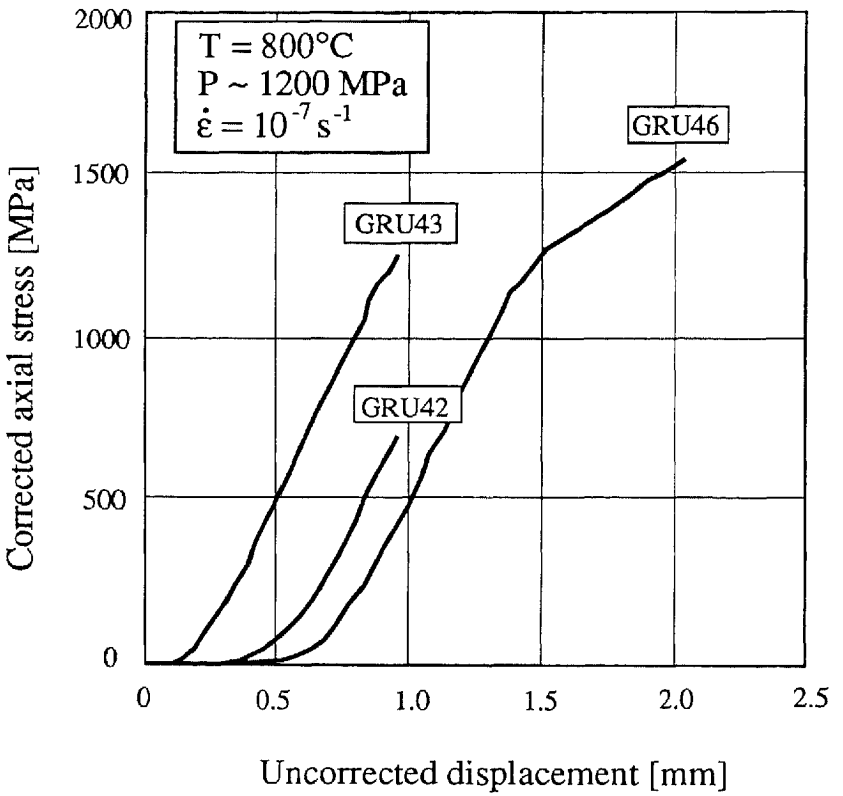

Fig. A.12 *Determination of the apparatus stiffness using dry quartz single crystals (GRU42 & 43) and vacuum-dried Dongelberg quartzite (GRU46). Note yield point of GRU46 at an axial stress of ~1200 MPa. (T=800°C, P~1200 MPa, $\dot{\varepsilon}=10^{-7}\ s^{-1}$.). Stiffness was determined from the linear portions of the curves using least squares fitting.*

second case, part of the strain may be caused by deformation of the gold between the piston and the sample. Measurement of the sample length (±100 μm) after the experiments showed that the finite strains represented in the stress/strain curves were systematically higher than the measured permanent strains by 0.5-2% strain. No correction was made for this. Fig. A.11d shows the stress/strain curve after data reduction.

A.4.4 Summary of errors and uncertainties

The dominant errors that occur during the determination of the stress and strain in individual tests in the Griggs rig can now be summarized as follows. The strains are systematically overestimated by 0.5-2 %; the differential stresses may be systematically overestimated by 15-20% at the most; the *yield* stresses by approximately 2-6%; the error in the stress caused by variations in the pressure and the frictions is less than ~25 MPa; the confining pressure is known to within ±30-80 MPa. The magnitude of pressure gradients and the degree to which the pressure is non-hydrostatic is difficult to establish.

Appendix B

DETERMINATION OF WATER CONTENT OF DONGELBERG QUARTZITE

To determine the water content of the Dongelberg quartzite, Fourier-transform infrared (FTIR) spectroscopy and thermogravimetric analysis (TGA) were carried out. Six samples were examined which were cored from one block of the Dongelberg quartzite using a diamond coring tool with water as a lubricant. The size of the samples was similar to that used in the deformation experiments, i.e. ~12 mm long and ~6 mm in diameter. After coring, the samples were dried in a furnace at 50°C for 12 hr to remove superficial water.

First TGA was carried out (in a Nitrogen gas atmosphere to prevent any possible oxydation of minerals), then FTIR-spectra of the heated samples were determined, and from these the intragranular water content (c_w), in the way as described in detail in chapter 5. The experiments are listed in table B.1 and are described below.

Four samples (DBQ15, 13, 14 & 12) were linearly heated at a rate of 0.1 °C/min to respectively 220, 400, 520, and 910°C, and then held at that temperature until the total duration of the tests was ~15 hr (Fig. B.1a). The weight-loss curves are shown in Fig. B.1b. It was assumed that the weight-loss was entirely due to evaporation of water. (Samples contained no optically visible carbonates.)

Sample DBQ15 was heated to 220°C, and lost ~0.04% of its weight (Fig. B.1) (equivalent to ~4000 ppm H/Si). This must be entirely due to loss of *inter*granular

Table B.1 *Experimental data of TGA*

Sample Nr.	Max. Temp (°C)	heating rate (°C/min)	Duration of test (hr)	weightloss (wt%)
DBQ10	800	250-300	3.0	0.29
DBQ11	800	250-300	39.3	0.29
DBQ15	225	0.1	15.5	0.04
DBQ13	400	0.1	14.2	0.08
DBQ14	520	0.1	13.8	0.14
DBQ12	910	0.1	14.8	0.30

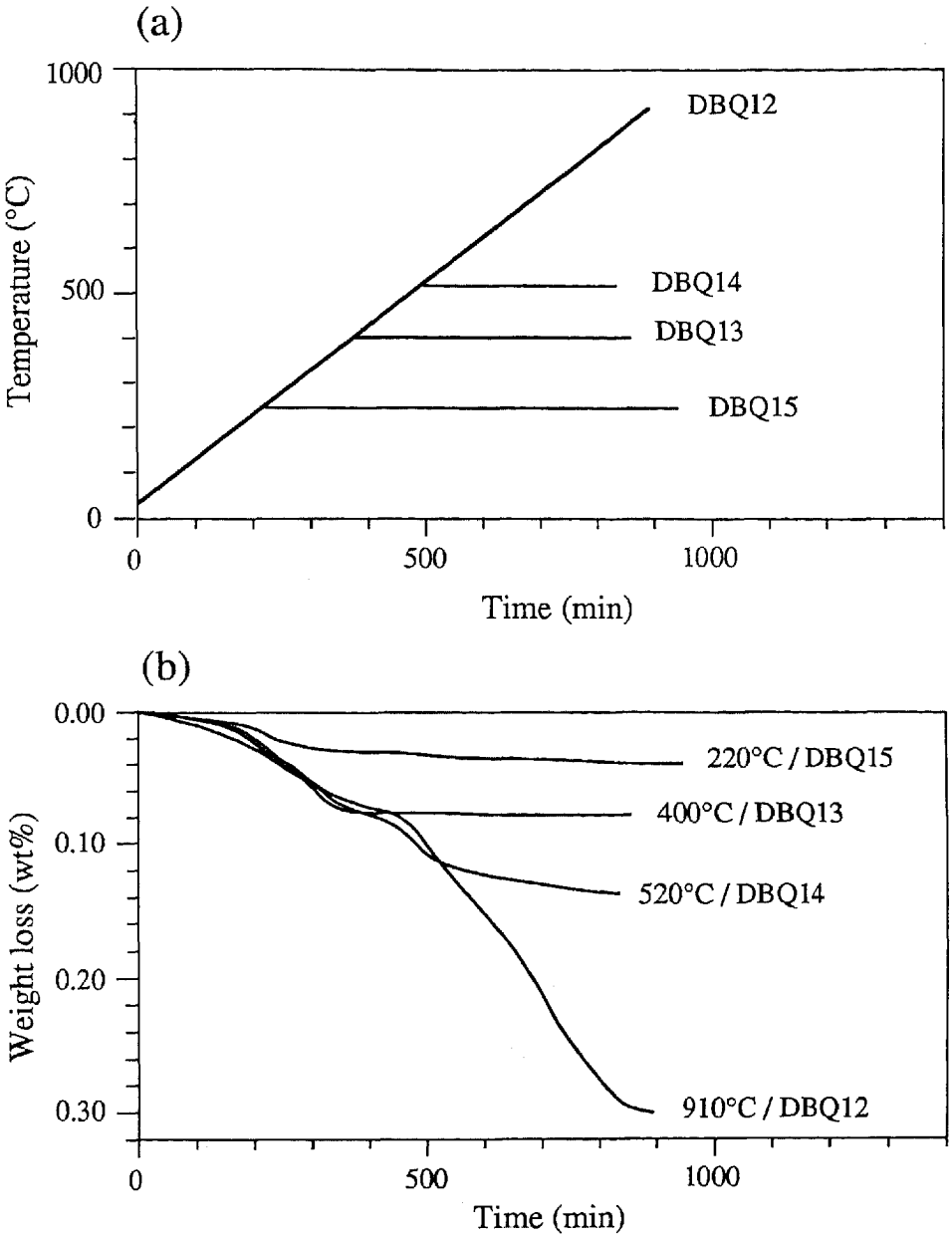

Fig. B.1 *TGA curves af samples DBQ12-15. (a) Heating path. Samples were heated at 0.1 °C/min to the indicated temperature and then kept at that temperature. Total run time was ~15 hr. (b) Corresponding weight-loss curves.*

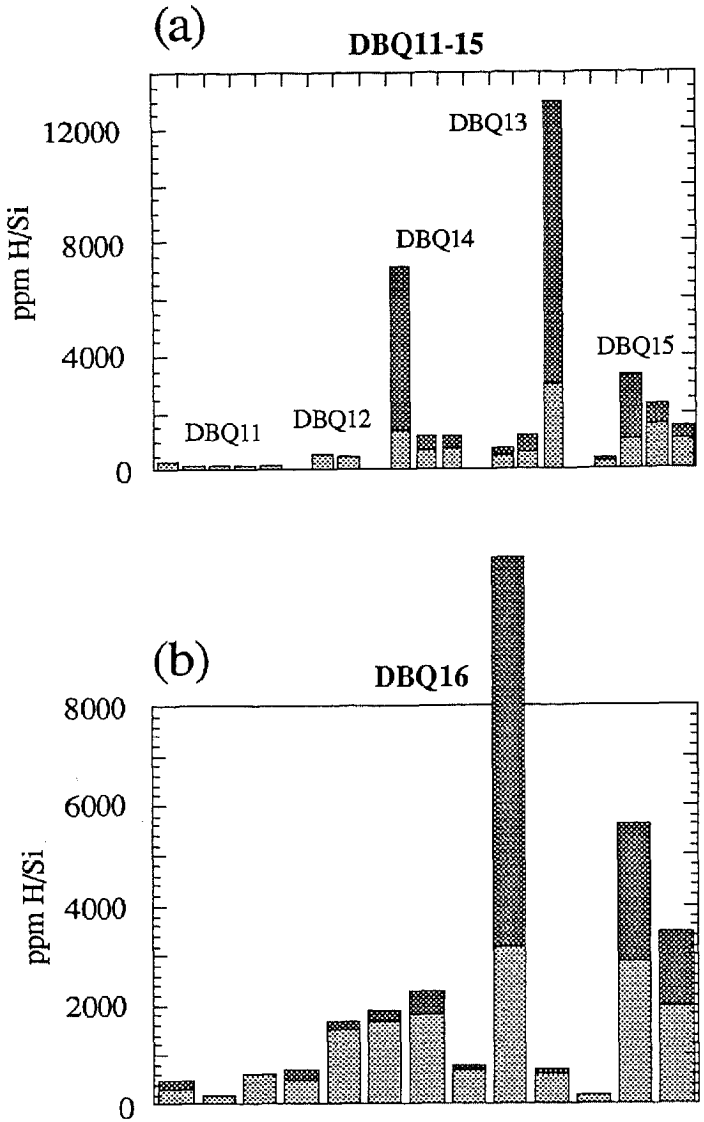

Fig. B.2 *Histograms showing intragranular water content measured by FTIR-spectroscopy (see chapter 5). (a) Water content per sample. Each column corresponds to one grain. 5 grains measured in sample DBQ11, 2 grains in sample DBQ12, 3 grains in sample DBQ13, 3 grains in sample DBQ14, and 5 grains in sample DBQ15. Hight of column refers to bulk water content. Dark stippled areas refer to structurally bound water, probably present in mica. (b) Intragranular water content of starting material. Each column corresponds to one grain. Not that water content is significantly lower in samples DBQ11 & 12 only.*

water, since FTIR-spectra revealed that c_w (Fig. B.2a) was similar to that of the starting material (Fig. B.2b). Other possible (mineral) water sources, such as Fe-hydroxides, illites or micas, dehydrate in TGA at higher temperatures (Blazek 1972). The FTIR-spectra also indicate that large amounts of water are still bound to micas.

Sample DBQ13 was heated up to 400°C and lost ~0.08% of its weight (or ~8000 ppm H/Si). FTIR-analysis revealed that c_w and the amount of water bound to micas was similar to that of the starting material. The additional 0.04% loss of weight (or ~4000 ppm H/Si), compared to the sample heated to 225°C, is probably caused by dehydration of Fe-hydroxides (goethite, lepidocrocite). These were recognized optically in the starting material, and during TGA these are well known to dehydrate between 250 and 400°C (Blazek 1972). Assuming that ~10 wt% of the Fe-hydroxides (FeOOH) consists of water, then this additional 0.04% weight loss would have been caused by dehydration of ~0.4 wt% (or ~0.2 vol%) Fe-hydroxide. This value agrees reasonably well with the optically estimated <1 vol% of opaque minerals, also including hematite and/or magnetite.

Sample DBQ14 was heated up to 520°C and lost ~0.14 wt% (or ~14000 ppm H/Si). FTIR-analysis revealed that the sample contained still grains with high c_w and large amounts of water bound to micas. Micas are well known to dehydrate above 550°C (Blazek 1972) so the extra ~6000 ppm H/Si very unlikely came from dehydration of micas. Fe-hydroxides should already have been dehydrated at this temperature. It is therefore not clear what process is responsible for this additional ~6000 ppm H/Si. Maybe the water originated from fluid inclusions located at grain boundaries, or by dehydration of a non-recognized hydrated mineral.

Sample DBQ12 was heated up to 900°C and lost ~0.30% of its weight (or ~30000 ppm H/Si). FTIR-analysis revealed that c_w was 400-600 ppm H/Si and no IR absorption by water bound to micas could be detected. This agrees with the dehydration values reported in the literature. For example, sericite dehydrates between 550 and 700°C, illite between 550 and 575°C, and muscovite between 750 and 890°C, (Blazek 1972). The weight-loss curve shows a jump at 700-750°C (typical for mica) indicating that most of this water came from dehydration of the micas. From the 16000 ppm H/Si lost between 520 and 900°C approximately 1000 to 2000 ppm H/Si must have been intragranular water (and the other 14000-15000 ppm H/Si from mica). Assuming that a mica contains 4-5 wt% structurally bound water, the weightloss of 0.14-0.15% must have been caused by dehydration of 3.8-4.0 wt% (or 3-3.3 vol%) mica. This is a reasonable value; the amount of mica was optically estimated to be ~2 vol%.

Samples DBQ10 & 11 were heated to 800°C at a much faster rate (200-300° C/min) and were kept at that temperature for respectively 3.0 and 39.3 hr (Fig. B.3a&b). The weight-loss with time of these samples is shown in Fig. B.3c-f. Both samples lost 0.29 (±0.01) % of their weight, corresponding to approximately 29000 ppm H/Si. FTIR-spectroscopy of sample DBQ11 revealed that c_w was below the detectability, i.e. <200-300 ppm H/Si (Fig. B.2a). No FTIR-spectrum was taken

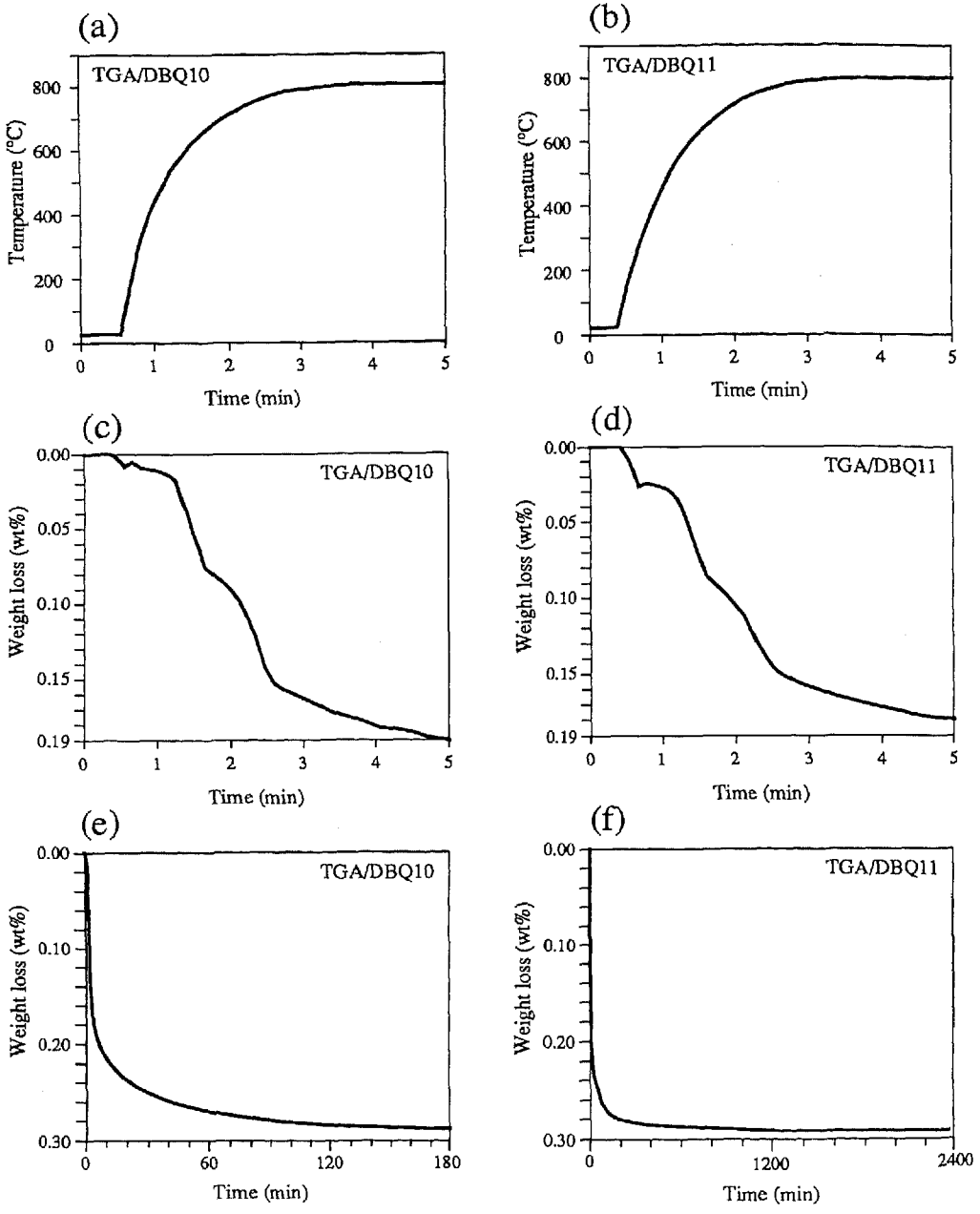

Fig. B.3 *TGA curves of samples DBQ10 & 11, heated to 800°C in ~3 min. (a) & (b) temperature increase with time in first part of the test respectively in sample DBQ10 & 11. (c) & (d) Detail of weight-loss versus time of sample DBQ10 & 11. Note shoulders on the curves indicating that different processes are active. (e) & (f) Total eight-loss curves of samples DBQ10 & 11. Most of the weight is lost after less than ~1 hr.*

from sample DBQ10 since this sample was used in deformation experiment GRU46.

Summarized, the following conclusions may be drawn regarding the water content of the as-received Dongelberg quartzite (table 3.2): the bulk water content is 0.29-0.30 wt% (corresponding to 29000-30000 ppm H/Si). Approximately 0.04 wt% (or 4000 ppm H/Si) is present as intergranular water which will probably be 'free' during the deformation. Another ~0.04 wt% (or 4000 ppm H/Si) is structurally bound to Fe-hydroxides. This will probably be 'free' as well during deformation, since the Fe-hydroxides are far outside their stability field at 800°C and ~1200 MPa (e.g. Langmuir 1971) and will react to hematite. Approximately 1000-2000 ppm H/Si is present as intragranular water (as the FTIR-spectra revealed), mostly in the form of fluid inclusions (>50% is freezable; see chapter 5) and it is not known whether this water is 'free' during deformation. Approximately 0.14-0.15 wt% (14000-15000 ppm H/Si) of the water is structurally bound to mica. This will probably not be 'free' during the deformation of the as-received material. The experiments were carried out inside the stability field of muscovite plus quartz plus water absent (Storre 1972), and large amounts of micas were present after deformation in all of the tests on as-received material. The experiments were, however, carried out outside the stability field of muscovite plus quartz plus excess (20-30 wt%) water (Storre & Karotke 1971, 1972). The amount of 'free' water in the as-received material is of the order of 8000-14000 ppm H/Si (or 0.08-0.14 wt%), 200-300 times less than the excess 20-30 wt%. The micas will therefore probably be stable and its water will not be 'free'. The source of ~6000 ppm H/Si could not be identified. It is not clear whether this water will be 'free' during deformation.

The as-received samples are therefore believed to contain 8000-14000 ppm H/Si *inter*granular water during the experiments (0.08-0.14 wt%).

Appendix C

DETERMINATION OF FLUID PRESSURE IN THE EXPERIMENTS USING FLUID INCLUSION HOMOGENISATION TEMPERATURES

The homogenisation temperatures of 15 fluid inclusions in sample GRU26 and 12 fluid inclusions in sample GRU11 were determined on a heating-freezing stage. From the homogenisation temperature, the fluid density can be determined (assuming that the fluid was pure H_2O; no second phases were observed optically, with SEM only very small amounts of Fe-oxides were observed). From the thus obtained fluid densities the fluid pressures were calculated using the equation-of-state of pure H_2O of Belonoshko & Saxena (1991; this equation is based on experimental and molecular dynamics simulated data). The size, homogenisation temperature, density (molar volume), fluid pressure and effective confining pressure, obtained per fluid inclusion are given in table C.1.

In the starting material, fluid inclusions were also present, but these are relatively rare and typically <2 μm diameter, i.e., too small to measure. Nevertheless, some of the measured fluid inclusions may naturally have been non-equilibrated original fluid inclusions, in which case the calculated fluid pressure is meaningless.

It is not known at which stage during the experiment the fluid inclusions were formed; they may well have been formed during the initial loading stage (at lower temperature and pressure than the final experimental conditions) in which case the calculated fluid pressures, again, are meaningless. But the fact that samples GRU29 & 35, deformed by 40 to 46%, contain significantly more fluid inclusions than samples deformed by 5-15% (GRU10, 11, 20, 21, 23 & 26), and that samples hydrostatically loaded only contain very small amounts of fluid inclusions, indicates that fluid inclusions mainly formed *during* the deformation process.

The measurements indicate that the fluid pressures were high (800-1000 MPa) and consequently, that the effective confining pressures were low (100-300 MPa).

Table C.1 *Homogenisation temperatures and calculated fluid pressures of samples GRU26 (T=1047-1083K; P_c=1130±50 MPa) and sample GRU11 (T=1047-1083K; P_c=1040±50 MPa).*

Nr	Size (µm)	Homogenisation temperature (°C)	Molar volume (ft^3/lbm)	P_{fluid} (MPa)	$P_{effective}$ (MPa)
GRU26					
1	34	178.7 (±0.1)	0.01803 (±0.00001)	940-970	110-210
2	26	203.4 (±0.1)	0.01864	840-870	240-310
3	17	211.6 (±0.1)	0.01882	820-850	260-330
4	26	>210.1 (decrip)	0.01878	>830	>250
5	11	208.6 (±0.1)	0.01874	830-860	250-320
6	9	212.1 (±0.1)	0.01884	820-850	260-330
7	11	216 (±2)	0.01896 (±0.00006)	790-840	290-340
8	11	212.3 (±0.1)	0.01884	820-850	260-330
9	11	210 (±0.1)	0.01878	830-850	250-330
10	14	210-215	0.01878-0.01893	810-850	270-330
11	6	215-220	0.01893-0.01906	790-830	290-350
12	--	270.3 (±0.1)	0.02087	610-630	470-550
13	9	140.1 (±0.1)	0.01730	1070-1100	0-80
14	9	287 (±4)	0.02172 (±0.00012)	530-590	550-590
15	6	276.3 (±0.1)	0.02115	590-610	490-570
GRU11					
1	9	205.7 (±0.1)	0.01867	820-860	130-270
2	6	180 (±2)	0.01806 (±0.00005)	900-970	20-190

Table C.1 *(Continued).*

Nr	Size (μm)	Homogenisation temperature (°C)	Molar volume (ft^3/lbm)	P_{fluid} (MPa)	$P_{effective}$ (MPa)
GRU11					
3	4	163.4 (±0.1)	0.01772	970-1020	0-120
4	14	170 (±2)	0.01785 (±0.00005)	940-1010	0-150
5	6	177.9 (±0.1)	0.01801	920-970	20-170
6	11	195 (±5)	0.01841 (±0.00012	840-920	70-250
7	9	202.8 (±0.1)	0.01860	830-880	110-260
8	6	203.9 (±0.1)	0.01863	830-870	120-260
9	6	195.2 (±0.2)	0.01841	860-910	80-230
10	6	203.0 (±0.1)	0.01860	830-880	110-260
11	9	207 (±1)	0.01870 (±0.00002)	820-860	130-270
12	9	204.1 (±0.1)	0.01863	830-870	120-260

Appendix D

In order to estimate the relative importance of crystal-plasticity, solution transfer, and grain boundary sliding, to the total deformation of samples GRU29 & 35, I will assume that the total volume of new grains was developed by precipitation in arrays parallel to the shortening direction (Z). This material is further assumed to have been dissolved at grain boundaries oriented perpendicular to Z. Thus, the contribution of solution transfer ($\varepsilon_{b,st}$) to the bulk finite strain (ε_b) may be determined. Actually, this is a minimum value, since the part of solution transfer that is precipitated as syntaxial overgrowths is disregarded (Fig. 3.16). Where possible, syntaxial overgrowths were counted to the axial arrays of new grains, but the exact anount of syntaxial overgrowth is difficult to assess. The contribution of solution transfer leading to development of new grains in axial arrays ($\varepsilon_{b,st}$) may be estimated from the percentage of new grains (A) determined in a thin-section cut right through the middle of the sample parallel to Z, and by assuming that the new grains are homogeneously distributed on the scale of the thin-section. As illustrated in Fig. D.1, $\varepsilon_{b,st}$ is related to A by:

$$\varepsilon_{b,st}[\%] = 100 - 100\left(1 - \frac{A[\%]}{100}\right)^2 \qquad \text{(D.1)}$$

The percentage of new grains (A) in sample GRU29 was 10 to 15%, so that $\varepsilon_{b,st}$= 19 to 28% according to equation D.1. The other 12 to 21% strain (i.e. ε_b - $\varepsilon_{b,st}$) must consequently have been accommodated by other deformation processes, including crystal-plastic deformation, grain boundary sliding, and/or the syntaxial overgrowth part of solution transfer. To estimate the relative contribution of these processes to ε_b, the measured grain strain ($\bar{\varepsilon}_g$) will be compared with the value (ε_g) that it *should* be if no grain boundary sliding had occurred, but only solution transfer and crystal-plastic deformation. Any difference between these two values should be attributed to grain boundary sliding. The relation between ε_g, and ε_b and A is given by:

$$\varepsilon_g[\%] = 100\left[1 - \left(1 - \frac{\varepsilon_b[\%]}{100}\right)\left(1 - \frac{A[\%]}{100}\right)^{-2/3}\right] \qquad \text{(D.2)}$$

For A=10-15% and ε_b=40±%, a value of ε_g=34-36% is obtained, which is significantly larger than the measured grain strain $\bar{\varepsilon}_g$ of 29±1 %. (In other words, the original grains are less flattened than would be expected on the basis of the number of newly precipitated grains.) The difference, i.e., 4 to 8%, must consequently have

been caused by grain boundary sliding. The other 4 to 17% strain (of the remaining 12 to 21%; see above), must be due to grain-strain producing deformation mechanisms, most probably crystal-plastic deformation, or the syntaxial overgrowth part of solution transfer (Fig. D.1b & c). It is difficult to discriminate between these processes, because they both produce flattened grains, and because both deformation lamellae *and* syntaxial overgrowth features were abundant in GRU29. Since most of the original grains show syntaxial overgrowth features of *at least* 3 to 5 μm long (but they may naturally be much longer) a minimum amount of strain by solution transfer with syntaxial overgrowth may be estimated. Assuming an average grain size of 200 μm, the above length of the overgrowths would account for 2 to 7% strain (again assuming axial symmetry). Crystal-plastic processes may therefore have accounted for 0 to 15% strain.

In the same way as for sample GRU29, the contribution of the different deformation processes to the bulk deformation of sample GRU35 was estimated. With A=15 to 20%, a contribution of solution transfer of $\varepsilon_{b,st}$=28 to 36% is obtained, the remaining 10 to 18% strain (of the 46±1 % bulk strain) having been accomplished by the other deformation processes. From this, 7 to 12% strain was estimated to have been caused by grain boundary sliding, and the other 0 to 11% strain (of the remaining 10 to 18%), by either crystal-plastic deformation, or by the syntaxial overgrowth part of solution transfer. It is difficult to determine the mutual importance of these two processes, but for two reasons I believe that the latter process was the dominant: (i) only very small numbers of deformation lamellae were observed, indicating that crystal-plastic deformation did not significantly contribute to the strain. In sample GRU29, 65% of the original grains contained deformation lamellae, whereas the contribution of crystal-plastic deformation processes to the total strain was estimated to be less than 15%. In sample GRU35, only 12% of the original grains contained deformation lamellae, which is five times less than in sample GRU29. The contribution of crystal-plastic deformation in sample GRU35 is therefore also expected to be significantly less. (ii) The original grains mostly contain large numbers of healed micro-cracks, which also contributed significantly to the grain strain. The width of such fractures is typically 2 to 5 μm. Sealing of, say 5 of such fractures in original grains of on average 200 μm diameter, would account for 5 to 12.5% strain.

Fig. D.1 *Diagram illustrating relation between the strain accommodated by solution transfer (ε_{st}; as far as precipitation of new material occurs at grain boundaries parallel to Z), and the percentage of new grains (A) measured in a thin-section cut parallel to Z right through the middle of the sample. (a) Cross-section parallel to Z, right through the middle of a cylindrical grain, with cylinder axis oriented parallel to Z, after constant volume axial-symmetric shortening parallel to Z by dissolution at grain boundaries perpendicular to Z and precipitation of new grains at grain boundaries parallel to Z (light grey area). Cross-sectional area of undeformed original grain was 1. (b) Total*

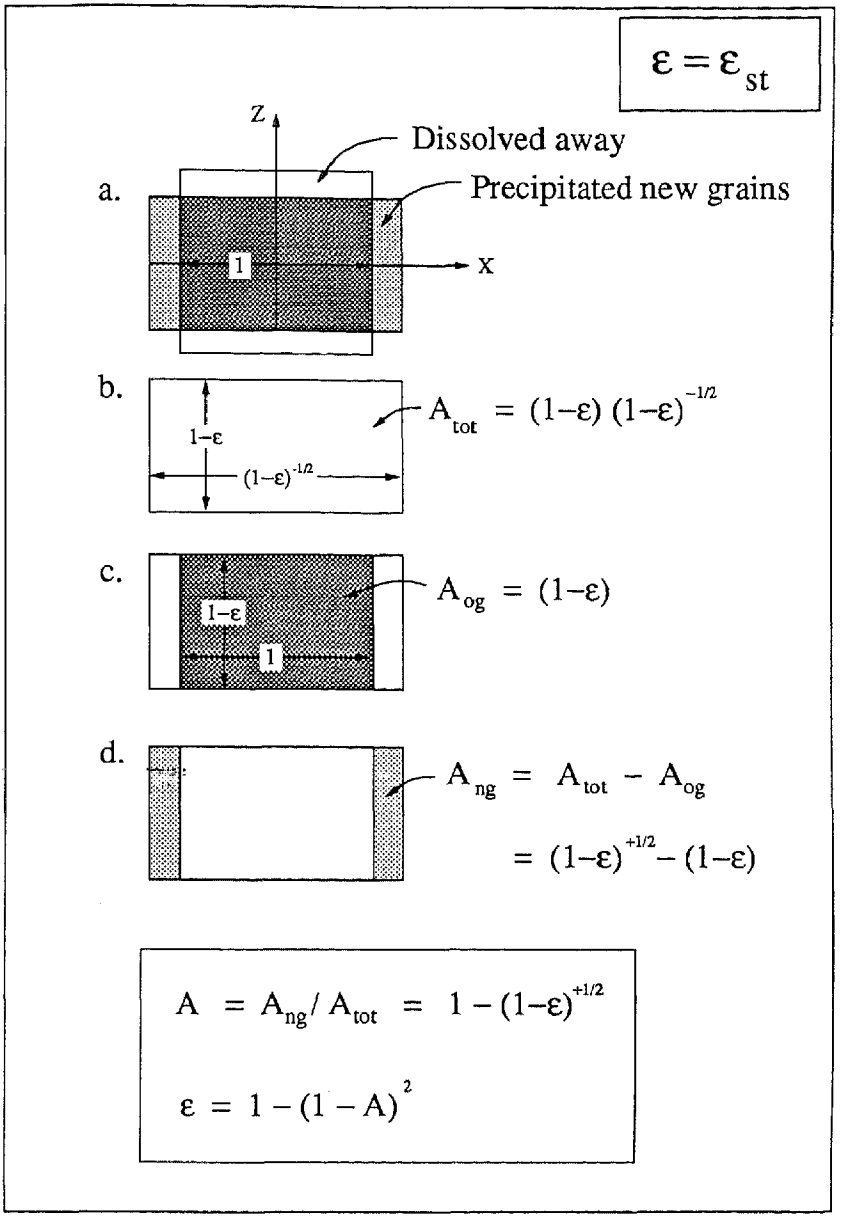

cross-sectional area (A_{tot}) after deformation, i.e. area of new grains (A_{ng}) plus area of original grains after deformation (A_{og}), equals $\sqrt{(1-\varepsilon_{st})}$. (c) Area of original grain after deformation (A_{og}) equals $(1-\varepsilon_{st})$. (d) Area of new grains (A_{ng}) equals A_{tot}-A_{og}, or $\sqrt{(1-\varepsilon_{st})}$-$(1-\varepsilon_{st})$. The fraction (A) of the total area (A_{tot}) that consists of new grains is equal to A_{ng}/A_{tot}, or $1-\sqrt{(1-\varepsilon_{st})}$. Or, inversely, the strain (ε_{st}) as a function of the fraction (A) of new grains equals $1-(1-A)^2$ or $\varepsilon_{st}[\%]=100-100(1-A[\%]/100)^2)$.

REFERENCES

Aines, R.D. & Rossman, G.R. 1984. Water in minerals? A peak in the infrared. *J. Geophys. Res.* **89,** 4059-4071.

Aines, R.D., Kirby, S.H. & Rossman, G.R. 1984. Hydrogen speciation in synthetic quartz. *Phys. Chem. Minerals* **11,** 204-212.

Alibert, C. & Delbove, F. 1980. Données préliminaires sur le rôle de l'eau dans la diffusion chimique entre rhyolite et phonolite fondues à 900°C sous une pression d'eau de 4 kbar. *C. R. Acad. Sc. Paris, Série D* **291,** 789-792.

Althaus, E., Karotke, E., Nitsch, K.H. & Winkler, H.G.F. 1970. An experimental re-examination of the upper stability limit of muscovite plus quartz. *N. Jahrb. Min. Petr.* **7,** 325-336.

Anderson, J.L. 1945. Deformation planes and crystallographic directions in quartz. *Bull. Geol. Soc. Am.* **56,** 409-430.

Anderson, G.N. & Burnham, C.W. 1965. The solubility of quartz in supercritical water. *Am. J. Sci.* **263,** 494-511.

Ardell, A.J., Christie, J.M. & Tullis, J. 1973. Dislocation substructures in deformed quartz rocks. *Crystal Lattice Defects* **4,** 275-285.

Baëta, R.D. & Ashbee, K.H.G. 1970. Mechanical deformation of quartz. I. Constant strain-rate compression experiments. *Philos. Mag.* **22,** 601-625.

Baëta, R.D. & Ashbee, K.H.G. 1973. Transmission electron microscopy studies of plastically deformed quartz. *Phys. Stat. Sol. (A)* **18,** 155-170.

Bailey, S.W., Bell, R.A. & Peng, C.J. 1958. Plastic deformation of quartz in nature. *Bull. Geol. Soc. Am.* **69,** 1443-1466.

Bakker, R.J. 1992. On modifications of fluid inclusions in quartz: re-equilibration experiments and thermodynamical calculations on fluids in natural quartz. *Geologica Ultraiectina* **94,** 189 pp.

Balashov, V.N., Zaraiskii, G.P., Tikhomirova, V.I. & Postnova, L.Ye. 1983. Diffusion of rock-forming components in pore solutions at 200°C and 100 MPa. *Geochemistry International* **20,** 28-40.

Balderman, M.A. 1974. The effect of strain rate and temperature on the yield point of hydrolytically weakened synthetic quartz. *J. Geophys. Res.* **79,** 1647-1652.

Balk, R. 1952. Fabric of quartzites near thrust faults. *J. Geology* **60,** 415-435.

Barber, D.J. & Wenk, H.R. 1991. Dauphiné twinning in deformed quartzites: implications of an in situ TEM study of the α-ß phase transformation. *Phys. Chem. Miner.* **17,** 492-502.

Beach, A. 1976. The interrelations of fluid transport, deformation, geochemistry and heat flow in early proterozoic shear zones in the Lewisian complex. *Phil. Trans. R. Soc. Lond. A* **280,**569-604.

Becke, F. 1893. Petrographische Studien am Tonalit der Riesenferner. *Tschermak. Mineral. Petrogr. Mitt.* **13,** 379-464

Bell, T.H. & Cuff, C. 1989. Dissolution, solution transfer, diffusion versus fluid flow and volume loss during deformation/metamorphism. *J. Metam. Geol.* **7,** 425-447.

Bell, T.H. & Etheridge, M.A. 1973. Microstructure of mylonites and their descriptive terminology. *Lithos* **6,** 337-348.

Bell, T.H. & Etheridge, M.A. 1976. The deformation and recrystallization of quartz in a mylonite zone, central Australia. *Tectonophysics* **32,** 235-267.

Belonoshko, A. & Saxena, S.K. 1991. A molecular dynamics study of the pressure-volume properties of super-critical fluids: I. H_2O. *Geochim. Cosmochim. Acta* **55**:381-387

Bitsanis, I., Somers, S.A., Davis, H.T. & Tirell, M. 1990. Microscopic dynamicsof flow in molecularly narrow pores. *J. Chem . Phys.* **93,** 3427-3431.

Blacic, J.D. 1975. Plastic-deformation mechanisms in quartz: the effect of water. *Tectonophysics* **27,** 271-294.

Blacic, J.D. & Christie, J.M. 1984. Plasticity and hydrolytic weakening of quartz single crystals. *J. Geophys. Res.* **89,** 4223-4239.

Blazek A. 1972. Thermal analysis. *Van Nostrand Reinhold series in analytical chemistry* (edited by R.A. Chalmers). Van Nostrand Reinhold Company, London, 1-286.

Bloss, F.D. 1957. Anisotropy of fracture in quartz. *Am. J. Sci.* **255,** 214-225.

Böhm, A. 1882. Ueber die Gesteine des Wechsels. *Mineralog. und petrogr. Mitth.* **1882,** 197-214.

Bouchez, J.-L. 1977. Plastic deformation of quartzites at low temperatures in an area of natural strain gradient. *Tectonophysics* **39,** 25-50.

Bowler, S. 1989. Shape fabric formation by cataclasis in a quartzite from the Moine thrust zone, northwest Scotland. *Geology* **17,** 353-356.

Brady, J.B. 1983. Intergranular diffusion in metamorphic rocks. *Am. J. Sci.* **283 A,** 181-200.

Byerlee, J.D., 1978. Brittle-ductile transition in rocks. *J. Geophys. Res.* **73,** 27-63.

Carstens, H. 1969. Arrays of dislocations associated with healed fractures in natural quartz. *Norges Geologiske Undersokelse, Arbok 1968,* Universitetsforlaget, 367-369.

Carter, N.L., Christie, J.M. & Griggs, D.T. 1961. Experimentally produced deformation lamellas and other structures in quartz sand (Abst). *J. Geophys. Res.* **66,** 2518-2519.

Carter, N. L., Christie, J. M. & Griggs, D. T. 1964. Experimental deformation and recrystallization of quartz. *J. Geol.* **72,** 687-733.

Carter, N.L. & Tsenn, M.C. 1987. Flow properties of continental lithosphere. *Tectonophysics* **136,** 27-63.

Chen, I.W. & Hwang, S.L. 1992. Shear thickening creep in superplastic silicon nitride. *J. Am. Ser. Soc.* **75,** 1073-1079.

Chernov, A.A. & Dimitrov, V.S. 1989. Interaction between dislocations and cellular front of crystallization: (0001) SiO_2 face. *J. Cryst. Growth* **96,** 304-315.

Christie, J.M. & Ardell, A.J. 1974. Substructures of deformation lamellae in quartz. *Geology* **2,** 405-408.

Christie, J.M. & Green, H.W. 1964. Several new slip mechanisms in quartz. *Trans. Am. Geophys. Union.* **45,** 103.

Christie, J.M. & Raleigh, C.B. 1959. The origin of deformation lamellae in quartz. *Am. J. Sci.* **257,** 385-407.

Christie, J.M., Ardell, A.J. & Balderman, M.A. 1973. The substructure of basal lamellae in experimentally deformed quartz. *EOS, Trans. AGU* **54,** 453.

Christie, J. M., Griggs, D. T. & Carter, N. L. 1964a. Experimental evidence of basal slip in quartz. *J. Geol.* **72,** 734-756.

Christie, J.M., Heard, H.C. & LaMorie, P.N. 1964b. Experimental deformation of quartz single crystals at 27 to 30 kilobars confining pressure and 24°C. *Am. J. Sci.* **262,** 26-55.

Clarke, D.R. 1987. On the equilibrium thickness of intergranular glass phases in ceramic materials. *J. Am. Ceram. Soc.* **70,** 15-22.

Clarke, D.R. 1989. High-temperature microstructure of a hot-pressed silicon nitride. *J. Am. Ceram. Soc.* **72,** 1604-1609.

Coble, R.L. 1963. A model for boundary diffusion controlled creep in polycrystalline materials. *J. Appl. Phys.* **34,** 1679-1682.

Connolly, J.A.D. & Thompson, A.B. 1989. Fluid and enthalpy production during regional metamorphism. *Contrib. Mineral. Petrol.* **102,** 347-266

Cooper, R.F. & Kohlstedt, D.L. 1984. Solution-precipitation enhanced diffusional creep of partially molten olivine-basalt aggregates during hot-pressing. *Tectonophysics* **107,** 207-233.

Cordier, P. & Doukhan, J.C. 1989. Water solubility in quartz and its influence on ductility. *Eur. J. Mineral.* **1,** 221-237.

Cordier, P. & Doukhan, J.C. 1991. Water speciation in quartz: A near infrared study. *Am. Miner.* **76,** 361-369.

Cox, S.F. & Etheridge, M.A. 1983. Crack-seal fibre growth mechanisms and their significance in the development of oriented layer silicate microstructures. *Tectonophysics* **92,** 147-170.

Cox, S.F. & Etheridge, M.A. 1989. Coupled grain-scale dilatancy and mass transfer during deformation at high fluid [pressures: examples from Mount Lyell, Tasmania. *J. Struct. Geol.* **11,** 147-162.

Crevola, G. 1987. Ortho-mica schists as products of synmetamorphic ductile shear deformation of granites with mass transfer: main features and examples from the Variscan fold belt of Southern France. *Geodynamica Acta* **1,** 207-221.

Dell'Angelo, L. N. & Tullis, J. 1986. A comparison of quartz c-axis preferred orientations in experimentally deformed aplites and quartzites. J. Struct. *Geol.* **8,** 683-692.

Dell'Angelo, L.N. & Tullis, J. 1989. Fabric development in experimentally sheared quartzites. *Tectonophysics* **169,** 1-21.

Den Brok, S.W.J. 1989. The effect of water on the experimental deformation of natural quartzite: evidence for diffusional creep. *Terra abstr.* **1,** nr. 1, EUG V, Strasbourg, 20-23 March 1989.

Den Brok, S.W.J. 1990. Experimental evidence for water-weakening of quartzite by microcracking plus solution-precipitation creep. *EOS Trans. AGU* **71,** 640.

Den Brok, S.W.J. 1991. Development of apparent crystal-plastic deformation microstructures in quartz by stable extensional microcracking plus solution-precipitation creep. *Int. Conf. on mechanical instabilities in rocks & tectonics, Montpellier, 4-6 september 1991. Terra Nova* **3,** *Abstr. Suppl.* **5,** 33.

Den Brok, S.W.J. & Spiers, C.J. 1991. Experimental evidence for water weakening of quartzite by microcracking plus solution-precipitation creep. *J. geol. Soc. London* **148,** 541-548.

De Roo, J.A. 1989. Mass transfer and preferred orientation development during extensional microcracking in slate-belt folds, Elura mine, Australia. *J. Metam. Geol.* **7,** 311-322.

De Roo, J.A. & Williams, P.F. 1990. Dynamic recrystallization and solution transfer in mylonitic rocks of the Tetagouche group, northern New Brunswick, Canada. *Geol. Soc. Am. Bull.* **102,** 1544-1554.

Doukhan, J.C. & Trépied, L. 1985. Plastic deformation of quartz single crystals. *Bull. Minéral.* **108,** 97-123.

Dudziak, K.H. & Franck, E.U. 1966. Messungen der Viskosität des Wassers bis 560°C und 3500 bar. *Ber. Bunsinges Phys. Cem.* **70,** 1120-1128.

Durney, D.W. 1972. Solution-transfer, an important geological deformation mechanism. *Nature* **235,** 315-317.

Elliott, D. 1973. Diffusion flow laws in metamorphic rocks. *Geol. Soc. Am. Bull.* **84,** 2645-2664.

Elphick, S.C., Dennis, P.F. & Graham, C.M. 1986. An experimental study of diffusion of oxygen in quartz and albite using an overgrowth technique. *Contrib. Mineral. Petrol.* **92,** 322-330.

Etchecopar, A. 1977. A plane kinematic model of progressive deformation in a polycrystalline aggregate. *Tectonophysics.* **39,** 121-139.

Etchecopar, A. & Vasseur, G. 1987. A 3-D kinematic model of fabric development in polycrystalline aggregates: comparisons with experimental and natural samples. *J. Struct. Geol.* **9,** 705-717.

Etzler, F.M. 1988. Enhancement of hydrogen bonding in vicinal water: heat capacity of water and deuterium oxide in silica pores. *Langmuir* **4,** 878-883.

Etzler, F.M. & Fagundus, D.M. 1987. The extent of vicinal water: implications from the density of water in silica pores. *J. Colloid Interface Sci.* **115,** 513-519.

Evans, B. & Dresen, G. 1991. Deformation of earth materials: six easy pieces. in: Contributions in Tectonophysics, U.S. National Report 1987-1990 *Reviews of Geophysics, Supplement,* 823-843.

Fairbairn, H.W. 1941. Deformation lamellae in quartz from the Ajibik formation, Michigan. *Bull. Geol. Soc. Am.* **52,** 1265-1278.

Farver, J.R. & Yund, R.A. 1991a. Oxygen diffusion in quartz: dependence on temperature and water fugacity. *Chemical Geology* **90,** 55-70.

Farver, J.R. & Yund, R.A. 1991b. Measurement of oxygen grain boundary diffusion in natural, fine-grained, quartz aggregates. *Geochim. Cosmochim. Acta* **55,** 1597-1607.

Fellows, R.E. 1943. Recrystallization and flowage in Appalachian quartzite. *Bull. Geol. Soc. Am.* **54,** 1399-1432.

Fisher, J.R. 1976. The volumetric properties of H_2O - a graphical portrayal. *J. Res. U.S. Geol. Survey* **4,** 189-193.

Fitz Gerald, J.D., Ord, A., Boland, J.N. & McLaren, A.C. 1987. The water-weakening effect in experimental deformation of quartz. Int. Conf. on Deformation of Crustal Rocks, *Geol. Soc. Australia, Abstr.* **19,** 68.

Fitz Gerald, J.D., Boland, J.N., McLaren, A.C., Ord, A. & Hobbs, B.E. 1991. Microstructures in water-weakened single crystals of quartz. *J. Geophys. Res.* **96,** 2139-2155.

Fletcher, R.C. & Hofmann, A.W. 1974. Simple models of diffusion and combined diffusion-infiltration metasomatism. *Geochemical transport and kinetics* (editors: Hofmann, A.W. et al.) Carnegie Inst. of Washington, 243-259.

Fyfe, W.S., Price, N.J. & Thompson, A.B. 1978. *Fluids*

in the earth's crust. Elsevier, Amsterdam

Gee, M.L., McGuiggan, P.M. & Israelachvili, J.N. 1990. Liquid to solidlike transitions of molecularly thin films under shear. *J. Chem. Phys.* **93,** 1895-1906.

Gerretsen, J., Paterson, M.S. & McLaren, A.C. 1989. The uptake and solubility of water in quartz at elevated pressure and temperature. *Phys. Chem. Miner.* **16,** 334-342.

Gleason, G., Tullis, J. & Heidelbach, F. 1990. The effect of dynamic recrystallization on the lattice preferred orientation of quartz aggregates. *Abstracts with Programs* **A137.**

Goltrant, O., Cordier, P. & Doukhan, J.C. 1991. Planar deformation features in shocked quartz; a transmission electron microscopy investigation. *Earth Planet. Sci. Lett.* **106,** 103-115.

Grant, P.R. & White, S.H. 1978. Cathode luminescence and microstructure of quartz overgrowth on quartz. *Scann. Electr. Microsc.* **1,** 189-194.

Gratier, J.P. & Jenatton, L. 1984. Deformation by solution-deposition, and re-equilibration of fluid inclusions in crystals depending on temperature, internal pressure and stress. *J. Struct. Geol.* **6,** 189-200.

Gratz, A.J. 1991. Solution-transfer compaction of quartzites: progress toward a rate law. *Geology* **19,** 901-904.

Gratz, A.J., Bird, P. & Quiro, G.B. 1990. Dissolution of quartz in aquous basic solution, 106-236°C: surface kinetics of "perfect" crystallographic faces. *Geochim. Cosmochim. Acta* **54,** 2911-2922.

Green, H. W. & Borch, R.S. 1989. A new moltem salt cell for precision stress measurement at high pressure. *Eur. J. Mineral.* **1,** 213-219.

Green, H. W., Griggs, D. T. & Christie, J. M. 1970. Syntectonic and annealing recrystallization of fine-grained quartz aggregates. In: *Experimental and Natural Rock Deformation* (edited by Paulitsch, P.) Springer Verlag, Berlin-Heidelberg, 272-335.

Griggs, D.T. 1967. Hydrolytic weakening of quartz and other silicates. *Geophys. J. R. Astr. Soc.* **14,** 19-31.

Griggs, D.T. 1974. A model of hydrolytic weakening in quartz. *J. Geophys. Res.* **79,** 1653-1661.

Griggs, D. T. & Bell, J. F. 1938. Experiments bearing on the orientation of quartz in deformed rocks. *Geol. Soc. Am. Bull.* **49,** 1723-1746.

Griggs, D.T. & Blacic, J.D. 1964. The strength of quartz in the ductile regime. *Trans. Am. Geophys. Union* **45,** 102-103.

Griggs, D.T. & Blacic, J.D. 1965. Quartz: anomalous weakness of synthetic crystals. *Science* **147,** 292-295.

Hacker, B.R., Yin, A., Christie, J.M. & Snoke, A.W. 1990. Differential stress, strain rate, and temperature of mylonitization in the Ruby Mountains, Nevada: implications for the rate and duration of uplift. *J. Geophys. Res.* **95,** 8569-8580.

Heard, H.C. & Carter, N.L. 1968. Experimentally induced "natural" intragranular flow in quartz and quartzite. *Am. J. Sci.* **266,** 1-42.

Heggie, M. & Jones, R. 1986. Models of hydrolytic weakening in quartz. *Phil. Mag., A* **53,** L65-L70.

Hickman, S.H. & Evans, B. 1991. Experimental pressure solution in halite: the effect of grain/interphase boundary structure. *J. Geol. Soc. Lond.* **148,** 549-560.

Hietanen, A. 1938. On the petrology of the Finnish quartzites. *Bull. Comm. Geol. Finlande* **122,** 1-118.

Hirth, G. & Tullis, J. 1992. Dislocation creep regimes in quartz aggregates. *J. Struct. Geol.* **14,** 145-159.

Hobbs, B.E. 1968. Recrystallization of single crystals of quartz. *Tectonophysics* **6,** 353-401.

Hobbs, B.E., McLaren, A.C. & Paterson, M.S. 1972. Plasticity of single crystals of synthetic quartz. In: Flow and fracture of rocks, edited by: Heard, H.C., Borg, I.Y., Carter, N.L. & Raleigh, C.B. *Geophys. Monogr.* **16,** 29-53.

Hobbs, B.E., Means, W.D. & Williams, P.F. 1976. *An outline of structural geology.* John Wiley & Sons, Inc., New York, 571 pp.

Hofmann, J. 1973. c-Achsenorientierung von Quarz in kataklastisch deformierten Sandsteinen und in Quarzharnischen der Lagerstätte Nikitowka/Donezk-Becken (UdSSR). *Z. Geol. Wiss. Berlin* **1,** 683-701.

Horn, R.G., Clarke, D.R. & Clarkson, M.T., 1988. Direct measurement of surface forces between sapphire crystals in aqueous solutions. *J. Mat. Res.* **3,** 413-416.

Horn, R.G., Smith, D.T. & Haller, W. 1989. Surface forces and viscosity of water measured between silica sheets. *Chemical Physics Letters.* **162,** 404-408.

Hwang, C.M.J. & Chen, I.W. 1990. Effect of a liquid phase on superplasticity of 2-mol%-Y_2O_3-stabilized terragonal zirconia polycrystals. *J. Am. Cer. Soc.* **73,** 1626-1632.

Ildefonse, J.P. & Gabis, V. 1976. Experimental study of silica diffusion during metasomatic reactions in the presence of water at 550°C and 1000 bars. *Geochim. Cosmochim. Acta* **40,** 297-303.

Israelachvili, J.N. 1986. Measurement of the viscosity of liquids in very thin films. *J. Colloid Interface Sci.* **110,** 263-271.

Israelachvili, J.N. 1992. Adhesion forces between surfaces in liquids and condensable vapours. *Surface Science Reports* **14,** 109-159.

Israelachvili, J.N. & Kott, S.J. 1989. Shear properties and structure of simple liquids in molecularly thin films: the transition from bulk (continuum) to molecular behaviour with decreasing film thickness. *J. Colloid Interface Sci.* **129,** 461-467.

Israelachvivili, J., McGuiggan, P., Gee, M., Homola, A., Robbins, M. & Thompson, P. 1990. Liquid dynamics in molecularly thin films. *J. Phys. Condens. Matter.* **2,** SA89-SA98.

Israelachvili, J.N., McGuiggan, P.M. & Homola, A.M. 1988. Dynamic properties of molecularly thin liquid films. *Science Reports* **240,** 189-191.

Jaoul, O., Shelton, G. & Tullis, J. 1981. Quartzite deformation as a function of water at 15 kb: preliminary results. *EOS, Trans. AGU* **62,** 396.

Jaoul, O., Tullis, J. & Kronenberg, A.K. 1984. The effect of varying water content on the creep behaviour of Heavitree quartzite. *J. Geophys. Res.* **89,** 4298-4312.

Jessel, M. W. & Lister, G. S. 1990. A simulation of the temperature dependence of quartz fabrics. In: *Deformation Mechanisms, Rheology & Tectonics* (edited by Knipe, R. J. & Rutter, E. H.) *Geol. Soc. Spec. Publ.* **54,** 353-362.

Kamb, W.B. 1959. Theory of preferred orientation developed by crystallization under stress. *J. Geol.* **67,** 153-170.

Kano, T. 1991. Metasomatic origin of augen gneisses and related mylonitic rocks in the Hida metamorphic complex, central Japan. *Mineralogy and Petrology* **45,** 29-45.

Karato, S. & Masuda, T. 1989. Anisotropic grain growth in quartz aggregates under stress and its implication for foliation development. *Geology* **17,** 695-698.

Kats, A., Haven, Y. & Stevels, J.M. 1962. Hydroxyl

groups in α-quartz. *Phys. Chem. Glasses* **3**, 69-75.
Kekulawala, K.R.S.S., Paterson, M.S. & Boland, J.N. 1978. Hydrolytic waekening in quartz. *Tectonophysics* **46**, T1-T6.
Kekulawala, K.R.S.S., Paterson, M.S. & Boland, J.N. 1981. An experimental study of the role of water in quartz deformation. In: Mechanical behaviour of crustal rocks, edited by: Carter, N.L. et al. *Geophys. Monogr.* **24**, 49-60.
Kern, H. 1977. Preferred orientation of experimentally deformed limestone marble, quartzite and rock salt at different emperatures and states of stress. *Tectonophysics* **39**, 103-120.
Kerrich, R., Allison, I., Barnett, R.L., Moss, S. & Starkey, J. 1980. Microstructural and chemical transformations accompanying deformation of granite in a shear zone at Miéville, Switzerland; with implications for stress corrosion cracking and superplastic flow. *Contrib. Mineral. Petrol.* **73**, 221-242.
Kirby, S.H. 1985. Rock mechanics observations pertinent to the rheology of the continental lithosphere and the localization of strain along shear zones. *Tectonophysics* **119**, 1-27.
Kirby, S.H. & McCormick, J.W. 1979. Creep of hydrolytically weakened synthetic quartz crystals oriented to promote {2$\underline{1}$10}<0001> slip: a brief summary of work to date. *Bull. Minéral.* **102**, 124-137.
Kirby, S.H. & Kronenberg, A.K. 1984. Hydrolytic weakening of quartz: uptake of molecular water and the role of microfracturing. *EOS AGU Trans.* **65**, 277.
Knipe, R.J. 1989. Deformation mechanisms - recognition from natural tectonites. *J. Struct. Geol.* **11**, 127-146.
Knipe, R.J. 1990. Microstructural analysis and tectonic evolution in thrust systems: examples from the Assynt region of the Moine Thrust Zone, north-west Scotland. In: *Deformation processes in minerals, ceramics, and rocks* (edited by Barber, D.J. & Meredith, P.G.), Unwin Hyman, London, 228-261.
Koch, P.S., Christie, J.M, Ord, A. & George, R.P., Jr. 1989. Effect of water on the rheology of experimentally deformed quartzite. *J. Geophys. Res.* **94**, 13975-13996.
Kozlovsky, Ye.A. (editor) 1984. *The superdeep well of the Kola peninsula-exploration of the deep continental crust*. Springer-Verlag Berlin, 588 p.
Kronenberg, A.K. & Tullis, J. 1984. Flow strengths of quartz aggregates: grain size and pressure effects due to hydrolytic weakening. *J. Geophys. Res.* **89**, 4281-4297.
Kronenberg, A.K. & Wolf, G.H. 1990. Fourier transform infrared spectroscopy determinations of intragranular water content in quartz-bearing rocks: implications for hydrolytic weakening in the laboratory and within the earth. *Tectonophysics* **172**, 255-271.
Kronenberg, A.K., Segall, P. & Wolf, G.H. 1990. Hydrolytic weakening and penetrative deformation within a natural shear zone. In: The brittle-ductile transition in rocks (edited by Duba, A.G. et al.). *Geophys. Monogr.* **56**, 21-36.
Kronenberg, A.K., Kirby, S.H., Aines, R.D. & Rossman, G.R. 1986. Solubility and diffusional uptake of hydrogen in quartz at high water pressures: Implications for hydrolytic weakening. *J. Geophys. Res.* **91**, 12723-12744.
Kwon Oh-Hun & Messing, G.L. 1991. A theoretical analysis of solution-precipitation controlled densification during liquid phase sintering. *Acta metall. mater.* **39**, 2059-2068.
Langmuir, D. 1971. Particle size effect on the reaction: goethite = hematite + water. *Am. J. Sci.* **271**, 147-156.
Law, R.D. 1990. Crystallographic fabrics: a selective review of their applications to research in structural geology. in: *Deformation mechanisms, rheology and tectonics,* (edited by Knipe, R.J. & Rutter, E.H.) Geological Society Special Publication **54**, 35-352.
Lehner, F.K. 1990. Thermodynamics of rock deformation by pressure solution. *Deformation processes in minerals, ceramics & rocks* (edited by Barber & Meredith), 296-333.
Lehner, F.K. & Bataille, J. 1984. Non-equilibrium thermodynamics of pressure solution. *Pure and Applied Geophysics* **122**, 53-85.
Linker, M.F. & Kirby, S.H. 1981. Anisotropy in the rheology of hydrolytically weakened quartz-crystals. In: Mechanical behaviour of crustal rocks, edited by: Carter, N.L. et al. *Geophys. Monogr.* **24**, 29-48.
Linker, M.S., Kirby, S.H., Ord, A. & Christie, J.M. 1984. Effects of compression direction rheology of hydrolytically weakened synthetic quartz crystals at atmospheric pressure. *J. Geophys. Res.* **91**, 12723-12744.
Lister, G. S. & Hobbs, B. E. 1980. The simulation of fabric development during plastic deformation and its application to quartzite: the influence of deformation history. *J. Struct. Geol.* **2**, 355-370.
Lister, G.S. & Paterson, M.S. 1979. The simulation of fabric development during plastic deformation and its application to quartzite: fabric transitions. *J. Struct. Geol.* **1**, 99-115.
Lister, G. S., Paterson, M. S. & Hobbs, B. E. 1978. The simulation of fabric development in plastic deformation and its application to quartzite: the model. *Tectonophysics* **45**, 107-158.
Mackwell, S.J. & Weathers, M.S. 1987. The effects of fluid environments on the transport of metallic cations in quartzites. *EOS, Trans. AGU* **68**, 1490.
Mackwell, S.J., Lee, V.W. & Brantley, S.L. 1989. Fluid distribution in crustal rocks and effects on rheology. *28th Int. Geol. Congr., Washington, abstr.* **2**, July 9-19, 1989, USA.
Magda, J.J., Tirrell, M. & Davis, H.T. 1985. Molecular dynamics of narrow, liquid-filled pores. *J. Chem. Phys.* **83**, 1888- 1901.
Mainprice, D.H. 1981. *The experimental deformation of quartz polycrystals*, PhD-thesis Austr. Nat. Univ., Canberra, 171 p.
Mainprice, D.H. & Paterson, M.S. 1984. Experimental studies on the role of water in the plasticity of quartzites. *J. Geophys. Res.* **89**, 4257-4269.
Masuda, T. & Fujimura, A. 1981. Microstructural development of fine-grained quartz aggregates by syntectonic recrystallization. *Tectonophysics* **72**, 105-128.
McLaren, A.C. & Hobbs, B.E. 1972. Transmission electron microscope investigation of some naturally deformed quartzites. In: Flow and fracture of rocks, edited by: Heard, H.C., Borg, I.Y., Carter, N.L. & Raleigh, C.B. *Geophys. Monogr.* **16**, 55-66.
McLaren, A.C. & Phakey, P.P. 1965. Dislocations in quartz observed by transmission electron microscopy. *J. Appl. Phys.* **36**, 3244-3246.
McLaren, A.C. & Retchford, J.A. 1969. TEM studyof the dislocations in experimentally deformed synthetic

quartz. *Phys. Stat. Sol.* **33,** 657-668.
McLaren, A.C., Retchford, J.A., Griggs, D.T. & Christie, J.M. 1967. Transmission electron microscopy study of Brazil twins and dislocations experimentally produced in natural quartz. *Phys. Stat. Sol.* **19,** 631-644.
McLaren, A.C., Turner, R.G. & Boland, J.N. 1970. Dislocation structure of the deformation lamellae in synthetic quartz: a study by electron and optical microscopy. *Contr. Mineral. Petrol.* **29,** 104-115.
McLaren, A.C., Fitzgerald, J.D. & Gerretsen, J. 1989. Dislocation nucleation and multiplication in synthetic quartz: relevance to water weakening. *Phys. Chem. Minerals* **16,** 465-482.
Mitra, G. 1979. Ductile deformation zones in Blue Ridge basement rocks and estimation of finite strains. *Geol. Soc. Am. Bull.* **90,** 935-951.
Morrison-Smith, D.J., Paterson, M.S. & Hobbs, B.E. 1976. An electron microscope study of plastic deformation in single crystals of synthetic quartz. *Tectonophysics* **33,** 43-79.
Mügge, O. 1896. Der Quarzporphyr der Bruchhäuser-Steine in Westfalen. *N. Jb. Mineral. Geol. Paleont.* Beil.-Band **10,** 757-787.
Mügge, O. 1898. Ueber Translationen und verwandte Erscheinungen in Krystallen. *N. Jb. Min. Geol. Paleont.* **1,** 71-158.
Naha, K. 1958. Time of formation and kinematic significance of deformation lamellae in quartz. *J. Geol.* **66,** 120-124.
Nicolas, A. 1984. *Principes de tectonique.* Masson, Paris, 196 pp.
Nicolas, A., & Poirier, J.P. 1976. *Crystalline plasticity and solid state flow in metamorphic rocks.* Wiley Interscience, London, 444 pp.
Norris, R.J. & Henley, R.W. 1976. Dewatering of a metamorphic pile. *Geology* **4,** 333-336.
Nyman, M.W., Law, R.D. & Smelik, E.A. 1992. Cataclastic deformation mechanism for the development of core-mantle structures in amphibole. *Geology* **20,** 455-458.
Ord, A. & Hobbs, B.E. 1986. Experimental control of the water weakening effect in quartz. In Mineral and Rock Deformation: Laboratory Studies, edited by B.E. Hobbs and H.C. Heard. *Geophys. Monogr.* **36,** 51-72, AGU, Washington.
Ord, A. & Hobbs, B.E. 1987. The plastic deformation of quartz. Int. Conf. on Deformation of Crustal Rocks, *Geol. Soc. Australia, Abstr.* **19,** 70-72.
Ord, A. & Hobbs, B.E. 1989. The strength of the continental crust, detachment zones and the development of plastic instabilities. *Tectonophysics* **158,** 269-289.
Parrish, D.K., Krivz, A.L. & Carter, N.L. 1976. Finite-element folds of similar geometry. *Tectonophysics* **32,** 183-207.
Parks, G.A. 1984. Surface and interfacial free energies of quartz. *J. Geophys. Res.* **89,** 3997-4008.
Paterson, M.S. 1982. The determination of hydroxyl by infrared absorption in quartz, silicate glasses and similar materials. *Bull. Minéral.* **105,** 20-29.
Paterson, M.S. 1986. The thermodynamics of water in quartz. *Phys. Chem. Miner.* **13,** 245-255
Paterson, M.S. 1989. The interaction of water with quartz and its influence in dislocation flow - an overview. In: *Rheology of Solids and of the Earth* (edited by Karato, S. & Toriumi, M.). Oxford University Press, New York, NY, 107-142.
Paterson, M.S. & Luan, F.C. 1990. Quartzite rheology under geological conditions. In: Deformation mechanisms, Rheology and Tectonics (edited by Knipe, R.J. & Rutter, E.H.). *Geol. Soc. Spec. Publ.* **54,** 299-307.
Peschel, G. & Adlfinger, K.H. 1970. Viscosity anomalies in liquid surface zones. IV. The apparent viscosity of water in thin layers adjacent to hydroxylated fused silica surfaces. *J. Colloid Interface Sci.* **34,** 505-510.
Peschel, G., Belouschek, P., Müller, M. M., Müller, M.R. & König, R. 1982. The interaction of solid surfaces in aqueous systems. *Colloid & Polymer Science.* **260,** 444-451.
Phillips, W.J. 1965. The deformation of a basement granite and the development of major silicified shear zones in Uganda. *Am. J. Sci.* **263,** 696-711.
Power, W. L. & Tullis, T. E. 1989. The relationship between slickenside surfaces in fine-grained quartz and the seismic cycle. *J. Struct. Geol.* **11,** 879-893.
Price, G. P. 1985. Preferred orientations in quartzites. In: Preferred Orientation in Deformed Metals and Rocks: *An Introduction to Modern Texture Analysis* (edited by Wenk, H. R.) Academic Press, London, 385-406.
Raj, R. 1982. Creep in polycrystalline aggregates by matter transport trhough a liquid phase. *J. Geophys. Res.* **87,** 4731-4739.
Raj, R. & Chyung, C.K. 1981. Solution-precipitation creep in glass ceramics. *Acta Metall.* **29,** 159-166.
Ralser, S. 1990. Shear zones developed in an experimentally deformed quartz mylonite. *J. Struct. Geol.* **12,** 1033-1045.
Ralser, S., Hobbs, B. E. & Ord, A. 1991. Experimental deformation of a quartz mylonite. *J. Struct. Geol.* **13,** 837-850.
Riley, N.A. 1947. Structural petrology of the Baraboo quartzite. *J. Geology* **55,** 453-475.
Rovetta, M.R., Holloway, J.R. & Blacic, J.D. 1986. Solubility of hydroxyl in natural quartz annealed in water at 900°C and 1.5 GPa. *Geophys. Res. Lett.* **13,** 145-148.
Rubie, D.C. 1986. The calatysis of minetal reactions by water and restrictions on the presence of aqueous fluid during metamorphism. *Mineral. Mag.* **50,** 399-415.
Rutter, E.H. 1976. The kinetics of rock deformation by pressure solution. *Phil. Trans. R. Soc. Lond.* A **283,** 203-219.
Rutter, E.H. 1983. Pressure solution in nature, theory and experiment. *J. Geol. Soc. Lond.* **140,** 725-740.
Sander, B. 1911. Über Zusammenhänge zwischen Teilbewegung und Gefüge in Gesteinen. *Tscherm. Mineral. Petrogr. Mitt.* **30,** 281-314.
Schmid, S.M. & Casey,, M. 1986. Complete texture analysis of commonly observed quartz c-axis patterns. In: Mineral and rock deformation: laboratory studies (edited by Hobbs, B.E. & Heard, H.C.), *Geophys. Monogr.* **36,** 263-286.
Schmid, S.M. & Handy, M.R. 1991. Towards a genetic classification of fault rocks: geological usage and tectonophysical implications. *Controversies in modern geology* (edited by Muller, D.W., McKenzie, J.A. & Weissert, H.), academic press, London, 339-361.
Schoen, M., Cushman, J.H., Diestler, D.J. & Rhykerd, C.L. 1988. Fluids in micropores. II. Self-diffusion in a simple classical fluid in a slit pore. *J. Chem. Phys.* **88,** 1394-1407.
Sederholm, J.J. 1895. Über einen metamorphosirten Preacambrischen Quarzporphyr von Karvia in der Provinz Åbo. *Bull. Comm. Geol. Finlande* **I (2),** 1-16.
Schutjens, P.M.T.M. 1991. Intergranular pressure solution

in halite aggregates and quartz sands: an experimental investigation. *Geologica Ultraiectina* **76,** 233 pp.

Sharma, N.K., Ward, I.D., Fraser, H.L. & Williams, W.S. 1980. STEM analysis of grain boundaries in cemented carbides. *J. Am. Ceram. Soc.* **63,** 194-196.

Shelley, D. 1989. Plagioklase and quartz preferred orientations in alow-gradeschist: the roles of primary growth and plastic deformation. *J. Struct. Geol.* **11,** 1029-1037.

Sibson, R.H. 1983. Continental fault structure and the shallow earthquake source. *J. Geol. Soc.* **140,** 741-767

Simpson, C. 1983. Strain and shape-fabric variations associated with ductile shear zones. *J. Struct. Geol.* **5,** 61-72.

Spiers, C.J. & Brzesowsky, R.H. 1992. Densification behaviour of wet granular salt: theory versus experiment. *Proceedings of the Seventh International Symposium on Salt,* 6-9 april 1992, Kyoto, Japan, In press.

Spiers, C.J. & Schutjens, P.M.T.M. 1990. Densification of crystalline aggregates by fluid phase diffusional creep. In: *Deformation processes in minerals, ceramics, and rocks* (edited by Barber, D.J. & Meredith, P.G.), Unwin Hyman, London, 334-353.

Spiers, C.J., Schutjens, P.M.T.M., Brzesowsky, R.H., Peach, C.J., Liezenberg, J.L. & Zwart, H.J. 1990. Experimental determination of constitutive parameters governing creep of rocksalt by pressure solution. *Deformation mechanisms, rheology and tectonics,* (edited by Knipe, R.J. & Rutter, E.H.) Geological Society Special Publication **54,** 215-227.

Spiers, C.J., Urai, J.L., Lister, G.S., Boland, J.N. & Zwart, H.J. 1986. The influence and fluid-rock interaction on the rheology of salt rock. *Nuclear Science and Technology,* **EUR 10399 EN.** Office for Official Publications of the European Communities, Luxembourg. 131 pp.

Starkey, J. & Sutherland, I. 1978. A re-investigation of the orientation of quartz in a shear zone from Castell Odair, Scotland. *Can. J. Earth Sci.* **15,** 664-667.

Storre, B. 1972. Dry melting of muscovite + quartz in the range P_s = 7 kb to P_s = 20 kb. *Contrib. Min. Petr.* **37,** 87-89.

Storre, B. & Karotke, E. 1971. An experimental determination of the upper stability limit of muscovite + quartz in the range 7-20 kb water pressure. *N. Jahrb. Min. Monatsh.* **1971,** 237-240.

Storre, B. & Karotke, E. 1972. Experimental data on melting reactions of muscovite + quartz in the system K_2O - Al_2O_3 - SiO_2 - H_2O to 20 kb water pressure. *Contrib. Min. Petr.* **36,** 343-345.

Thompson, A.B. & Connolly, A.D. 1992. Migration of metamorphic fluid: some aspects of mass and heat transfer. *Earth-Science Reviews* **32,** 107-121.

Trépied, L. & Doukhan, J.C. 1982. Transmission electron microscopy study of quartz
single crystals deformed at room temperature and atmospheric pressure by indentations. *J. Physique* **43,** L77-L81.

Tullis, J. 1977. Preferred orientation of quartz produced by slip during plane strain. *Tectonophysics* **39,** 87-102.

Tullis, J. 1990. Experimental studies of deformation mechanisms and microstructures in quartzo-feldspathic rocks. *Deformation processes in minerals, ceramics & rocks* (edited by Barber & Meredith), 190-227

Tullis, J. & Yund, R.A. 1982. Grain growth kinetics of quartz and calcite aggregates. *J. Geol.* **90,** 301-318.

Tullis, J. & Yund, R.A. 1985. Hydrolytic weakening of quartz aggregates: requirement for rapid water penetration. *EOS, Trans. AGU* **66,** 1084.

Tullis, J. & Yund, R.A. 1989. Hydrolytic weakening of quartz aggregates: the effects of water and pressure on recovery. *Geophys. Res. Lett.* **16,** 1343-1346.

Tullis, J., Christie, J.M. & Griggs, D.T. 1973. Microstructures and preferred orientations of experimentally deformed quartzites. *Bull. Geol. Soc. Am.* **84,** 297-314.

Tullis, J., Dell'Angelo, L. & Yund, R.A. 1990. Ductile shear zones from brittle precursors in feldspathic rocks: the role of dynamic recrystallization. In: The brittle-ductile transition in rocks (edited by Duba, A.G. et al.). *Geophys. Monogr.* **56,** 67-81.

Tullis, T.E. & Tullis, J. 1986. Experimental rock deformation techniques. In Mineral and Rock Deformation: Laboratory Studies, edited by B.E. Hobbs and H.C. Heard. *Geophys. Monogr.* **36,** 297-324, AGU, Wahington.

Turner, F.J. 1948. Note on the tectonic significance of deformation lamellae in quartz and calcite. *AGU Trans.* **29,** 565-569.

Turner, F.J. & Weiss, L.E. 1963. *Structural analysis of metamorphic tectonites.* New York, McGraw-Hill Book Co., 545 p.

Urai, J.L. 1983. Water-assisted dynamic recrystallization and weakening in polycrystalline bischofite. *Tectonophysics* **96,** 125-157.

Urai, J.L., Means, W.D. & Lister, G.S. 1986. Dynamic recrystallization of minerals. in: Mineral and rock deformation: laboratory studies (edited by Hobbs, B.E. & Heard. H.C.), *Geophys. Monogr.* **36,** 161-199.

Vanderlick, T.K. % Davis, H.T. 1987. Self-diffusion in fluids in microporous solids. *J. Chem. Phys.* **87** (3), 1791- 1795.

Voll, G. 1960. New work on petrofabrics. *Liverpool & Manchester Geol. J.* **2,** 503-567.

Walther, J.V. & Wood, B.J. 1986. Mineral-fluid reaction rates. In: *Fluid-rock interactions during metamorphism.* edited by: Walther, J.V. & Wood, B.J. Springer, New York Berlin Heidelberg Tokyo, 194-211.

Walton, M. 1960. Molecular diffusion rates in supercritical water vapor estimated from viscosity data. *Am. J. Sci.* **258,** 385-401.

Wang, J.G. & Raj, R. 1984. Mechanism of superplastic flow in a fine-grained ceramic containing some liquid phase. *J. Am. Ceram. Soc.* **67,** 399-409.

Watson, E.B. & Brenan, J.M. 1987. Fluids in the lithosphere, 1. Experimentally-determined wetting characteristics of CO_2-H_2O fluids and their implications for fluid transport, host-rock physical properties, and fluid inclusion formation. *Earth Planet. Sci. Lett.* **85,** 497-515.

Weinschenk, E. 1902. Ueber die Plasticität der Gesteine. *Centralblatt für Mineralogie, Geologie und Paleontologie* **1902,** 161-171.

Wenk, H.R. (editor) 1985. *Preferred orientation in deformed metals and rocks: an introduction to modern texture analysis.* Academic Press Inc., Orlando, Florida, 610 p.

Wenk, H.R. & Christie, J.M. 1991. Comments on the interpretation of deformation textures in rocks. *J. Struct. Geol.* **13,** 1091-1110.

Wenk, H.R., Canova, G., Molinari, A. & Kocks, U.F. 1989. Viscoplastic modeling of texture development in quartzite. *J. Geophys. Res.* **94,** 17895-17906.

Weyl, P.K. 1959. Pressure solution and the force of crystallization - a phenomenological theory. *J. Geophys. Res.* **64**, 2001-2025.

White, J.C. & White, S.H. 1981. The structure of grain boundaries in tectonites. *Tectonophysics* **78**, 613-628.

White, S.H. 1971. Natural creep deformation of quartzites. *Nature Phys. Sci.* **234**, 175-177.

White, S.H. 1973a. The dislocation structures responsible for the optical effects in some naturally deformed quartzites. *J. Mater. Sci.* **8**, 490-499.

White, S.H. 1973b. Deformation lamellae in naturally deformed quartz. *Nature Phys. Sci.* **245**, 26-28.

White, S.H. 1975. The effects of polyphase deformation on the intracrystalline defect structures of quartz. *N. Jb. Miner. Abh.* **123**, 237-252.

White, S.H. 1976. The effects of strain on the microstructures, fabrics, and deformation mechanisms in quartzites. *Phil. Trans. R. Soc. Lond.* A. **283**, 69-86.

White, S.H., Crosby, A. & Evans, P.E. 1971. Dislocations in naturally deformed quartzite. *Nature Phys. Sci.* **231**,85-86.

Wickham, J.S. 1972. Structural history of a portion of the Blue Ridge, Northern Virginia. *Geol. Soc. Am. Bull.* **83**, 723-760.

Wilson, C.J.L. 1973. The prograde microfrabric in a deformed quartzite dequence, Mount Isa, Australia. *Tectonophysics* **19**, 39-81.

Winkler, H.G.F. 1979. *Petrogenesis of metamorphic rocks*. Fifth Edition, Springer-Verlag, New York.

Wintsch, R.P. & Dunning, J. 1985. The effect of dislocation density on the aqueous solubility of quartz and some geologic implications: a theoretical approach. *J. Geophys. Res.* **90**, 3649-3657.

Wollast, R. & Garrels, R.M. 1971. Diffusion coefficient of silica in seawater. *Nature Phys. Sci.* **229**, 94.

Wood, B.J. & Walther, J.V. 1983. Rates of thydrothermal reactions. *Science* **222**, 413-415.

Wood, B.J. & Walther, J.V. 1986. Fluid flow during metamorphism and its implications for fluid-rock ratios. In: *Fluid-rock interactions during metamorphism*. edited by: Walther, J.V. & Wood, B.J. Springer, New York Berlin Heidelberg Tokyo, 89-108.

NEDERLANDSE SAMENVATTING

Uit bestudering van de "keiharde" brosse gesteenten op het aardoppervlak, is gebleken dat deze diep in de aardkorst bij hoge temperatuur (T) en druk (P) gemakkelijk en duktiel, d.w.z. vloeiend, van vorm kunnen veranderen. Voor structureel geologen en geofysici is het van groot belang om te begrijpen *hoe* deze duktiele vormverandering nu eigenlijk precies in z'n werk gaat. Pas dan zijn zij in staat de struktuur (plooien, breuken) en het mechanische gedrag van de aardkorst (het ontstaan van de gebergten, het schuiven van de kontinenten langs elkaar, de aardbevingen) te interpreteren en te modelleren. Een van de belangrijkste mineralen in de kontinentale aardkorst is kwarts. Er is daarom veel experimenteel onderzoek gedaan naar het vloeigedrag van dit mineraal onder hoge P-T kondities. Uit deze experimenten is gebleken dat kwarts onmogelijk duktiel vervormd kan worden als er niet een hele kleine hoeveelheid water in het gesteente aanwezig is. Droge kwarts is "keihard" en bros onder hoge P-T kondities, maar met ongeveer 1 volume procent water is kwarts (onder bepaalde P-T kondities) duktiel en ongeveer 100 keer zo zwak. Dit "water-weakening" effekt is nu al bijna dertig jaar bekend en bestudeerd, maar wordt nog steeds niet goed begrepen. In dit proefschrift wordt de oorzaak van het water-weakening effekt opnieuw onderzocht.

Tot nu toe heeft men altijd aangenomen dat de verzwakkende en duktielmakende werking van het water wordt veroorzaakt doordat het water het kwartskristalrooster in diffundeert in de vorm van punt defekten, en dat hierdoor intrakristallijne, kristal-plastische deformatie mogelijk wordt gemaakt. Deze door water ontstane punt defekten zouden verantwoordelijk zijn voor de vorming van lijn defekten (dislokaties), en bovendien voor het gemakkelijker klimmen, glijden en vermenigvuldigen van deze lijn defekten. In dit proefschrift wordt echter een andere oorzaak voor het water-weakening effekt voorgesteld, namelijk dat het water niet het kristalrooster in diffundeert, maar dat het op de grenzen van de korrels waaruit het kwarts gesteente bestaat oplossings, neerslag, en korrelgrensdiffusie processen mogelijk maakt. Het gesteente kan op die manier van vorm veranderen doordat de kwarts oplost in het water langs de korrelgrenzen loodrecht op de drukrichting, en weer uitkristalliseert langs korrelgrenzen of in mikroskopische barstjes evenwijdig aan de drukrichting.

In hoofdstuk 1 van dit proefschrift wordt de probleemstelling en het doel van het huidige onderzoek uiteengezet. In hoofdstuk 2 wordt beschreven waarom men eigenlijk altijd heeft gedacht dat het water-weakening effekt een intrakristallijn, kristal-plastisch effekt is, en wordt gekonkludeerd dat de argumenten daarvoor niet deugen. De resultaten van de experimenten die ik zelf heb uitgevoerd ter bestudering van het water-weakening effekt in kwarts gesteente worden beschreven in hoofdstuk 3. Hieruit blijkt dat de het natte kwarts gesteente duktiel van vorm verandert door oplossing, diffusie en neerslag processen in het water langs de korrel-grenzen. Dit nieuwe resultaat wordt in de hoofdstukken 4, 5 en 6 verder uitgewerkt.

NAWOORD

Fijn, dat ik nu al diegenen kan bedanken die op de een of andere manier hebben bijgedragen aan de totstandkoming van dit proefschrift. Zo zijn daar allereerst mijn ouders die mij altijd mijn eigen gang hebben laten gaan en die mij hebben leren kijken naar de dingen. Zonder hen zou er van dit proefschrift überhaupt geen sprake zijn geweest. Ook mijn promotor Professor H.J. Zwart en mijn co-promotor Chris Spiers, die mij in staat stelden om te promoveren, hebben mij altijd mijn eigen gang laten gaan, wat ik erg waardeer. Alleen op het eind, toen plotseling bleek dat mijn proefschrift welhaast astronomische proporties had aangenomen, grepen zij in, en met name Chris, die toen die allerlei belangrijks schrapte en de rest herschreef. Ook Magda Martens en Mirjam van Daalen grepen toen in en zorgden dat alles net op tijd toch in orde kwam.

Gert Kastelein, Colin Peach en Eimert de Graaff ben ik in het biezonder dank verschuldigd voor al het werk dat zij voor mij deden in het HPT-lab en aan het 10 kb gas-apparaat. Janos Urai stelde mij in de gelegenheid om met het Griggs apparaat te gaan werken, heeft mij geleerd er mee om te gaan en was steeds geïnteresseerd in de resultaten.

Het fijnste van het promoveren was eigenlijk het begeleiden van de eerste-jaars in Cagli samen met Cees van den Ende, en met Ronald, Hans, en Rob en Albert. Als ik aan mijn promotie terug denk, dan is het vooral aan die tijd - aan de veldtochten, aan het eten, aan het drinken. Dit stond alles in schril kontrast met het leven op het instituut - daar zwoegden kollega-promovendi/voorgangers, die 's nachts en in vaak deerniswekkende toestand door de gangen waarden. Niks geen fijne Italianen, maar bleke, bezorgde, ongezonde hoofden die profeteerden hoe mijn laatste jaar zou zijn.

Professor B. Stöckhert, Jörg Meinecke en Klaus Röller van de Ruhruniversität in Bochum wil ik hartelijk bedanken voor de mogelijkheid en hulp die zij geboden hebben om de FTIR metingen te doen (hoofdstuk 5). Samen met Jörg Meinecke en Klaus Röller werd het onderzoek gedaan dat is beschreven in hoofdstuk 5. Professor H.J. Behr uit Göttingen verleende de mogelijkheid om kathode-luminiscentie metingen te doen op zijn scanning elektronen mikroskoop.

Domingo Aerden, Ronald Bakker, Paul Bons, Hans de Bresser, Rolf Brzesowsky, Mirjam van Daalen, Timon Fliervoet, Siese de Meer, Alice Post, Peter Schutjens, Alfons Simons, en Rian Visser, lazen en korrigeerden stukken tekst, gaven weerwoord, aandacht, betuigden steun, verleenden nu en dan een hand en span dienst, of spraken een bemoedigend woord al dan niet in de kroeg. Dat laatste, en van die aandacht, dat geldt in het biezonder ook voor professor Bernard de Jong.

Verder wil ik nog bedanken: Peter van Krieken (die de TGA kurves maakte), Joop Pieters (die mij met de SEM heeft leren werken), Timon Fliervoet en professor Stan White (die de TEM opnames maakten), Otto, Wout en Inge van de

slijpkamer, Birgit van de fotokamer (die de meeste van de foto's van dit proefschrift heeft afgedrukt), het overige tekenkamer personeel, het personeel van de bibliotheek en Cees, de portier, van wie ik altijd goede zin kreeg.

En niet te vergeten: Rolf Brzesowsky, mijn kamergenoot, die mij trachtte te leren telefoneren, regelen, ordenen, opruimen, en die mij verder met alle benodigde aandacht en bezorgdheid heeft omringd.

En lieve Mirjam, dank je wel.

CURRICULUM VITAE

Bas den Brok werd geboren op 16 september 1961 in Venray in Noord Limburg. Hij behaalde in juni 1979 het Atheneum-B diploma aan de Rooms-Katholieke Scholengemeenschap "Jerusalem" te Venray en begon in september van datzelfde jaar met de studie geologie aan de Rijksuniversiteit te Utrecht. Het kandidaats examen G3 (geologie met wis-, natuur- en scheikunde) werd afgelegd in maart 1982; het doktoraal examen met als hoofdvak strukturele geologie en als bijvakken materiaalkunde en exploratie geofysika (seismische methoden) werd behaald in oktober 1986. Zijn hoofdvaksskriptie handelde over de (mikro) strukturele geologie van het Lys-Caillaouas gebied in de centrale Pyreneeën.

Van 1 januari tot 1 augustus 1987 was hij in dienst als assistent-in-opleiding bij de afdeling strukturele geologie/HPT van de vakgroep geologie en onderzocht hij het effekt van water op het vloeigedrag van synthetische zout aggregaten in het HPT-laboratorium. Daarna werkte hij tot 1 augustus 1991 als onderzoeker-in-opleiding, en vanaf 1 augustus 1991 tot heden als onderzoeker bij dezelfde afdeling en werden de experimenten uitgevoerd die in dit proefschrift zijn beschreven. Vanaf 16 november 1992 zal hij als onderzoeker werkzaam zijn aan het Intstitut de Physique du Globe te Straatsburg.